BACTERIOPHAGE ENGINEERING FOR INDUSTRIAL APPLICATION

Marina Papaianni

Dottorato in Biotecnologie – XXXII ciclo

Università di Napoli Federico II

Dottorato in Biotecnologie – XXXII ciclo

Università di Napoli Federico II

BACTERIOPHAGE ENGINEERING FOR INDUSTRIAL APPLICATION

Marina Papaianni

Dottorando:	Marina Papaianni
Relatore:	Prof.ssa Rosanna Capparelli
Coordinatore:	Prof. Marco Moracci
Settore Scientifico Disciplinare	MED/04

"Scientists have
become the bearers of the torch
of discovery in our quest for knowledge"
Stephen Hawking

INDICE

RIASSUNTO

Introduzione

Xanthomonas campestris pv. *Campestris (Xcc)* è un batterio patogeno appartenente al phylum Proteobacteria, Gram-negativo, aerobico, catalasi positivo e ossidasi negativo. Presenta una forma bastoncellare ed una larghezza che va da 0.7 a 2.0 µm; è dotato di mobilità grazie alla presenza di un unico flagello.

L'infezione di *Xcc* provoca nell'ospite lesioni necrotiche a forma di "V" presenti sul margine fogliare, l'annerimento vascolare, avvizzimento, e problemi nel corretto sviluppo della pianta. *Xcc* è noto anche come agente eziologico della "black rot" una malattia che colpisce in particolar modo la famiglia delle Brassicacea. Essa si manifesta sulla superfice delle piante contaminate. Tale infezione, si verifica maggiormente nelle giovani piante e la contaminazione è favorita durante la stagione delle piogge, in quanto *Xcc* possiede pili che permettono un movimento a vela attraverso le foglie.

La caratteristica principale della "black rot" è la sua diffusione e colonizzazione all'interno dello xylema della pianta. Il batterio penetra nei tessuti della foglia attraverso gli stomi, gli idatodi, le radici o le lesioni. Negli stadi avanzati il tessuto colpito assume una colorazione marrone e necrotica, e una volta che la malattia si è estesa al sistema vascolare, possono comparire lesione da invasione sistemica lungo le nervature centrali delle foglie. Inoltre, una caratteristica bel nota di questo batterio è la sua capacità di produrre biofilm.

Il termine biofilm fu utilizzato per la prima volta nel XVII secolo quando si raggiunse la consapevolezza che microorganismi potessero colonizzare superfici di diversa natura e formare specifiche comunità. Questi in presenza di fattori ambientali e nutrizionali favorevoli, possono crescere sia singolarmente e fluttuare in un mezzo liquido (forma planctonica) oppure adesi a superfici biotiche o abiotiche come aggregati sessili. Il processo di formazione del biofilm è suddiviso generalmente in diverse fasi:

- Adesione alla superficie reversibile (adsorbimento), reso possibile grazie specifiche forze chimico fisiche che si instaurano tra il microorganismo e la superficie dove esso aderisce;

- Adesione irreversibile, ovvero un aumento dell'adesività e formazione di un unico strato di cellule batteriche adese alla superficie;
- Formazione di micro-colonie favorita dalla produzione di EPS;
- Maturazione del biofilm con la produzione di micro-colonie ed in seguito di macro-colonie;
- Distacco delle cellule batteriche in specifiche condizioni sia ambientali e nutritive.

Quando l'adesività risulta irreversibile, la concentrazione dei batteri inizia ad aumentare favorendo la produzione di materiale polimerico extracellulare (EPS) che costituisce la matrice del biofilm e forma le micro-colonie. Queste ultime andranno poi a formare le prime strutture tridimensionali definite come macro-colonie, fino a formare la complessa matrice del biofilm. Grazie alla capacità di fermentare, *Xcc* produce lo xantano, un polisaccaride extracellulare che dona alle colonie un aspetto mucoide. Questo polisaccaride è considerato un importante fattore di virulenza in quanto, protegge la cellula dalla disidratazione e favorisce l'adsorbimento alla cellula ospite. A maturazione ultimata, in specifiche condizioni ambientali, i batteri possono separarsi dal biofilm per riprendere la forma planctonica. Per il mantenimento di una comunità funzionale all'interno del biofilm è fondamentale che ci siano tali equilibri

Lo scopo primario della formazione del biofilm è sicuramente la protezione dei microorganismi dall'aggressione dell'ambiente esterno favorendo così il periodo di sopravvivenza. Infatti, quando crescono all'interno della matrice di biofilm, i batteri hanno una resistenza maggiore rispetto alle singole colonie. Inoltre, un fattore determinante è la resistenza del biofilm nei confronti degli antibiotici; tale resistenza sembra essere dovuta all'incapacità dell'antibiotico di penetrare all'interno del biofilm agendo di conseguenza, solo suoi microorganismi presenti sulla superfice più esterna mentre quelli posti all'interno agiscono come nucleo per una continua riproduzione. Anche il ridotto metabolismo di questi microorganismi fa in modo che questi siano meno sensibili agli antibiotici. Ulteriori meccanismi che favoriscono l'antibiotico resistenza sono dovuti alla matrice polisaccaridica che impedisce all'antibiotico di penetrare all'interno del biofilm e di conseguenza ne ritarda la diffusione.

Negli ultimi tempi risulta essere sempre più rilevante lo sviluppo di terapie alternative ai farmaci antibiotici, per questo l'impiego di batteriofagi (fagi) o molecole antimicrobiche naturali, sta diventando un argomento interessante nell'ambito della ricerca scientifica. Da un punto di vista strutturale i batteriofagi presentano un diametro di 23-32 nm, sono suddivisi in 6 morfotipi fondamentali, la cui organizzazione più complessa presenta un contenitore proteico isometrico (capside) che racchiude l'acido nucleico (DNA o RNA), collegato con un'appendice tubulare (coda) e appendici caudali con apparato contrattile in grado di iniettare il materiale genetico nel citoplasma del batterio. L'acido nucleico più comune risulta essere il DNA a doppio filamento, meno frequente quello a singolo filamento. Essendo i batteriofagi parassiti obbligati sono in grado di sopravvivere integrando il proprio genoma con quello di cellule batteriche che colonizzano.

I batteriofagi sono classificati in base alla morfologia, la natura e le caratteristiche del materiale genico ed il ciclo vitale: litico o lisogenico. In base a quale dei due cicli compiano, i batteriofagi posso essere classificati come: virulenti se attuano il ciclo litico o temperati quando attuano quello lisogenico. Il ciclo litico presenta diverse fasi:

- la fase di adsorbimento e penetrazione che prevede il legame di fibre presenti sulla coda del fago a recettori (lipopolisaccaidi, lipoproteine e acidi teicoici) situati sulla superfice batterica, in questo modo la placca basale si posiziona sulla membrana batterica, la coda si contrae e iniettano il loro genoma nell'ospite. A seguito di ciò la cellula batterica risponde producendo enzimi e proteine che permettono la sintesi di materiale genico ex novo causando la replicazione virale.
- la fase dell'assemblaggio che prevede l'immagazzinamento dell'acido nucleico all'interno del capside e la produzione di proteine che compongono la particella fagica quali la placca basale, la coda e le fimbrie.

Infine, la cellula va incontro a lisi mediante enzimi litici quali lisine, rilasciando le particelle virali assemblate.

Nel ciclo lisogenico in seguito alle due fasi di adsorbimento e penetrazione, il materiale genico del fago viene integrato nel cromosoma batterico ed ereditato dalle cellule figlie. In questo caso il fago viene chiamato profago e conferisce al batterio infettato l'immunità

contro fagi dello stesso tipo, inoltre il profago rimane latente all'interno della cellula infettata fino a quando stimoli esterni o stress non ne determinano la fuoriuscita causando la lisi della cellula con un meccanismo simile al ciclo litico.
La specificità dei fagi nei confronti di determinati batteri fa sì che l'utilizzo di quest'ultimi per il trattamento di particolari infezioni, comporti l'eliminazione di solo il ceppo specifico. Per ovviare a questo problema si possono realizzare cocktail di fagi ognuno in grado di infettare il proprio ceppo al fine di poter contrastare anche infezioni pluri-batteriche.
Un ulteriore vantaggio è rappresentato dalla crescita rapida ed esponenziale dei fagi quindi è possibile utilizzarne una piccola dose per poter controllare un'infezione batterica, e dato che questi si riproducono tramite i batteri, una volta debellata l'infezione batterica anche i fagi vengono eliminati o comunque rimangono latenti senza provocare alcun danno. Inoltre, contrariamente agli antibiotici che si diffondono in tutte le cellule, i batteriofagi si replicano solamente nel sito dell'infezione.
Sia l'identificazione che l'isolamento dei fagi risultano essere più rapide rispetto alla produzione di antibiotici, inoltre la resistenza dei batteri ai fagi risulta essere minore di circa dieci volte rispetto al numero di batteri che diventano resistenti agli antibiotici.
L'Idrossiapatite (HA) ha una struttura cristallina esagonale costituita da tetraedri di ioni PO_4^{3-}, in cui due atomi di ossigeno sono sul piano orizzontale, mentre gli altri due si trovano sugli assi paralleli, è un minerale appartenente alla famiglia delle apatiti e costituisce lo scheletro dei vertebrati. Si presenta in natura con una morfologia laminare, avente lunghezza di circa 110nm, larghezza 20nm e spessore di 8nm.
L'Idrossiapatite possiede specifiche caratteristiche chimico fisiche: è caratterizzato da alte temperature di fusione, durezza, un'alta resistenza alla compressione ma al tempo stesso una certa fragilità ed una difficile processabilità. Termodinamicamente, l'idrossiapatite è il composto più stabile rispetto ad altri fosfati di calcio in condizioni fisiologiche come temperatura e pH.

Obiettivi

il mio progetto di dottorato si inserisce nell'ambito della ricerca di nuove molecole che possano superare il problema dell'antibiotico resistenza che sta emergendo sempre di più. In dettaglio, partendo dal problema insorgente della lotta contro la *Xylella fastidiosa* che sta coinvolgendo oltre che tutto il sud Italia anche la maggior parte dell'Europa mi sono occupata dello studio di un metodo alternativo che potesse contrastare questo tipo di infezioni. Inoltre, dato la peculiarità di infezione che prevede la formazione del biofilm, mi sono occupata di identificare e caratterizzare un complesso costituito da un batteriofago litico, l'idrossiapatite, un noto carrier, e una molecola anti-biofilm prendendo come modello il batterio *Xanthomonas campestris* pv. *campestris* a causa delle restrizioni per l'utilizzo della *Xylella*. Lo studio si è basato in primis sull'analisi dei singoli elementi e successivamente sull'utilizzo sinergico dei tre.

Risultati

Capitolo I

È stato isolato e caratterizzato il ceppo utilizzato per tutti gli esperimenti futuri da piante che presentavano i sintomi della malattia black rot. La classificazione è avvenuta mediante Biolog. Successivamente è stato isolato il batteriofago e caratterizzato al fine di poterlo utilizzare sulle piante (*in vivo*). Le analisi molecolari e metaboliche effettuate dopo trattamento sulle piantine hanno permesso la caratterizzazione dell'attività litica del fago.

Capitolo II

È stato analizzato il biofilm di *Xanthomonas campestris* pv. *campestris* dopo trattamento con diverse molecole anti-biofilm al fine di determinare il composto che avesse maggior attività. Successivamente è stato testato l'acido eicosanoico, il composto scelto precedentemente, complessato con l'idrossiapatite (molecola carrier) e tramite analisi di microscopia confocale e real-time ne è stata validata l'attività anti-biofilm.

Capitolo III

Infine, l'analisi metabolica è stata effettuata al fine di determinare con precisione in che modo il fago potesse andare ad interagire non solo con il batterio, lisandolo, ma anche con il biofilm.

SUMMARY

The use of bacteriophages for controlling plant bacterial diseases is an increasing research field with great potential. Public concerns about environmental abuse of pesticides are increasing the popularity of organic production, that contributed to the growth of biological control agent studies, and their use in plant disease management. However, the efficient use of biocontrol agents requires good understanding of their biological characteristics and efficacy. Furthermore, phage therapy is an attractive option to prevent and control biofilm related infections, supposed to contribute to an improved success of such an integrated bacterial spot control strategy and to reduce the use of conventional pesticides, which is beneficial to the environment, and human and animal health.

Phage therapy is carried out by countless positive aspects that facilitate the battle against bacterial infections. The study of these processes has provided important scientific background about new intermediates, unusual nanoparticles, different gene organizations and special regulatory mechanisms, thus expanding older disciplines such as biochemistry, genetics and microbiology.

Several bacterial strains develop into resistant from different types of antibiotics; it is called multiple resistance antimicrobials if the resistance is for four or more different classes of antimicrobials.

In this contest, my PhD project aimed to the engineer a lytic bacteriophage in order to overcome the antibiotic resistance problems. Moreover, based to the biofilm problem the idea is to use an anti-biofilm molecule in synergy with the bacteriophage.

For this reason, my project was focused on the characterization of a bacteriophage, an anti-biofilm molecule, and a carrier that help the complexation.

The first part of my PhD was dedicated on the isolation of *Xanthomonas campestris* pv. *campestris*-specific bacteriophage from soil. It was further characterized by studying its plaque morphology, host range, pH stability, and morphology.

The second part of my project was focused on the detection of an anti-biofilm molecule and its possible application in combination with the phage carried by the hydroxyapatite.

The last part was on the study of the metabolic changed of the biofilm carried out by the phage and the anti-biofilm molecule.

All these results helped for better understand the best way to engineer the phage for translate all the result carried out to other bacterial infection.

INTRODUCTION

1) Xylella fastidiosa

Xylella fastidiosa is a gram-negative and xylem-limited bacterium [1], which assembles into biofilms, it is a xylem-limited bacterium transmitted to other plant species by Hemiptera insects which predict use xylem-fluid as main nutritional element. The presence of this bacteria can cause economic losses of both woody and herbaceous plant species [2]. There are over 150 host species of *X. fastidiosa* plants. This bacterium grows in the xylem vessels of the host plant, causing an obstruction and subsequent onset of the disease. Its virulence has been associated to biofilm formation in xylem vessels that prevent the passage of water and nutrients from the roots to the leaves [3]. *X. fastidiosa*, like related Xanthomonas plant pathogens, uses one or more related signal molecules known as diffusible signalling factor (DSFs) to regulate its behaviour in a cell density-dependent manner. DSFs are synthesized by RpfF, which has 3-hydroxyacyl-acyl carrier protein (ACP) dehydratase and thioesterase activity [4]. When DSF reaches a threshold concentration outside the cell, the bacteria activate their cognate receptor RpfC, a hybrid membrane sensor kinase that phosphorylates the intracellular response regulator RpfG. RpfG then converts the intercellular signal into an intracellular signal through its cyclic di-GMP phosphodiesterase activity, which in turn alters the expression of target genes [5]. RpfF-dependent signaling involving DSF species accumulation has been shown to regulate motility, biofilm formation, and virulence in several Xanthomonas species and in *X. fastidiosa* [6]. The spread of Hemiptera and the serious damage that *Xylella* is able to provide, identify it as relevant economic bacterium (Figure 1).

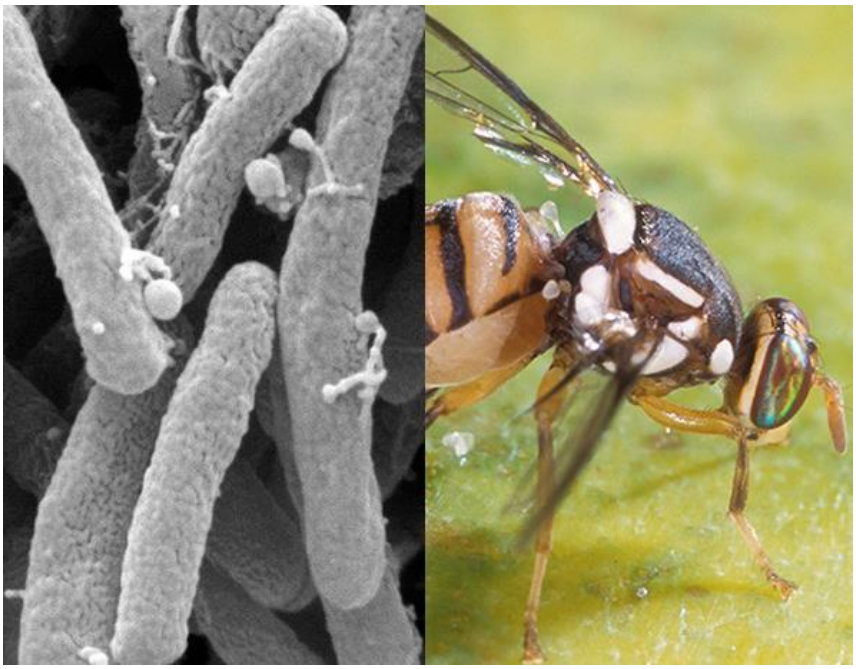

Figure 1: *xylella*-bactrocera https://www.ponteproject.eu/news/ippc-opens-expert-consultation-for-xylella-fastidiosa-and-bactrocera-dorsalis-complex/.

Some researchers have shown the ability of the bacterium to colonize new different geographic areas as Puglia, Corsica and Provenza-Alpi-Costa Azzurra; this represents a serious damage for all Europe. In the EU, *X. fastidiosa* has been identified as quarantine organism by the Council Directive 2000/29/EC ('Plant Health Directive') which contain the protective measures against the introduction of organisms harmful for plants or plant products into the Community. Due to 'Plant Health Directive', the bacterial species used for the experiments was *Xanthomonas campestris* pv. *campestris* which are very similar to *Xylella*.

Using the BLAST program (Basic Local Alignment Search Tool, https://blast.ncbi.nlm.nih.gov/Blast.cgi), the genome of *Xylella* species could be matched with *Xanthomonas* species after comparative analyses (Figure 2). *Xylella* shares ca. 74% of its genes with *Xanthomonas* species [7].

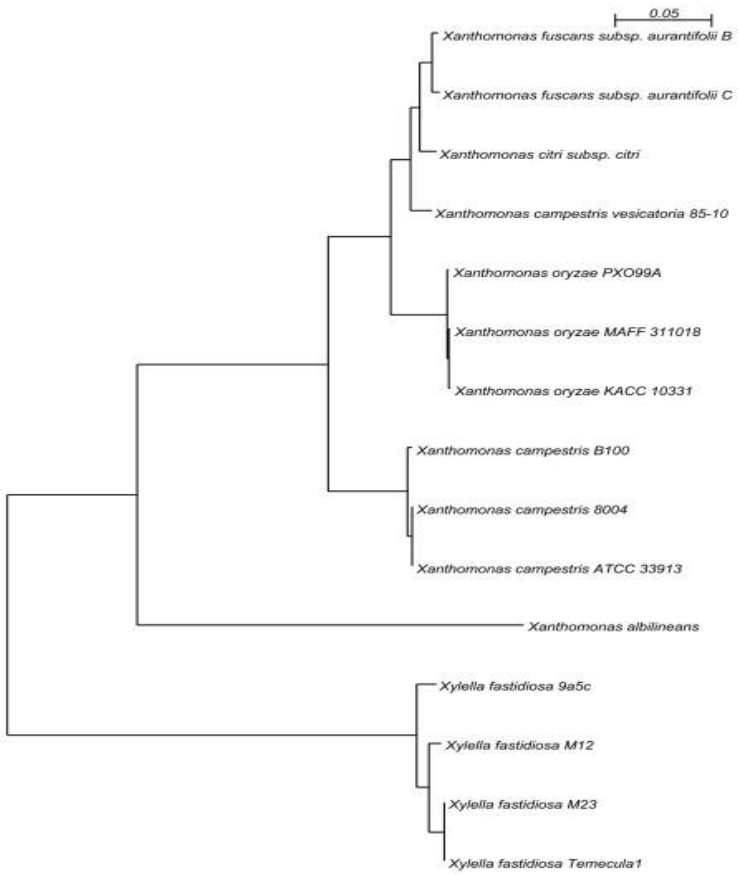

Figure 2 : https://www.researchgate.net/publication/43133302

Bacteriophages with dsDNA can infect many different bacterial species. With the sequencing of entire bacterial genomes, homologous genes of phages and prophages are described sometimes where no phage particles have been isolated. Each of these genomes accommodates at least one copy of a prophage, or remnants of a prophage, related to P2 coliphage or CTX of the *Pseudomonas aeruginosa* genomes. The genomes of *Xylella* strains have a high number of phage-related sequences integrated in the genome, constituting 7% of the Xf-CVC (strain 9a5c) genome and 9.02% of the Xf-PD (Temecula strain) genome [8]. Differently from *Xanthomonas*, *Xylella* genomes display large-scale genomic rearrangements probably because the presence of prophages or prophage-like elements [9]. Based on the previus study that describe the isolation of different phage from *X. fastidosa* that

are able to lysis both Xylella that *Xanthomonas* strain it seem to be plausible to focus the attencion on *Xanthomonas* strains [10].

2) Xanthomonas campestris pv. *campestris*

Xanthomonas campestris pv. *campestris (Xcc)* is the etiological agent of the “black rot”, describe for the first time by Harrison Garman in the 1889. This bacterium can infect both monocotyledon that dicotyledon - in particular *Brassica oleracea* such as cabbage, cauliflower, broccoli, and kale - cried and after the colonization of the host it start to produce xanthan that accumulates in the xylemic bundles stopping the contribution of the nutrient’s substances. When the bundles are completely jammed leaf, necrosis is determined seems a V, the browning whit the development of yellow border and the following drying of the stakeholders (Figure 3) [11].

Figure *3:* Leaf of infected cabbage by *Xcc.*

Due to the lack of water and nutrients, the plant remains small and weak, favouring the possible infection of other pathogenic microorganisms. The symptoms of the infection appear in the host 3 to 7 days after the colonization of the bacterium. *Xcc* are able to infect the host during the whole vital cycle of the plant (Figure 4). For example, it's verified during the flowering through the pollination by the insect that vehicles the bacteria [12]. The contaminated flower generates infected seeds. Unlike, the seeds can be infected less generally following the harvesting or the storage; at the last the contamination in carried out by the external surface of the seed but not in the inside [13].

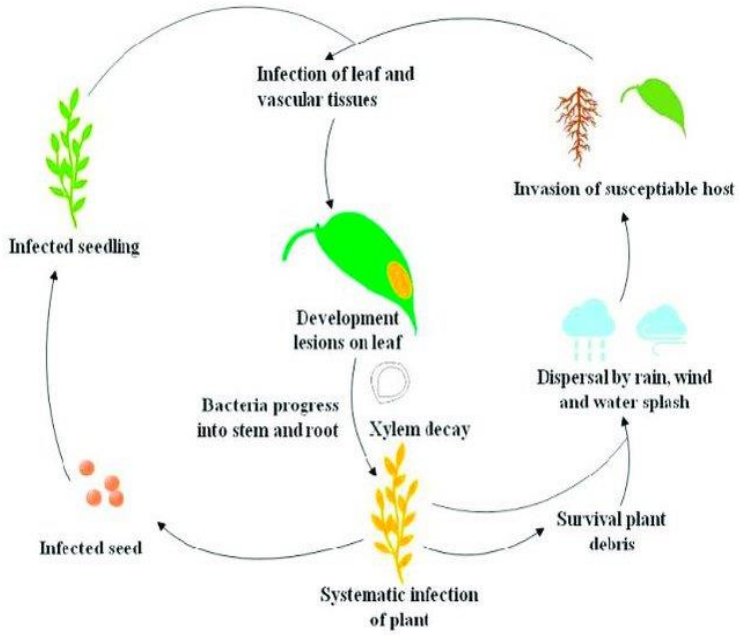

Figure 4: Infection cycle by *Xcc*. Researchgate.net/publication/338167535_Cupriavidus_sp_HN-2_a_Novel_Quorum_Quenching_Bacterial_Isolate_is_a_Potent_Biocontrol_Agent_Against_Xanthomonas_campestris_pv_campestris/figures?lo=1

It secretes biofilm that contains degradative extracellular enzymes such as cellulase, mannanase, pectinase, and protease, secreted by the type II secretion system [14]. The extracellular enzymes are able to degrade plant cell elements and induce plant tissue necrosis, and the effector proteins can interfere with cell plant immunity [15]. Moreover, it secretes the exopolysaccharide xanthan, which act as virulence factors [16].

3) Biofilm

The bacteria that produce biofilm undergo profound changes during their transition from planktonic (free-swimming) organisms to cells that are part of a complex, surface-attached community. These changes are reflected in the new phenotypic characteristics developed by biofilm bacteria and occur in response to a variety of environmental signals. Recent genetic and molecular approaches used to study microbial biofilms have identified genes and regulatory circuits important for initial cell-surface interactions, biofilm maturation, and the return of biofilm microorganisms to a planktonic mode of growth. Briefly, the planktonic-biofilm transition is a complex and highly regulated process. Basically,

the biofilm development has been characterized as a well-defined succession of different stages (Figure 5).

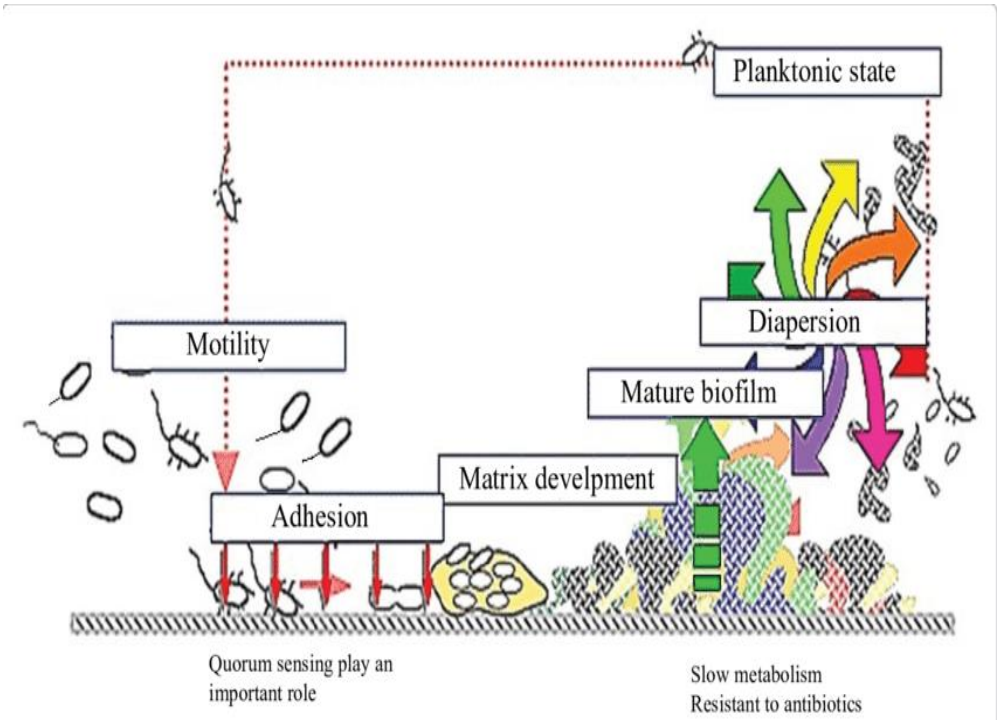

Figure 5: https://www.researchgate.net/publication/325091259_Bacterial_Biofilm_and_its_Clinical_Implications/figures?lo=1

First, an attachment phase, regulated by electrostatic interactions, hydrophobic interactions and Van der Waals forces, which involves an initial and reversible attraction of bacterial cells to the surface, and a subsequent but more tenacious and irreversible adhesion of the same. Then, a maturation phase, during which cells irreversibly attached to surfaces begin cell division forming microcolonies and produce exopolysaccharides (EPS) that allows the formation of the first three-dimensional structures of biofilm, macro-colonies.
Finally, a dispersal phase, which involves the detachment of single cells or groups of cells that can colonize surrounding or remote sites and promote the origin of a new biofilm.
One of the peculiarities of the *Xcc* and *Xylella* too is the DSF-mediated signalling that can regulate the transition from a non-adhesive, motile phenotype that allows systemic plant colonization to more adhesive cells that can form biofilms (Figure 6) [17]. DSF synthesis and signalling

is a well-known pathways that influence the virulence of several *Xanthomonas* spp., *X. fastidiosa*, and other strains know as opportunistic human pathogens [18,19]. DSF-deficient mutants have a reduced capacity to colonize their insect vector and to form biofilms in the insect foregut. This reduced retention leads to poor transmission to uninfected plants [20].

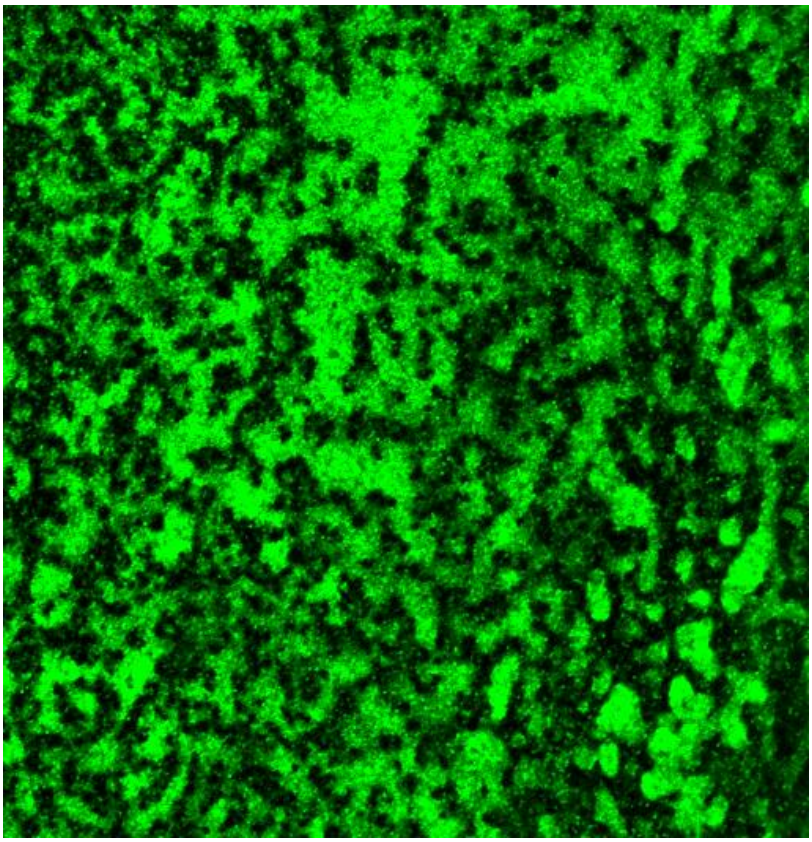

Figure 6: Representative image of Biofilm - using Confocal laser Scanner Microscopy- of Xcc

In particular, *rpfB* is a fatty Acyl-CoA ligase involved in the turnover of the DSF family of signals accumulate in the early stationary phase of growth, and their levels subsequently decline sharply [21]. This suggested the existence of a naturally occurring DSF signal turnover system which might be responsible for this decline in DSF signal levels during the stationary phase of growth. In Xcc, the *rpfB* gene located immediately upstream of *rpfF* was initially predicted to be involved in DSF biosynthesis [16]. Even though erstwhile results showed that *rpfF* also has its own promoter which would permit its expression in an independent way from *rpfB* [22]. Hence, it was suggested that *rpfB* may

be involved in DSF production in *Xcc* and *X*. *fastidiosa*, affecting the profile of DSF-like fatty acids as showed by Almeida R.P. [23]. Furthermore, different biochemical and genetic study had showed that, in Xcc, *rpfB* could functionally replace the archetypal bacterial fatty acyl-CoA ligase (FCL) *fadD*, a key enzyme involved in the beta-oxidation pathway in E. coli [4]. And in *X. fastidiosa rpfB* coordinates host vector and plant colonization [19].

4) Plant response

Plants are regularly exposed to several microorganisms in the environment, and present complex mechanisms to recognize and defend themselves against possible pathogens. Several studies have shown the concomitant downregulation of photosynthesis and other processes associated with primary metabolism, and upregulation of several primary metabolism that occurs during plant-pathogen interactions. It has been proposed that the energy released by down-regulation of primary metabolism is rerouted into defense responses. In addition, the upregulation of primary metabolism modulates signal transduction cascades [24].

The dynamic co-evolutionary conflict between phytopathogens and plants over the host nutritional resources has shaped distinct invasion strategies. Plants have developed several strategies to strip pathogens of nutrients. Upon timely perception of the presence of pathogenic microorganisms, a resistant plant can deploy assorted types of defense strategies to halt pathogen progress [25]. To support this hypothesis, several studies reported the evidence that upon exposure to pathogen, plants can modulate different genes associated with primary metabolic pathways, such as those involved in the synthesis or degradation of carbohydrates, amino acids and lipids. Furthermore, genetic analysis has confirmed the association of these metabolic pathways and plant defense responses [26].

The upregulation of several genes is associated with processes involved in energy production, such as glycolysis and the pentose phosphate pathway, TCA cycle, mitochondrial electron transport, ATP biosynthesis and biosynthesis of some amino acids such as lysine and methionine. The amino acids catabolism leads to energy production, as well as biosynthesis of glutamic acid, arginine, serine and glycine that are associated with photorespiration [27].

For the above reasons, the best way to understand the plant-pathogen interaction and system-wide alteration during the infection seems to be the metabolomic analysis. It is able to provide significant information

about compounds that play a pivotal role in plant innate immunity [28,29].

5) Bacteriophage

In agriculture several approaches are being developed to use natural antimicrobial agents that have no impact on humans or other non-target organisms [30]. For example fatty acid [31], secondary metabolite from *Trichoderma* [32]. Among natural antimicrobial agents, the bacteriophage (phage) is one of the best candidates. In disease control, phages have several potential advantages because they: undergo self-replication and self-limitation (when the infection is removed, they leave the host) [33]; are natural components and can be easily isolated from different environments [34]; are nontoxic for eukaryotic cells [35]; are specific or highly discriminatory, eliminating only target bacteria without damaging other, possibly beneficial, members of the indigenous flora [36].

The phage therapy is carried out by countless positive aspects that facilitate the battle against bacterial infections. The study of these processes has provided important scientific background about new intermediates [37], unusual nanoparticles [38], different gene organizations and special regulatory mechanisms [39], thus expanding older disciplines such as biochemistry, genetics and microbiology.

Multidrug resistance is one of the top three threats to global public health and is mostly lead to excessive drug management or prescription, improper use of antimicrobials, and substandard pharmaceuticals (pharmaceutical products that do not satisfy their quality standards and specifications) [40]. it is not surprising that expansion of antibiotic resistant bacteria has considerable interest in the scientific and medical community. This is evident from the number of researches that is being done on the subject [41].

Several bacterial strains develop into resistant from different types of antibiotics; it is called multiple resistance antimicrobials if the resistance is for four or more different classes of antimicrobials [42].

The phenomenon of antibiotic resistance was recognized in the 50s but during the last years has undergone a rapid increase not only in the health sector, but also in the veterinary, food, and environmental as there are interactions between man and the environment [43].

It is called Bacteriophage, or phage, a viral particle able to infect and replicate within bacteria. The use of phages has been studied to prevent the phenomenon of antibiotic-resistant bacteria [44]. Phages are ubiquitarian organisms that have been found in saltwater and sweet, in soil, plants, animals and humans (especially in the gastro-intestinal tract) [45].

If it concerns the phage therapy, the focus is on virulent phages that are associated to three main families such as *Myoviridae*, *Siphoviridae* and *Podoviridae* [46,47]. The lithic cycle starts with the adsorption and penetration in which phages are bound by the tail fimbriae to the receptors on the bacterial surface (lipopolysaccharides and lipoproteins) (Figure 7); in this way the basal plate is placed on the bacterial membrane, by the production of an enzyme (lysozyme) located in the tail, there is the reduction of the bacterial membrane stiffness.

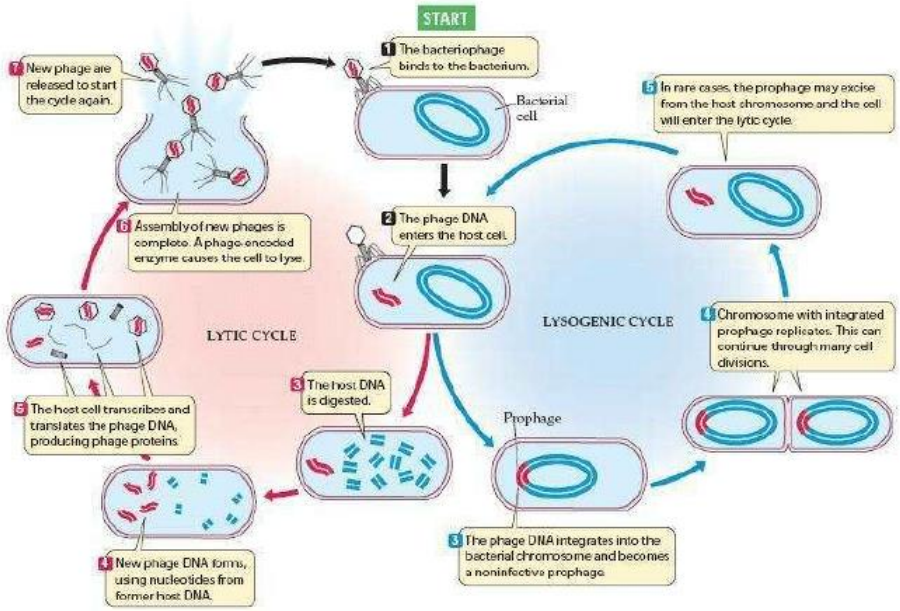

Figure 7: https://www.researchgate.net/publication/225987979_Mutual_mobile_membranes_with_objects_on_surface

The main advantage of the use of bacteriophages is the high specificity, because each phage is selective for a specie or for an individual strain. This characteristic is essential because, in this way, only the bacteria involved in a specific infection will be the targets of the phage. Based on specificity of bacteriophages against bacteria, is possible to personalize the bacteriophage therapy against an infection, so it is necessary to identify the responsible microorganism and consequently the specific phage.

A further advantage of phage therapy is that applying phages in only a single dose takes advantage of the phage potential to replicate and obtain an ‘active’ therapy, moreover significant phage development via auto “dosing” that results in greater bacterial cure. Achieving efficacy

following only a single dose, or far less frequent dosing, is an improvement, though in many or most instances a single dosage of phages should not be sufficient to obtain desired efficacy [48].
Since they reproduce through bacteria, once the infection has been eradicated, the phages are also eliminated [49].
The resistance to phages, however, could be the cause of a reduction in the virulence of the bacterium, making the resistant less virulent than the wild one [50].
Bacteriophages are used both as biological control or as therapy against bacteria in the agriculture and fishing [49]. In the United States, the FDA (Food and Drug Administration) has approved the use of phage, as alternative methods, for the decontamination of animals, plants and their derivatives meant to be human consumption.
Moreover, the classes of drugs that normally were used worldwide in agriculture, such as tetracyclines, aminoglycosides, β-lactams, lincosamides, macrolides, pleuromutilins, and sulphonamides create concern for their potential adverse effects [51]. Gelband et al., for example, noted that these antibiotics act in the same manner as those used for humans [52].

1. Sabella, E.; Aprile, A.; Genga, A.; Siciliano, T.; Nutricati, E.; Nicolì, F.; Vergine, M.; Negro, C.; De Bellis, L.; Luvisi, A. Xylem cavitation susceptibility and refilling mechanisms in olive trees infected by Xylella fastidiosa. *Sci. Rep.* **2019**, *9*, 1–11.
2. Marcelletti, S.; Scortichini, M. Genome-wide comparison and taxonomic relatedness of multiple Xylella fastidiosa strains reveal the occurrence of three subspecies and a new Xylella species. *Arch. Microbiol.* **2016**, *198*, 803–812.
3. Monteiro, M.P.; Clerici, J.H.; Sahoo, P.K.; Cesar, C.L.; de Souza, A.A.; Cotta, M.A. Stiffness signatures along early stages of Xylella fastidiosa biofilm formation. *Colloids Surfaces B Biointerfaces* **2017**, *159*, 174–182.
4. Bi, H.; Christensen, Q.H.; Feng, Y.; Wang, H.; Cronan, J.E. The Burkholderia cenocepacia BDSF quorum sensing fatty acid is synthesized by a bifunctional crotonase homologue having both dehydratase and thioesterase activities. *Mol. Microbiol.* **2012**, *83*, 840–855.
5. Ionescu, M.; Baccari, C.; Da Silva, A.M.; Garcia, A.; Yokota, K.; Lindow, S.E. Diffusible signal factor (DSF) synthase RpfF of Xylella fastidiosa is a multifunction protein also required for response to DSF. *J. Bacteriol.* **2013**, *195*, 5273–5284.
6. He, Y.W.; Xu, M.; Lin, K.; Ng, Y.J.A.; Wen, C.M.; Wang, L.H.; Liu, Z.D.; Zhang, H.B.; Dong, Y.H.; Dow, J.M.; et al. Genome scale analysis of diffusible signal factor regulon in Xanthomonas campestris pv. campestris: Identification of novel cell-cell communication-dependent genes and functions. *Mol. Microbiol.* **2006**, *59*, 610–622.
7. Moreira, L.M.; De Souza, R.F.; Digiampietri, L.A.; Da Silva, A.C.R.; Setubal, J.C. Comparative Analyses of *Xanthomonas* and *Xylella* Complete Genomes. *Omi. A J. Integr. Biol.* **2005**, *9*, 43–76.

8. Monteiro-Vitorello, C.B.; De Oliveira, M.C.; Zerillo, M.M.; Varani, A.M.; Civerolo, E.; Van Sluys, M.A. Xylella and Xanthomonas mobil'omics. *Omi. A J. Integr. Biol.* **2005**, *9*, 146–159.
9. Van Sluys, M.A.; De Oliveira, M.C.; Monteiro-Vitorello, C.B.; Miyaki, C.Y.; Furlan, L.R.; Camargo, L.E.A.; Da Silva, A.C.R.; Moon, D.H.; Takita, M.A.; Lemos, E.G.M.; et al. Comparative analyses of the complete genome sequences of Pierce's disease and citrus variegated chlorosis strains of Xylella fastidiosa. *J. Bacteriol.* **2003**, *185*, 1018–1026.
10. Ahern, S.J.; Das, M.; Bhowmick, T.S.; Young, R.; Gonzalez, C.F. Characterization of novel virulent broad-host-range phages of Xylella fastidiosa and Xanthomonas. *J. Bacteriol.* **2014**, *196*, 459–471.
11. Sundin, G.W.; Wang, N. Antibiotic Resistance in Plant-Pathogenic Bacteria. *Annu. Rev. Phytopathol.* **2018**, *56*, 161–180.
12. Van Der Wolf, J.; Van Der Zouwen, P. Colonization of Cauliflower Blossom (Brassica oleracea) by Xanthomonas campestris pv. campestris, via Flies (Calliphora vomitoria) Can Result in Seed Infestation. *J. Phytopathol.* **2010**, *158*, 726–732.
13. van der Wolf, J.M.; van der Zouwen, P.S.; van der Heijden, L. Flower infection of Brassica oleracea with Xanthomonas campestris pv. campestris results in high levels of seed infection. *Eur. J. Plant Pathol.* **2013**, *136*, 103–111.
14. Liao, C.-T.; Chiang, Y.-C.; Hsiao, Y.-M. Functional characterization and proteomic analysis of lolA in Xanthomonas campestris pv. campestris. *BMC Microbiol.* **2019**, *19*, 20.
15. Roux, B.; Bolot, S.; Guy, E.; Denancé, N.; Lautier, M.; Jardinaud, M.F.; Fischer-Le Saux, M.; Portier, P.; Jacques, M.A.; Gagnevin, L.; et al. Genomics and transcriptomics of Xanthomonas campestris species challenge the concept of core type III effectome. *BMC Genomics* **2015**, *16*.
16. Dow, J.M.; Crossman, L.; Findlay, K.; He, Y.Q.; Feng, J.X.; Tang, J.L. Biofilm dispersal in Xanthomonas campestris is controlled by cell-cell signaling and is required for full virulence to plants. *Proc. Natl. Acad. Sci. U. S. A.* **2003**, *100*, 10995–11000.
17. Beaulieu, E.D.; Ionescu, M.; Chatterjee, S.; Yokota, K.; Trauner, D.; Lindow, S. Characterization of a diffusible signaling factor from Xylella fastidiosa. *MBio* **2013**, *4*.
18. Chatterjee, S.; Newman, K.L.; Lindow, S.E. Cell-to-cell signaling in Xylella fastidiosa suppresses movement and xylem vessel colonization in grape. *Mol. Plant-Microbe Interact.* **2008**, *21*, 1309–1315.
19. Newman, K.L.; Almeida, R.P.P.; Purcell, A.H.; Lindow, S.E. Cell-cell signaling controls Xylella fastidiosa interactions with both insects and plants. *Proc. Natl. Acad. Sci. U. S. A.* **2004**, *101*, 1737–1742.
20. Ryan, R.P.; An, S. qi; Allan, J.H.; McCarthy, Y.; Dow, J.M. The DSF Family of Cell–Cell Signals: An Expanding Class of Bacterial Virulence Regulators. *PLoS Pathog.* **2015**, *11*.
21. Slater, H.; Alvarez-Morales, A.; Barber, C.E.; Daniels, M.J.; Maxwell Dow, J. A two-component system involving an HD-GYP domain protein links cell-cell signalling to pathogenicity gene expression in Xanthomonas campestris. *Mol. Microbiol.* **2000**, *38*, 986–1003.
22. Barber, C.E.; Tang, J.L.; Feng, J.X.; Pan, M.Q.; Wilson, T.J.G.; Slater, H.; Dow, J.M.; Williams, P.; Daniels, M.J. A novel regulatory system required for pathogenicity of Xanthomonas campestris is mediated by a small diffusible

signal molecule. *Mol. Microbiol.* **1997**, *24*, 555–566.
23. Almeida, R.P.P.; Killiny, N.; Newman, K.L.; Chatterjee, S.; Ionescu, M.; Lindow, S.E. Contribution of rpfB to cell-to-cell signal synthesis, virulence, and vector transmission of Xylella fastidiosa. *Mol. Plant-Microbe Interact.* **2012**, *25*, 453–462.
24. Rojas, C.M.; Senthil-Kumar, M.; Tzin, V.; Mysore, K.S. Regulation of primary plant metabolism during plant-pathogen interactions and its contribution to plant defense. *Front. Plant Sci.* **2014**, *5*, 17.
25. Bostock, R.M.; Pye, M.F.; Roubtsova, T. V. Predisposition in Plant Disease: Exploiting the Nexus in Abiotic and Biotic Stress Perception and Response. *Annu. Rev. Phytopathol.* **2014**, *52*, 517–549.
26. Rojas, C.M.; Senthil-Kumar, M.; Tzin, V.; Mysore, K.S. Regulation of primary plant metabolism during plant-pathogen interactions and its contribution to plant defense. *Front. Plant Sci.* **2014**, *5*, 17.
27. Brauc, S.; De Vooght, E.; Claeys, M.; Höfte, M.; Angenon, G. Influence of over-expression of cytosolic aspartate aminotransferase on amino acid metabolism and defence responses against Botrytis cinerea infection in Arabidopsis thaliana. *J. Plant Physiol.* **2011**, *168*, 1813–1819.
28. Hagemeier, J.; Schneider, B.; Oldham, N.J.; Hahlbrock, K. Accumulation of soluble and wall-bound indolic metabolites in Arabidopsis thaliana leaves infected with virulent or avirulent Pseudomonas syringae pathovar tomato strains. *Proc. Natl. Acad. Sci.* **2001**, *98*, 753–758.
29. Desbrosses, G.G.; Kopka, J.; Udvardi, M.K. Lotus japonicus metabolic profiling. Development of gas chromatography-mass spectrometry resources for the study of plant-microbe interactions. *Plant Physiol.* **2005**, *137*, 1302–18.
30. Kang, S.; Lander, G.C.; Johnson, J.E.; Prevelige, P.E. Development of bacteriophage P22 a platform for molecular display: Genetic and chemical modifications of the procapsid exterior surface. *ChemBioChem* **2008**, *9*, 514–518.
31. P. Desbois, A. Potential Applications of Antimicrobial Fatty Acids in Medicine, Agriculture and Other Industries. *Recent Pat. Antiinfect. Drug Discov.* **2012**, *7*, 111–122.
32. Vinale, F.; Marra, R.; Scala, F.; Ghisalberti, E.L.; Lorito, M.; Sivasithamparam, K. Major secondary metabolites produced by two commercial Trichoderma strains active against different phytopathogens. *Lett. Appl. Microbiol.* **2006**, *43*, 143–148.
33. Sabouri Ghannad, M.; Mohammadi, A. Bacteriophage: time to re-evaluate the potential of phage therapy as a promising agent to control multidrug-resistant bacteria. *Iran. J. Basic Med. Sci.* **2012**, *15*, 693–701.
34. Koskella, B.; Meaden, S. Understanding Bacteriophage Specificity in Natural Microbial Communities. *Viruses* **2013**, *5*, 806–823.
35. Górski, A.; Międzybrodzki, R.; Borysowski, J.; Dąbrowska, K.; Wierzbicki, P.; Ohams, M.; Korczak-Kowalska, G.; Olszowska-Zaremba, N.; Łusiak-Szelachowska, M.; Kłak, M.; et al. Phage as a Modulator of Immune Responses. In *Advances in virus research*; **2012**; Vol. 83, pp. 41–71.
36. Reddy, P.P. *Recent advances in crop protection*; Springer India: New Delhi, **2013**; ISBN 978-81-322-0722-1.
37. Malik, D.J.; Sokolov, I.J.; Vinner, G.K.; Mancuso, F.; Cinquerrui, S.; Vladisavljevic, G.T.; Clokie, M.R.J.; Garton, N.J.; Stapley, A.G.F.; Kirpichnikova, A. Formulation, stabilisation and encapsulation of

bacteriophage for phage therapy. *Adv. Colloid Interface Sci.* **2017**, *249*, 100–133.
38. Andriolo, J.M.; Hensleigh, R.M.; McConnell, C.A.; Pedulla, M.; Hailer, K.; Kasinath, R.; Wyss, G.; Gleason, W.; Skinner, J.L. Iron-doped apatite nanoparticles for improvement of phage therapy. *J. Vac. Sci. Technol. B, Nanotechnol. Microelectron. Mater. Process. Meas. Phenom.* **2014**, *32*, 06FD01.
39. Hagens, S.; Habel, A.; Von Ahsen, U.; Von Gabain, A.; Bläsi, U. Therapy of experimental Pseudomonas infections with a nonreplicating genetically modified phage. *Antimicrob. Agents Chemother.* **2004**, *48*, 3817–3822.
40. S, S.; N, I. Mechanisms of Antimicrobial Resistance in ESKAPE Pathogens. *Biomed Res. Int.* **2016**, *2016*.
41. Bhattacharjee, M.K. Development of Resistance to Antibiotics. In *Chemistry of Antibiotics and Related Drugs*; Springer International Publishing: Cham, **2016**; pp. 27–48.
42. Jassim, S.A.A.; Limoges, R.G. *Bacteriophages: Practical Applications for Nature's Biocontrol*;
43. Holmes, A.H.; Moore, L.S.P.; Sundsfjord, A.; Steinbakk, M.; Regmi, S.; Karkey, A.; Guerin, P.J.; Piddock, L.J.V. Understanding the mechanisms and drivers of antimicrobial resistance. *Lancet* **2016**, *387*, 176–187.
44. Yosef, I.; Manor, M.; Kiro, R.; Qimron, U. Temperate and lytic bacteriophages programmed to sensitize and kill antibiotic-resistant bacteria. *Proc. Natl. Acad. Sci. U. S. A.* **2015**, *112*, 7267–7272.
45. Andreoletti, O.; Budka, H.; Buncic, S.; Colin, P.; Collins, J.D.; De, A.; Griffin, J.; Havelaar, A.; Hope, J.; Klein, G.; et al. *The use and mode of action of bacteriophages in food production Scientific Opinion of the Panel on Biological Hazards Public consultation*; **2009**;
46. Furfaro, L.L.; Payne, M.S.; Chang, B.J. Bacteriophage Therapy: Clinical Trials and Regulatory Hurdles. *Front. Cell. Infect. Microbiol.* **2018**, *8*, 376.
47. Drulis-Kawa, Z.; Mackiewicz, P.; Kęsik-Szeloch, A.; Maciaszczyk-Dziubinska, E.; Weber-Dąbrowska, B.; Dorotkiewicz-Jach, A.; Augustyniak, D.; Majkowska-Skrobek, G.; Bocer, T.; Empel, J.; et al. Isolation and characterisation of KP34--a novel φKMV-like bacteriophage for Klebsiella pneumoniae. *Appl. Microbiol. Biotechnol.* **2011**, *90*, 1333–45.
48. Loc-Carrillo, C.; Abedon, S.T. Pros and cons of phage therapy. *Bacteriophage* **2011**, *1*, 111–114.
49. Inal, J.M. *Phage Therapy: a Reappraisal of Bacteriophages as Antibiotics*; **2003**; Vol. 51;.
50. Capparelli, R.; Nocerino, N.; Lanzetta, R.; Silipo, A.; Amoresano, A.; Giangrande, C.; Becker, K.; Blaiotta, G.; Evidente, A.; Cimmino, A.; et al. Bacteriophage-Resistant Staphylococcus aureus Mutant Confers Broad Immunity against Staphylococcal Infection in Mice. *PLoS One* **2010**, *5*, e11720.
51. Manyi-Loh, C.; Mamphweli, S.; Meyer, E.; Okoh, A. Antibiotic use in agriculture and its consequential resistance in environmental sources: Potential public health implications. *Molecules* **2018**, *23*.
52. The State of the World's Antibiotics, 2015 - Center for Disease Dynamics, Economics & Policy (CDDEP) Available online: https://cddep.org/publications/state_worlds_antibiotics_**2015**.

CHAPTER I

Article accepted to Frontiers in Microbiology

Plant dynamic metabolic response to bacteriophage treatment

Marina Papaianni[a,+], Debora Paris[b,+], Sheridan L. Woo[c,d], Andrea Fulgione[a,e], Maria M. Rigano[a], Ermenegilda Parrilli[f], Maria L. Tutino[f], Roberta Marra[a], Gelsomina Manganiello[a], Angela Casillo[f], Antonio Limone[e], Astolfo Zoina[g], Andrea Motta[b], Matteo Lorito[a,d,*] and Rosanna Capparelli[a,d,*].

a Department of Agricultural Sciences, University of Naples Federico II, 80055 Portici, Naples, Italy.
b Institute of Biomolecular Chemistry, National Research Council, 80078 Pozzuoli, Naples, Italy.
c Department of Pharmacy, University of Naples Federico II, 80131 Naples, Italy.
d Task Force on Microbiome Studies, University of Naples Federico II, 80131 Naples, Italy.
e Istituto Zooprofilattico Sperimentale del Mezzogiorno (IZSM), 80055 Portici, Naples, Italy.
f Department of Chemical Sciences, University of Naples "Federico II", 80126 Naples, Italy.
g Institute for Sustainable Plant Protection, National Research Council, 80055 Portici, Naples, Italy.
+ These authors contributed equally to this work

***Corresponding Authors**

Rosanna Capparelli

Department of Agricultural Sciences, University of Naples Federico II Via Università n. 133, 80055 Portici, Naples, Italy

Tel. 0039 0812539274

Fax.0039 0812531730

e-mail: capparel@unina.it

Matteo Lorito

Department of Agricultural Sciences, University of Naples Federico II Via Università n. 100, 80055 Portici, Naples, Italy

Tel. 0039 0812539376

Fax.0039 0812539339

e-mail: matteo.lorito@unina.it

Running Title: Metabolic changes triggered by bacteriophage

Author Summary

The use of bacteriophages (phages) could represent an alternative and efficient crop protection strategy able to control plant diseases. This study demonstrated the efficacy of a lytic bacteriophage to reduce the *Xanthomonas campestris* pv. *campestris* proliferation in *Brassica oleracea* var. *gongylodes.* Furthermore, for the first time, the effects of the phage treatment - in planta - were also investigated by metabolic analysis which allowed to evaluate the occurring changes based on a holistic approach.

Abstract

Periodic epidemics of black rot disease occur worldwide causing substantial yield losses. *Xanthomonas campestris* pv. *campestris* (*Xcc*) represents one of the most common bacteria able to cause the above disease in cruciferous plants such as broccoli, cabbage, cauliflower,

and *Arabidopsis thaliana*.
In agriculture, several strategies are being developed to contain the *Xanthomona*s infection. The use of bacteriophages could represent a valid and efficient approach to overcome this widespread phenomenon. Several studies have highlighted the potential usefulness of implementing phage therapy to control plant diseases as well as *Xcc* infection.
In the present study, we characterized the effect of a lytic phage on the plant *Brassica oleracea* var. *gongylodes* infected with *Xcc* and, for the first time, the correlated plant metabolic response.
The results highlighted the potential benefits of bacteriophages: reduction of bacterium proliferation, alteration of the biofilm structure and/or modulation of the plant metabolism and defense response.

Xanthomonas campestris pv. *campestris* | bacteriophages | plant infection | metabolic response |

Introduction

Xanthomonas campestris pv. *campestris* (*Xcc*) is an economically important bacterial plant pathogen worldwide causing black rot disease that devastates many cultivated cruciferous crops, producing V-shaped necrotic lesions on the foliar margins and blackened veins [1]. *Xcc* lives epiphytically on the leaf surface, infects the host penetrating stomas, hydathodes or wounds, and colonizes the vascular system of many Brassicaceae, including broccoli, cabbage, cauliflower, radish, and the model plant *Arabidopsis thaliana* [2]. *Xcc* infection is particularly harmful due to the formation of biofilm, which contains degradative extracellular enzymes and other virulence factors [3].

Plants have developed different defense mechanisms against pathogens [4]. They respond to “pathogen associated molecular patterns” (PAMPs) by activating a PAMP-triggered immunity (PTI) or an effector-triggered immunity (ETI) mediated by receptors able to specifically recognize pathogens [5,6]. The consequence can be the establishment of a “systemic acquired resistance” (SAR) status, which may increase resistance in the whole plant to subsequent attacks [5,7,8].

Defense responses have metabolic costs in terms of energy and resources, normally used to support processes of development and reproduction [9]. Indeed, during pathogen infection, photosynthesis is down regulated, as result of primary metabolism reorganization. Transcriptional analysis confirms that the metabolic reprogramming

caused by pathogen infection is mainly associated with genetic and biochemical changes in basic pathways, such as those involved in the synthesis or degradation of carbohydrates, amino acids, and lipids, as well as in defense response [10]. Contact with the pathogen often causes up-regulation of genes involved in energy production processes, such as glycolysis, the pentose phosphate pathway, Krebs cycle, mitochondrial electron transport, ATP and amino acid biosynthesis [11].

In agriculture, crop protection strategies based on beneficial microorganisms or naturally-derived antimicrobial agents are being developed in order to reduce the impact on non-target organisms, including humans [12]. To this end, bacteriophages (phages) may be particularly useful. They self-replicate only as long as the bacterial host is present, which may reduce the need of multiple applications [13]. Moreover, phages - being considered the most common biological entities on earth [14] - can be found in a variety of forms and environments [15]. They are nontoxic for eukaryotic cells and, due to their specificity, may not harm the soil beneficial microbiota [16–18].
Several studies have stressed the potential usefulness of implementing phage therapy to control plant diseases [19]. This is the case also of *Xcc*, for which different research groups have isolated specific phages [20]. However, the use of phage therapy in plants is still poorly studied.

Metabolomics is particularly apt to investigate plant-pathogen interactions, and to understand the mechanisms of innate immunity [21–23]. High-resolution NMR spectroscopy and multivariate data analysis have been widely used in order to evaluate the occurring changes based on a holistic approach [24]. However, to date, the metabolic impact of phage-bacterial infections on the plant have not yet been described.

In the present study, we isolated and characterized a lytic bacteriophage (Xccφ1) able to control the disease caused by *Xcc* to *Brassica oleracea* var. *gongylodes* and investigated the effect of *Xcc* and Xccφ1, applied singly or combined, on plant metabolome. Finally, our results indicate that phage-based treatments limit the bacterium proliferation, due to lysis of the host, to alteration of the biofilm structure and/or modulation of plant defense response.

Materials and Methods

Isolation of *Xanthomonas campestris* pv. *campestris* (*Xcc*). Leaves of cauliflower and kohlrabi plants with symptoms of Black rot were

collected from cultivated crops in Campania (Piana del Sele, Italy) during January - February 2017. After a thorough washing with tap water, tissue fragments were ground in sterile distilled water (SDW) and streaked on mCS20ABN agar medium [25]. Yellow mucoid colonies were extensively purified on Nutrient Agar (Sigma Aldrich, Milan, Italy) supplemented with glucose 0.5% (NAG). Single colonies were then suspended in SDW and stored at 4° C. The isolates were identified by the Biolog™ System (Hayward, CA, USA) as *Xcc*.

Species-specific PCR of *Xcc.* Molecular diagnosis of *Xcc* was carried out using the primers HrcCF2 (5'- CGTGTGGATGT GCAGACC-3') and HrcCR2 (5'-CAGATCTGTCT GATCGGTGTCG-3'), which amplify an internal fragment of 519 bp of hrcC [26].

Morphological characterization of *Xcc.* Curli and cellulose productions were detected by growing bacteria on Nutrient Agar supplemented with Congo-red (4 mg/ml Sigma Aldrich) and on Nutrient Agar supplemented with calcofluor (10 mg/ml Sigma Aldrich) respectively. Plates were incubated at 24- 25°C for 72 h. Calcofluor colonies were visualized under a 366-nm light source [27].

Isolation and growth of Xcc phages. Ten grams of rhizospheric soil of 100 cauliflower and kohlrabi plants with Black rot symptoms were suspended in 15 ml of Nutrient broth (Sigma Aldrich), and agitated for 30 min at 20° C. Soil sediments were removed by centrifugation, and the supernatants transferred to sterile flasks. Log-phase cultures of Xcc were added and flasks incubated overnight at 24°C in shaking condition. Cultures were clarified by centrifugation and filtered through a Millipore 0.22µm-pore-size membrane filter (MF-Millipore, Darmstadt, Germany). The filtrates were assayed for the presence of Xcc-infecting phage by plating (10 µl) on soft agar overlay for 48h. The clear plaque on soft-agar containing phage were picked and incubated for 4h at 37°C, centrifuged for 30 min at 5000 rpm and filtered through 0.22-µm-pore-size membrane filters 55. The experiment was performed for 5 time. At least, suspensions were stored at 4°C.

Host range analysis. The lytic activity of al the phage lysate was tested on 40 different Xanthomonas isolates (Tab). Individual Xanthomonas strains grown in NB to the exponential phase were added (500 µl) individually to tubes containing 4 ml of 0.7% agar (Sigma Aldrich, Milan, Italy). The suspension was transferred to a Petri dish with nutrient agar and let to solidify. Ten µl of all the phage were spotted on agar plates,

which were then incubated at 25°C for 48h (Garbe et al., 2010). The experiment was performed in triplicate.

Multiplicity of infection (MOI). The ratio between virus particles and host cells was used to determine the MOI 56. The Xcc strain was grown in Nutrient Broth (NB) at 24 °C to the concentration of 10^8 CFU/ml, as determined by measuring the optical density at 600 nm. Cells at the exponential growth phase, were infected with phage (10^3 to 10^{-3} PFU/CFU) in a 96 well plates (Corning® 96 Well CellBIND® Microplates, Sigma Aldrich), then incubated at 24° C for 48h. CFUs were counted by standard soft agar overlay assay [57,58]. Experiments were performed in triplicate. Optimal MOI, that resulted in the highest phage titer within 48 h incubation, was used in subsequent phage propagation.

Burst size analysis. One ml of exponential-growth-phase culture of Xcc in NB (10^8 CFU/ml) and phage suspension were mixed at MOI of 0.1. The mixture was incubated at 24 ° for 5 min to allow phage adsorption. Immediately after, the mixture was diluted to 10^{-4} in 50 ml Erlenmeyer flasks. Samples were taken from the diluted fraction at ten-minute intervals, serially diluted ten-fold and spotted on NA plates using the agar overlay technique. The experiment was repeated three times. The latent period was expressed as the time interval between phage adsorption (which does not include the 5-min pre-incubation time) and the first burst [59,60]. Burst size was calculated as the ratio between the final count of liberated phage particles and the initial count time of infected bacterial cells during the latent period.

pH stability. The phage stability at different pH was assessed using the double-layer agar technique. The pH of SM buffer was adjusted to the following values using 1M NaOH or 1M HCl: pH 1 to 11 61. Subsequently, the plates were incubated at 25°C for 48h. The lysis spots were picked and inoculated into 500 µl of buffer SM solutions at different pH and incubated at 37°C for 4h. The solutions were centrifuged at 5000 rpm at room temperature for 30 min, filtered through 0.22 µm filters (MF-Millipore) and incubated at RT for 7 days. Ten-fold dilutions of each solution were spotted (10 µl) on the agar plate. The plates were incubated at 25°C for 48h and evaluated the final concentration of each condition.

Phage purification. To purify Xccφ1, 1 ml of the lysate was centrifuged at 14K RPM for 2h at room temperature, then the supernatant was

discarded and 200 µl of 5 mM $MgSO_4$ (Sigma Aldrich) was added, and the pellet was incubated overnight at 5°C. The pellet was resuspended by gently pipetting up and down, diluted 2x and 4x in 5 mM $MgSO_4$.

Transmission Electron Microscopic analysis. The Xccφ1 stock (10^8 PFU/ml) was purified by CsCl density gradient ultracentrifugation (Centrifuge for 2.5 h 24K in the SW 28.1) and dialyzed against SM buffer overnight at 4°C. Phage particles were negatively stained with 2% phosphotungstic acid (pH 7.2) for 5 min. Phages were observed in a Philips EM 300 electron microscope.

Chemical analysis. Glycosyl analysis was performed as reported by Fresno et al., and Casillo et al. [28,29].

Confocal laser scanning microscopy. Biofilms were formed on polystyrene Nunc™ Lab-Tek® 8-well Chamber Slides (n° 177445; Thermo Scientific, Ottawa, ON, Canada). For this purpose, overnight cultures of *Xcc* in Nutrient broth were diluted to a cell concentration of about 0.001 ($OD_{600\ nm}$) and inoculated into each well of a chamber slide. The bacterial culture was incubated at 24°C for 72h in order to assess the biofilm thickness and cell viability. After 10^6 and 10^8 PFU/ml of phage was added for 6h. The biofilm cell viability was determined with the FilmTracer™ LIVE/DEAD® Biofilm Viability Kit (Molecular Probes, Invitrogen, Carlsbad, California) according to Papaianni et al. [14].

Static biofilm analysis. Biofilm formation was monitored using the Christal violet assay. *Xcc* bacteria were incubated for 72h in NB at 24°C and after the biofilm formation the galactose was added at different concentrations (from 0.5% to 2%) and incubated for 4h at 24°C. The biofilm was analyzed at 590 nm after the staining with Crystal violet (Sigma Aldrich) [30].

***In-planta* experiments.** Seeds of *B. oleracea* var. *gongylodes* – susceptible to the disease – were sown in 60-well Styrofoam planting trays containing steamed sterile soil peat mixture. The trays were kept for 48h in a germination chamber and then transferred to a glasshouse. All the experiments were carried out with a temperature of 15±2°C (night) and 25±2°C (day). At the stage of the second true leaf, the plantlets were used for the experiments. The *Xcc* strain was grown on NAG Petri dishes for 36 h at 28 °C and the bacterial growth suspended in SDW. The final bacterial concentration was spectrophotometrically

adjusted to the established level. Seedlings were treated using a hand-held plastic sprayer with SDW and suspensions of phage and *Xcc* supplemented with Tween 20 (5 µl per 100 ml). Two experiments were conducted. The first trial was performed to determine if the timing of phage application had any influence on the pathogenic activity of *Xcc* when the bacterium was inoculated on a host plant. Kohlrabi (*B. oleracea* var. *gongylodes)* plantlets were treated as follows: a) SDW, b) Xccφ1, c) *Xcc*, d) Xccφ1 24 hours before inoculation with *Xcc*, e) Xccφ1 and *Xcc* together, f) Xccφ1 24 hours after *Xcc,* g) Xccφ1 48 hours after *Xcc*. Both phage and bacterium were suspended in SDW at 10^7 PFU/mL and 10^7 CFU/mL respectively.
The second trial was performed to determine if the concentration of the phage application influenced the pathogenic activity of *Xcc;* the plantlets were treated as follows: a) SDW, b) Xccφ1 10^9 PFU/mL, c) *Xcc* 10^8 CFU/mL, d) Xccφ1 10^9 PFU/mL and *Xcc* 10^8 CFU/mL together. Trials were planned according to a randomized block design with three replications for each treatment. Each replication was made up of one tray with 60 plantlets. After inoculation, the plantlets were kept under clear plastic storage boxes, irrigated daily and misted with distilled water twice a day to maintain a high level of relative humidity to aid infection by the pathogen. Fifteen days after inoculation, infection symptoms were rated according to a four-level arbitrary disease scale whereby: 0 (no symptoms) to 3 (all leaves with symptoms and/or strong defoliation). The empirical scale allowed the calculation of McKinney's index, expressed both as the weighted average of the disease and as a percentage of the maximum possible level [31]. The non-transformed values of the McKinney indexes were submitted to analysis of variance (ANOVA) and the significance of the differences was calculated by Tukey's multiple range test ($p<0.05$).

RNA extraction and expression profiling by qPCR. Plantlets treated as described in the second trial of the *in planta*-experiments were used to analyze the expression profiling of genes involved in (1) synthesis/degradation of GABA at 15 days post-inoculation (dpi) or (2) in disease resistance at 48 h post inoculation (hpi). Plants were washed with SDW and immediately frozen in liquid nitrogen. Total RNA was extracted and purified using PureLink® RNA Mini Kit (Ambion Inc., Austin, TX, USA) from a pool of equal amounts of the powdered plant tissue obtained from 3 biological replicates for each treatment. Removal of genomic DNA was performed by digestion with DNase I, Amplification Grade (Invitrogen, USA). The Qubit™ RNA BR Assay Kit

and Qubit™ 2.0 Fluorometer (Life Technologies, Thermo Fisher Scientific Inc., Denver, CO, USA) were used to assess total RNA quantity, while the quality was verified by NanoDrop® ND-1000 (Thermo Fisher Scientific Inc.). Only RNA samples with 230/260 and 260/280 ratios >2 were used in the further analyses. One µg of purified total RNA was used as a template for first-strand cDNA synthesis using SuperScript® III Reverse Transcriptase (Invitrogen). Gene transcript levels were measured using Power SYBR® Green PCR Master Mix (Applied Biosystems®) on a QuantStudio™ 3 Real-Time PCR System (Applied Biosystems®, Thermo Fisher Scientific, Waltham, MA, USA) with the following conditions: an initial step at 95 °C for 10 min, followed by 45 cycles of 95 °C for 10 s, 60 °C for 20 s and 72 °C for 10 s. QuantStudio Design & Analysis Sofware v1.1 (Applied Biosystems) was used for analysis of gene expression. All samples were normalized to actin as reference housekeeping gene. The relative quantitative expression was determined using the $2^{-\Delta\Delta CT}$ method [32]. All primers used in this work are reported in Table S2 [33,34].

Extraction procedure and sample preparation for NMR. Forty plants (0,5 g/plant) from each of the four conditions tested in the second trial were used for the sample preparations. To extract the metabolites of interest (*e.g.*, lipids, carbohydrates, amino acids and other small metabolites), while leaving DNA, RNA and proteins in the tissue pellet, tissues were mechanically disrupted. Combined extraction of polar and lipophilic metabolites was carried out by using a methanol/chloroform protocol [23].
Prior to NMR analysis, the methanol/water fractions were resuspended in 630 µl of phosphate buffer saline (PBS, pH 7.2), and 70 ml of a deuterated-water solution (containing 1 mM sodium 3-trimethylsilyl [2,2,3,3-$^{2}H_4$] propionate (TSP) as a chemical shift reference for ^{1}H spectra). The deuterated solvent was added to provide a field-frequency lock so that each sample reached 700 ml of total volume into the NMR tubes.

NMR analysis. One-dimensional (1D) spectra were recorded on a Bruker Avance III–600 MHz spectrometer (Bruker BioSpin GmbH, Rheinstetten, Germany), equipped with a TCI CryoProbe*™* fitted with a gradient along the Z–axis, at a probe temperature of 27°C. One-dimensional (1D) proton spectra were acquired at 600 MHz by using the excitation sculpting sequence [35]. A double-pulsed field gradient echo was used, with a soft square pulse of 4 ms at the water resonance

frequency, with the gradient pulse of 1 ms each in duration, adding 516 transients of 16384 points with a spectral width of 8417.5 Hz. Time-domain data were all zero-filled to 32768 points, and prior to Fourier transformation, an exponential multiplication of 0.8 Hz was applied. For two-dimensional (2D) clean total correlation spectroscopy (TOCSY) [36,37] spectra we used a standard pulse sequence with a spin-lock period of 64 ms, achieved with the MLEV–17 pulse sequence, and incorporating the excitation sculpting sequence for water suppression. In general, 256 equally spaced evolution-time period t_1 values were acquired, averaging 64 transients of 2048 points, with 8403.36 Hz of spectral width. Time-domain data matrices were all zero-filled to 4096 points in both dimensions, thus yielding a digital resolution of 2.04 Hz/pt. Prior to Fourier transformation, a Lorentz-to-Gauss window with different parameters was applied for both t_1 and t_2 dimensions for all the experiments. Spectra in water were referred to internal 0.1 mM TSP, assumed to resonate at δ = 0.00 ppm. Natural abundance 2D ^{1}H–^{13}C heteronuclear single quantum coherence (HSQC) spectra were recorded at 150.90 MHz for ^{13}C, using an echo-antiecho phase sensitive pulse sequence with adiabatic pulses for decoupling [38,39] and pre- saturation for water suppression [9]. 128 equally spaced evolution time period t_1 values were acquired, averaging 240 transients of 2048 points and using GARP4 for decoupling. The final data matrix was zero-filled to 4096 in both dimensions, and apodized before Fourier transformation by a shifted cosine window function in t_2 and in t_1. Linear prediction was also applied to extend the data to twice its length in t_1. HSQC spectra in water were referred to the α-glucose doublet resonating at 5.24 ppm for ^{1}H and 93.10 ppm for ^{13}C.

Multivariate data analysis. The 0.70–9.70 ppm spectral region of aqueous extracts was automatically data reduced to integrated regions (buckets) of 0.02-ppm width using the AMIX 3.9.7 package (Bruker Biospin GmbH). The residual water resonance region (4.50–5.06 ppm) was excluded, and each integrated region was normalized to the total spectrum area. To discriminate samples using NMR profiles, a multivariate statistical data analysis was carried out using projection methods. The matrix of the integrated data was imported into SIMCA14 package (Umetrics, Umeå, Sweden) and Principal Component Analysis (PCA) and Orthogonal Projection to Latent Structures Discriminant Analysis (OPLS–DA) were performed. Unit variance scaling was used as data pre-treatment for both PCA and OPLS–DA. PCA was first

applied as unsupervised strategy to identify data trends. Next, OPLS-DA was used to better define clustering and relate metabolic variations to pathophysiological changes [40]. Validation of the models was carried out using 7-fold cross–validation and permutation tests (800 repeats) to verify possible model overfit. The quality of all PCA and OPLS–DA models was evaluated using the regression correlation coefficient R^2 and the cross-validate correlation coefficient Q^2. Normality test (Shapiro-Wilk and D'Agostino K squared) on normalized buckets of discriminant metabolites and non-parametric Kruskal-Wallis Anova test were performed with the OriginPro 9.1 software package (OriginLab Corporation, Northampton, USA). Moreover, for multiple comparisons, the Dunn Kruskal-Wallis test with Bonferroni correction was implemented in R [41] (https://www.R-project.org), all the test results and the adjusted p-values are presented in supporting information material. Signal variations were presented as chemical shift assignments (Table S1). Results were considered statistically significant at $p<0.05$.

Pathway Analysis. Pathway topology and biomarker analysis on selected and more representative discriminating metabolites were carried out using specific tools in Metaboanalyst 4.0 [42]. We calculated the centrality through the Pathway Impact, a combination of the centrality and pathway enrichment results. Metabolites were selected by evaluating both VIP values >1 in class discrimination and correlation values |pq[corr]| >0.7. *Arabidopsis thaliana* pathway library was chosen and analyzed using Fisher's Exact Test for over representation and Relative- betweenness Centrality for pathway topology analysis.

Results

Isolation and characterization of *Xcc*. Twenty-seven bacterial isolates were obtained from *B. oleracea* plants displaying typical symptoms of *Xcc* infection and identified by PCR using *Xcc*-specific primers. Ten isolates resulted positive (Figure 1A) and were found to produce the main components of *Xanthomonas* biofilm (cellulose and curli) (Figure 1B and 1C).

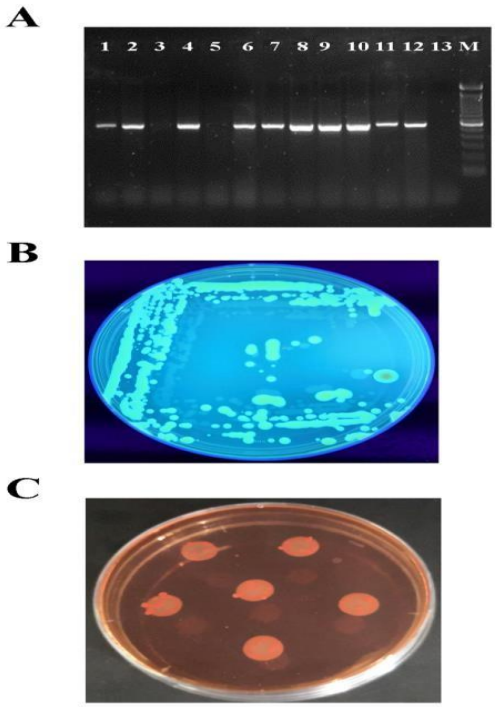

Figure 1. *Xanthomonas campestris* pv. *campestris* characterization: (A)Identification of the isolates by PCR amplification of the *Xcc* specific gene HrcC. Lanes 1-13: bacterial DNA; M: Marker (100 bp DNA Ladder). (B)Colony fluorescence on calcofluor agar plates due to cellulose synthesis. (C) Colonies on Congo red demonstrating the pdar phenotype due to the presence of fimbriae.

Isolation and characterization of phage Xccφ1. Phages were isolated from 17 soil samples obtained from the rhizosphere of *Brassica* plants. All phages displayed the same host range, were specific to X. campestris pathovar campestris only, forming clear plaques on all Xcc isolated from different area. Any phage isolated and tested are able to lyse the other X. campestris strains tested (Table S1). On soft agar, Xccφ1 consistently formed clear plaques of approximately 2-3 mm in diameter (Figure 2A). Analysis by transmission electron microscopy (TEM) revealed a structure typical of the *Myoviridae* family, with a contractile, long and relatively thick tail (120x30nm), and a central core separated from the head by a neck (Figure 2B) [43]. Adsorption rate of Xccφ1 (27°C; 20 min) was 85%, 70% and 65% at 10^5, 10^6, and 10^7 PFU/ml, respectively. The latent period and burst size were 30 min and 42±4 viral particles per infected cell, respectively, while the rise period was 30 min (Figure 2C). The phage growth curve displayed the canonical phases of latency, replication, and host lysis (Figure 2C). The

lytic activity was phage concentration independent (Figure 2 D). The host range of Xccφ1 included 12 bacterial isolates from Brassica plants (cauliflower, kohlrabi and rocket). The concentration of the phage was not affected at pH 5 and 7.5 in SM buffer or in water (Figure 2E).

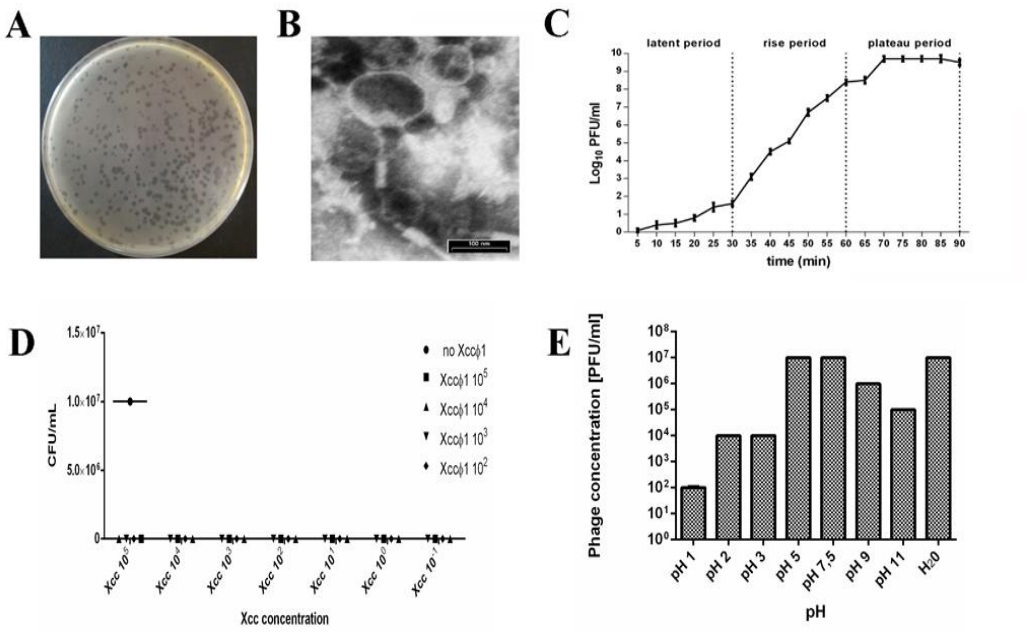

Figure 2. Xccφ1 characterization: (A) plaques on soft agar of approximately 2-3 mm in diameter. (B) Phage structure as observed by Transmission Electron Microscopy (TEM). Bar = 100 nm. (C) One step growth curve of phage. (D) Representation of phage activity on a Xcc growing. The figure shows the final bacterial plate counts (CFU/mL) after the treatment with the phage and growth on Nutrient Agar. Each value is the mean ± DS of 3 independent experiments. (E) Phage stability in SM buffer at different pH and H_2O control. ***, $p<0.001$. Statistical analysis was performed with Student's t test. Values are the mean ± SD from 3 independent experiments with 3 replicates for each data point.

Chemical analysis. Glycosyl analysis of *Xcc* cells in biofilm (Figure 3A) revealed the presence of rhamnose (Rha), mannose (Man), glucose (Glc), and traces of galactosamine (GalN) and glucosamine (GlcN), all main components of exopolysaccharides (EPS) [44]. Phage analysis (Figure 3B) indicated the presence of Glc, galactose (Gal) and, at a lower concentration, Man, whereas the latter two are uncompetitive inhibitors of bacterial biofilm stability. These findings may suggest the role of galactose instead of mannose on biofilm maintenance and thus on the phage activity [45].

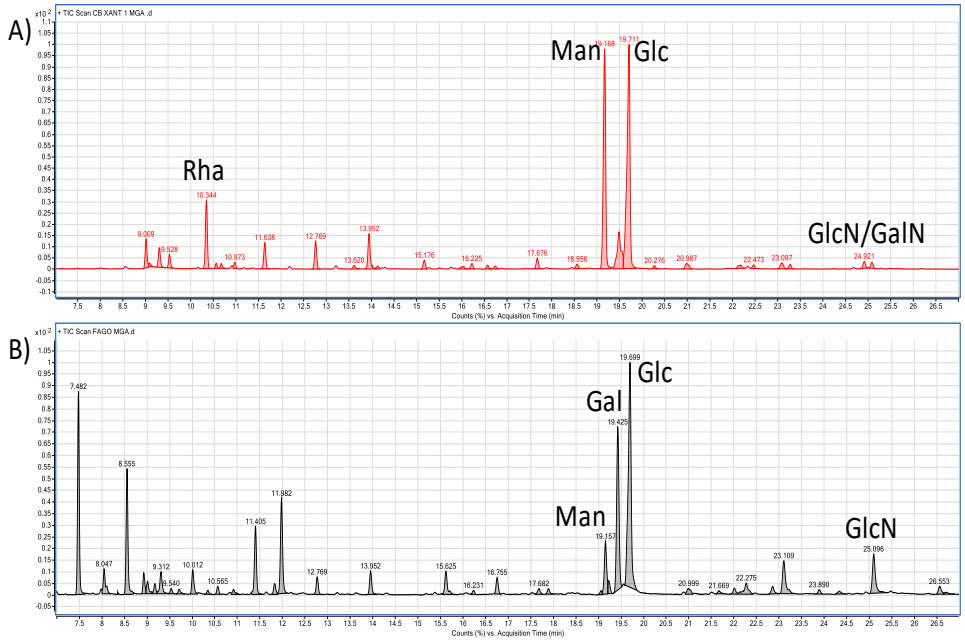

Figure 3. Gas chromatography-mass spectrometry (GC-MS) analysis of (A) *Xcc* cells in biofilm, and (B) Xccφ1 particles. Rha, Rhamnose; Man, mannose; Glc, glucose; GalN, galactosamine; GlcN, glucosamine; Gal, galactose.

Confocal laser scanning microscopy (CLSM). The biofilm analyzed by CLSM showed a structure that appeared thick and multi-layered in the absence of the phage and collapsed when bacteria were treated with Xccφ1 (Figure 4). The effect of the phage was concentration dependent, with a dose of 10^8 PFU/ml added to the bacterial culture demonstrating a greater reduction in the structure of the biofilm in comparison to a dose of 10^6 PFU/ml (cfr. Figs 4B and C). The biofilm was also reduced by a treatment with galactose, a sugar present as a component of the Xccφ1 capsid (Fig 3B)[46], whereby different non-toxic concentrations (from 0.5% to 2%) were effective on the biofilm and 1.5 and 2% are significant ($p<0,001$)(Figure S1). These findings indicate that the efficacy of biofilm disaggregation activity exerted by the phage may be supported by galactose, a result in line with a previous study [47].

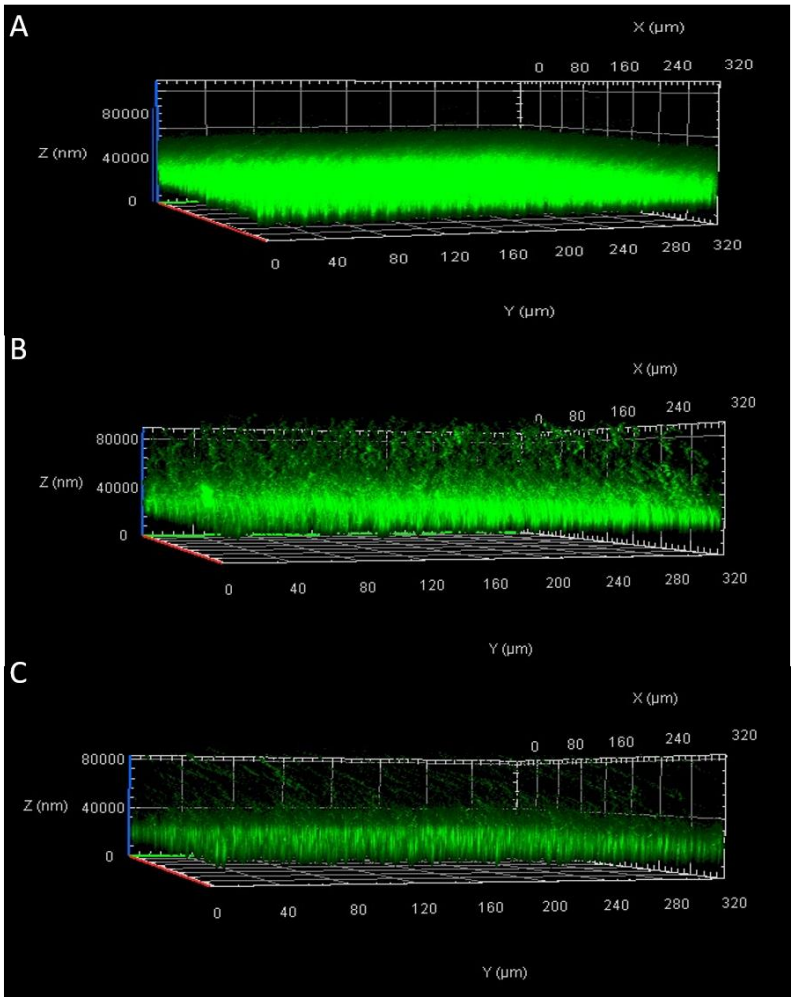

Figure 4. Effect of Xccφ1 phage concentration on the structure of *Xcc* biofilm as analysed by Confocal Laser Scanning Microscopy (CLSM): (A), *Xcc* alone; (B), *Xcc* after 6h of incubation with phage at 10^6 PFU/ml; (C), *Xcc* after 6h of incubation with phage at 10^8 PFU/ml. Bacteria were grown for 72 h in 8-well chamber slides and stained with LIVE/DEAD reagents. Green fluorescence (SYTO9) indicates viable and red fluorescence (PI) dead cells.

Phage activity *in planta*. *B. oleracea* var. *gongylodes* plantlets were treated by spraying the aerial vegetative parts with suspensions of the phage and the bacterium at different times and concentrations. The results of the first trial showed a statistically significant decrease (20%) in disease symptoms on plants treated with the anticipated application of the phage 24 hours before *Xcc* (Figure S2). The effects on disease development were not significant when the phage and bacteria were sprayed together, at the same time. When the phage was applied 24 or 48 hours after the *Xcc* inoculation, there was no disease control. In the

second trial, Xccφ1 was applied together with *Xcc*, both at higher concentrations than those used previously (Xccφ1 at 10^9 PFU/ml and *Xcc* at 10^8 CFU/ml). In this case, the development of the disease symptoms was reduced by about 45% (Figure 5). Interestingly, in the glasshouse Xccφ1 survived and was detected on the plant leaf surfaces up to six weeks after application. Furthermore, plants that received the treatments with the phage alone exhibited no symptoms but were visually greener in vegetative growth than the water-treated controls (data not shown).

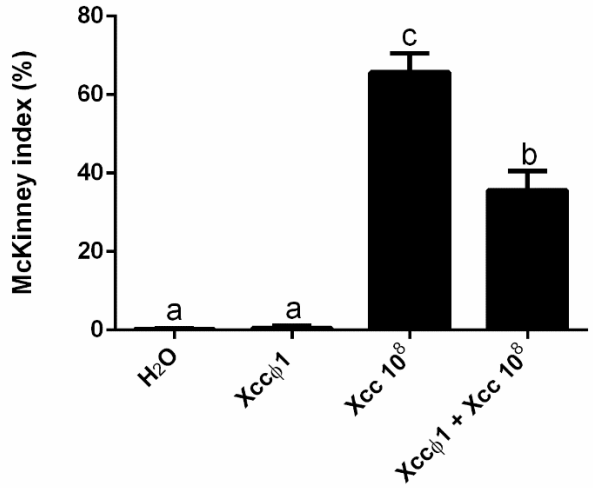

Figure 5. Effect of the Xccφ1 phage treatments on *Xcc* disease severity, as measured by the McKinney index, with foliar applications to plants of *B. oleracea* var. *gongylodes*. Xcc was inoculated at 10^8 CFU/ml, while Xccφ1 at 10^9 PFU/ml. In the combined treatment, phage and bacterium were applied simultaneously. Values are the mean ± SD of three replicates (60 plantlets each) per treatment. Bars labeled with the same letter are not statistically different at the Tukey test (p< 0,05).

NMR-based metabolomic analysis. We acquired 92 ^{1}H-NMR spectra from extracts (polar fraction) obtained from leaves of *B. oleracea* var. *gongylodes* receiving the phage and bacterium treatments conducted in the second trial. For each treatment, the most representative samples were analyzed by 2D NMR analysis. All resonances were identified by comparing 2D data with the literature and/or online databases (Table S1). 1D-NMR metabolic profiles were subjected to multivariate statistical analysis in order to detect trends and clusters [48].

We tested the following leaf samples: 26 untreated (NT), 25 infected with *Xcc (Xcc)*, 23 treated with *Xcc* plus the phage (*Xcc*+Xccφ1), and 18 treated with the phage alone (Xccφ1).

Unsupervised PCA models (data not shown) displayed a clear clustering into four distinct groups that corresponded to the treatments and excluded the potential presence of outliers.

OPLS-DA was applied to improve group separation. Regression analysis generated a robust model (R^2 = 0.97, Q^2 = 0.96) with three predictive components, and a clear separation in the scores plot (Figure 6A). In particular, the first component t[1] clearly differentiated the *Xcc* (red squares) and the *Xcc* + Xccφ1 groups (blue squares) from the phage Xccφ1 group (purple squares), with the NT group (green squares) located in the middle (Figure 6A). The second component t[2] discriminated between the *Xcc* and the *Xcc* + Xccφ1 groups, with the latter located very close to the control group (Figure 6A). The third component (t[3] on t[1]) differentiated the NT group along the t[3] positive axis (Figure S3).

Hence, the projection of all samples along the combination of the first and the second components reflected the specific metabolic alterations among different groups, which cluster in specific areas of the statistical model. The *Xcc* and the Xccφ1 groups appeared in the III and the IV quadrants of the score plot, respectively, while the *Xcc*+Xccφ1 group is placed in the II quadrant, adjacent to the NT group (Figure 6A). This result indicates a small metabolic variation between healthy controls and leaves infected with both the phage and the bacterium. Therefore, the presence of Xccφ1 may have resulted in a significant variation of the disease-associated plant metabolome.

The loadings plot helped in the identification of NMR variables responsible for group separation (Figure 6B). We considered as discriminating only signals (bins) with variable influence on projection (VIP) values >1 and |pq[corr]| >0.7.

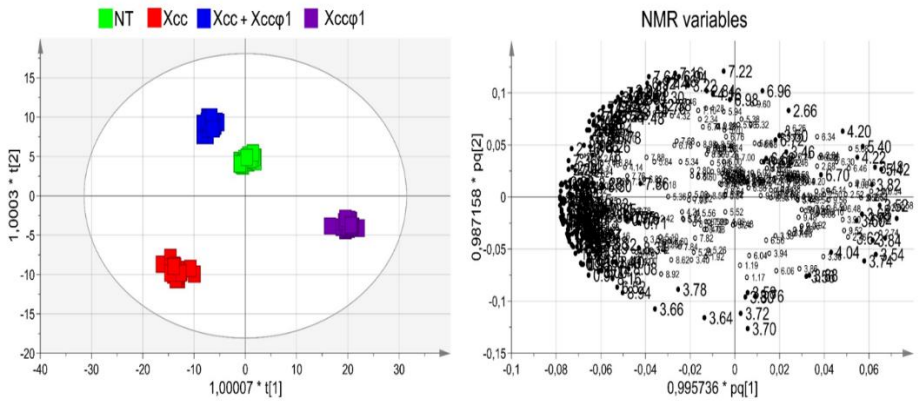

Figure 6. Metabolomic analysis (OPLS-DA of NMR data) of leaf extracts from *B. oleracea* var. *gongylodes* treated with *Xcc* and *Xcc*+Xccφ1. (A) Scores plot (97%, $p < 0.0001$) showing the separation of the treatments: NT (water); *Xcc* (bacteria alone); *Xcc*+Xccφ1 (*Xcc* plus Xccφ1 phage); Xccφ1 (phage alone). R^2 was 0.97 and Q2 was 0.96. (B) Loadings plot associated with the OPLS-DA analysis reported in (A), indicating determining NMR variables. Numbers refer to buckets' chemical shifts (spectral positions), and their size indicated the more discriminating buckets. The pq[1] and pq[2] values refer to the weight that combines the X and Y loadings (p and q).

Statistically relevant biochemical information was obtained from discriminating metabolites in the OPLS-DA model, by using a univariate statistical analysis. Metabolite set enrichment analysis (MSEA) identified 30 major metabolic pathways involved and significantly modified processes in the plants. Among these: alanine, aspartate and glutamate ($p = 3.1 \times 10^{-5}$, impact = 0.44); arginine and proline ($p = 4.5 \times 10^{-3}$, impact = 11); valine, leucine and isoleucine biosynthesis ($p = 1.1 \times 10^{-2}$, impact = 0.04); galactose ($p = 1.1 \times 10^{-2}$, impact = 0.05); lysine biosynthesis ($p = 1.4 \times 10^{-2}$, impact = 0.07); sucrose ($p = 1.7 \times 10^{-2}$, impact = 0.09), and glyoxylate and dicarboxylate ($p = 3.8 \times 10^{-2}$, impact = 0.27). The characteristics of the pathway are correlated with the size and color of the circles shown in Figure S4. In particular, the relative size and the color (from yellow to red) of the circles indicates the pathway relevance for this study and the number of metabolites differentially produced and associated to a specific pathway. Although the alanine, aspartate and glutamate metabolism (Holm $p = 2.7 \times 10^{-3}$, FDR $= 1.3 \times 10^{-3}$) appeared to be the most affected, all the pathways involved were considered and shown.

The water control (NT) and the three treatments (*Xcc*, *Xcc*+Xccφ1, Xccφ1 alone) produced different changes in the plant metabolic profile. The effect on the accumulation of each single metabolite is reported in Figure 7. Specifically, in the *Xcc* group higher levels of branched chain amino acids (valine, leucine and isoleucine), threonine, lysine, alanine and GABA (γ-aminobutyric acid) were observed compared to the other groups. Interestingly, there was a lower concentration of these metabolites in the *Xcc*+Xccφ1 group compared to the *Xcc* group. Similarly, the concentrations of glucose and fructose were higher in the *Xcc* group compared to the treatment *Xcc*+Xccφ1.

Pipecolate appeared in relatively high concentrations in both the *Xcc* and the *Xcc*+Xccφ1 groups compared to the other groups. The treatment with both bacterium and phage (*Xcc*+Xccφ1) increased the concentration of aspartate, which is the precursor of lysine, asparagine and glutamine, compared to all the other samples.

Finally, in the Xccφ1 group, higher levels of citrate and lower concentrations of valine, leucine and isoleucine, threonine, lysine, alanine, GABA and pipecolate were observed compared to all the other treatments.

To the best of our knowledge, this is the first study specifically addressing the changes of metabolic profile occurring in plants infected by pathogenic bacteria and concurrently inoculated with a disease-controlling bacteriophage.

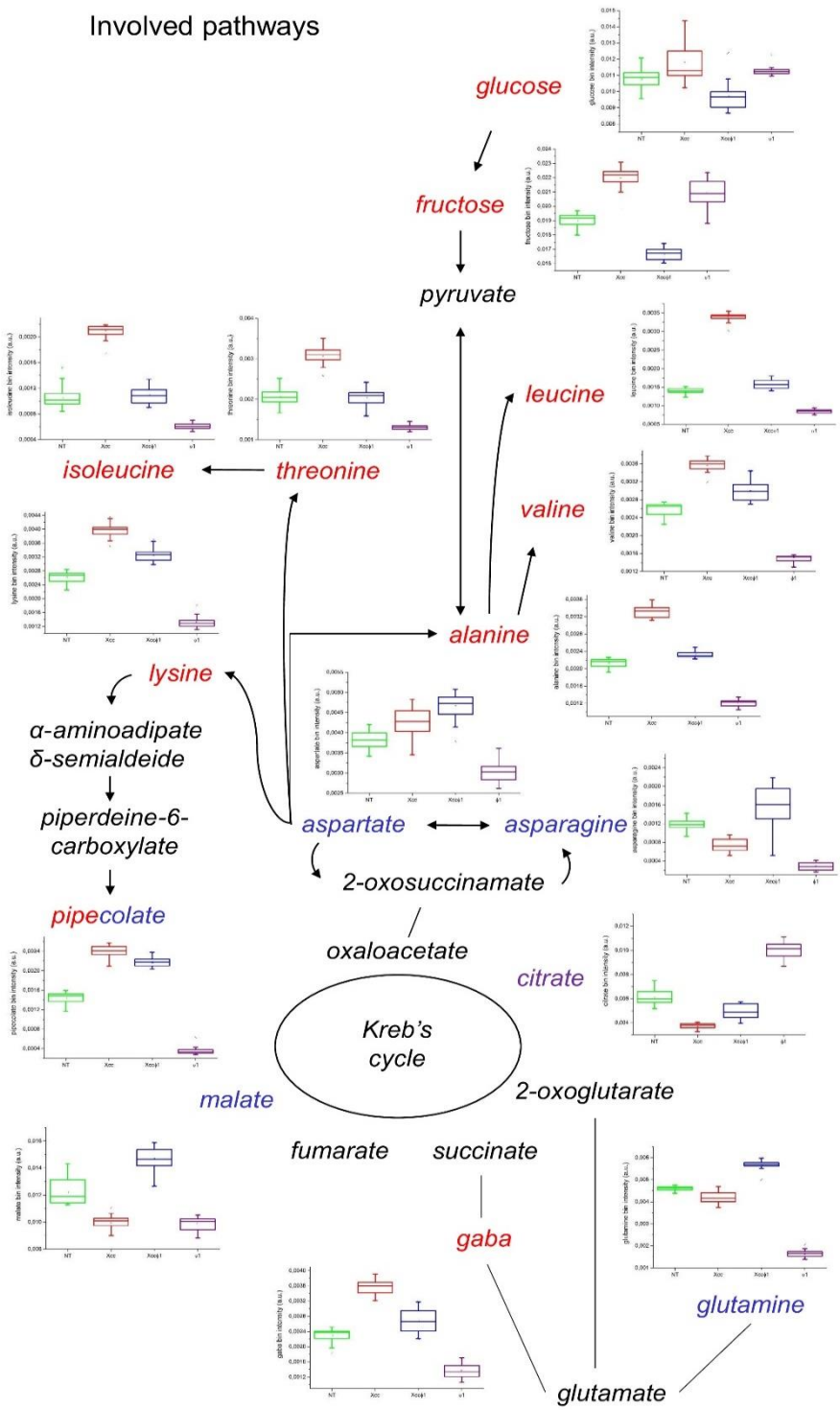
Involved pathways
glucose
fructose
pyruvate
leucine
isoleucine
threonine
valine
alanine
lysine
α-aminoadipate
δ-semialdeide
piperdeine-6-
carboxylate
pipecolate
aspartate
asparagine
2-oxosuccinamate
oxaloacetate
citrate
Kreb's
cycle
malate
2-oxoglutarate
fumarate
succinate
gaba
glutamine
glutamate

Figure 7. Discriminating metabolites and metabolic pathways observed in the *B. oleracea* var. *gongylodes* metabolome after treatments with NT, *Xcc*, *Xcc*+ Xccφ1 and Xccφ1 classes as in Figure 6. Box-and-whisker plots show the variations of the metabolite concentration (green=NT, red=*Xcc*, blue=*Xcc*+ Xccφ1, purple= Xccφ1). The relationships among the metabolites are indicated by lines and arrows. The names of the metabolites is related to the color legend that corresponds to the treatment where they are most accumulated.

Expression profiling of plant genes by qPCR

Quantitative real time PCR (qPCR) was used as a validation tool to confirm metabolomic data. In particular, the expression of the key genes in GABA synthesis (Gad1) and degradation (GABA-T4) were analyzed 15-days after treatments. As shown in Figure 8A, in *Xcc*-infected plants Gad1 was found to be significantly up-regulated. On the other hand, in infected plants treated with the phage (*Xcc*+Xccφ1), the up-regulation of GABA-T4 was observed. No significant differences were observed in the expression of both genes in plant treated with the phage alone (Xccφ1).

In addition, the expression profiles of resistance genes WRKY transcription factor 70 (WRKY 70), legume lectin and osmotin 34 were investigated at 48 hours post inoculation (hpi) (Figure 8B). *Xcc*-infected plants showed a consistent over-expression of WRKY 70 and osmotin genes compared to the control (>25 and >37 Fold Change, respectively). No significant differences were observed in the expression of these genes in plants treated with the phage alone or combined with the bacterium. Similarly, the expression of legume lectin gene resulted to be unaffected by the treatments.

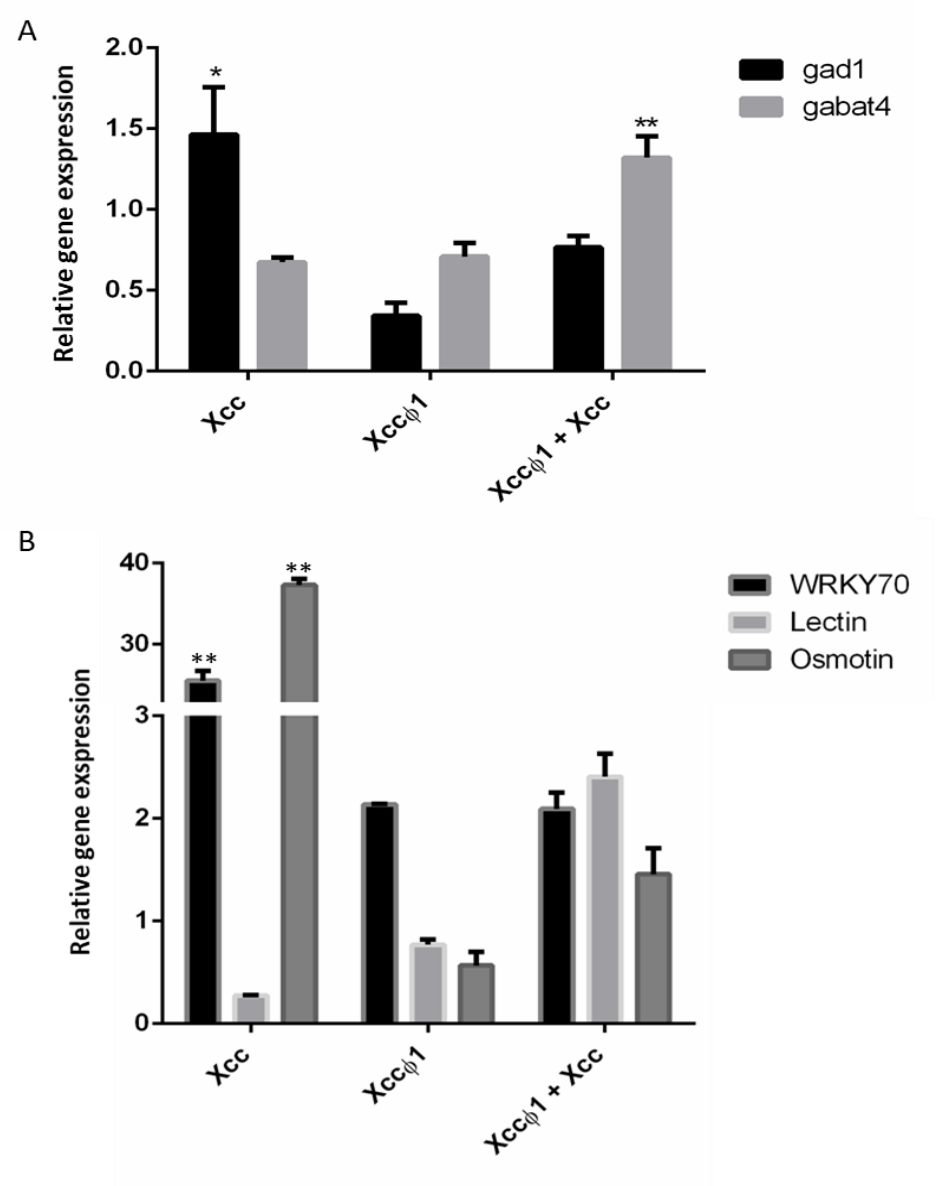

Figure 8. Expression profiling of *B. oleracea* var. *gongylodes* genes by quantitative real time PCR (qPCR). (A): Analysis of genes involved in GABA synthesis (Glutamate decarboxylase- 1, GAD1) and degradation (GABA-transaminase 4, GABA-T4). Plant samples were collected at 15 days post inoculation with *Xcc*, *Xcc*+Xccφ1 or Xccφ1. (B): Analysis of genes involved in plant disease resistance. Plant samples were collected at 48 hours post inoculation with *Xcc*, *Xcc*+Xccφ1 or Xccφ1. WRKY 70: WRKY transcription factor 70. Lectin: legume lectin family protein. Osmotin: osmotin 34. Statistical analysis was performed with Student's t tests (* = $p < 0.05$; ** = $p < 0.001$).

Discussion

Phage therapy represents a research field with great potential as a new and environmentally sustainable crop protection strategy [49]. Several studies have already described the *in vitro* efficacy of bacteriophages against different pathogenic strains of *Xcc* [20,50], *Dickeya solani* [51], *Ralstonia solanacearum* [52], *X. campestris* pv. *vesicatoria* [53] and *X. axonopodis* pv*. citri* [54]. In all these cases, a high dose of phages combined with antimicrobial molecules was needed to reach a moderate level of disease control, typically up to 20% reduction of symptoms. In a field application, disease symptoms caused by *X. arboricola* pv*. pruni* on peach trees and fruits were reduced by using a bacteriophage [55].

In the present study, we describe the phage Xccφ1, that, applied alone at a Multiplicity of infection (MOI) of 10, reduces *in vivo* the symptoms of black rot disease by up to 45% (Figure 5).

Disease control requires bacterial biofilm disruption, as demonstrated at least in the case of human pathogens [56,57]. Using CLSM analysis, we found that after 6h of incubation, Xccφ1 disrupts the stability of *Xcc* biofilm (Figure 4). Moreover, we observed the presence of galactose as one of the main components of Xccφ1 particles (Figure 3B). The crystal violet assay highlighted the significant effect of the galactose in reducing the amount of biofilm (Figure S1), thus confirming the well documented inhibitory activity of galactose in biofilm formation [45]. We therefore suggest that the efficacy of the phage is, at least in part, mediated by phage galactose.

Plant-pathogen interaction causes a drastic metabolic reprogramming, needed to accumulate sugars as C source and amino acids as N source [58,59] (Figure 7). Amino acids provide also precursors of secondary metabolites, including a variety of antimicrobial compounds involved in plant defenses [58,60]. In line with the above evidence, leaves of *B. oleracea* infected with *Xcc* showed increased levels of glucose, fructose, branched chain amino acids (BCAAs), and lysine, indicating a metabolic transition from photosynthesis to a respiratory metabolism, required to initiate a full defense response [61]. This is in accordance with what observed in crucifers infected with compatible or incompatible *Xcc* strains and in *Arabidopsis thaliana* infected by *P. syringae* pv*. maculicola* [11,58]. BCAAs have a role also in human and animal metabolism as modulators of glycolysis and inflammation [62], supporting analogies between plant and animal innate defense mechanisms.

An additional non-protein amino acid, pipecolate, accumulated in *Xcc*-infected and, interestingly, also in *Xcc*+Xccφ1 treated plants.

Pipecolate accumulation is involved in the host response to bacterial infection and the establishment of SAR, possibly leading to a long-lasting and broad-spectrum resistance [5,12,61]. In addition, this compound supports the activation of enhanced pathogen-induced defense responses associated with salicylic acid biosynthesis and priming [5,63]. However, since pipecolate is a common lysine-catabolite, our data suggest that its accumulation at 15 dpi is more related to lysine degradation than to SAR response. This observation is supported by the over-accumulation of the lysine amino acid in plants treated with the bacterium alone or combined with the bacteriophage.

On the other hand, we observed the up-regulation of two resistance-genes (WRKY 70 and osmotin 34) in *Xcc*-infected plants at 48 hpi. The WRKY 70 is considered a key-player in plant responses mediated by salicylic and jasmonic acids and its over-expression is related to the activation of SAR [64]. Furthermore, the *Xcc*+Xccφ1 treatment did not determine effects on the expression of these genes, suggesting that the phage act directly on the bacterium rather than on the activation of plant defense responses.

In plants, the four-carbon non proteinogenic amino acid γ-aminobutyric acid (GABA) regulates multiple functions: cytosolic pH, osmolarity, cell signaling and reactive oxygen species (ROS) production [51,65,66]. Since it is a molecule synthesized mainly from glutamate and strongly associated with the Krebs cycle, GABA is an important component of the balance between carbon and nitrogen metabolism in plant cells [67]. Interestingly, an increased production of GABA was observed only in *B. oleracea* infected with *Xcc.* Moreover, the key gene involved in the GABA biosynthetic pathway (i.e. GAD1) was over-expressed in *Xcc*-infected plants. This evidence is consistent with metabolomic results. On the other hand, the up-regulation of GABA-T4 could explain the decrease of GABA accumulation in infected plants treated with the phage (*Xcc*+ Xccφ1).

In plants treated with both the bacterium and the phage (*Xcc*+ Xccφ1) there was an increase in the concentration of primary products of nitrogen assimilation (aspartate and glutamine) and of amino acids normally used as nitrogen storage and transport compounds, such as asparagine [51].

Finally, a significant effect of the phage alone on plant metabolism was observed (Figure 7). Plants treated with Xccφ1, compared to the water control (NT in Figure 7), displayed a general decreased accumulation of amino acids and nitrogen-containing compounds. Interestingly, this effect concerned all of the nine amino acids analyzed, as well as pipecolate, malate and fumarate. On the contrary, citrate accumulation

strongly increased, while the level of glucose and fructose were substantially unaffected. Possibly, the presence of the phage alone stimulated the conversion of the amino acid carbon skeleton into precursors/intermediate of the Krebs cycle, in order to support mitochondrial metabolism and the production of ATP [52]. Coherently, an increased catabolism of amino acids produced a higher level of citrate production compared to control (Figure 7) [65]. A better understanding of this phenomenon may support an effective application of phages to control plant diseases.

In conclusion, the *Xcc*-phage interaction discussed here may represent a model to study other combinations of plants with biofilm-producing bacteria, such as olive trees (*Olea europaea* L.) and *Xylella fastidiosa,* with the latter sharing a high genome homology with *Xcc* [68]. The resulting knowledge may also be useful in the fight against human pathogens, such as strains of *Pseudomonas aeruginosa*, that form biofilm and are highly resistant to antibiotic therapy [69].

References

1. Alvarez, A.M. Black Rot of Crucifers. In *Mechanisms of Resistance to Plant Diseases*; Springer Netherlands: Dordrecht, 2000; pp. 21–52.
2. Danhorn, T.; Fuqua, C. Biofilm Formation by Plant-Associated Bacteria. *Annu. Rev. Microbiol.* **2007**, *61*, 401–422.
3. Dow, J.M.; Crossman, L.; Findlay, K.; He, Y.-Q.; Feng, J.-X.; Tang, J.-L. Biofilm dispersal in Xanthomonas campestris is controlled by cell-cell signaling and is required for full virulence to plants. *Proc. Natl. Acad. Sci. U. S. A.* **2003**, *100*, 10995–1000.
4. Bostock, R.M.; Pye, M.F.; Roubtsova, T. V. Predisposition in Plant Disease: Exploiting the Nexus in Abiotic and Biotic Stress Perception and Response. *Annu. Rev. Phytopathol.* **2014**, *52*, 517–549.
5. Navarova, H.; Bernsdorff, F.; Doring, A.-C.; Zeier, J. Pipecolic Acid, an Endogenous Mediator of Defense Amplification and Priming, Is a Critical Regulator of Inducible Plant Immunity. *Plant Cell* **2012**, *24*, 5123–5141.
6. Boller, T.; He, S.Y. Innate immunity in plants: an arms race between pattern recognition receptors in plants and effectors in microbial pathogens. *Science* **2009**, *324*, 742–4.
7. Shah, J.; Chaturvedi, R.; Chowdhury, Z.; Venables, B.; Petros, R.A. Signaling by small metabolites in systemic acquired resistance. *Plant J.* **2014**, *79*, 645–658.
8. Schwachtje, J.; Fischer, A.; Erban, A.; Kopka, J. Primed primary metabolism in systemic leaves: a functional systems analysis. *Sci. Rep.* **2018**, *8*, 216.
9. Schleucher, J.; Schwendinger, M.; Sattler, M.; Schmidt, P.; Schedletzky, O.; Glaser, S.J.; S$\diamond$rensen, O.W.; Griesinger, C. A general enhancement scheme in heteronuclear multidimensional NMR employing pulsed field gradients. *J. Biomol. NMR* **1994**, *4*, 301–306.
10. Rojas, C.M.; Senthil-Kumar, M.; Tzin, V.; Mysore, K.S. Regulation of primary plant metabolism during plant-pathogen interactions and its contribution to

plant defense. *Front. Plant Sci.* **2014**, *5*, 17.
11. Brauc, S.; De Vooght, E.; Claeys, M.; Höfte, M.; Angenon, G. Influence of over-expression of cytosolic aspartate aminotransferase on amino acid metabolism and defence responses against Botrytis cinerea infection in Arabidopsis thaliana. *J. Plant Physiol.* **2011**, *168*, 1813–1819.
12. Kang, W.; Zhu, X.; Wang, Y.; Chen, L.; Duan, Y. Transcriptomic and metabolomic analyses reveal that bacteria promote plant defense during infection of soybean cyst nematode in soybean. *BMC Plant Biol.* **2018**, *18*, 86.
13. Sabouri Ghannad, M.; Mohammadi, A. Bacteriophage: time to re-evaluate the potential of phage therapy as a promising agent to control multidrug-resistant bacteria. *Iran. J. Basic Med. Sci.* **2012**, *15*, 693–701.
14. Papaianni, M.; Contaldi, F.; Fulgione, A.; Woo, S.L.; Casillo, A.; Corsaro, M.M.; Parrilli, E.; Marcolungo, L.; Rossato, M.; Delledonne, M.; et al. Role of phage ϕ1 in two strains of Salmonella Rissen, sensitive and resistant to phage ϕ1. *BMC Microbiol.* **2018**, *18*, 208.
15. Koskella, B.; Meaden, S. Understanding Bacteriophage Specificity in Natural Microbial Communities. *Viruses* **2013**, *5*, 806–823.
16. Reddy, P.P. *Recent advances in crop protection*; Springer India: New Delhi, 2013; ISBN 978-81-322-0722-1.
17. Capparelli, R.; Nocerino, N.; Lanzetta, R.; Silipo, A.; Amoresano, A.; Giangrande, C.; Becker, K.; Blaiotta, G.; Evidente, A.; Cimmino, A.; et al. Bacteriophage-Resistant Staphylococcus aureus Mutant Confers Broad Immunity against Staphylococcal Infection in Mice. *PLoS One* **2010**, *5*, e11720.
18. Górski, A.; Jończyk-Matysiak, E.; Międzybrodzki, R.; Weber-Dąbrowska, B.; Łusiak-Szelachowska, M.; Bagińska, N.; Borysowski, J.; Łobocka, M.B.; Węgrzyn, A.; Węgrzyn, G. Phage Therapy: Beyond Antibacterial Action. *Front. Med.* **2018**, *5*, 146.
19. Svircev, A.; Roach, D.; Castle, A. Framing the Future with Bacteriophages in Agriculture. *Viruses* **2018**, *10*.
20. Weiss, B.D.; Capage, M.A.; Kessel, M.; Benson, S.A. Isolation and characterization of a generalized transducing phage for Xanthomonas campestris pv. campestris. *J. Bacteriol.* **1994**, *176*, 3354–9.
21. Hagemeier, J.; Schneider, B.; Oldham, N.J.; Hahlbrock, K. Accumulation of soluble and wall-bound indolic metabolites in Arabidopsis thaliana leaves infected with virulent or avirulent Pseudomonas syringae pathovar tomato strains. *Proc. Natl. Acad. Sci.* **2001**, *98*, 753–758.
22. Desbrosses, G.G.; Kopka, J.; Udvardi, M.K. Lotus japonicus metabolic profiling. Development of gas chromatography-mass spectrometry resources for the study of plant-microbe interactions. *Plant Physiol.* **2005**, *137*, 1302–18.
23. Lindon, J.C.; Nicholson, J.K.; Holmes, E.; Keun, H.C.; Craig, A.; Pearce, J.T.M.; Bruce, S.J.; Hardy, N.; Sansone, S.-A.; Antti, H.; et al. Summary recommendations for standardization and reporting of metabolic analyses. *Nat. Biotechnol.* **2005**, *23*, 833–838.
24. Saviano, G.; Paris, D.; Melck, D.; Falasca, A.; Trupiano, D.; Iorizzi, M.; Scippa, G.S.; Motta, A. Monitoring spatial and temporal metabolic dynamics of woody poplar root under mechanical stress conditions by NMR-based metabolomics. *Metabolomics* **2016**, *12*, 65.
25. Schaad, N.W.; Frederick, R.D.; Shaw, J.; Schneider, W.L.; Hickson, R.;

Petrillo, M.D.; Luster, D.G. Advances in molecular-based diagnostics in meeting crop biosecurity and phytosanitary issues. *Annu. Rev. Phytopathol.* **2003**, *41*, 305–24.
26. Zaccardelli, M.; Campanile, F.; Spasiano, A.; Merighi, M. Detection and identification of the crucifer pathogen, Xanthomonas campestris pv. campestris, by PCR amplification of the conserved Hrp/type III secretion system gene hrcC. *Eur. J. Plant Pathol.* **2007**, *118*, 299–306.
27. Barak, J.D.; Gorski, L.; Naraghi-Arani, P.; Charkowski, A.O. Salmonella enterica Virulence Genes Are Required for Bacterial Attachment to Plant Tissue. *Appl. Environ. Microbiol.* **2005**, *71*, 5685–5691.
28. Fresno, S.; Jiménez, N.; Canals, R.; Merino, S.; Corsaro, M.M.; Lanzetta, R.; Parrilli, M.; Pieretti, G.; Regué, M.; Tomás, J.M. A second galacturonic acid transferase is required for core lipopolysaccharide biosynthesis and complete capsule association with the cell surface in Klebsiella pneumoniae. *J. Bacteriol.* **2007**, *189*, 1128–37.
29. Casillo, A.; Papa, R.; Ricciardelli, A.; Sannino, F.; Ziaco, M.; Tilotta, M.; Selan, L.; Marino, G.; Corsaro, M.M.; Tutino, M.L.; et al. Anti-Biofilm Activity of a Long-Chain Fatty Aldehyde from Antarctic Pseudoalteromonas haloplanktis TAC125 against Staphylococcus epidermidis Biofilm. *Front. Cell. Infect. Microbiol.* **2017**, *7*, 46.
30. Merritt, J.H.; Kadouri, D.E.; O'Toole, G.A. Growing and analyzing static biofilms. *Curr. Protoc. Microbiol.* **2005**, *Chapter 1*, Unit 1B.1.
31. McKinney, H.H.; 1889- mosaic disease of winter wheat and winter rye 1925.
32. Livak, K.J.; Schmittgen, T.D. Analysis of Relative Gene Expression Data Using Real-Time Quantitative PCR and the 2−ΔΔCT Method. *Methods* **2001**, *25*, 402–408.
33. Kim, Y.B.; Lee, M.-K.; Kim, S.-J.; Kim, H.H.; Chung, E.; Lee, J.-H.; Park, S.U. *Accumulation of γ-aminobutyric acid and transcription of glutamate decarboxylase in Brassica juncea (L.) Czern*; 2013; Vol. 6;.
34. Faës, P.; Niogret, M.-F.; Montes, E.; Cahérec, F. Le; Bouchereau, A.; Deleu, C. Transcriptional profiling of genes encoding GABA-transaminases in Brassica napus reveals their regulation by water deficit. *Environ. Exp. Bot.* **2015**, *116*, 20–31.
35. Hwang, T.L.; Shaka, A.J. Water Suppression That Works. Excitation Sculpting Using Arbitrary Wave-Forms and Pulsed-Field Gradients. *J. Magn. Reson. Ser. A* **1995**, *112*, 275–279.
36. Griesinger, C.; Otting, G.; Wuethrich, K.; Ernst, R.R. Clean TOCSY for proton spin system identification in macromolecules. *J. Am. Chem. Soc.* **1988**, *110*, 7870–7872.
37. Bax, A.; Davis, D.G. MLEV-17-based two-dimensional homonuclear magnetization transfer spectroscopy. *J. Magn. Reson.* **1985**, *65*, 355–360.
38. Lee, J.H.; Okuno, Y.; Cavagnero, S. Sensitivity enhancement in solution NMR: emerging ideas and new frontiers. *J. Magn. Reson.* **2014**, *241*, 18–31.
39. Kay, L.; Keifer, P.; Saarinen, T. Pure absorption gradient enhanced heteronuclear single quantum correlation spectroscopy with improved sensitivity. *J. Am. Chem. Soc.* **1992**, *114*, 10663–10665.
40. Trygg, J.; Wold, S. Orthogonal projections to latent structures (O-PLS). *J. Chemom.* **2002**, *16*, 119–128.
41. Core Team A language and environment for statistical computing Available online: https://www.researchgate.net/publication/223190053_A_language_and_envir

onment_for_statistical_computing (accessed on Oct 8, 2019).
42. Chong, J.; Soufan, O.; Li, C.; Caraus, I.; Li, S.; Bourque, G.; Wishart, D.S.; Xia, J. MetaboAnalyst 4.0: towards more transparent and integrative metabolomics analysis. *Nucleic Acids Res.* **2018**, *46*, W486–W494.
43. International Committee on Taxonomy of Viruses.; King, A. *Virus taxonomy : ninth report of the International Committee on Taxonomy of Viruses*; Elsevier, 2011; ISBN 9780123846846.
44. Casillo, A.; Parrilli, E.; Filomena, S.; Lindner, B.; Lanzetta, R.; Parrilli, M.; Tutino, M.L.; Corsaro, M.M. Structural Investigation of the Oligosaccharide Portion Isolated from the Lipooligosaccharide of the Permafrost Psychrophile Psychrobacter arcticus 273-4. *Mar. Drugs* **2015**, *13*, 4539–55.
45. Ryu, E.-J.; Sim, J.; Sim, J.; Lee, J.; Choi, B.-K. D-Galactose as an autoinducer 2 inhibitor to control the biofilm formation of periodontopathogens. *J. Microbiol.* **2016**, *54*, 632–637.
46. Kaur, T.; Nafissi, N.; Wasfi, O.; Sheldon, K.; Wettig, S.; Slavcev, R. Immunocompatibility of Bacteriophages as Nanomedicines. *J. Nanotechnol.* **2012**, *2012*, 1–13.
47. Doolittle, M.M.; Cooney, J.J.; Caldwell, D.E. Tracing the interaction of bacteriophage with bacterial biofilms using fluorescent and chromogenic probes. *J. Ind. Microbiol.* **1996**, *16*, 331–41.
48. Eriksson, L. *Multi- and megavariate data analysis : Part I: Basic principles and applications*; Umetrics: Umeå, 2006;
49. Fernández, L.; Gutiérrez, D.; Rodríguez, A.; García, P. Application of Bacteriophages in the Agro-Food Sector: A Long Way Toward Approval. *Front. Cell. Infect. Microbiol.* **2018**, *8*, 296.
50. Renu; Bhoyar, M.S.; Singh, U.B.; Sahu, U.; Nagrale, D.T.; Sahu, P.K. CHARACTERIZATION OF LYTIC BACTERIOPHAGE XCC9SH3. *J. Plant Pathol.* **2017**, *99*, 233–238.
51. Hildebrandt, T.M.; Nunes Nesi, A.; Araújo, W.L.; Braun, H.-P. Amino Acid Catabolism in Plants. *Mol. Plant* **2015**, *8*, 1563–1579.
52. Fujiwara, A.; Fujisawa, M.; Hamasaki, R.; Kawasaki, T.; Fujie, M.; Yamada, T. Biocontrol of Ralstonia solanacearum by Treatment with Lytic Bacteriophages. *Appl. Environ. Microbiol.* **2011**, *77*, 4155.
53. Balogh, B.; Jones, J.B.; Momol, M.T.; Olson, S.M.; Obradovic, A.; King, P.; Jackson, L.E. Improved Efficacy of Newly Formulated Bacteriophages for Management of Bacterial Spot on Tomato. *Plant Dis.* **2003**, *87*, 949–954.
54. Iriarte, F.B.; Balogh, B.; Momol, M.T.; Smith, L.M.; Wilson, M.; Jones, J.B. Factors affecting survival of bacteriophage on tomato leaf surfaces. *Appl. Environ. Microbiol.* **2007**, *73*, 1704–11.
55. Zaccardelli, M.; Saccardi, A.; Gambin, E.; Mazzucchi, U. Xanthomonas campestris pv. pruni bacteriophages on peach trees and their potential use for biological control. *Phytopathol. Mediterr.* 1992, *31*, 133–140.
56. Morris, J.; Kelly, N.; Elliott, L.; Grant, A.; Wilkinson, M.; Hazratwala, K.; McEwen, P. Evaluation of Bacteriophage Anti-Biofilm Activity for Potential Control of Orthopedic Implant-Related Infections Caused by *Staphylococcus aureus*. *Surg. Infect. (Larchmt).* **2019**, *20*, 16–24.
57. Fong, S.A.; Drilling, A.; Morales, S.; Cornet, M.E.; Woodworth, B.A.; Fokkens, W.J.; Psaltis, A.J.; Vreugde, S.; Wormald, P.-J. Activity of Bacteriophages in Removing Biofilms of Pseudomonas aeruginosa Isolates from Chronic Rhinosinusitis Patients. *Front. Cell. Infect. Microbiol.* **2017**, *7*, 418.

58. Fagard, M.; Launay, A.; Clement, G.; Courtial, J.; Dellagi, A.; Farjad, M.; Krapp, A.; Soulie, M.-C.; Masclaux-Daubresse, C. Nitrogen metabolism meets phytopathology. *J. Exp. Bot.* **2014**, *65*, 5643–5656.
59. Vogel-Adghough, D.; Stahl, E.; Návarová, H.; Zeier, J. Pipecolic acid enhances resistance to bacterial infection and primes salicylic acid and nicotine accumulation in tobacco. *Plant Signal. Behav.* **2013**, *8*, e26366.
60. Camañes, G.; Scalschi, L.; Vicedo, B.; González-Bosch, C.; García-Agustín, P. An untargeted global metabolomic analysis reveals the biochemical changes underlying basal resistance and priming in Solanum lycopersicum, and identifies 1-methyltryptophan as a metabolite involved in plant responses to Botrytis cinerea and Pseudomonas sy. *Plant J.* **2015**, *84*, 125–139.
61. Wishart, D.S.; Tzur, D.; Knox, C.; Eisner, R.; Guo, A.C.; Young, N.; Cheng, D.; Jewell, K.; Arndt, D.; Sawhney, S.; et al. HMDB: the Human Metabolome Database. *Nucleic Acids Res.* **2007**, *35*, D521–D526.
62. Papathanassiu, A.E.; Ko, J.-H.; Imprialou, M.; Bagnati, M.; Srivastava, P.K.; Vu, H.A.; Cucchi, D.; McAdoo, S.P.; Ananieva, E.A.; Mauro, C.; et al. BCAT1 controls metabolic reprogramming in activated human macrophages and is associated with inflammatory diseases. *Nat. Commun.* **2017**, *8*, 16040.
63. Hartmann, M.; Kim, D.; Bernsdorff, F.; Ajami-Rashidi, Z.; Scholten, N.; Schreiber, S.; Zeier, T.; Schuck, S.; Reichel-Deland, V.; Zeier, J. Biochemical Principles and Functional Aspects of Pipecolic Acid Biosynthesis in Plant Immunity. *Plant Physiol.* **2017**, *174*, 124–153.
64. Li, L.; Maher, K.; Navarre-Sitchler, A.; Druhan, J.; Meile, C.; Lawrence, C.; Moore, J.; Perdrial, J.; Sullivan, P.; Thompson, A.; et al. Expanding the role of reactive transport models in critical zone processes. *Earth-Science Rev.* **2017**, *165*, 280–301.
65. Batushansky, A.; Kirma, M.; Grillich, N.; Toubiana, D.; Pham, P.A.; Balbo, I.; Fromm, H.; Galili, G.; Fernie, A.R.; Fait, A. Combined Transcriptomics and Metabolomics of Arabidopsis thaliana Seedlings Exposed to Exogenous GABA Suggest Its Role in Plants Is Predominantly Metabolic. *Mol. Plant* **2014**, *7*, 1065–1068.
66. Kim, Y.-B.; Kim, Y.S.; Kim, W. Bin; Shen, F.-Y.; Lee, S.W.; Chung, H.J.; Kim, J.S.; Han, H.C.; Colwell, C.S.; Kim, Y.I. GABAergic excitation of vasopressin neurons: possible mechanism underlying sodium-dependent hypertension. *Circ. Res.* **2013**, *113*, 1296–307.
67. Michaeli, S.; Fromm, H. Closing the loop on the GABA shunt in plants: are GABA metabolism and signaling entwined? *Front. Plant Sci.* **2015**, *6*, 419.
68. Moreira, L.M.; De Souza, R.F.; Digiampietri, L.A.; Da Silva, A.C.R.; Setubal, J.C. Comparative Analyses of *Xanthomonas* and *Xylella* Complete Genomes. *Omi. A J. Integr. Biol.* **2005**, *9*, 43–76.
69. Rasamiravaka, T.; Labtani, Q.; Duez, P.; El Jaziri, M. The Formation of Biofilms by *Pseudomonas aeruginosa* : A Review of the Natural and Synthetic Compounds Interfering with Control Mechanisms. *Biomed Res. Int.* **2015**, *2015*, 1–17.

Acknowledgments. The authors thank Claudio Altomare for discussions and revisions to the manuscript. Special thanks are due to Prof. Antonio Evidente for his skillful assistance in extraction procedures and sample preparation for NMR.

All the authors acknowledge the following founding: Community Scientific Program 2016, Proposal 1966-CSP 2016; Project ProBio - IZSM (Portici), n. D01 6309, 14/12/2016; Project LINFA - MIUR-PON, n. 03PE_00026_1, 09/04/2014; Project SIX, Regione Puglia, n. 111 del 23/09/2016.

Author Contributions. RC have made major contributions to the conception and design of the study; MP, MMR, EP, RM, AL, MLT, AM to the acquisition, analysis, or interpretation of the data; MP, AF, AC, GM, AZ, DP performed the experiments and participated to the interpretation of data; RC, ML, SLW wrote the manuscript. All authors read and approved the final manuscript.

Competing Interests: The authors declare that they have no competing interests.

Supplementary material

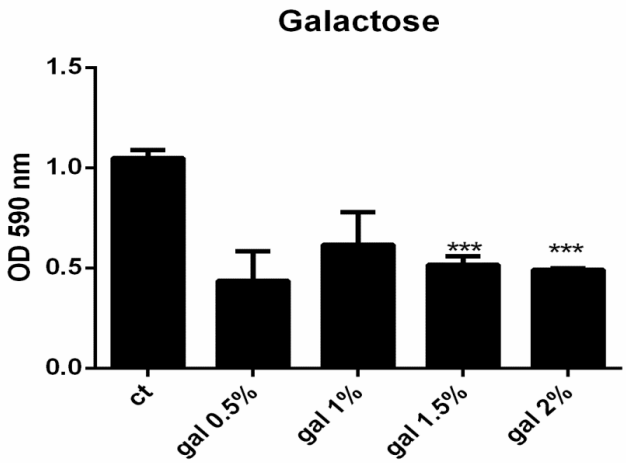

Figure S1. Detection of *Xcc* biofilm production using Christal violet assay after 4h of treatment with different concentrations of galactose (gal), as compared to control (ct). Each value is the mean ± DS of 3 independent experiments. *** $p<0.001$. Statistical analysis was performed with Student's t tests.

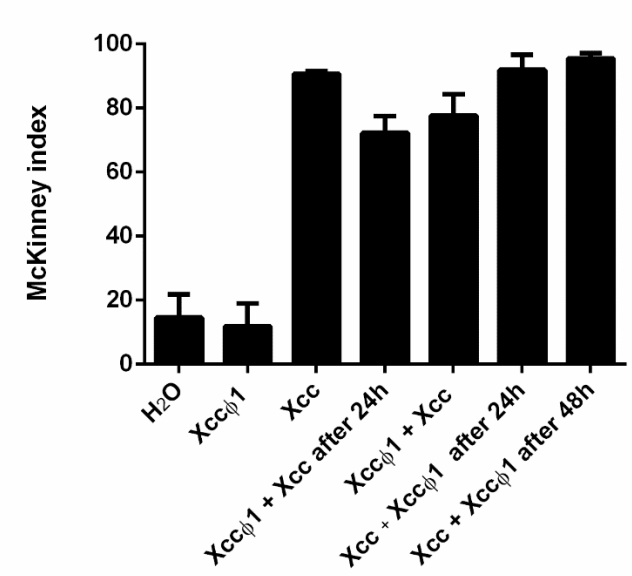

Figure S2. Effect of the Xccφ1 phage treatments on *Xcc* disease severity, as measured by the McKinney index, with foliar applications to *B. oleracea* var. *gongylodes*. Different timing of phage and pathogen applications to the plant, using equal concentrations of the phage and bacterium.

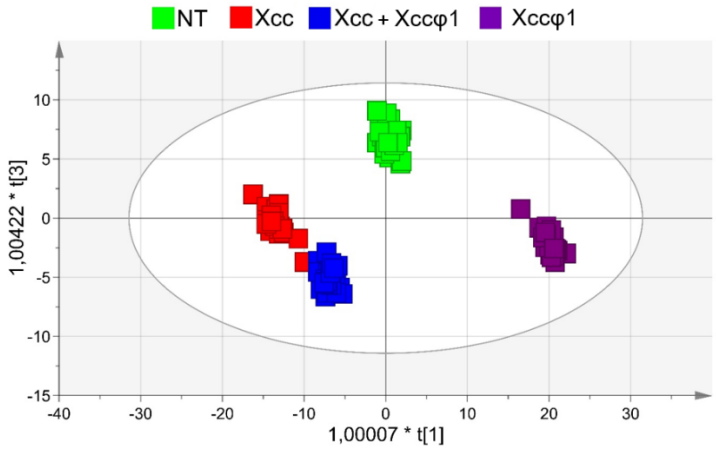

Figure S3. Score plot t[3]/t[1] showing the projection of the leave extracts NMR spectra onto the third and the first components associated to the OPLS-DA statistical model.

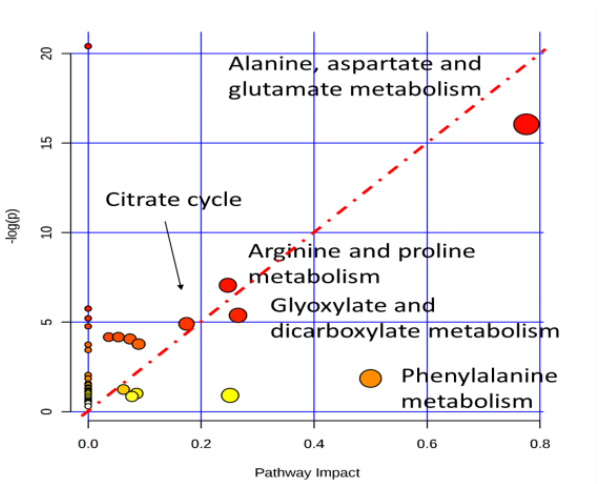

Figure S4. Pathway topology and biomarker analysis of *B. oleracea* var. *gongylodes* of discriminating metabolites and processes. Class separation was performed by using Metaboanalyst *4.0.*

Table S1. Phage host range determination on different Xanthomonas campestris strains.

Bacteria strains	**Lytic activity**
X. albilineans (3 different samples)	-
X. cyanopsidis	-
X. citri (3 different samples)	-
X. vasicola	-
X. vesicatoria	-
X. cucurbitae (3 different samples)	-
X. perforans	-
X. gardneri	-
X. malvacearum (3 different samples)	-
X. maltophilia	-
Xcc. from kohlrabi from Terracina (7 different samples)	-

Xcc. from cabbage (antiserum)	+
Xcc. from cauliflower (4 different samples)	+
Xcc. from kohlrabi (antiserum) (3 different samples)	+
Xcc. from cauliflower from Latina	+
Xc. Phelargoni from Ercolano	-
Xc. Pherlagoni from Eboli	-
Xc. Phaesoli (3 different samples)	-
Xcc. From cauliflower from nursery	+
Xc. From violaciocca	-

-, Negative lysis result; +, positive lysis result.

Table S2. 1H and 13C chemical shift assignment (δ, ppm) of metabolites found in 1H-TOCSY and 1H- 13HSQC-NMR spectra of B. oleacea var. gongylodes leaves extracts.

Entry	Metabolite	□ ^{1}H	□ ^{13}C	Group	Entry	Metabolite	□^{1}H	□^{13}C	Group
1	Ile	0.94 1.01 1.48 1.98	11.80 15.40 - 36.60	□CH_3 □'CH_3 □'CH □CH	19	Gln	2.14 2.45 3.77	27.13 31.70 55.06	□CH_2 □CH_2 □CH
2	Leu	0.96 1.71	22.70 40.50	□CH_3 □CH_2	20	Succinate	2.39	34.96	□, □CH_2
3	Val	0.98 1.04 2.28 3.62	17.40 18.60 29.70 61.10	□CH_3 □'CH_3 □CH □CH	21	Malate	2.40 2.68 4.30	- 43.43 71.24	□'CH □CH □CH
4	Propionate	1.05 2.19	11.05 31.51	□CH_3 □CH_2	22	Citrate	2.52 2.65	46.47 46.47	□,□CH □',□'CH

5	Ethanol	1.19 3.67	17.2 56.8	CH_3 CH_2	23	Asp	2.68 2.79 3.89	37.10 - 52.70	βCH β 'CH αCH
6	Fucose	1.27 3.60 3.85 4.12 5.20	19.41 75.59 70.91 96.21 96.76	CH_3 γCH εCH □CH αCH	24	Methyl-guanidine	2.83	38.00	CH_3
7	SFA	1.31 1.56 2.17		CH_2	25	Choline	3.13 3.43 3.96	55.00 56.60 68.30	N-CH_3 βCH_2 αCH_2
8	Lactate	1.32 4.11	20.76 69.33	βCH_3 αCH	26	Ethanolamine	3.13 3.81	43.93 60.57	-$C\underline{H_2}$- NH_2 OH-$C\underline{H_2}$-
9	Thr	1.32 3.60 4.25	20.00 61.00 66.60	γCH_3 αCH βCH	27	His	3.14 3.23 3.98 7.07 7.87	- 29.15 55.30 117.50 137.17	βCH β ' CH αCH C4H,ring C2H,ring
10	Acetoin	1.37 2.23 4.43	19.54 24.94 73.16	$C\underline{H_3}$-CH-$C\underline{H_3}$-C=CH	28	Glucose	3.24 3.40 3.46 3.53 3.73 3.82 3.90 4.63 5.24	76.95 72.34 78.57 74.19 63.35 74.13 63.47 98.71 94.93	C3H C5H C6H C3H C4H; CH_2 C6H;CH 2 CH_2 C2H C2H
11	Ala	1.48 3.79	16.80 51.10	βCH_3 αCH	29	Betaine	3.25 3.90	55.85 68.64	CH_2 CH_3
12	Pipecolate	1.63 1.87 2.21 3.01 3.60	29.36 24.55 24.57 46.66 61.92	β CH_2; γCH_2; δCH_2. βCH_2;;γ CH_2 εCH_2 β CH_2 CH	30	myo-Inositol	3.29 3.54 4.07	75.13 73.29 73.10	C5H C1H C2H

13	Lys	1.65 1.88 3.01	26.70 30.20 39.50	δCH_2 βCH_2 εCH_2	31	Methanol	3.34	51.43	CH_3
14	Arg	1.68 1.92 3.23 3.78	24.40 28.00 41.00 54.60	γCH_2 βCH_2 δCH_2 αCH	32	β Galactose	3.48 3.63-3.65 3.70 3.75 3.93	72.90 73.80 76.00 62.00 69.70	C2H C3H C5H C6H C4H
15	GABA	1.88 2.28 3.00	24.54 35.17 40.11	βCH_2 αCH_2 γCH_2	33	Fructose	3.50 3.60 3.70-3.73 3.82 3.90	66.53 64.73 66.52 70.00 72.37	$C10H_2$ $C2H_2$ $C10H_{2;}$ $C2H_2$ C3H;C4H C5H
16	Acetate	1.92	24.07	CH_3	34	Sucrose	3.58 3.77 5.42	71.90 73.40 93.00	G2H G3H G1H
17	Pro	2.01 2.08 2.34 3.33 3.40 4.14	23.90 - 29.20 - 46.00 61.10	γCH_2 β ' CH βCH □□'CH □CH αCH	35	α Galactose	3.73 3.84 5.26	62.20 70.20 93.20	C6H C3H C1H
18	Glu	2.09 2.34 3.75	27.60 34.00 55.20	$\beta CH;\beta$ 'CH γCH_2 αCH	36	Tyr	6.88 7.18	117.00 130.00	C3, 5H,ring C2, 6H,ring
37	Fumarate	6.52	136.08	α, βC=C					

Table S3: List of genes selected for qPCR analysis. For each one, primer name, sequences and the references were reported.

Gene name	Primer name	Primer sequences 5'-3'	Reference
Glutamate decarboxylase 1	Bj_GAD_f	ATGGTGCTCTCTCACGCCGC	Kim et al., 2013
	Bj_GAD1_r	CTTGGATTACCGTCAAGCATCAACTC	
GABA-transaminase 4	GABA-T4_f	CGCAAGAAAGAAATCGTATCA	Faës et al., 2015
	GABA-T4_r	GTGAGGGCAATCTGTGTGT	
WRKY 70	WRKY_f	TCTGCTCTTGATTCCTTAGAACCCG	Wu et al., 2017
	WRKY_f	GGTCCAAGTCTTTTCCGACTATCAC	
Legume lectin family protein	Lectin_f	GAAAGCTGGTTACTGGGTTCAGACA	Wu et al., 2017
	Lectin_r	GCGAGCGTAATGGTAATCCTATTG	
Osmotin 34	Osmo34_f	GGCTGAGTATGCTTTGAACCAGTTC	Wu et al., 2017
	Osmo34_r	AGGACACTGTCCGTTTATGTCTG	
Actin_HK	Bj_Actin_f	CCGACCGTATGAGCAAGGAAATC	Kim et al., 2013
	Bj_Actin_r	TTCCTGTGGACAATGGATGGAC	

CHAPTER II

The union is strength: The synergic action of an anti-biofilm molecule and a bacteriophage-hydroxyapatite complex against *Xanthomonas campestris* biofilm

Introduction

The crop normally is under the attack by a variety of pathogens both in the nursery as well as in field. However, some diseases directly interfere with the quality of the product, generating economic damages. *Xanthomonas campestris pv. campestris* (*Xcc*) [1], is responsible for Black rot one of the most problematic diseases for cauliflower and other crucifers [2][3]. For the control of this disease, there are some approaches used as crop management based on exclusion of whole or parts of infected plants, but for the control of the disease, there are no products registered until now [4]. The peculiarity of Black rot is that the biofilm produced by *Xcc* obstructs the xylem vessels inducing tissue necrosis [5].

Biofilm formation is a key virulence factor for a wide range of microorganisms that cause chronic infections, since bacteria in biofilm show an increased tolerance towards antibiotics that leads in the hardest eradication with conventional treatment strategies [6–8]. The multifactorial nature of biofilm development and drug tolerance imposes great challenges for the use of conventional antimicrobials and indicates the need for multi-targeted or combinatorial strategy.

Bacteriophages are a potent, natural antibacterial capable of inducing rapid bacterial cell lysis. Billions of years of this co-evolutionary predator-prey relationship have made bacteriophages a potentially rich source of antibacterial agents [9]. An added advantage, in contrast to antibiotics, is that the concentration of bacteriophages increases after reaching the site of infection due to self-replication [10]. They can coexist with their host by integrating them self into the bacterial genome (lysogenic bacteriophages) or killing them (lytic bacteriophages) and lysis of the host not only kills the bacterium but also releases the progeny copies of the phage for re-infection of other bacteria (10). As a result, the required dose of phages would generally be much less than that of antibiotics [11]. Economic considerations also favour bacteriophage therapy over conventional antibiotics, as the cost and complexity of developing a phage system is less than that of developing a new antibiotic [12]. A further advantage of using phages is that they grow rapidly and exponentially and therefore a single dose is enough to control infection. Since they reproduce through bacteria, once the infection has been eradicated, the phages are also eliminated [13]. Bacteriophages are

species-specific, and so allows a targeted therapy limiting the deleterious effect on the normal microbial flora preventing some adverse effects associated with antibiotic use [14].
There are some limits that explains the reduced role of bacteriophages in empirical therapy [15], one drawback in using phages could be their lack of stability over time and their low activity against same intracellular infections, while recently it was demonstrated that hydroxyapatite (HA) was able to chemically interact with bacteriophages increasing and stabilizing the activity of bacteriophages at different pH values [16].
Very recently a lytic bacteriophage (Xccφ1) able to reduce the *Xanthomonas campestris pv. campestris* proliferation was isolated and characterized (Papaianni et al submitted), the phage Xccφ1 displayed the ability, *in vivo*, to reduce the symptoms of black rot disease (Papaianni et al submitted).
In order to set up a new strategy for a possible treatment of Black rot disease, in this paper the use of the lytic bacteriophage Xccφ1 is proposed in combination with an anti-biofilm molecule able to eradicate of *Xanthomonas campestris* mature biofilm.
Previously reported results demonstrated that Polar bacteria, belonging to different genera showed anti-biofilm activity against P. aeruginosa PAO1, S. aureus and S. epidermidis [17] and recently it has been demonstrated that the Antarctic bacterium *Pseudoalteromonas haloplanktis* TAC125 produces a long-chain fatty aldehyde, the pentadecanal [18], endowed with a strong anti-biofilm activity against *Staphylococcus epidermidis* [19,20]. Additionally, pentadecanal derivatives (corresponding acid, acetal and ester of the pentadecanal) resulted endowed with strong anti-biofilm activity against [21].

Starting from the above-described results in this paper a multi-target strategy was set up. In particular, the combined use of an effective antimicrobic like a bacteriophage, complexed with HA, with the use of a molecule specifically directed against biofilm was optimized to eradicate *Xanthomonas campestris* mature biofilm.

Material and Method

Bacterial strains and culture conditions

The bacteria strain used in this work was isolated from leaves of cauliflower and kohlrabi plants with symptoms of Black rot. Briefly, the leaves were washing with distillate water, and disrupted mechanically, tissue fragments were ground and streaked on mCS20ABN agar medium [22]. Yellow mucoid colonies were purified on Nutrient Agar

(Sigma Aldrich, Milan, Italy) supplemented with glucose 0.5% (NAG). Single colonies were then suspended in SDW and stored at 4°C. The isolates were identified by the BiologTM System (Hayward, CA, USA) as Xcc.

Synthesis of pentadecanal derivatives

Dodecanoic acid (C12), pentadecanoic acid (C15), and hexadecanoic acid (C16) were purchased from Sigma Aldrich. The octadecanoic and eicosanoic acid (C18 and C20, respectively) were synthesized starting from the corresponding alcohols purchased from Sigma Aldrich. The oxidation of the alcohols was obtained as already reported [23]. A solution of 1-octadecanol (30 mg, 0.19 mmol) in $CHCl_2$ (3 mL) and H_2O (650 µL) was added, in an ice-water bath, to aqueous solutions of: NaBr (1M, 95 µL), tetrabutylammonium bromide (1M, 190 µL), TEMPO (8.36 mg, 0.053 mmol), and $NaHCO_3$ (475 µL). The obtained mixture was treated with an aqueous solution of NaOCl (570 µL), kept under magnetic stirring until room temperature, and after neutralized with HCl. After neutralization, 2.66 mL of *t*BuOH, 5.32 mL of 2-methylbut-2-ene in THF, and a solution of $NaClO_2$ (150 mg) and NaH_2PO_4 (120 mg) in 700 µL of water, were added. After 2 hours at room temperature, the mixture was diluted with a saturated aqueous solution of NaH_2PO_4 (15 mL) and extracted with ethyl acetate. The organic layer was then dried over Na_2SO_4, filtrated, and concentrated in vacuum. Then, the solution was completely dried under a stream of argon. The same procedure was then utilized for the alcohols 1- 1-eicosanol for the obtainment of the corresponding acid.

The pentadecanal (aldehyde), pentadecanoic acid methyl ester (ester), and 1,1-dimethoxypentadecane (acetal) were prepared as already reported [24].

To verify the purity of the derivatives, the compounds were analysed on an Agilent 7820 A GC System-5977B MSD spectrometer equipped with the automatic injector 7693A and a Zebron ZB-5 capillary column (Phenomenex, Toornace, CA, USA; flow rate 1 ml min^{-1} ; He as carrier gas), using the following temperature program: 150°C for 3 min, 150°C to 300°C at 15°C/min, 300°C for 5 min.

Pentadecanal derivatives anti-biofilm activity

The biofilm formation with or without the different treatment was measured using crystal violet staining. The experiment was performed for characterized the anti-biofilm activity of the pentadecanal derivatives on different biofilm step formation, attachment and mature. All the molecules were tested for different concentration (60 µg/mL, 120

µg/mL, 240 µg/mL). In the first experiment 200 µL of bacterium was incubated in each well of sterile 96—well flat-bottomed polystyrene plate (Falcon) for 72h at 24 °C without shaking, to allow bacterial attachment and after the pentadecanal derivatives were added for 8h. In the second experiment 200 µL of bacterium was incubated with the molecules at different concentration on sterile 96—well for 72h at 24°C. After treatment, planktonic cells were gently removed; each well was washed with H_2O for thee times. To quantify the biofilm formation, each well was marked with 0.1% crystal violet and incubated for 10 min at RT, washed with double-distilled water. The colourant bound to adherent cells was solubilized with 20% (v/v) acetone and 80% (v/v) ethanol. After 10 min of incubation at RT, (OD) was measured at 600 nm to quantify the total biomass of biofilm formed in each well. Each data point is composed of three independent experiments, each performed in six replicates.
The different acids were screening for choose the best candidate using the same experimental procedure above.

Complex HA– ϕ1C20

The HA– ϕ1C20 complex was prepared by mixing 1 mL of HA (100 mg/mL) with 1 mL of Xcc ϕ1 (10^8 PFU/mL) and C20 (60 µg/mL) and incubated - under shaking condition - at room temperature for: 0, 30', 90',180', 300' and 24h. After the proper incubation time, sample was centrifuged, and the pellet was suspended in H_2O buffer. The concentration of the active phage particles was evaluated by the DLA method [25]. After the overnight incubation, the results allowed us to select the optimal incubation time.
After that the evaluation of the complex was carried out using all the molecules (60 µg/mL) and compared the activity of the phage alone (10^9 PFU/mL), the phage and the molecules (10^9 PFU/mL and 60 µg/mL, respectively) and the complex using Crystal Violet staining.

Statistical analysis

The statistical analysis was performed using the measured absorbance of the biofilm (triplicate) when the phages, HA and the several acids were combined among them.
In particular, for this type of analysis, it has been convenient to introduce the parameters ρ (normalization as function of control absorbance) and C_{syn} (synergistic coefficient).

Once defined the ρ parameter as:

$$\rho_a = 1 - \frac{abs_{ctrl} - abs_a}{abs_{ctrl}}$$

it has been possible to estimate the synergistic coefficient C_{syn} as:

$$C_{syn} = \frac{\rho_a * \rho_b}{\rho_{ab}}$$

Moreover, for the calculation of the error analysis we used:

$$R = R(X, Y, \dots)$$

$$\partial R = \sqrt{\left(\frac{dR}{dX} \cdot \partial X\right)^2 + \left(\frac{dR}{dY} \cdot \partial Y\right)^2 + \cdots \dots}$$

If R is a function of X and Y, written as R(X,Y), then the uncertainty in R is obtained by taking the partial derivatives of R with respect to each variable, multiplication with the uncertainty in that variable, and addition of these individual terms in quadrature

Optimization of the complex

The optimization of the complex, minimum biofilm inhibitory concentration (MBIC) and the minimum biofilm eradication concentration (MBEC) was performed using Crystal Violet staining with different concentration of the compounds and different time of incubation, in particular HA (10 and 5 mg/mL), Xccϕ1 (10^9 and 10^8 PFU/mL), C18 and C20 (30 µg/mL) for three and hours. To quantify the biofilm formation, each well was stained with 0.1% crystal violet and incubated for 10 min at RT, washed with double-distilled water. The dye bound to adherent cells was solubilized with 20% (v/v) acetone and 80% (v/v) ethanol. After 10 min of incubation at RT, (OD) was measured at 600 nm to quantify amount of biofilm present in each well. Each data point is composed of three independent experiments, each performed in six replicates.

CLSM analysis for static biofilm evaluation

The anti-biofilm activity of the selected samples was also evaluated by Confocal laser scanning microscopy (CLSM). Xcc biofilms were formed on Nunc™ Lab-Tek® 8-well Chamber Slides (n◦ 177445; Thermo Scientific, Ottawa, ON, Canada). Briefly, the wells of the chamber slide were filled with overnight growth of *Xcc* diluted of about 0.001

(OD)600nm. The bacterial culture was incubated at 24°C for 96h to allow the *Xcc* biofilm formation. Then, the mature biofilms were incubated for 4h in the absence and in the presence of only C20, and phage (10^8 CFU/ml) plus HA (10 mg/ml) and C20 (30µg/ml) in order to assess their anti-biofilm activity and their influence on cell viability. The biofilm cell viability was determined by the FilmTracerTM LIVE/DEAD® Biofilm Viability Kit (Molecular Probes, Invitrogen, Carlsbad, California) following the manufacturer's instructions.
After rinsing with filter-sterilized PBS, each well of the chamber slide were filled with 300 µL of working solution of fluorescent stains, containing the SYTO® 9 green fluorescent nucleic acid stain (10 µM) and propidium iodide, the red-fluorescent nucleic acid stain (60 µM), and incubated for 20-30 min at room temperature, protected from light. Excess stain was removed by gently rinsing with filter-sterilized PBS.
All microscopic observations and image acquisitions were performed with a confocal laser scanning microscope (CLSM; LSM700-Zeiss, Jena, Germany) equipped with an Ar laser (488 nm), and a He-Ne laser (555 nm). Images were obtained using a 20x/0.8 objective. The excitation/emission maxima for these dyes are ~480/500nm for SYTO® 9 stain and 490/635nm for propidium iodide. Z-stacks were obtained by driving the microscope to a point just out of focus on both the top and bottom of the biofilms. Images were recorded as a series of .tif files with a file-depth of 16 bits.

CLSM for dynamic biofilm evaluation
The effect of the selected samples on *Xcc* biofilm was evaluated using flow cell methods, that allows non-invasive and non-destructive examination of biofilms. In parallel analysis of *Xcc* biofilms was performed using a 3-channel flow cell chamber (IBI Scientific. Peosta, IA). For this study, a solution of phosphate-buffered saline (PBS, pH 7) was flown into each channel of the cell at a controlled flow rate of 160 µl/min using Ismatec™ IPC 4 Peristaltic Pump (Cole-Parmer GmbH, Germany). The flow system was kept free of air bubbles using a bubble trap, which created a low positive pressure with PBS flow, thus mitigating undesirable peristaltic pulsation in liquid delivery to the flow cell. The flow system was kept free of air bubbles using a bubble trap, which created a low positive pressure with medium solution flow, thus mitigating undesirable peristaltic pulsation in liquid delivery to the flow cell. Then, a bacterial suspension of *Xcc* at 0,5 od ml^{-1} was circulated through the system for 2h and the non-adhering cells were washed away with sterile PBS for 15 min. Finally, fresh medium (Nutrient Broth 50% v/v in PBS) was circulated for 48h through the system to let the

biofilm form. After incubation, three different solutions were circulated for 3h into each channel of the cell: only fresh medium into the first channel (NT), fresh medium containing only phage (10^8 CFU/ml) into the second channel, fresh medium containing HA– ϕ1C20 complex into the third channel. Biofilms formed in absence and in presence of the tested samples were evaluated by confocal laser scanning microscopy (CLSM). PDMS surfaces were evaluated by Confocal laser scanning microscopy (CLSM). The biofilm cell viability was determined by the FilmTracer™ LIVE/DEAD® Biofilm Viability Kit (Molecular Probes, Invitrogen, Carlsbad, CA, USA) following the manufacturer's instructions. In detail, a volume of 500 µl of a working solution of fluorescent stains, containing the SYTO® 9 green fluorescent nucleic acid stain (10 µM) and propidium iodide, and the red-fluorescent nucleic acid stain (60 µM), was injected with a syringe into each channel, without removing the flow cell from the flow system, and incubated for 20-30 min at room temperature, protected from light. Then, fresh PBS was flown to remove the excess stain. All microscopic observations and image acquisitions were performed as previously described.

SEM image

Water suspensions of the samples HA– ϕ1C20 complex, HA (10 mg/mL), Xccϕ1 (10^8 PFU/mL) and C20 (30 µg/mL) -previously centrifuged at 13.000 rpm for 15 min- were deposited on 5 x 5 mm silicon chips and the solvent was evaporated under vacuum at 30°C. The silicon supports were mounted on 13 mm SEM aluminum stubs and sputtered with a nanometric conductive layer of Au/Pd alloy using a Desk V TSC coating system (Denton Vacuum, Moorestown, NJ, USA). SEM micrographs were recorded with a Field Emission Gun Scanning Electron Microscope (FEGSEM) Nova NanoSem 450 (FEI/Thermofisher, Hillsboro, OR, USA), under high vacuum conditions.

Z-potential

Water suspensions of the samples HA– ϕ1C20 complex, HA (10 mg/mL), Xccϕ1 (10^8 PFU/mL) and C20 (30 µg/mL) were analyzed for the measurement of zeta potential in disposable Folded Capillary Cells (Malvern Instruments, DTS1070) using a Zetasizer Nano ZS (Malvern Instruments). Each analysis was carried out in triplicate for three independent experiments. The analysis temperature was 25 °C and about 1 mL of sample was used for the test. The results were analysed, and for each sample, the zeta potential average value was determined.

RNA extraction and expression profiling by qPCR.

Fifty mL of bacterium was incubated in an Erlenmeyer Flask, Narrow Mouth - Glassfor for 72h at 24°C in a static manner for biofilm formation and after were added phage (10^8 PFU/ml), C20 (30µg/ml) and HA–ϕ1C20. Each 30 min 10 ml of biofilm was taken until 2h. Total RNA was extracted using trizol protocol (Rio et al 2010). NanoDrop® ND-1000 (Thermo Fisher Scientific Inc.) were used to assess total RNA quantity. One µg of purified total RNA was used as a template for first-strand cDNA synthesis using SuperScript® III Reverse Transcriptase (Invitrogen). The primer were designed using the https://www.eurofinsgenomics.eu/en/ecom/tools/qpcr-assay-design/ for the all genes:

clp (Fw 5'-GACGGGAAAGGGGGCAATTA -3'; Rw 5'-CACAACCGTCGTGTTCCCTA-3'),

manA (Fw 5'- CACCTTCCGCAGCAACAATC-3'; Rw 5'-AGCACGATATCCAGCGACTG -3'),

rpf (Fw 5'-CGACGCTTTCCAATAGCACG-3'; Rw 5'-AGCGTCGATACCTGCTGATG-3'),

gumB (Fw 5'-GGTTCGACCTGACCGAGATC-3'; Rw 5'-CGCCGCCATAAATCTCAGGA-3').

Gene transcript levels were measured using Power SYBR® Green PCR Master Mix (Applied Biosystems®) on a QuantStudio™ 3 Real-Time PCR System (Applied Biosystems®, Thermo Fisher Scientific, Waltham, MA, USA).with the following conditions: an initial step at 95 °C for 10 min, followed by 40 cycles of 95 °C for 15 s, (*clp* 57,1 °C; *manA* 55°C, *rpf* 59,9 °C, *gumB* 63,7°C) for 40 s and 72 °C for 1 min. QuantStudio Design & Analysis Sofware v1.1 (Applied Biosystems) was used for analysis of gene expression. All samples were normalized to HcrC as reference housekeeping gene. The relative quantitative expression was determined using the $2^{-\Delta\Delta CT}$ method [26].

Results

The effect of pentadecanal and Its derivatives on Xcc biofilm formation and eradication.

The anti-biofilm activity of pentadecanal and its derivatives, pentadecanoic acid (acid), pentadecanoic acid methyl ester (ester) and 1,1-dimethoxypentadecane (acetal), was evaluated on biofilm formation of *Xcc*. In detail, a bacterial suspension of *Xcc* was inoculated into the wells of a 96-well polystyrene plate in absence and in presence of pentadecanal or its derivatives, at different concentrations, and incubated for 72h at 25°C. Obtained results

showed a decrease in the biofilm formation in all the tested conditions (Fig. 1A), demonstrating the capability of these molecules to prevent *Xcc* biofilm formation.
Furthermore, to assess if the anti-biofilm molecules were able to eradicate a preformed biofilm, a 72h mature *Xcc* biofilm was treated with pentadecanal or its derivatives for 8h at 25°C. Results indicated a clear reduction of *Xcc* mature biofilm after the treatment with all the tested molecules, with the highest eradication percentages, of about 80%, when biofilm was treated with pentadecanoic acid (Fig. 1B).

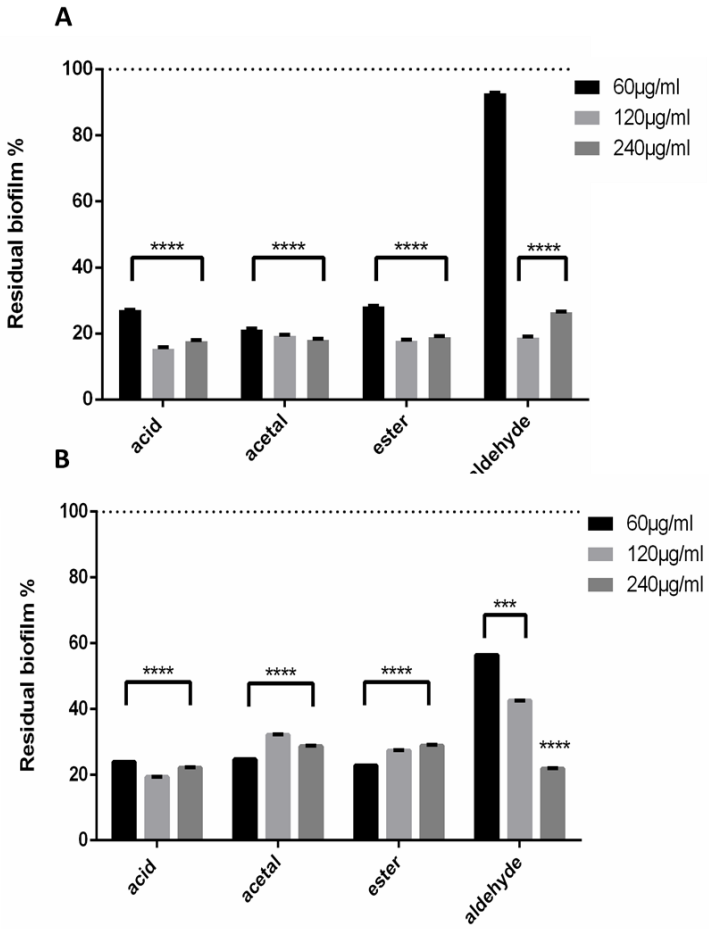

Figure 1 (A) Analysis of the effect of pentadecanal derivatives on *Xcc* biofilm formation after 72h of incubation at 25° C. The data are reported as percentages of residual biofilm. Each value is the mean ± DS of 3 independent experiments. Statistical analysis was performed with the absorbance compared to the untreated control and considered statistically significant when $p < 0.05$ (*$p < 0.05$, **$p < 0.01$, ***$p < 0.001$, ****$p<0.0001$) according to Two Way Anova Multiple comparisons. (B) Analysis of the effect of pentadecanal derivatives on *Xcc* mature biofilm after 72h of incubation at 25° C and 8h of treatment. The data are reported as

percentages of residual biofilm. Each value is the mean ± DS of 3 independent experiments. Statistical analysis was performed with the absorbance compared to the untreated control and considered statistically significant when $p < 0.05$ (*$p < 0.05$, **$p < 0.01$, ***$p < 0.001$, ****$p<0.0001$) according to Two Way Anova Multiple comparisons.

Then, to understand whether the chain length affect the biofilm-inhibiting effect, different long-chain fatty acids (pentadecanoic acid (C15), the dodecanoic (C12), hexadecanoic (C16), octadecanoic (C18) and eicosanoic (C20) were tested on *Xcc* mature biofilm. The results showed that the acids C12, C16, C18 and C20 displayed an anti-biofilm activity comparable with pentadecanoic acid (Fig. 2A).

Synergic treatment of mature Xcc biofilm with HA– Xccϕ1 and long-chain fatty acids

The anti-biofilm activity of the different long-chain fatty acids (C12, C15, C16, C18 and C20) was evaluated in presence of HA–Xccϕ1 complex on *Xcc* mature biofilm. In particular, the anti-biofilm agent's efficacy was evaluated in combination with the Xccϕ1 alone or the HA–Xccϕ1 complex. The results demonstrated that the addition of the HA–Xccϕ1 complex resulted in a more effective anti-biofilm treatment, regardless of the acid used (Fig. 2B).

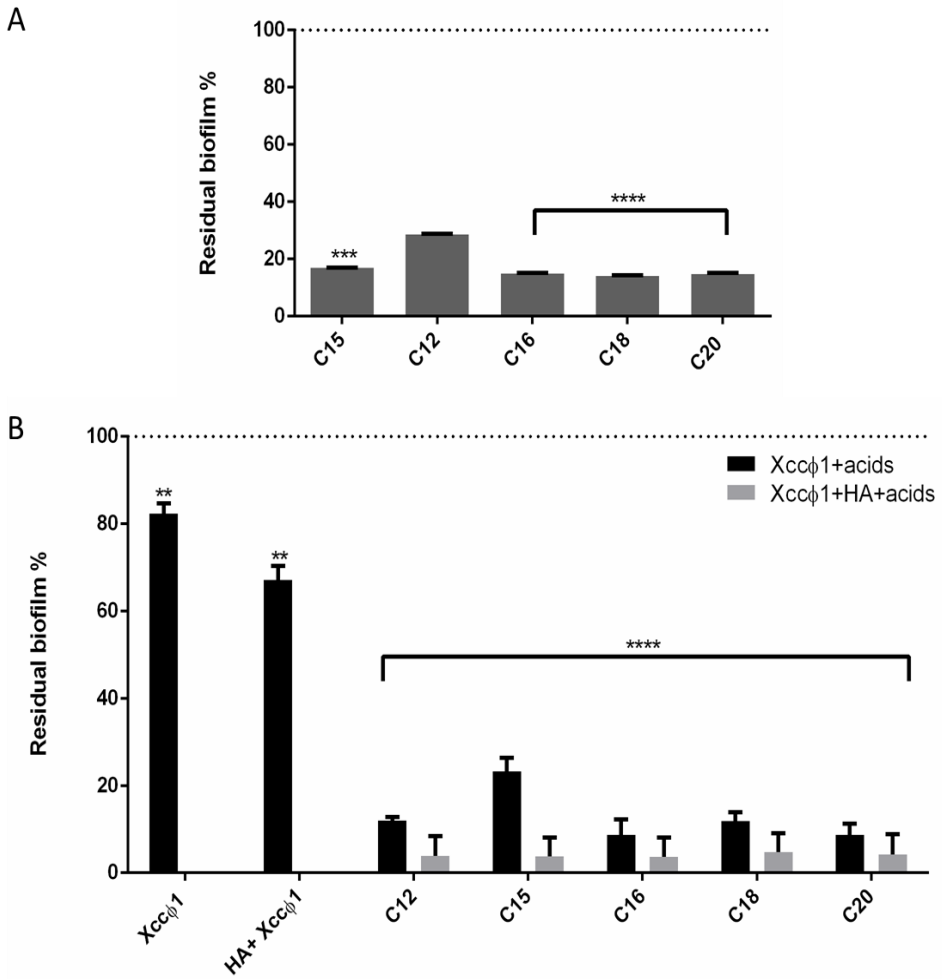

Figure 2 (A) Analysis of the effect of different acids on *Xcc* mature biofilm structure after 72h of incubation at 25° C and 8h of treatment. The data are reported as percentages of residual biofilm. Each value is the mean ± DS of 3 independent experiments. Statistical analysis was performed with the absorbance compared to the untreated control and considered statistically significant when $p < 0.05$ (*$p < 0.05$, **$p < 0.01$, ***$p < 0.001$, ****$p<0.0001$) according to Two Way Anova Multiple comparisons. (B) Analysis of the effect of all the acids r with Xccϕ1 or Xccϕ1 plus HA on *Xcc* biofilm structure using Christal violet assay after 72h of incubation at 25° C and 8h of treatment. The data are reported as percentages of residual biofilm. Each value is the mean ± DS of 3 independent experiments. Statistical analysis was performed with the absorbance compared to the untreated control and considered statistically significant when $p < 0.05$ (*$p < 0.05$, **$p < 0.01$, ***$p < 0.001$, ****$p<0.0001$) according to Two Way Anova Multiple comparisons.

Moreover, in order to assess if the effect induced by the simultaneous treatment with the HA– Xccϕ1 complex and fatty acids was additive or synergistic, the results reported in figure 2B were analysed using a statistical approach. Two parameters (ρ and C_{syn}), described in materials and methods, were used to perform this evaluation. Taking

into account that high C_{syn} values correspond to a clear synergistic effect, as reported in table 1,the best synergistic effect was obtained when the anti-biofilm treatment was performed using C20 and HA–Xccϕ1 complex, even if a synergistic behaviour was also recorded in presence of C12 and C18 (Table 1).

Table 1. The values in table (C_{syn}) are the result of the mathematical analysis used to obtain the combination of acids, phage and HA showing the best synergistic effect.

	C12	C15	C16	C18	C20
ϕ	2.97 ± 1.33	1.31 ± 0.61	0.84 ± 0.34	1.59 ± 0.91	1.28 ± 0.53
ϕ + HA	7.92 ± 3.21	1.31 ± 0.56	1.58 ± 0.69	5.0 ± 2.0	7.94 ± 3.22

The combination of C20 and HA–Xccϕ1 was selected for the following experiments. In particular, the optimization of the treatment with C20 and HA–Xccϕ1 complex was performed by modifying the concentrations of C20, Xccϕ1 and HA (Supplementary figure 1), and exploring different incubation times (data not shown). The optimal condition to eradicate *Xcc* mature biofilm was obtained using Xccϕ1 (10^8 CFU/mL), HA (5 mg/mL) and C20 (30 µg/mL) for a 3h treatment.

Characterization of anti-biofilm activity of HA– Xccϕ1 and C20 combined treatment on Xcc mature biofilm

The anti-biofilm activity of C20 alone and in combination with HA-Xccϕ1 on Xcc mature biofilm was evaluated by confocal laser scanning microscopy (CLSM). In detail, 72 h mature biofilm of Xcc was incubated in the presence of HA– Xccϕ1 + C20. As shown in Figure 3A, although the C20 led to a significative reduction in the biofilm biomass, when it is used in combination with HA– Xccϕ1, a stronger biofilm inhibiting effect was obtained.

Moreover, the anti-biofilm effect of HA–Xccϕ1 + C20 treatment on *Xcc* mature biofilm was explored also in dynamic conditions, using a flow cell system. A 3-channel flow cells were used for analysis of Xcc biofilm formation, in absence and in presence of C20 or HA–Xccϕ1+ C20. Mature biofilms were treated for 3h, under a flow rate of 160 µl/min, with only fresh medium, or with C20 or HA– Xccϕ1 + C20. After treatment the biofilms were observed by CLSM (Figure 3B). Although a substantial reduction in biofilm biomass was obtained in both cases, it is clear that the multi-agent treatment results in a more evident

reduction of *Xcc* mature biofilm, leading to the formation of inhomogeneous and unstructured biofilms (supplementary figure 2).

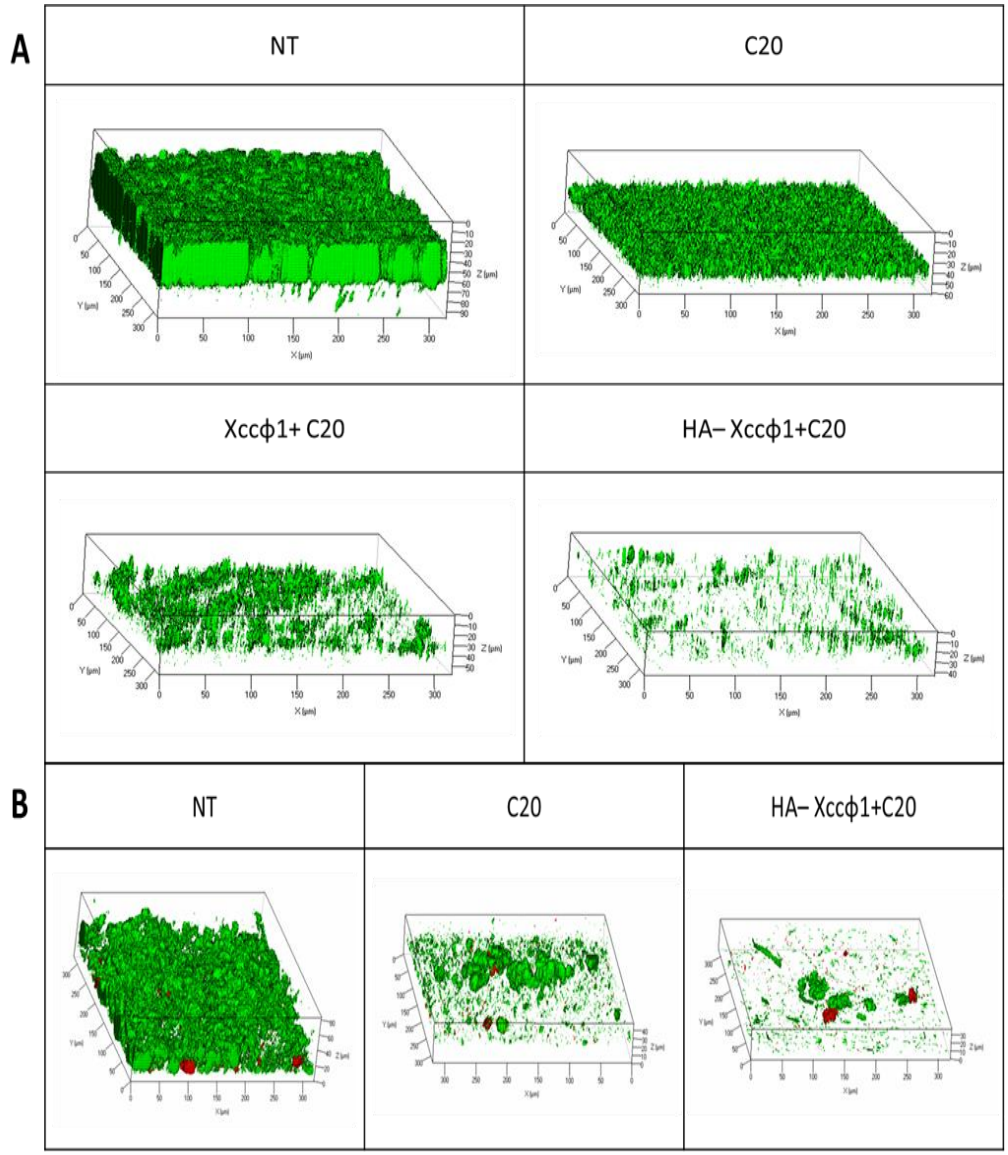

Figure 3 (A) Analysis of the anti-biofilm effect of the eicosanoic acid (C20) alone, with Xccϕ1 and in combination with Xccϕ1 and HA on XCC mature biofilm. The experiment was performed in a static manner. CLSM analysis were performed on 72h mature Xcc biofilms after 3h incubation at RT in the presence and in the absence of the anti-biofilm samples. Three-dimensional biofilm structures were obtained using the LIVE/DEAD® Biofilm Viability Kit. (B) Evaluation of biofilm formation of Xcc in dynamic condition – under a constant flux of nutrients - in presence and in absence of the C20 and the complex ϕHAC20. Biofilm formation was performed in a 3-channel flow cell for 48h. CLSM analysis were performed after 3h incubation at RT in the presence and in the absence of the anti-biofilm samples.

Characterization of the complex HA– Xccϕ1 in presence of C20
In order to investigated how the Xccϕ1, HA and C20 interact each other, scanning electron microscopy (SEM) analysis were carried out. In particular, SEM images of pristine HA show porous spherical aggregates of elongated crystallites, with variable dimensions from few hundreds of nanometres to some microns (Fig. 4A). When HA is functionalized with C20 acid, the porous structure appears filled with the organic and only the external shape of the aggregates is visible (Fig. 4B). In the case of HA+Xccϕ1 the porous structure of HA is still visible, although partially filled. A deeper investigation of the particle surface showed HA crystallites were effectively functionalized with Xccϕ1, as it can be appreciated by comparison of inset A and C of Figure 8. A similar level of functionalization was observed in the case of HA– ϕ1C+20 complex (Fig. 4D).

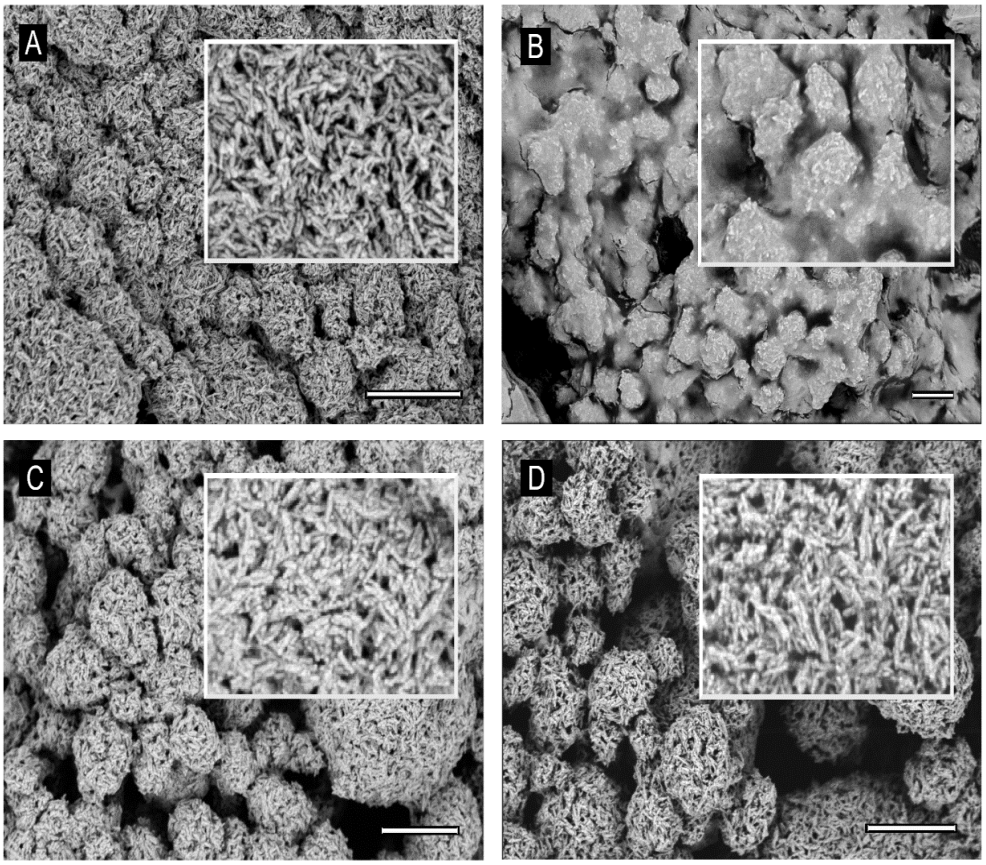

Figure 4 SEM image of HA (A), HA+C20 (B), HA-Xccϕ1 (C) and HA-Xccϕ1+C20 (D). Scale bar is 1μm.

Moreover, the zeta potential measurements were performed for HA, HA– Xccϕ1 and HA– Xccϕ1 + C20 in order to investigate the change of the surface charge of the different samples. Obtained results confirmed the interaction of the phage with hydroxyapatite, because the zeta potential value of the complex is about -3 mV compared the only HA and only phage which values are 0 mV and -15 mV respectively (Fig 5).

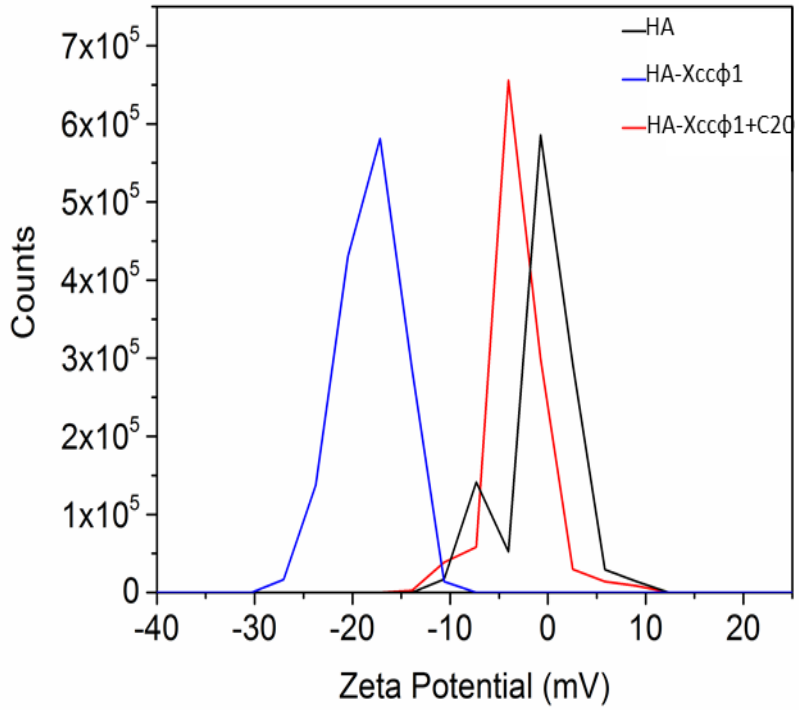

Figure 5 Zeta potential analysis of HA, HA-Xccϕ1, and HA Xccϕ1+C20.

No particular evidence of the modification of surface charge were observed, conversely, when the only HA is previously treated with C20 since the peak value is approximately 0 mV. On the contrary, the peak moves towards positive values (4 mV) with HA– ϕ1+C20 complex. Thus, the presence of the C20 seems to affect, even if for small changes, the surface charge of the HA.

Effect of C20 treatment on genes involved in Xcc quorum sensing

In order to collect information on the molecular mechanisms involved in the anti-biofilm activity of C20, the expression of some key genes in quorum sensing and biofilm formation of *Xcc* were investigated. In

particular, the gene expression of *rpfF*, *gumB*, *clp* and *manA* was evaluated using the Ct method. The *rpfF* gene encodes a enoyl—CoA hydratase that is involved in the synthesis of DSF [27], *gumB* encodes an outer membrane xanthan exporter and is essential for in xanthan biosynthesis [28] *clp* gene encodes a global regulator (cAMP receptor protein-like protein) involved in *Xcc* QS regulatory pathway [29] and *manA* gene encodes endo-1,4-mannanase [30]. The absolute Ct values from the qPCR assays were used to calculate the expression ratios of the *rpfF* [31], *gum*B [28] and *clp* [29] and *man*A [30] genes in *Xcc* biofilm cells treated or not treated with C20. The expression of *gum*B is not affected by the treatment with C20, *rpf*F resulted up regulated while *clp* is downregulated in presence of C20 (Fig. 6). *man*A gene expression was deeply influenced by C20 treatment; indeed, a clear overexpression of this gene was recorded after 60 minutes of treatment.

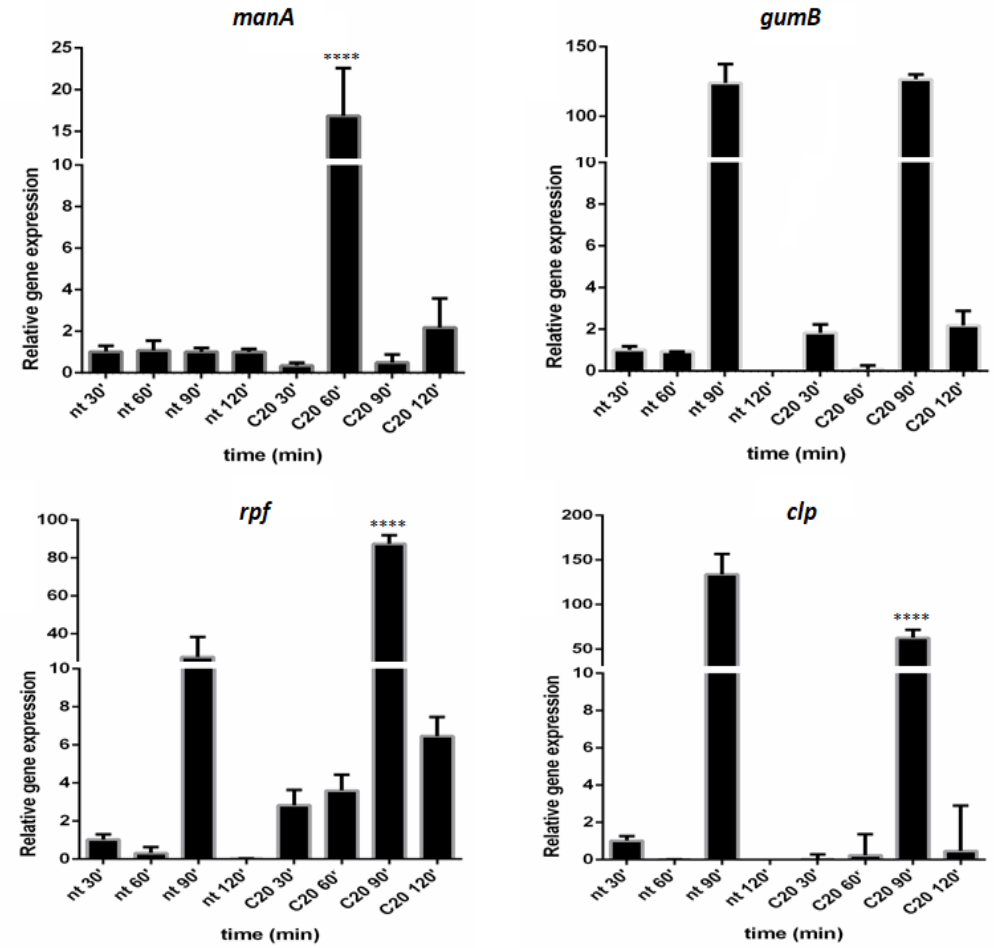

Figure 6 Expression profiling of *Xcc* genes by quantitative real time PCR (qPCR) of different gene involved in biofilm formation and quorum sensing. Biofilm samples were collected at different time of treatment whit C20. The relative gene expression was normalized to HcrC as reference housekeeping gene. Statistical analysis was performed with the relative gene expression compared to the untreated control and considered statistically significant when $p < 0.05$ (*$p < 0.05$, **$p < 0.01$, ***$p < 0.001$, ****$p<0.0001$) according to Two Way Anova Multiple comparisons

Discussion

The formation of biofilms is an important adaptation affecting the survival and persistence of bacteria in most habitats on earth, for plant-associated bacteria, the formation of biofilms has evolved as an adaptive strategy to successfully achieve host colonization and as a key strategy for pathogenesis [32]. Biofilm development contributes to virulence of phytopathogenic bacteria through various mechanisms, including blockage of xylem vessels, increased resistance to plant microbial compounds and/or enhanced colonization of specific habitats, For instance, biofilms are commonly formed by xylem-dwelling pathogens like Xanthomonas campestris pathovar campestris (Xcc) the causal agent of black rot disease of cruciferous plants [33]. This pathogen invades the plant through hydathodes at the leaf margins and moves into the vascular tissues, interrupting water transport and causing general foliar necrosis, wilt, and stunt.

Therefore, a possible treatment for black rot disease could be devoted to the eradication of biofilm, however, an anti-biofilm approach in agricultural microbiology has been rare [34]. This condition leaves opportunity for discovery of novel approaches to crop disease management [35] by an effective anti-biofilm approach against *Xcc*, the multifactorial nature of biofilm implies the use of a multi-targeted or combinatorial strategy.

Recently, it was isolated and characterized a lytic bacteriophage (Xccφ1) able to control the disease caused by *Xcc* to *Brassica oleracea var. gongylodes* (Papaianni et al submitted), the phage-based treatments resulted to be able to limit the bacterium proliferation and to influence the biofilm structure of *Xcc* (Papaianni et al submitted). Starting these results in this paper the phage-based treatment was applied using the hydroxyapatite to increase and stabilize the activity of bacteriophage, this strategy resulted effective against other pathogens [16] and also in the present work the use of HA increased the anti-biofilm activity of Xccφ1 (Figure 2B). Following the idea of a multi-targeted strategy, the anti-biofilm treatment with the complex HA–Xccϕ1 was combined with the use of an anti-biofilm molecule. The identification of a molecule able to act as anti-biofilm against *Xcc* was

performed testing molecules differing for the functional group (i.e. acid, acetal, ester and aldehyde) that share an aliphatic long chain of fifteen carbon atoms. The molecules were evaluated for their capability to prevent the biofilm formation and their efficacy on mature biofilm, although the interest was mainly focused on the action on mature biofilm, and the tests indicated the pentadecanoic acid as a most promising compound. Then, the research was extended to different long fatty acids looking for the acid that, in combination with HA– Xccϕ1, resulted to be able to eradicate the mature biofilm of Xcc. Several long-chain fatty acids resulted to be effective against *Xcc* mature biofilm, but the best synergistic effect was obtained when the anti-biofilm treatment was performed using eicosanoic acid (C20) in combination with HA–Xccϕ1 complex and the treatment was optimized to reduce the action time and the quantity of C20, HA and Xccϕ1 necessary to eradicate the *Xcc* mature biofilm.

Since biofilm evolution inflow condition is more closely related to natural biofilms and can differ from static biofilms the anti-biofilm activity of HA– Xccϕ1+ C20 was demonstrated also in a flow cell system. Moreover, the CLSM analyses on treated biofilm revealed that the synergic action of HA– Xccϕ1+ C20, not only reduces the biofilm biomass but deeply modify the *Xcc* biofilm structure also.

To collect information on the molecular mechanism responsible for the synergic anti-biofilm effect of HA– Xccϕ1+ C20 treatment, the SEM images of HA in the presence of Xccϕ1 or C20 or Xccϕ1+ C20 were recorded and compared. The investigation confirmed the previously reported functionalization of HA crystallites with Xccϕ1 and indicated a similar level of functionalization in case of HA–ϕ1C+20 complex, demonstrating that the synergic effect is not related with a different functionalization. The zeta potential analysis indicated that the change of the surface charge of the HA– Xccϕ1 is slightly affected by the presence C20, therefore is not feasible that the synergy is related with this difference in surface charge.

The chemical structure of C20 is similar to which of diffusible signal factor DSF molecules [36] indeed DSF-family signals share a fatty acid carbon chain with variations in chain length, double-bond configuration and side-chain [37].This similarity pointed the attention on a possible interference of C20 on in *Xcc* Quorum sensing as a potential mechanism responsible for the synergy between HA– Xccϕ1 and C20. Signal molecules of the diffusible signal factor (DSF) family are cis-2-unsaturated fatty acids and the paradigm is cis-11-methyl-2-dodecenoic acid from *Xanthomonas campestris* pv. *Campestris* [36]. Both the synthesis and perception of the DSF signal require products

of the *rpf* (regulation of pathogenicity factors) gene cluster. The synthesis of DSF is dependent on RpfF, whereas the two-component system comprising the sensor kinase RpfC and regulator RpfG is implicated in DSF perception and signal transduction [38,39]. At low bacterial cell density, RpfC binds to and represses the DSF synthase RpfF preventing production of DSF [40]. At high cell density, high concentration of extracellular DSF activates RpfC-RpfG system to degrade the second messenger bis (3', 5')-cyclic diguanosine monophosphate (cyclic di-GMP) c-di-GMP [41], releasing the suppression of c-di-GMP on a global transcription factor *Clp* that controls the expression of multiple virulence factors [29].
The Rpf/DSF system positively influences the expression of the manA gene, encoding the extracellular enzyme beta (1,4)-mannanase implicated in biofilm dispersal [42]. The regulatory effect of the DSF/rpf system on the expression of *manA* involves the transcriptional regulator *Clp*, that positively regulated *manA* transcription [30]. Elevated levels of cyclic di-GMP, the inhibitory ligand of clp, negatively influence the ability of *Clp* to bind to DNA [43] and therefore *manA* si not positively regulated, while in presence of DSF cyclic di-GMP is degraded and *Clp* drives the expression of several genes including *manA*.
Results reported in the present paper demonstrated that after 60' from the treatment of *Xcc* mature biofilm with C20 the *manA* gene is induced, indicating that C20 works as a DSF like molecule. Previously reported paper [44] demonstrated that DSF structurally related molecules may influence the bacterial antibiotic susceptibility by multiple ways, including modulation of the biofilm formation, although it was not reported if their functionality is related to their chemical properties or associated with their potential roles in interference of bacterial signalling and regulatory networks [44]. Instead in this paper, we demonstrated that the DSF structurally related molecules C20 interfere with the transcription and regulation of a gene coding for an enzyme involved in biofilm dispersion stage. Indeed, DSF-inducible enzyme, endo-b-1,4-mannanase ManA, is able to disperse the mature biofilm of *Xcc* [30]. The action of *manA* could explain the anti-biofilm effect of C20 and the ability of this molecule to modify the biofilm structure (figure 4) that resulted, if treated with C20, to be more heterogeneous.Indeed an increase roughness coefficient in treated sample is observed (Supplementary figure 2), this dimensionless factor provides a measure of how much the thickness of a biofilm varies, and it is thus used as a direct indicator of biofilm heterogeneity.
If C20 works as a DSF like molecule is expected that it has no strong effect on r*pfF* and *Clp* gene expression, indeed the DSF synthesis in

Xcc is not auto-inductive [45] and the influence of DSF molecules on Clp is not transcriptional [46], *gum*B gene is essential for the production of xanthan [28,47] one of exopolysaccharide produced by *Xcc* cells. Previously reported paper suggested that Clp controls xanthan synthesis by upregulating the gum promoter via direct binding to two atypical tandem CBSs lacking a GTG motif [48]. While a more recent paper demonstrated that, in *Xcc,* the *gumB* is under the control of HpaR1, a regulator belonging to the GntR family [49], that positively regulates the production of extracellular enzymes and xanthan production. In the experimental condition used in this paper, the C20 seems to be not involved in *gumB* regulation, although further experiments will be devoted to clarifying this point.

The proposed idea is that the C20 treatment induces the synthesis of ManA that is able to hydrolase the mannan promoting the mature biofilm dispersion and the making the biofilm more penetrable, this effect is combined with the antimicrobial activity of the complex HA–Xccϕ1 allowing very efficient removal of *Xcc* mature biofilm.

It's interesting to note that this strategy has several advantages, indeed the virus replication at the site of infection allows to obtain high concentration of phages in the biofilm, increasing the antimicrobial treatment efficiency, moreover, since virus are able to infect dormant cells the proposed approach should reduce the occurrence of recurrent infections.

References

1. Liao, C.-T.; Chiang, Y.-C.; Hsiao, Y.-M. Functional characterization and proteomic analysis of lolA in Xanthomonas campestris pv. campestris. *BMC Microbiol.* **2019**, *19*, 20.
2. Akimoto-Tomiyama, C.; Tanabe, S.; Kajiwara, H.; Minami, E.; Ochiai, H. Loss of chloroplast-localized protein phosphatase 2Cs in Arabidopsis thaliana leads to enhancement of plant immunity and resistance to Xanthomonas campestris pv. campestris infection. *Mol. Plant Pathol.* **2018**, *19*, 1184–1195.
3. Integrated management of black rot of cabbage caused by Xanthomonas campestris (Pammel) Dowson. Available online: https://www.cabi.org/ISC/abstract/20013171495 (accessed on Nov 19, 2019).
4. Agrofit, 2019 MAPA - Ministério da Agricultura, Pecuária e Abastecimento Available online: http://agrofit.agricultura.gov.br/primeira_pagina/extranet/AGROFIT.html (accessed on Nov 27, 2019).
5. Büttner, D.; Bonas, U. Regulation and secretion of *Xanthomonas* virulence factors. *FEMS Microbiol. Rev.* **2010**, *34*, 107–133.
6. Hall-Stoodley, L.; Costerton, J.W.; Stoodley, P. Bacterial biofilms: From the natural environment to infectious diseases. *Nat. Rev. Microbiol.* 2004, *2*, 95–

108.
7. Stewart, P.S.; Costerton, J.W. Antibiotic resistance of bacteria in biofilms. **2001**, *358*, 135–138.
8. Burmølle, M.; Thomsen, T.R.; Fazli, M.; Dige, I.; Christensen, L.; Homøe, P.; Tvede, M.; Nyvad, B.; Tolker-Nielsen, T.; Givskov, M.; et al. Biofilms in chronic infections - A matter of opportunity - Monospecies biofilms in multispecies infections. *FEMS Immunol. Med. Microbiol.* 2010, *59*, 324–336.
9. Rakhuba, D. V.; Kolomiets, E.I.; Szwajcer Dey, E.; Novik, G.I. Bacteriophage receptors, mechanisms of phage adsorption and penetration into host cell. *Polish J. Microbiol.* 2010, *59*, 145–155.
10. Verbeken, G.; Pirnay, J.P.; Lavigne, R.; Jennes, S.; De Vos, D.; Casteels, M.; Huys, I. Call for a dedicated European legal framework for bacteriophage therapy. *Arch. Immunol. Ther. Exp. (Warsz).* 2014, *62*, 117–129.
11. Payne, R.J.H.; Jansen, V.A.A. Phage therapy: The peculiar kinetics of self-replicating pharmaceuticals. *Clin. Pharmacol. Ther.* 2000, *68*, 225–230.
12. Miedzybrodzki, R.; Fortuna, W.; Weber-Dabrowska, B.; Górski, A. Phage therapy of staphylococcal infections (including MRSA) may be less expensive than antibiotic treatment. *Postepy Hig. Med. Dosw. (Online)* **2007**, *61*, 461–465.
13. Inal, J.M. *Phage Therapy: a Reappraisal of Bacteriophages as Antibiotics*; 2003; Vol. 51;.
14. Hanlon, G.W. Bacteriophages: an appraisal of their role in the treatment of bacterial infections. *Int. J. Antimicrob. Agents* **2007**, *30*, 118–28.
15. Doss, J.; Culbertson, K.; Hahn, D.; Camacho, J.; Barekzi, N. A review of phage therapy against bacterial pathogens of aquatic and terrestrial organisms. *Viruses* 2017, *9*.
16. Fulgione, A.; Ianniello, F.; Papaianni, M.; Contaldi, F.; Sgamma, T.; Giannini, C.; Pastore, S.; Velotta, R.; Della Ventura, B.; Roveri, N.; et al. Biomimetic hydroxyapatite nanocrystals are an active carrier for Salmonella bacteriophages. *Int. J. Nanomedicine* **2019**, *14*, 2219–2232.
17. Papa, R.; Selan, L.; Parrilli, E.; Tilotta, M.; Sannino, F.; Feller, G.; Tutino, M.L.; Artini, M. Anti-Biofilm Activities from Marine Cold Adapted Bacteria Against Staphylococci and Pseudomonas aeruginosa. *Front. Microbiol.* **2015**, *6*, 1333.
18. Casillo, A.; Papa, R.; Ricciardelli, A.; Sannino, F.; Ziaco, M.; Tilotta, M.; Selan, L.; Marino, G.; Corsaro, M.M.; Tutino, M.L.; et al. Anti-Biofilm Activity of a Long-Chain Fatty Aldehyde from Antarctic Pseudoalteromonas haloplanktis TAC125 against Staphylococcus epidermidis Biofilm. *Front. Cell. Infect. Microbiol.* **2017**, *7*, 46.
19. Papa, R.; Parrilli, E.; Sannino, F.; Barbato, G.; Tutino, M.L.; Artini, M.; Selan, L. Anti-biofilm activity of the Antarctic marine bacterium Pseudoalteromonas haloplanktis TAC125. *Res. Microbiol.* **2013**, *164*, 450–456.
20. Parrilli, E.; Papa, R.; Carillo, S.; Tilotta, M.; Casillo, A.; Sannino, F.; Cellini, A.; Artini, M.; Selan, L.; Corsaro, M.M.; et al. Anti-biofilm activity of pseudoalteromonas haloplanktis tac125 against staphylococcus epidermidis biofilm: Evidence of a signal molecule involvement? *Int. J. Immunopathol. Pharmacol.* **2015**, *28*, 104–113.
21. Ricciardelli, A.; Casillo, A.; Papa, R.; Monti, D.M.; Imbimbo, P.; Vrenna, G.; Artini, M.; Selan, L.; Corsaro, M.M.; Tutino, M.L.; et al. Pentadecanal inspired molecules as new anti-biofilm agents against *Staphylococcus epidermidis*. *Biofouling* **2018**, *34*, 1110–1120.

22. Schaad, N.W.; Frederick, R.D.; Shaw, J.; Schneider, W.L.; Hickson, R.; Petrillo, M.D.; Luster, D.G. Advances in molecular-based diagnostics in meeting crop biosecurity and phytosanitary issues. *Annu. Rev. Phytopathol.* **2003**, *41*, 305–24.
23. Huang, L.; Teumelsan, N.; Huang, X. A facile method for oxidation of primary alcohols to carboxylic acids and its application in glycosaminoglycan syntheses. *Chem. - A Eur. J.* **2006**, *12*, 5246–5252.
24. Ricciardelli, A.; Casillo, A.; Papa, R.; Monti, D.M.; Imbimbo, P.; Vrenna, G.; Artini, M.; Selan, L.; Corsaro, M.M.; Tutino, M.L.; et al. Pentadecanal inspired molecules as new anti-biofilm agents against *Staphylococcus epidermidis*. *Biofouling* **2018**, *34*, 1110–1120.
25. Papaianni, M.; Contaldi, F.; Fulgione, A.; Woo, S.L.; Casillo, A.; Corsaro, M.M.; Parrilli, E.; Marcolungo, L.; Rossato, M.; Delledonne, M.; et al. Role of phage ϕ1 in two strains of Salmonella Rissen, sensitive and resistant to phage ϕ1. *BMC Microbiol.* **2018**, *18*, 208.
26. Livak, K.J.; Schmittgen, T.D. Analysis of Relative Gene Expression Data Using Real-Time Quantitative PCR and the 2−ΔΔCT Method. *Methods* **2001**, *25*, 402–408.
27. Dow, J.M.; Crossman, L.; Findlay, K.; He, Y.Q.; Feng, J.X.; Tang, J.L. Biofilm dispersal in Xanthomonas campestris is controlled by cell-cell signaling and is required for full virulence to plants. *Proc. Natl. Acad. Sci. U. S. A.* **2003**, *100*, 10995–11000.
28. Torres, P.S.; Malamud, F.; Rigano, L.A.; Russo, D.M.; Marano, M.R.; Castagnaro, A.P.; Zorreguieta, A.; Bouarab, K.; Dow, J.M.; Vojnov, A.A. Controlled synthesis of the DSF cell-cell signal is required for biofilm formation and virulence in Xanthomonas campestris. *Environ. Microbiol.* **2007**, *9*, 2101–2109.
29. Tao, F.; He, Y.W.; Wu, D.H.; Swarup, S.; Zhang, L.H. The cyclic nucleotide monophosphate domain of Xanthomonas campestris global regulator Clp defines a new class of cyclic di-GMP effectors. *J. Bacteriol.* **2010**, *192*, 1020–1029.
30. Hsiao, Y.M.; Liu, Y.F.; Fang, M.C.; Tseng, Y.H. Transcriptional regulation and molecular characterization of the manA gene encoding the biofilm dispersing enzyme mannan endo-1, 4-β-mannosidase in xanthomonas campestris. *J. Agric. Food Chem.* **2010**, *58*, 1653–1663.
31. Dow, J.M.; Crossman, L.; Findlay, K.; He, Y.-Q.; Feng, J.-X.; Tang, J.-L. Biofilm dispersal in Xanthomonas campestris is controlled by cell-cell signaling and is required for full virulence to plants. *Proc. Natl. Acad. Sci. U. S. A.* **2003**, *100*, 10995–1000.
32. Koczan, J.M.; Mcgrath, M.J.; Zhao, Y.; Sundin, G.W. Contribution of Erwinia amylovora Exopolysaccharides Amylovoran and Levan to Biofilm Formation: Implications in Pathogenicity. **2009**, *99*, 1237.
33. Nuñez, A.M.P.; Rodríguez, G.A.A.; Monteiro, F.P.; Faria, A.F.; Silva, J.C.P.; Monteiro, A.C.A.; Carvalho, C. V.; Gomes, L.A.A.; Souza, R.M.; De Souza, J.T.; et al. Bio-based products control black rot (Xanthomonas campestris pv. campestris) and increase the nutraceutical and antioxidant components in kale. *Sci. Rep.* **2018**, *8*.
34. Harding, M.; Nadworny, P.; Buziak, B.; Omar, A.; Daniels, G.; Feng, J. Improved methods for treatment of phytopathogenic biofilms: Metallic compounds as anti-bacterial coatings and fungicide tank-mix partners. *Molecules* **2019**, *24*.

35. Villa, F.; Cappitelli, F.; Cortesi, P.; Kunova, A. Fungal biofilms: Targets for the development of novel strategies in plant disease management. *Front. Microbiol.* **2017**, *8*.
36. Ryan, R.P.; Dow, J.M. Communication with a growing family: Diffusible signal factor (DSF) signaling in bacteria. *Trends Microbiol.* 2011, *19*, 145–152.
37. Deng, Y.; Wu, J.; Tao, F.; Zhang, L.H. Listening to a new language: DSF-based quorum sensing in gram-negative bacteria. *Chem. Rev.* **2011**, *111*, 160–179.
38. Barber, C.E.; Tang, J.L.; Feng, J.X.; Pan, M.Q.; Wilson, T.J.; Slater, H.; Dow, J.M.; Williams, P.; Daniels, M.J. A novel regulatory system required for pathogenicity of Xanthomonas campestris is mediated by a small diffusible signal molecule. *Mol. Microbiol.* **1997**, *24*, 555–66.
39. Slater, H.; Alvarez-Morales, A.; Barber, C.E.; Daniels, M.J.; Maxwell Dow, J. A two-component system involving an HD-GYP domain protein links cell-cell signalling to pathogenicity gene expression in Xanthomonas campestris. *Mol. Microbiol.* **2000**, *38*, 986–1003.
40. Huedo, P.; Yero, D.; Martínez-Servat, S.; Estibariz, I.; Planell, R.; Martínez, P.; Ruyra, À.; Roher, N.; Roca, I.; Vila, J.; et al. Two different rpf clusters distributed among a population of Stenotrophomonas maltophilia clinical strains display differential diffusible signal factor production and virulence regulation. *J. Bacteriol.* **2014**, *196*, 2431–2442.
41. Ryan, R.P.; Fouhy, Y.; Lucey, J.F.; Crossman, L.C.; Spiro, S.; He, Y.W.; Zhang, L.H.; Heeb, S.; Cámara, M.; Williams, P.; et al. Cell-cell signaling in Xanthomonas campestris involves an HD-GYP domain protein that functions in cyclic di-GMP turnover. *Proc. Natl. Acad. Sci. U. S. A.* **2006**, *103*, 6712–6717.
42. Tao, F.; Swarup, S.; Zhang, L.H. Quorum sensing modulation of a putative glycosyltransferase gene cluster essential for Xanthomonas campestris biofilm formation. *Environ. Microbiol.* **2010**, *12*, 3159–3170.
43. Leduc, J.L.; Roberts, G.P. Cyclic di-GMP allosterically inhibits the CRP-like protein (Clp) of Xanthomonas axonopodis pv. citri. *J. Bacteriol.* **2009**, *191*, 7121–7122.
44. Deng, Y.; Lim, A.; Lee, J.; Chen, S.; An, S.; Dong, Y.-H.; Zhang, L.-H. Diffusible signal factor (DSF) quorum sensing signal and structurally related molecules enhance the antimicrobial efficacy of antibiotics against some bacterial pathogens. *BMC Microbiol.* **2014**, *14*, 51.
45. Cheng, Z.; He, Y.W.; Lim, S.C.; Qamra, R.; Walsh, M.A.; Zhang, L.H.; Song, H. Structural basis of the sensor-synthase interaction in autoinduction of the quorum sensing signal DSF biosynthesis. *Structure* **2010**, *18*, 1199–1209.
46. Ryan, R.P.; An, S. qi; Allan, J.H.; McCarthy, Y.; Dow, J.M. The DSF Family of Cell–Cell Signals: An Expanding Class of Bacterial Virulence Regulators. *PLoS Pathog.* **2015**, *11*.
47. Katzen, F.; Becker, A.; Zorreguieta, A.; Pühler, A.; Ielpi, L. Promoter analysis of the Xanthomonas campestris pv. campestris gum operon directing biosynthesis of the xanthan polysaccharide. *J. Bacteriol.* **1996**, *178*, 4313–4318.
48. Chen, C.H.; Lin, N.T.; Hsiao, Y.M.; Yang, C.Y.; Tseng, Y.H. Two non-consensus Clp binding sites are involved in upregulation of the gum operon involved in xanthan polysaccharide synthesis in Xanthomonas campestris pv. campestris. *Res. Microbiol.* **2010**, *161*, 583–589.
49. An, S.Q.; Lu, G.T.; Su, H.Z.; Li, R.F.; He, Y.Q.; Jiang, B. Le; Tang, D.J.;

Tang, J.L. Systematic mutagenesis of all predicted gntR genes in xanthomonas campestris pv. campestris reveals a GntR family transcriptional regulator controlling hypersensitive response and virulence. *Mol. Plant-Microbe Interact.* **2011**, *24*, 1027–1039.

Supplementary figure

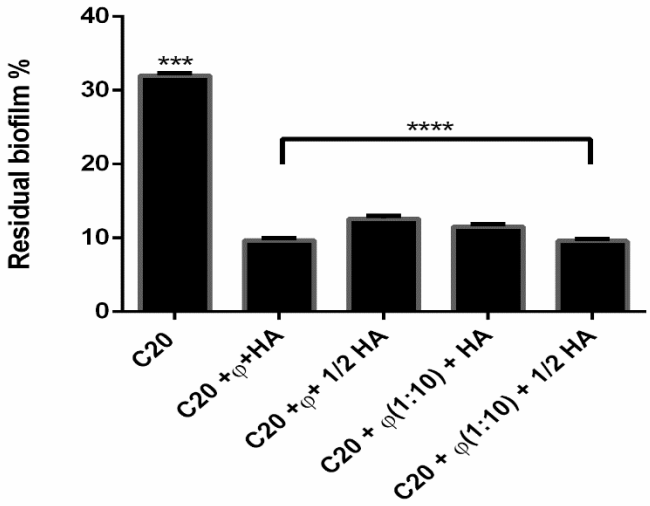

Figure S1 Analysis of the effect of C20 alone (30µg/mL) or with Xccϕ1 (ϕ) 10^8 /10^9 PFU/mL or Xccϕ1 plus HA on *Xcc* biofilm structure using Christal violet assay after 72h of incubation at 25° C and 3h of treatment. The data are reported as percentages of residual biofilm. Each value is the mean ± DS of 3 independent experiments. Statistical analysis was performed with the absorbance compared to the untreated control and considered statistically significant when $p < 0.05$ (*$p < 0.05$, **$p < 0.01$, ***$p < 0.001$, ****$p<0.0001$) according to Two Way Anova Multiple comparisons.

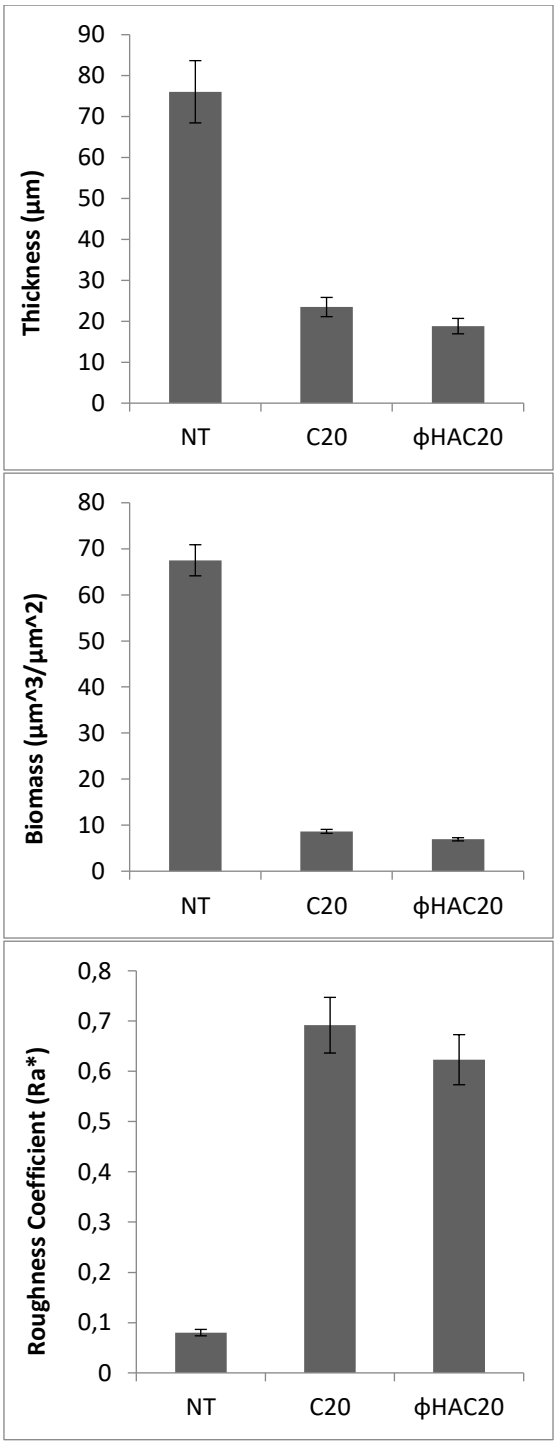

Figure S2 Quantitative analysis of biomass, average thickness and roughness coefficient of Xanthomonas campestris pv. campestris biofilms were reported. Each data point represents

the mean ± the SD of two independent samples. The mean values of the treated samples were compared to the untreated control and considered significant when $p < 0.05$ (* $p < 0.05$, ** $p < 0.01$, *** $p < 0.001$) according to the Student t-test.

CHAPTER III

Article accepted to Microorganism
Phages promote metabolic changes in bacteria biofilm

Papaianni M.[1+], Cuomo P.[1+], Fulgione A.[1,2], Albanese D[3], Paris D[4], Motta A[4], Iannelli D.[1], Capparelli R.[1*]

1 Department of Agricultural Sciences, University of Naples Federico II, 80055 Portici, Naples, Italy.

2 Istituto Zooprofilattico Sperimentale del Mezzogiorno (IZSM), 80055 Portici, Naples, Italy.

3 Department of Industrial Engineering University of Salerno, 84084, Fisciano Italy.

4 Institute of Biomolecular Chemistry, National Research Council, 80078 Pozzuoli, Naples, Italy.

*Corresponding Author

Tel.: +39 081 2539276. E-mail: capparel@unina.it

+ These authors also contributed equally to this work.

Abstract

Background: Bacterial biofilm is a matrix of polysaccharides, extracellular DNA, proteins and lipids. It provides bacteria with resistance to antimicrobial molecules, radiation, desiccation, UV, pH change and osmotic shock. Biofilm also confers protection against conventional antimicrobial agents and the host immune system. Bacteriophages are known to move across the biofilm and make it permeable to antimicrobials. Several studies have demonstrated the property of mineral hydroxyapatite to improve the lytic activity of bacteriophages, and the efficacy of eicosanoic acid isolated from Antarctic bacteria to destroy the biofilm structure. **Results:** The present study exploits the efficacy of the combined use of bacteriophage, hydroxyapatite and eicosanoic acid against *Xanthomonas campestris* pv. *campestris* biofilm. **Conclusion:** The approach might be extended to the study of other biofilm-producing bacteria. Our data also show that Xccϕ1 - alone or combined with hydroxyapatite and eicosanoic acid - interferes with the metabolic pathways involved in biofilm formation.

Keyword: Bacteriophages; biofilm; NMR analysis.

Introduction

The concern about bacterial resistance to antibiotics and microbial biofilm production is rapidly increasing, regardless of the many actions taken by the World Health Organization to control these phenomena. The latest data collected by the European Centre for Disease Prevention and Control highlight a persistent increase of antibiotic-resistant bacteria in the clinical area, as well as that of the food industry and agriculture [1].

Biofilm production is the response of bacteria to adverse environmental conditions [2], such as the presence of antibiotics or the need to establish a chronic colonization [3–5]. At present, microbial biofilm production represents a major economic as well as clinical problem. Prevention and treatment of bacterial biofilm formation is therefore a prime concern.

Bacteriophages (phages) are viruses infecting bacteria. Several studies highlight the potential of phages to lyse bacteria protected by the biofilm [6–8], a property that many antibiotics do not possess [9]. In addition, phages are species specific, and therefore can be used to target pathogenic bacteria, without disturbing non-harmful commensal bacteria [10]. These properties make phages an attractive means against bacterial biofilms. At present, the regulatory agencies limit the use of phages to the control of pathogens in food industry and agriculture [11]. The use of phages for the treatment of human infections might follow once the functions of phage genes are better known and the risk of unwanted effects is acceptable [12]. During the last century antibiotics have contrasted life threatening bacterial infections. Now that these molecules have lost much of their power against bacteria, the progress of synthetic biology and the renewed interest in phages make realistic the anticipation that in the near future phages may have a major role in the contrast of resistant bacterial strains that continually emerge from the host-pathogen evolutionary arms race.
Previous studies have demonstrated that hydroxyapatite (HA) enhances the activity of phages [13], eicosanoic acid (C20) weaken the bacterial biofilm structure [14–16], phage Xccϕ1 can control Xcc infection in plant (Papaianni submitted), and finally, that metabolomics is particularly effective to learn how phages act against the biofilm [6,17]. Using this technique, here we demonstrate that HA, C20 and Xccϕ1 impair the *Xanthomonas campestris* pv. *campestris* (*Xcc*) biofilm, when used simultaneously. In the future, this design might easily be extended to phages selected for rapid replication in the biofilm, or to a pool of phages producing different depolymerases effective against a multispecies biofilm.

Material and method

Isolation and growth of *Xcc* phages. Ten g of rhizospheric soil from *Brassica oleracea* plants with black rot symptoms (characteristic of *Xcc* infection) were suspended in 15 ml of nutrient broth (Sigma Aldrich, Milan, Italy), and shacked for 30 min at 24° C. Soil sediment was

removed by centrifugation (5000 rpm for 10 min), and individual supernatants (15 mL) transferred into sterile flasks. To each flask were added 40 mL 10^6 colony forming units (CFU) per mL of *Xcc* bacteria in exponential growth phase. Flasks were incubated overnight at 24°C. Cultures were treated with chloroform, clarified by centrifugation, and filtered through Millipore 0.22 µm-pore-size membrane filters (MF-Millipore, Darmstadt, Germany). Filtrates were tested for the presence of *Xcc*-specific phages as described [13].

Activity of C20 against biofilm: The eicosanoic acid (C20) activity was tested by the crystal violet staining test [18]. Individual wells of a polystyrene 96 flat-well plate (Falcon) were spotted with 200 µl of *Xcc* bacteria (10^6 colony forming units per ml). To facilitate bacterial attachment, the plates were incubated for 72h at 24 °C without shaking. C20 was then added (60 µg/mL, 120 µg/mL, or 240 µg/mL per well) and again incubated for 8h. After treatment, planktonic cells were gently removed, and the wells washed three times with H2O. For NMR studies C20 was used at the lowest concentration.

Preparation of supernatants for metabolic analysis: In order to facilitate biofilm formation, the *Xcc* bacterial suspension was distributed in Erlenmeyer flasks (50 mL/flask) and incubated for 72h at 24°C under a static condition. Next, 5 mL of phages (10^8 plaque forming units (PFU)/mL), acid (30 µg/mL) or Xccϕ1+HA+C20 (10^8 PFU/mL, 5 mg/mL and 30 µg/mL respectively) were added to each flask. After 3h of incubation at 24°C, the cultures were collected, centrifuged (13.000 rpm for 20 min) and the supernatants stored at +4°C for NMR analysis.

NMR analysis: NMR spectra were recorded on a Bruker Avance III-600 MHz spectrometer (Bruker BioSpin GmbH, Rheinstetten, Germany), equipped with a TCI CryoProbe™ fitted with a gradient along the Z-axis, at a probe temperature of 27°C. One-dimensional (1D) proton spectra were acquired
at 600 MHz by using the excitation sculpting sequence [19]. wo-dimensional (2D) total correlation spectroscopy (TOCSY) spectra[20,21] were acquired using MLEV-17 pulse sequence incorporating the excitation sculpting sequence for water suppression. Spectra in water were referenced to internal 0.1 mM TSP, assumed to resonate at δ = 0.00 ppm. 2D ^{1}H-^{13}C heteronuclear single quantum coherence (HSQC) spectra were recorded at 150.90 MHz for ^{13}C using pre-saturation for water suppression [22]. HSQC spectra in water were

referenced to the α-glucose doublet resonating at 5.24 ppm for ^{1}H and 93.10 ppm for ^{13}C.

Multivariate data analysis: The spectral region 0.50–9.50 ppm for each aqueous supernatant was automatically binned into integrated regions (buckets) of 0.02-ppm width using the AMIX 3.9.7 package (Bruker Biospin GmbH, Rheinstetten, Germany). The residual water resonance (4.40–5.60 ppm) was removed prior to the normalization process to the total spectrum area. To discriminate samples according to their metabolic variations, NMR profiles were analysed using SIMCA14 package (Umetrics, Umeå, Sweden). Principal Component Analysis (PCA) and Orthogonal Projection to Latent Structures Discriminant Analysis (OPLS–DA) [23] were performed. The quality of all PCA and OPLS–DA models was evaluated using the regression correlation coefficient R^2 and the cross-validate correlation coefficient Q^2. Normality test and ANOVA test with Bonferroni correction were performed with the OriginPro 9.1 software package (Origin Lab Corporation, Northampton, USA).

Pathway Analysis: Pathway topology and biomarker analysis were carried using Metaboanalyst 4.0 [24]. Metabolites were selected by evaluating both VIP values > 1 in class discrimination and correlation values |pq[corr]| > 0.7.

Results

Phage Xccφ1, hydroxyapatite, and eicosanoic acid modulate *Xcc* biofilm. The efficacy of hydroxyapatite (HA) to stabilize and enhance the activity of phages [13], and of eicosanoic acid (C20) to modify the microbial biofilm structure [14–16] have been already described. Transmission electron microscopy (TEM) examination identified Xccϕ1 as a member of the Myoviridae family by the contractile, long, relatively thick tail, and a central core separated from the head by the neck (Figure 1). The C20 is approximately equally active at 60 µg/mL, 120 µg/mL, or 240 µg/mL, and reduces the amount of biofilm approximately by 80% (Figure 2). In this study the degrading activity of phage Xccϕ1, HA, and C20 cocktail against *Xcc* biofilm is evaluated using NMR.

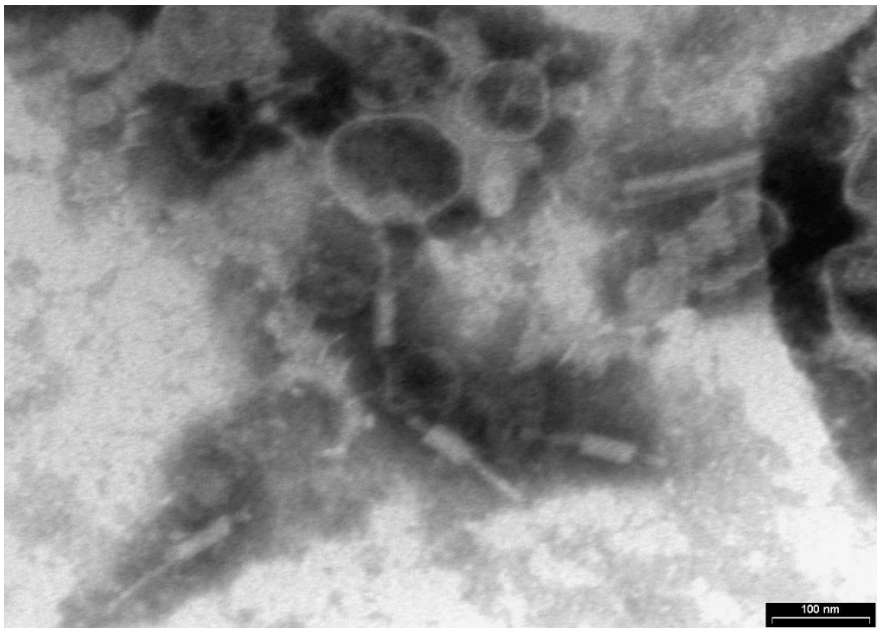

Figure 1: Phage Xccϕ1structure as observed by Transmission Electron Microscopy (TEM). Bar = 100 nm.

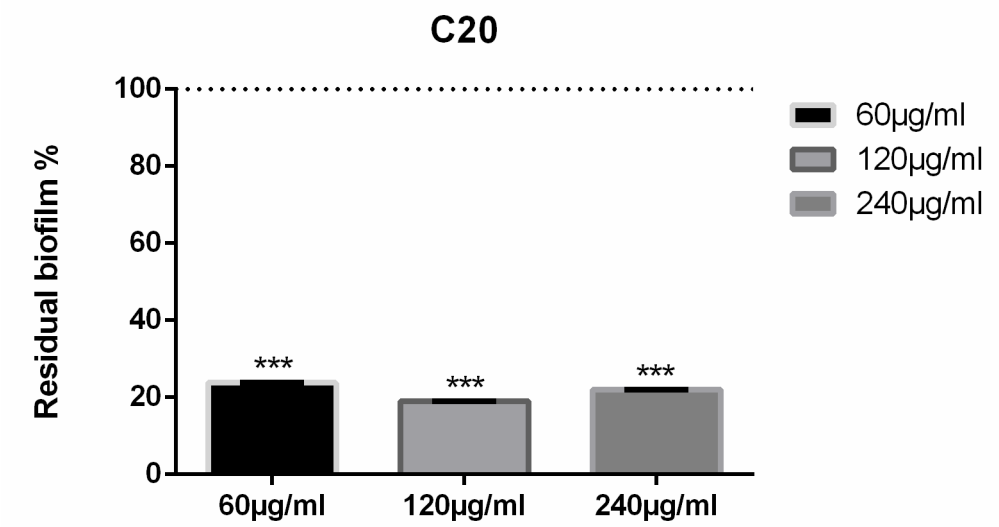

Figure 2: Activity of eicosanoic acid (C20) on *Xcc* biofilm formation. Data expressed as percent of residual biofilm. Each value indicates mean ± SD of 3 independent experiments. Absorbance values of treated and untreated samples were compared by two way ANOVA multiple comparisons analysis. ***$p < 0.001$.

NMR analysis: class discrimination. The biofilms from *Xcc* cultures treated with phage (Xccϕ1), C20 or with both plus HA Xccϕ1+HA+C20 were analysed by NMR spectroscopy. Ten replicas of each condition were analysed. Two of the 40 samples were tested twice for quality control. Data homogeneity of the 42 samples was tested by unsupervised PCA (data not shown). Differences between the metabolic profiles of single samples were detected by supervised OPLS-DA. The NMR data regression provided a robust statistical model with 2 predictive components (parameters: R^2= 0.70, significant; Q^2= 0.71, significant; CV-ANOVA test: p value =3.7x10^{-21}, significant; 900 hits permutation test: R_{fit} = 0.08; Q_{fit}= -0.31, both indicating a non-overfitting model). The projection of all spectra into the 2 principal predictive components showed a total class discrimination (Figure 3A). In particular, the first component t[1] accounts for the main differences between the Xccϕ1/Xccϕ1+HA+C20 classes placed at t[1] negative coordinates versus the XccNT/C20 classes placed at positive t[1]. The second component t[2] accounts for the main differences between the Xccϕ1+HA+C20 and C20 classes placed at t[2] negative coordinates versus those XccNT and Xccϕ1 (not treated with acid) placed at t[2] positive coordinates.

In conclusion, the first and second components show the effect of the phage, and the eicosanoic acid on the biofilm, respectively.

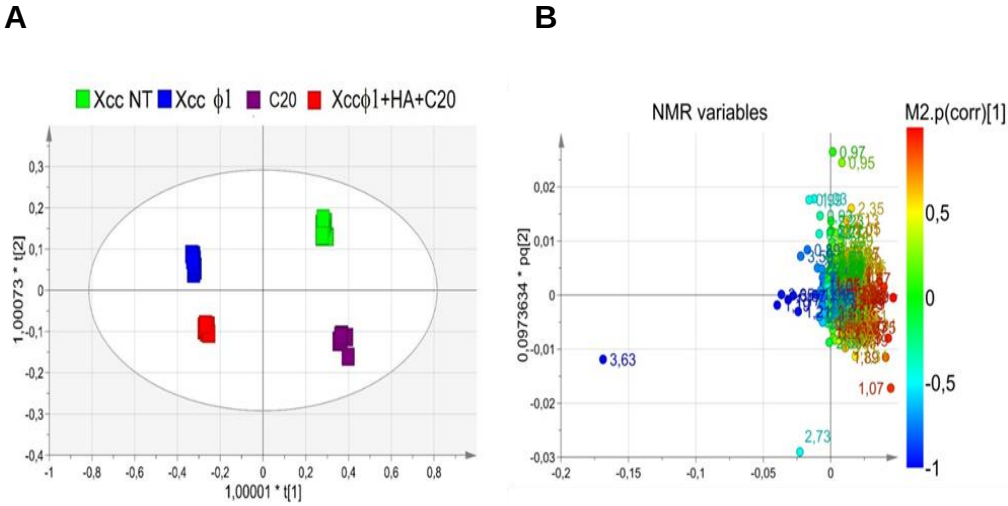

Figure 3: Orthogonal projection to latent structure discriminant analysis (OPLS-DA) of *Xcc* biofilm. **(A)** Scores plot showing the separation between *Xcc* biofilm (green squares), *Xcc*

biofilm treated with Xccϕ1 (blue squares), with C20 (purple squares), or Xccϕ1+HA+C20 (red squares). **(B)** Loadings plot showing NMR variables corresponding to metabolites responsible for class separation. Metabolites relevant for between-classes separation displaying |p(corr)|>0.7.

NMR analysis: discriminating metabolites. To identify the main discriminating metabolites, we inspected the loadings plot, selecting NMR signals with VIP >1 and p(corr) > 0.7 (Figure 3B). The Xccϕ1 and the Xccϕ1+HA+C20 classes, both placed along the t[1] negative component, show up-regulation of galactomannan, ethanol, fatty acids, valine, isoleucine and down-regulation of pyroglutamate, lysine, propionate, iso-butyrate, arginine, lactate and glycine (Table 1). The main differences between the four classes grouped along the t[1] predictive component are clearly attributable to the presence/absence of phage.

On the other hand, the Xccϕ1+HA+C20 and C20 classes, both placed along the t[2] negative component, show up-regulation of dimethylamine (particularly in C20 group) and α-methyl-histidine, and down-regulation of 2-aminoadipate, leucine, isoleucine, methionine, betaine, 3-hidroxy-isobutyrate and glutamate (Table 1). The main differences between the four classes grouped along the t[2] predictive component this time are clearly attributable to the presence/absence of eicosanoic acid.

In conclusion, Figure 3A clearly depicts how the phage and the acid both alter the biofilm metabolism, though by different means. This conclusion well fits with the unique lytic activity of ϕ1 and that of the C20 to clear biofilm.

Metabolites	**XccNT**	**Xccϕ1**	**C20**	**Xccϕ1+HA+C20**
2-Aminoadipate	+ +	+	- -	-
Arginine	+ -	- -	++	-
Betaine	+	-	-	-
Dimethylamine	-	-	-	+
Ethanol	-	+	-	+

Galactomanann	/	+	/	+
Glutamate	+	-	+	- -
Isobutyrate	+ -	-	+ +	-
Isoleucine	+ +	+	-	-
Lactate	+	-	+	-
Leucine	+ +	+	-	-
Lysine	+	-	+	-
Methionine	+ +	- +	+ -	- -
Pyroglutamate	+	-	+	-
Propionate	+	-	+	-
Saturated Fatty Acids	-	+	- -	+
t-methyl histidine	- +	-	+	+ -
Tyrosine	+	-	+	-

Table 1: Metabolites dysregulated +: upregulated, -: downregulated.

NMR analysis: pathway analysis. NMR signals with VIP >1 and p(corr) > 0.7 were used to identify the main metabolic pathways dysregulated between sample classes. The phenylalanine pathway displayed the highest impact, followed by the alanine, aspartate, and glutamate pathway; arginine and proline; glycine, serine, and proline; glutamine and glutamate pathways (Figure 4).

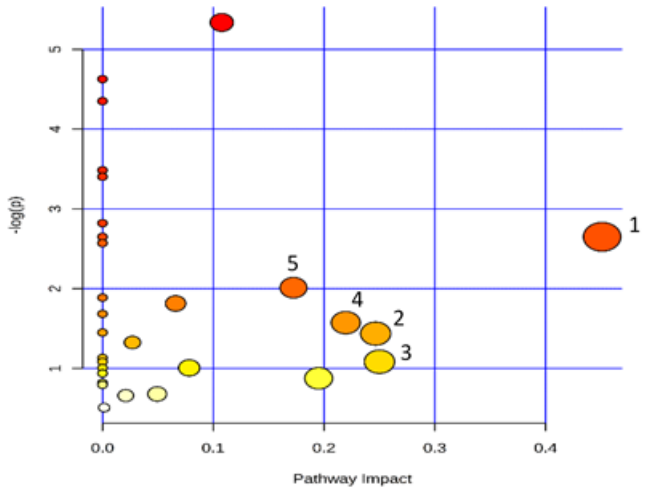

Figure 4: Pathway analysis based on most relevant metabolites identified by the OPLS-DA. Impacts and statistical significance of pathways: 1, phenylalanine metabolism (Impact: 0.45; p: $7.06x10^{-2}$); 2, alanine, aspartate and glutamate metabolism (Impact: 0.25; p: $3.38x10^{-1}$); 3, arginine and proline metabolism (Impact: 0.25; p: $2.37x10^{-1}$); 4, glycine, serine and threonine metabolism (Impact: 0.22; p: $2.07x10^{-1}$); 5, glutamate and glutamine metabolism (Impact: 0.17; p: $1.34x10^{-1}$).

A

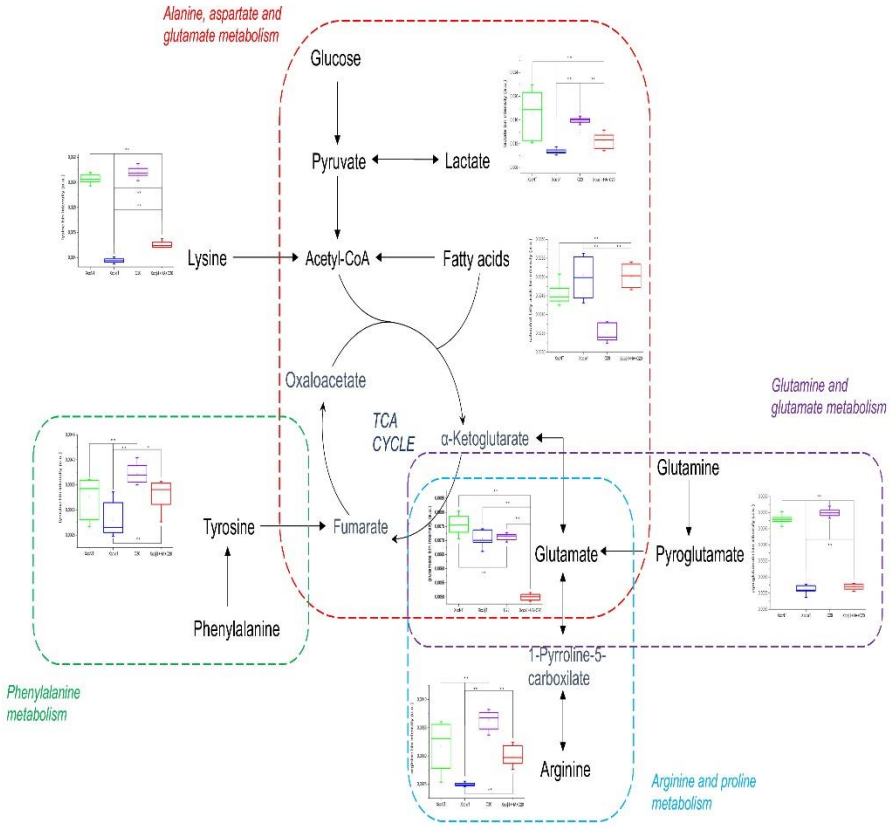

B

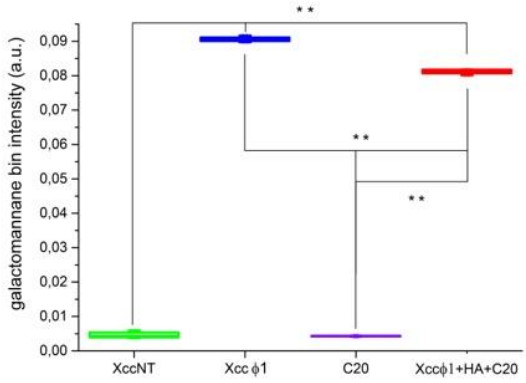

Figure 5: (A) Schematic presentation of altered pathways and associated metabolites. The figure shows bin intensity plot and statistical significance (* p<0.05; ** p<0.01) of single

metabolites. **(B)** Bin intensity plot of the metabolite galactomannan (statistical significance: ** $p<0.01$).

Discussion

In the present study, NMR-based metabolomic analysis resulted highly functional to understand how the different components Xccϕ1-Ha-C20 act against the *Xcc* biofilm. We focused on the metabolites that distinguish the different cell classes. Specifically, the score plot (Figure 3A) shows that the Xccϕ1-HA-C20 class is placed at negative coordinates of both t[1] and t[2] components. This allocation indicates that the metabolic alterations of this cell class can be attributed to the activity of both the phage and C20. However, screening for metabolic changes induced by C20 alone, did not show a clear association of C20 with *Xcc* biofilm.

Before proceeding in the discussion, it may help reminding that: 1) amino acids metabolism participates to the formation of the bacterial biofilm [25], and are an important energy source since feed the TCA cycle (Figure 5A); 2) that here we are describing a mature (72-h old) biofilm, potentially marked by reduced levels of oxygen, a condition promoting anaerobic glycolysis and inhibition of the TCA cycle [26].

In this study we find highly dysregulated amino acids pathways and altered levels of lactate. Specifically, we find that the classes without phage (XccNT and C20) display high levels of lysine, glutamate, tyrosine, pyroglutamic acid and arginine, all involved in biofilm formation, and maturation [25]. Instead, the classes with phage (Xccϕ1 and Xccϕ1+ HA+C20) display low levels of these same amino acids (Figure 5A).

The same pattern holds for lactate. The classes without phage (same as above) show high levels of lactate. This result is in line with the evidence that lactate contributes to biofilm production [27] and that addition of lactate to minimal medium favours bacterial cell adherence to surfaces and biofilm formation [28]. The classes treated with phage (same as above) instead show low levels of lactate (Figure 5A). This result also conforms to the literature [25,27].

In this study, we find that the classes treated with phage show high levels of saturated fatty acids (SFAs) (Figure 5A). Very likely, this result reflects the cell lysis caused by the phage and subsequent release of SFAs in the exogenous environment (the supernatant, in this case). This interpretation is enforced by the evidence that bacteria in the biofilm state increase their membrane stability and rigidity by incorporating exogenous fatty acids into the membrane [29].

The same classes show also high levels of galactomannan (Figure 5B). Several studies demonstrate that xanthan and galactomannan synergistically increase the biofilm viscosity of *Xanthomonas campestris* [30]. In the classes with the phage, xanthan was not detected, while galactomannan was present at high level. Galactomannan gel is unstable since loses up to 50% of its water by syneresis [31]. Thus, the absence of xanthan and the high level of galactomannan in the classes with the phage suggest that the phage reduces the viscosity of the biofilm through the production of galactomannan.

More importantly, these results show the ability of the phage to down-regulate the metabolites associated with bacterial biofilm production and up-regulate the production of galactomannan, that weakens the biofilm.

In conclusion, the case described here – the action of the complex Xccϕ1+ HA+C20 against bacterial biofilm – is a proof-of-concept that a complex problem (bacterial biofilm control) can be solved starting from empirical data. The approach might be extended to the study of other biofilm-producing bacteria, like *Escherichia coli*, and *Pseudomonas aeruginosa* in which Pf4 bacteriophage (filamentous bacteriophage) has demonstrated inhibit the metabolic activity of *Aspergillus fumigatus* biofilms [32]. Our data also show that Xccϕ1 - alone or combined with HA and C20 - interferes with the metabolic pathways involved in biofilm formation. Furthermore, the altered pathways, reflecting the most relevant metabolic change, may become the possible targets for the treatment of bacterial biofilm.

Finally, Metabolomic analysis might also be used to understand how phages act on the host metabolism.

Author Contributions

M.P., P.C., and D.P. performed the experiments; M.R., A.F., C.M. A.M. and D.A. analysed the data, R.C., conceived the work; and D.I. and R.C. wrote the manuscript. All authors have given approval to the final version of the manuscript.

Notes

The authors declare no competing financial interest.

Reference

1. ECDC *Surveillance of antimicrobial resistance in Europe. Annual report of EARS - NET 2017.*; 2017; ISBN 9789294982797.
2. Hall-Stoodley, L.; Costerton, J.W.; Stoodley, P. Bacterial biofilms: From the natural environment to infectious diseases. *Nat. Rev. Microbiol.* 2004, *2*, 95–108.
3. Costerton, J.W.; Stewart, P.S.; Greenberg, E.P. Bacterial biofilms: A common cause of persistent infections. *Science (80-.).* 1999, *284*, 1318–

1322.
4. Stewart, P.S.; William Costerton, J. Antibiotic resistance of bacteria in biofilms. *Lancet* **2001**, *358*, 135–138.
5. Burmølle, M.; Thomsen, T.R.; Fazli, M.; Dige, I.; Christensen, L.; Homøe, P.; Tvede, M.; Nyvad, B.; Tolker-Nielsen, T.; Givskov, M.; et al. Biofilms in chronic infections - A matter of opportunity - Monospecies biofilms in multispecies infections. *FEMS Immunol. Med. Microbiol.* 2010, *59*, 324–336.
6. Hughes, K.A.; Sutherland, I.W.; Jones, M. V. Biofilm susceptibility to bacteriophage attack: The role of phage-borne polysaccharide depolymerase. *Microbiology* **1998**, *144*, 3039–3047.
7. Doolittle, M.M.; Cooney, J.J.; Caldwell, D.E. Tracing the interaction of bacteriophage with bacterial biofilms using fluorescent and chromogenic probes. *J. Ind. Microbiol.* **1996**, *16*, 331–41.
8. Roy, B.; Ackermann, H.W.; Pandian, S.; Picard, G.; Goulet, J. Biological inactivation of adhering Listeria monocytogenes by listeriaphages and a quaternary ammonium compound. *Appl. Environ. Microbiol.* **1993**, *59*, 2914–7.
9. Kortright, K.E.; Chan, B.K.; Koff, J.L.; Turner, P.E. Phage Therapy: A Renewed Approach to Combat Antibiotic-Resistant Bacteria. *Cell Host Microbe* 2019, *25*, 219–232.
10. Hanlon, G.W. Bacteriophages: an appraisal of their role in the treatment of bacterial infections. *Int. J. Antimicrob. Agents* **2007**, *30*, 118–28.
11. Moye, Z.D.; Woolston, J.; Sulakvelidze, A. Bacteriophage applications for food production and processing. *Viruses* 2018, *10*.
12. Morley, V.J.; Woods, R.J.; Read, A.F. Bystander Selection for Antimicrobial Resistance: Implications for Patient Health. *Trends Microbiol.* 2019, *27*, 864–877.
13. Fulgione, A.; Ianniello, F.; Papaianni, M.; Contaldi, F.; Sgamma, T.; Giannini, C.; Pastore, S.; Velotta, R.; Della Ventura, B.; Roveri, N.; et al. Biomimetic hydroxyapatite nanocrystals are an active carrier for Salmonella bacteriophages. *Int. J. Nanomedicine* **2019**, *14*, 2219–2232.
14. Papa, R.; Selan, L.; Parrilli, E.; Tilotta, M.; Sannino, F.; Feller, G.; Tutino, M.L.; Artini, M. Anti-Biofilm Activities from Marine Cold Adapted Bacteria Against Staphylococci and Pseudomonas aeruginosa. *Front. Microbiol.* **2015**, *6*, 1333.
15. Papa, R.; Parrilli, E.; Sannino, F.; Barbato, G.; Tutino, M.L.; Artini, M.; Selan, L. Anti-biofilm activity of the Antarctic marine bacterium Pseudoalteromonas haloplanktis TAC125. *Res. Microbiol.* **2013**, *164*, 450–456.
16. Casillo, A.; Parrilli, E.; Filomena, S.; Lindner, B.; Lanzetta, R.; Parrilli, M.; Tutino, M.L.; Corsaro, M.M. Structural Investigation of the Oligosaccharide Portion Isolated from the Lipooligosaccharide of the Permafrost Psychrophile Psychrobacter arcticus 273-4. *Mar. Drugs* **2015**, *13*, 4539–55.
17. Hansen, M.F.; Svenningsen, S. Lo; Røder, H.L.; Middelboe, M.; Burmølle, M. Big Impact of the Tiny: Bacteriophage–Bacteria Interactions in Biofilms. *Trends Microbiol.* 2019, *27*, 739–752.
18. Papaianni, M.; Contaldi, F.; Fulgione, A.; Woo, S.L.; Casillo, A.; Corsaro, M.M.; Parrilli, E.; Marcolungo, L.; Rossato, M.; Delledonne, M.; et al. Role of phage ϕ1 in two strains of Salmonella Rissen, sensitive and resistant to phage ϕ1. *BMC Microbiol.* **2018**, *18*, 208.
19. Hwang, T.L.; Shaka, A.J. Water Suppression That Works. Excitation Sculpting Using Arbitrary Wave-Forms and Pulsed-Field Gradients. *J. Magn.*

Reson. Ser. A **1995**, *112*, 275–279.
20. Griesinger, C.; Otting, G.; Wuethrich, K.; Ernst, R.R. Clean TOCSY for proton spin system identification in macromolecules. *J. Am. Chem. Soc.* **1988**, *110*, 7870–7872.
21. Bax, A.; Davis, D.G. MLEV-17-based two-dimensional homonuclear magnetization transfer spectroscopy. *J. Magn. Reson.* **1985**, *65*, 355–360.
22. Schleucher, J.; Schwendinger, M.; Sattler, M.; Schmidt, P.; Schedletzky, O.; Glaser, S.J.; S�rensen, O.W.; Griesinger, C. A general enhancement scheme in heteronuclear multidimensional NMR employing pulsed field gradients. *J. Biomol. NMR* **1994**, *4*, 301–306.
23. Trygg, J.; Wold, S. Orthogonal projections to latent structures (O-PLS). *J. Chemom.* **2002**, *16*, 119–128.
24. Chong, J.; Soufan, O.; Li, C.; Caraus, I.; Li, S.; Bourque, G.; Wishart, D.S.; Xia, J. MetaboAnalyst 4.0: towards more transparent and integrative metabolomics analysis. *Nucleic Acids Res.* **2018**, *46*, W486–W494.
25. Wong, H.S.; Maker, G.L.; Trengove, R.D.; O'Handley, R.M. Gas chromatography-mass spectrometry-based metabolite profiling of Salmonella enterica serovar typhimurium differentiates between biofilm and planktonic phenotypes. *Appl. Environ. Microbiol.* **2015**, *81*, 2660–2666.
26. Santi, L.; Beys-Da-Silva, W.O.; Berger, M.; Calzolari, D.; Guimarães, J.A.; Moresco, J.J.; Yates, J.R. Proteomic profile of Cryptococcus neoformans biofilm reveals changes in metabolic processes. *J. Proteome Res.* **2014**, *13*, 1545–1559.
27. Goodwine, J.; Gil, J.; Doiron, A.; Valdes, J.; Solis, M.; Higa, A.; Davis, S.; Sauer, K. Pyruvate-depleting conditions induce biofilm dispersion and enhance the efficacy of antibiotics in killing biofilms in vitr o and in vivo. *Sci. Rep.* **2019**, *9*.
28. Ene, I. V.; Heilmann, C.J.; Sorgo, A.G.; Walker, L.A.; De Koster, C.G.; Munro, C.A.; Klis, F.M.; Brown, A.J.P. Carbon source-induced reprogramming of the cell wall proteome and secretome modulates the adherence and drug resistance of the fungal pathogen Candida albicans. *Proteomics* **2012**, *12*, 3164–3179.
29. Dubois-Brissonnet, F.; Trotier, E.; Briandet, R. The biofilm lifestyle involves an increase in bacterial membrane saturated fatty acids. *Front. Microbiol.* **2016**, *7*.
30. Flemming, H.C.; Wingender, J. Relevance of microbial extracellular polymeric substances (EPSs) - Part I: Structural and ecological aspects. In Proceedings of the Water Science and Technology; 2001; Vol. 43, pp. 1–8.
31. Dea, I.C.M.; Morris, E.R.; Rees, D.A.; Welsh, E.J.; Barnes, H.A.; Price, J. Associations of like and unlike polysaccharides: Mechanism and specificity in galactomannans, interacting bacterial polysaccharides, and related systems. *Carbohydr. Res.* **1977**, *57*, 249–272.
32. Penner, J.C.; Ferreira, J.A.G.; Secor, P.R.; Sweere, J.M.; Birukova, M.K.; Joubert, L.M.; Haagensen, J.A.J.; Garcia, O.; Malkovskiy, A. V.; Kaber, G.; et al. Pf4 bacteriophage produced by Pseudomonas aeruginosa inhibits Aspergillus fumigatus metabolism via iron sequestration. *Microbiol. (United Kingdom)* **2016**, *162*, 1583–1594.

Papers and Communications
Paper:
The tumor necrosis factor g1022G>A polymorphism is associated with resistance to tuberculosis in water buffalo (Bubalus bubalis).
Papaianni M, Cosenza G, Borriello G, Galiero G, Grasso F, Della Ventura B, Iannaccone M, Capparelli R.
Animal Genetics, 2016.
Structural data and immunomodulatory properties of a water-soluble heteroglycan extracted from the mycelium of an Italian isolate of Ganoderma lucidum.
Carrieri R, Manco R, Sapio D, Iannaccone M, Fulgione A, Papaianni M, de Falco B, Grauso L, Tarantino P, Ianniello F, Lanzotti V, Lahoz E, Capparelli R.
Natural Product Research, 2017.
Role of phage ϕ1 in two strains of Salmonella Rissen, sensitive and resistant to phage ϕ1
Papaianni M., Contaldi F., Fulgione A., Woo S.L., Casillo A., Corsaro M.M., Parrilli E., Marcolungo L., Rossato M., Delledonne M., Garonzi M., Iannelli D., Capparelli R.
BMC microbiology, 2018.
Biometric Hydroxyapatite nanocrystals is an active carrier for Salmonella bacteriophages.
Fulgione A, Ianniello F, Papaianni M, Contaldi F, Sgamma T, Giannini C, Pastore S, Velotta R., Della Ventura B, Roveri N., Lelli M, Capuano F, Capparelli R.
Internation J of nanomedicine 2019.
Screen Printed Based Impedimetric Immunosensor for Rapid Detection of Escherichia coli in Drinking Water.
Cimafonte M., Fulgione A., Gaglione R., Papaianni M., Capparelli R., Arciello A., Bolletti Censi S., Borriello G., Velotta R., Della Ventura B.
Sensors 2020.

ORAL PRESENTATION
SALMONELLA RISSEN ϕ1: A MOLECULAR SWITCH
May 2018
PAPAIANNI, Marina; FULGIONE, Andrea; CONTALDI, Felice; IANNACCONE, Marco; CAPPARELLI, Rosanna.
Targeting phage and antibiotic resistance 2018
PHAGE THERAPY: A CROSSLINK BETWEEN HUMAN AND PLANTS BACTERIAL INFECTION
April 2019

PAPAIANNI, Marina; FULGIONE, Andrea; CAPPARELLI, Rosanna;
12th Edition of International Conference on Infection Disease 2019
PHAGE THERAPY: AN EMERGING TOOL AGAINST HUMAN AND PLANTS BACTERIAL INFECTION
October 2019
PAPAIANNI, Marina; FULGIONE, Andrea; CAPPARELLI, Rosanna;
15th World Congress on Infection Prevention and Control 2017

Poster:
Identification of a novel polymorphism in tre 3' untraslated region of the interferon gamma gene as potential marker associate with bovine tuberculosis in water buffalo (Bubalus Bubalis)
March 2017
Marco Iannaccone, Marina Papaianni, Flora Ianniello, Andrea Fulgione, Daniela Gallo, Gianfranco Cosenza, Rosanna Capparelli.
Italian Journal of Animal Science, ASPA conference 2017
The interleukin-10 polymorphism g.3936 G>A is uncoupled with bovine tuberculosis susceptibility in water buffalo (Bubalus Bubalis)
September 2017
Marco Iannaccone, Marina Papaianni, Flora Ianniello, Andrea Fulgione, Daniela Gallo, Gianfranco Cosenza, Rosanna Capparelli.
Italian Journal of Animal Science, ASPA conference 2017
Phage and aldehyde work in synergy to control Xanthomonas infection.
December 2017
Marina Papaianni, Sheridan Lois Woo, Francesco Vinale, Maria Luisa Tutino, Ermenegilda Parrilli, Maria Michela Corsaro, Angela Casillo, Rosanna Capparelli.
First Annual Conference of the COST Action EuroXanth, 2017.

APPENDIX

sensors

MDPI

Article

Screen Printed Based Impedimetric Immunosensor for Rapid Detection of *Escherichia coli* in Drinking Water

Martina Cimafonte [1], Andrea Fulgione [2,3], Rosa Gaglione [4], Marina Papaianni [3], Rosanna Capparelli [3], Angela Arciello [4], Sergio Bolletti Censi [5], Giorgia Borriello [2], Raffaele Velotta [1] and Bartolomeo Della Ventura [6,*]

1 Department of Physics "Ettore Pancini", University of Naples "Federico II", Via Cinthia, 26, 80126 Naples, Italy; martina.cimafonte@unina.it (M.C.); rvelotta@unina.it (R.V.)
2 Istituto Zooprofilattico Sperimentale del Mezzogiorno, Via Salute, 2, 80055 Portici Naples, Italy; andrea.fulgione@unina.it (A.F.); giorgia.borriello@cert.izsmportici.it (G.B.)
3 Department of Agriculture, University of Naples "Federico II", Via Università, 133, 80055 Portici Naples, Italy; marina.papaianni@unina.it (M.P.); capparel@unina.it (R.C.)
4 Department of Chemical Sciences, University of Naples "Federico II", Via Cinthia, 26, 80126 Naples, Italy; rosa.gaglione@unina.it (R.G.); angela.arciello@unina.it (A.A.)
5 Cosvitech Società Consortile a Responsabilità Limitata, 80142 Naples, Italy; sergiobolletti@cosvitec.eu
6 Department of Physics, Politecnico di Milano, Piazza Leonardo da Vinci, 32, 20133 Milano, Italy
* Correspondence: dellaventura@fisica.unina.it

Received: 29 November 2019; Accepted: 30 December 2019; Published: 3 January 2020

Abstract: The development of a simple and low cost electrochemical impedance immunosensor based on screen printed gold electrode for rapid detection of *Escherichia coli* in water is reported. The immunosensor is fabricated by immobilizing anti-*E. coli* antibodies onto a gold surface in a covalent way by the photochemical immobilization technique, a simple procedure able to bind antibodies upright onto gold surfaces. Impedance spectra are recorded in 0.01 M phosphate buffer solution (PBS) containing 10 mM $Fe(CN)_6^{3-}/Fe(CN)_6^{4-}$ as redox probe. The Nyquist plots can be modelled with a modified Randles circuit, identifying the charge transfer resistance R_{ct} as the relevant parameter after the immobilization of antibodies, the blocking with BSA and the binding of *E. coli*. The introduction of a standard amplification procedure leads to a significant enhancement of the impedance increase, which allows one to measure *E. coli* in drinking water with a limit of detection of 3×10^1 CFU mL^{-1} while preserving the rapidity of the method that requires only 1 h to provide a "yes/no" response. Additionally, by applying the Langmuir adsorption model, we are able to describe the change of R_{ct} in terms of the "effective" electrode, which is modified by the detection of the analyte whose microscopic conducting properties can be quantified.

Keywords: *Escherichia coli*; immunosensor; electrochemical impedance spectroscopy; antibodies; photochemical immobilization technique; cyclic voltammetry

1. Introduction

Water is a natural resource, essential for the life sustainment and significant for health in both developing and developed countries worldwide. In the recent years, the inappropriate handling of urban, industrial and agricultural wastewater has affected the quality of the drinking water which turns out to be alarmingly contaminated and chemically polluted [1]. Contaminated water causes a serious impact on the population as it induces a large number of diseases caused by microorganisms [2]. According to the World Health Organization (WHO), water-related diseases are a worldwide problem

and each year 3.4 million people, mostly children below the age five, suffer from waterborne diseases and die [3]. Pathogenic bacteria in water are mainly responsible for human infection diseases and one of the most common bacteria associated with the sanitary risk of water is the species *Escherichia coli*.

Escherichia coli is a gram-negative bacterium of the genus *Escherichia* identified for the first time in 1885 by the German paediatrician and bacteriologist Theodor Escherich. *E. coli* is a rod-shaped gut bacterium, natural inhabitant in the intestinal tracts of humans and warm-blooded animals. It is considered one of the most dangerous pathogens because some strains can cause serious illness, including severe diarrhoea, urinary tracts infections, inflammations and peritonitis. As a consequence, the presence of *E. coli* in drinking water is considered as a possible indicator of the microbiological water quality deterioration and the presence of *E. coli* in processed food products can indicate faecal contamination [1]. In fact, according to WHO and the European Union [4] no *E-coli* should be detected in 100 mL of water. Such a limit can only be reached by time-consuming measurements carried out in equipped laboratories; therefore, nowadays one of the challenges in food industry and environmental monitoring is the development of methods for the rapid detection of low levels of *E. coli*

Conventional methods for the detection of *E. coli* include multiple-tube fermentation, membrane filter and plate counting. Although, these culture-based methods are accurate, reliable and have low detection limits, they are typically labor-intensive and time-consuming since they require 2–3 days to yield initial results and up to 7–10 for the confirmation [5]. Other detection methods, such as ELISA [6] and PCR [7,8] are less time consuming but they require expensive equipment and initial sample pre-treatment which make the application of these methods limited only to the laboratory environment [9–11]. Thus, the research for new strategies that could be promising alternatives to the conventional techniques to be used in industrial applications is very timely.

Detection techniques based on biosensors are widely recognized as powerful tools for the detection of bacteria due to their several advantages such as fast response, robustness, low cost, sensitivity, specificity and real time detection [12]. Among them, biosensors based on antibody-antigen interaction (the so-called immunosensors) are broadly investigated, and, in fact, immunosensors using electrochemical [13], surface plasmon resonance (SPR) [14], piezoelectric [15] and cantilever [16] based transducers have been applied for *E. coli* detection. Electrochemical biosensors are considered powerful instruments overcoming the limitations of the conventional methods due to their multiple advantages such as low cost, high sensitivity, fast response, robustness and simple operation [17–19]. Among different electrochemical techniques, electrochemical impedance spectroscopy (EIS) is very commonly used to investigate the recognition events at electrode/electrolyte interface [11,20] and EIS based biosensors are particularly attractive since they allow antigen detection with high sensitivity. In the last decade, different impedimetric immunosensors for the detection of *E. coli* have already been developed [21–24].

The immobilization of antibodies (Abs) is a crucial step in the realization of an immunosensor because its analytical performance strongly depends both on the orientation of the antibodies and their density on the surface. Thus, it would highly desirable to rely on a surface functionalization procedure that would overcome such an issue [25,26]. Generally, antibodies can be immobilized via physical or chemical adsorption involving electrostatic or ionic bonds, hydrophobic interactions and van der Waals forces [27,28], via covalent attachment [29–32], by using the biotin–avidin approach [33,34] or immobilizing intermediate binding proteins, such as protein A or G [35–38] and through entrapment into a polymer matrix [39–42]. These approaches, particularly protein A and G method, are time-consuming, but even more important, require a surface modification or pre-treatment for an effective protein A/G binding [43] that can affect the robustness and reproducibility of the protocol.

Among all the possible strategies, self-assembled monolayers (SAMs) is currently one of the most widespread methods for electrode functionalization aiming at detecting *E. coli* by electrochemical approaches. For instance, an oriented anti-*E. coli* immobilization on gold electrode surfaces could be achieved by exploiting SAMs of thiolated carboxylic acid [44–46] or by immobilizing anti-*E. coli* on electrochemically deposited cysteamine layers [45]. The use of thiolated scaffolds such as protein

G [45,47] and cross-linkers as glutaraldehyde [48], the latter allowing the immobilization of anti-*E. coli* onto electrochemically synthesized polyaniline substrate, have also been reported with promising results for the immobilization of anti-*E. coli*.

Thus, SAMs are broadly used as linkers for the immobilization of antibodies onto gold electrode surfaces, but in spite of the many advantages they offer in many applications, there are several issues that should be considered in order to find out and control their physical and chemistry properties [49–51]. SAMs on gold surfaces are usually represented as perfect monolayers, with molecules in a closed packed configuration. Nevertheless, this concept is far from reality and the control of the quality of SAMs is a key point in many applications. The realization of a well-assembled monolayer strongly relies on the purity of the solutions used and the presence of even a low amount of contaminants, as for instance thiolated precursor molecules that are the typical impurities in thiol compounds, can lead to a non-uniform and, hence, non-ideal monolayer [52]. In addition, the electrode surface plays an important role in the realization of SAMs. EIS analysis of electrode surfaces with different roughness showed that the rougher substrate exhibited small and variable response as a result of a non-ideal SAM formation, while the smoother surface produces higher and more reproducible response due to the increase of the SAM homogeneity [53]. Moreover, over the years several studies have worked to clarify the true nature of the interaction gold-thiols SAMs [36,54–56]. Considering these issues, it is worth developing alternative methods to covalent bind antibodies on gold electrode surfaces in an easier, more rapid and reliable way.

In this paper, we propose a simple and low-cost EIS immunosensor based on screen printed gold electrodes (AuSPEs) for the detection of *Escherichia coli*. The anti-*E. coli* antibodies were immobilized on the gold electrode surface using the Photochemical Immobilization Technique (PIT) a simple procedure able to steer antibodies in a convenient orientation of the Fab region once immobilized onto gold surface [57,58]. In this work, PIT has been used for the first time in the functionalization of commercial gold electrodes in order to develop an "on-off" electrochemical immunosensor based on impedance spectroscopy (EIS) using $Fe(CN)_6^{3-}/Fe(CN)_6^{4-}$ as redox probe. The effectiveness of our approach is demonstrated by detecting *E. coli* ATTCC 25922 in drinking water. Our immunosensor exhibits a limit of detection (LOD) of 3×10^1 CFU mL^{-1}, with no need for pre-concentration and pre-enrichment steps. The selectivity against other bacteria was evaluated and the immunosensor was applied to the analysis of inoculated drinking water samples.

2. Materials and Methods

2.1. Chemicals and Materials

Gold screen printed electrodes (AuSPEs) were purchased from BVT Technologies (Strážek, Czech Republic). They include a gold disk-shaped (d = 1 mm) working electrode, a silver/silver chloride electrode and a gold counter electrode, all of them printed on a corundum ceramic base (0.7 cm × 2.5 cm). All potential values were referred to the silver/silver chloride reference electrode. Phosphate buffer solution (PBS) was prepared by dissolving PBS tablets (from GoldBio, St Louis, MO, USA) in Milli-Q water (each tablet prepares 100 mL of a 0.01 M PBS solution). Anti-*E. coli* polyclonal antibody (5.5 mg mL^{-1}) was obtained from Thermo Fisher Scientific (Rockford, IL, USA) and anti-*E. coli* solutions (25 μg mL^{-1}) were prepared in a 0.01 M PBS solution (pH 7.4). Bovine serum albumin (BSA), potassium hexacyanoferrate (II) trihydrate ($K_4Fe(CN)_6 \cdot 3H_2O$), potassium hexacyanoferrate (III) ($K_3Fe(CN)_6$) and sulphuric acid (H_2SO_4 98%) were purchased from Sigma-Aldrich (Milano, Italy). The microfluidic setup involves a fluidic cell, silicon tubes and a continuous pump (HNP Mikrosysteme GmbH, Schwerin, Germany). The total volume of the circuit is about 100 μL, the cell volume is about 10 μL and the flow rate is 6 μL s^{-1}.

2.2. Apparatus

Electrochemical impedance spectroscopy (EIS) and cyclic voltammetry (CV) measurements were carried out with a potentiostat/galvanostat and impedance analyzer PALMSENS (Utrecht, The Netherlands) model PalmSens3 controlled by a computer through the PSTRACE version 5 software. Cyclic voltammetry (CV) and electrochemical impedance spectroscopy (EIS) were conducted in the presence of $Fe(CN)_6^{3-}/Fe(CN)_6^{4-}$ (1:1, 10 mM) as redox probe in 0.01 M PBS solution (pH = 7.4). In CVs, potential was cycled from −0.6 V to 0.6 V with a scan rate of 0.15 V s^{-1} in 10 mM $Fe(CN)_6^{3-}/Fe(CN)_6^{4-}$. EIS measurements were performed at the frequency range from 5 Hz to 10000 Hz at the formal potential of 0.16 V and using an amplitude perturbation of 10 mV. The impedance data were shown in the Nyquist plot and the EIS spectrum Analyzer software, supplied with the instrument, was used to fit EIS data to the electrical equivalent circuit in order to obtain the fit-component parameters values.

A fluidic setup including a Plexiglas cell, silicon tubes and a continuous pump was used for the flowing of the different solutions (Abs, BSA and *E. coli*). A schematic representation of the cell is shown in Figure 1a. The main feature of the cell is its small volume that facilitate the interaction of the particles in the solutions (Abs, BSA, *E. coli*, etc.) with the electrode. Any solution was conveyed by a continuous pump at a flow rate of 6 µL s^{-1}. Although effective for the interaction, such a cell was unsuitable for electrochemical measurements in view of the small amount of electrolytes involved. Thus, after each interaction (i.e., each steps shown in Scheme 1), we took the electrode out of the cell and dipped it into a 1.5 mL beaker containing $Fe(CN)_6^{3-}/Fe(CN)_6^{4-}$ (Figure 1b), in which the electrochemical measurements were carried out at room temperature.

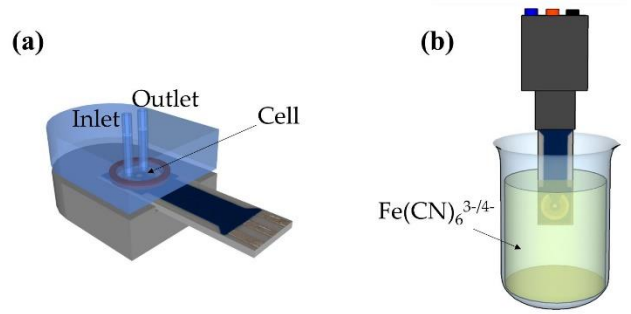

Figure 1. (**a**) Sketch of the fluidic cell used for an effective interaction of the solutions (Abs, BSA and *E. coli*) with the electrode and (**b**) scheme used for the electrochemical measurements: the AuSPE was dipped in a beaker containing 1.5 mL of $Fe(CN)_6^{3-/4-}$ and it was connected to the potentiostat through a holder (in grey) for the impedance/current measurements.

2.3. Preparation of the Biological Sample

Bacterial strain *E. coli* ATCC 25922 was grown in Muller Hinton Broth (MHB, Becton Dickinson Difco, Franklin Lakes, NJ, USA) and on Tryptic Soy Agar (TSA; Oxoid Ltd., Hampshire, UK). In all the experiments, bacteria were inoculated and grown overnight in MHB at 37 °C. The next day, bacteria were centrifuged and solubilized in drinking water at the desired cell densities (10^1–10^6 CFU mL^{-1}). By colony counting assays, it was verified that bacterial growth was negligible in PBS 1X with respect to MHB through a time interval of 3 hrs at room temperature, whereas bacterial death was not observed. Clinical isolated bacteria *Salmonella enteriditis 706 RIVM* [59] and *Acinetobacter baumannii* (ATCC 17978) were grown in the same way and diluted drinking water in order to verify the specificity of the immunosensor towards *E. coli* in comparison with non-target bacteria.

2.4. UV Activation of Antibody Solution

The gold SPE was functionalized with anti-*E. coli* antibodies, previously activated by the Photochemical Immobilization Technique (PIT) [57,58]. PIT is a functionalization method able to tether antibodies (Abs) upright on metal (gold or silver) surfaces with their binding sites well exposed to the environment [60], based upon the selective photochemical reduction of disulphide bridges in immunoglobulins (IgGs) produced by UV activation of near aromatic amino acid [61]. Briefly, a selective photoreduction of disulphide bridges produced by the UV activation of the trp/cys-cys triad occurs. This triad is a typical structural feature of IgGs and basically, the UV photon energy is adsorbed by tryptophan and transferred to near electrophilic species like the close cys-cys. The result is the cleavage of the disulphide bridges and the formation of new thiol (SH) groups able to bind, through a covalent bond, thiol reactive surfaces like gold ones (Figure 2b). Every IgGs have twelve triads but, it has recently been demonstrated [57] that only two of them are involved in this process. These triads are located in the constant variable region and allow the attack of the antibody to the surface with one of the two Fab regions exposed to the solution (Figure 2c) [57]. Considering that the triad of residues trp/cys-cys can be found in every IgGs, the PIT is applicable in a wide range of fields. PIT is accomplished by activating 300 µL of antibody samples (25 µg mL^{-1}) in a quartz cuvette by two low pressure mercury lamp (LP Hg lamp) emitting at 254 nm and manufactured by Procom Alta Tecnologia s.r.l. (Dicomano, FI, Italy) (Figure 2a). The two lamps (1.5 cm of diameter) are horseshoe-shaped and mounted in a stacked configuration so that its internal empty space fits with a (quartz) cuvette whose dimensions are 1 cm × 1 cm × 4 cm. The power of each lamp is 6 W and by considering that the cuvette containing the anti-*E. coli* IgG solution is close to the lamps, the effective irradiation intensity used for the antibody activation is about 0.3 W/cm^2. The samples are irradiated for 30 s. This time is the result of an optimized protocol that, as confirmed by the Ellman's assay [62], produces an high concentration of activated Abs while guaranteeing no denaturation of antibodies as evidenced by their efficiency in antigen binding in the developed biosensors.

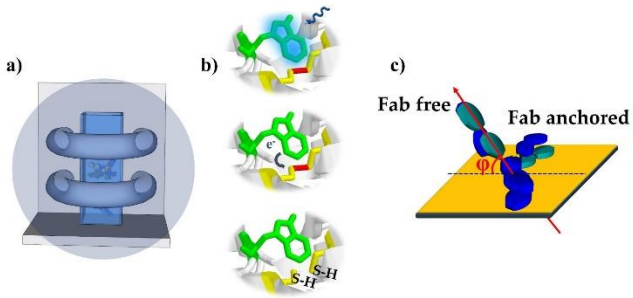

Figure 2. (**a**) UV lamp used for the UV activation of the antibodies. Emitting wavelength: 254 nm, diameter of each lamp: 1.5 cm, dimensions internal: space 1 cm × 1 cm × 4 cm, power of each lamp 6 W, irradiation intensity 0.3 W/cm^2; (**b**) Description of the reaction involved in PIT: the UV photon energy is adsorbed by tryptophan and transferred to near cys-cys. The result is the cleavage of the disulphide bridges and the formation of new thiol (SH) groups; (**c**) Antibody is immobilized onto the surface so that the angle φ is 45° on average thereby providing one Fab free and well-exposed to the environment.

After the activation, the Abs solution was conveyed to the electrode surface by means of a fluidic circuit. In previous works, this method has been used in a number of experiments to develop sensitive and selective QCM-based immunosensors [63–67] as well as colorimetric biosensors [68].

2.5. Immunosensor Development and E. coli Detection

Before the functionalization, the AuSPE was electrochemically cleaned by applying 10 cycles between −0.4 V and 1.4 V at a scan rate of 0.1 V s^{-1} in 0.1 M H_2SO_4. The electrode was rinsed with a copious amount of Milli-Q water and it was ready to use. The cleaned SPE was placed in the fluidic cell and the experimental procedure for impedance measurements consists in the flowing of different solutions onto the sensitive gold surface of the AuSPE. First, a solution of UV-activated anti-*E. coli* antibodies (25 µg mL^{-1}) was conveyed onto the gold sensitive surface for 15 min by applying a constant flow rate (6 µL s^{-1}). Since the Ab activation only lasts approximately five minutes [57], to saturate the gold electrode surface, such a step was repeated 4 times with a fresh irradiated Abs solution. Subsequently, the electrode was rinsed for 1 h with 0.01 M PBS buffer to remove the unbound antibodies. After that, a BSA solution (50 µg mL^{-1}) flowed into the cell for 15 min filling the remaining free space on the gold surface. This blocking step is crucial because, by filling the free remaining spaces on the gold electrode surface, the possible non-specific interactions of the following molecules are avoided. A 1mL aliquot of drinking water incubated with different concentration of *E. coli* cells (from 10^1 to 10^8 CFU mL^{-1}) flowed into the circuit for 30 min at room temperature and the bacteria cells were captured by the immobilized antibodies. The electrode was rinsed with 0.01 M phosphate buffer to remove non-specifically and weakly bound bacteria for 5 min. Each detection was repeated three times. The difference in impedance measured before and after *E. coli* incubation, normalized with the impedance value obtained after Abs immobilization, was taken as the signal produced by the binding between immobilized antibodies and target bacterial cells. An aliquot of 1 mL of drinking water, without incubation of bacteria, was used as negative control.

2.6. Enhanced Sensitivity Protocol

In order to improve the signal, an amplification step has been included in the experimental procedure. The response enhancement has been achieved by conveying anti-*E. coli* (25 µg mL^{-1}) into the microfluidic cell for 30 min. This additional step, which leads to the formation of a sandwich complex, was used to amplify the slight impedance increment obtained after *E. coli* detection at low concentration. In such a case, the formation of a sandwich complex further hinders the electron-transfer process thus improving the electrochemical response. A final washing phase with 0.01 M PBS is used to remove unbound or weakly bonded molecules.

3. Results and Discussion

3.1. Principle of the Impedimetric Biosensor

The different steps involved in the preparation of our immunosensor are schematically illustrated in Scheme 1 (not to scale). After cleaning the AuSPE with H_2SO_4, the surface is functionalized (step I) with previously activated antibodies using the LP Hg lamp above described. Then, bovine serum albumin (BSA) is used as blocking reagent to fill the free remaining spaces on the gold electrode (step II). In the next step (step III) a specific binding event occurs between the immobilized antibodies and the *E. coli* cells. Finally, in order to improve the sensitivity, a sandwich complex is realized by conveying a fresh anti-*E. coli* Abs solution to the circuit. Consecutive steps of the immunosensor development as well as the *E. coli* detection are described in detail in the Materials and Methods section above.

EIS is characterization techniques to study the electron transfer process and, specifically, the changes of charge transfer resistance caused by the adsorption of isolating molecules to the gold electrode. The impedance data are represented as Nyquist plots (see Figures 3–6), where the real and the imaginary components of impedance are plotted in the X and Y axes, respectively. The Nyquist plots consist of two portions: the semicircle portion at high frequencies indicates the electron-transfer process while the linear part at lower frequencies represents the diffusion-limited mass transfer process of the redox probe. A modified Randles circuit (shown as inset in Figures 3–6) was used to fit the experimental data over the whole frequency range. In this equivalent circuit, R_s stands for the resistance of the solution,

CPE is the constant phase element, R_{ct} is the charge transfer resistance and W the Warburg impedance. R_s and W represent bulk properties of the electrolyte solution and diffusion features of the redox probe in the solution. These parameters are not influenced by modification of the electrode surface and are not modified by the antibodies-bacteria interaction. On the contrary. R_{ct} depends critically on the dielectric and insulating features at the electrode-electrolyte interface and can be used as sensing parameter since it is very sensitive to electrode modifications. The CPE is introduced in the equivalent circuit instead of a simple capacitor to account for inhomogeneity and defect areas of the layer [69].

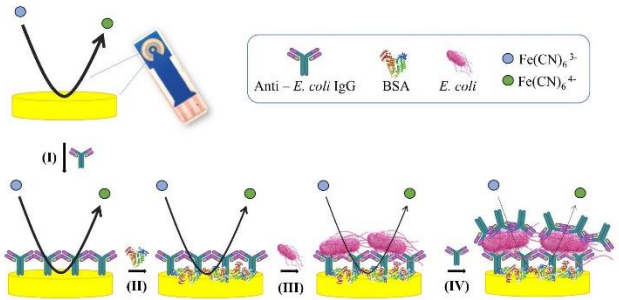

Scheme 1. Schematic diagram (not in scale) of the stepwise functionalization and detection. The black line represents the intensity of the redox reaction, which is inhibited as the surface covering grows. The reduction of its thickness is associated to a decrease of the "effective" area available for the electrolyte current, which is measured as an increase of the charge transfer resistance.

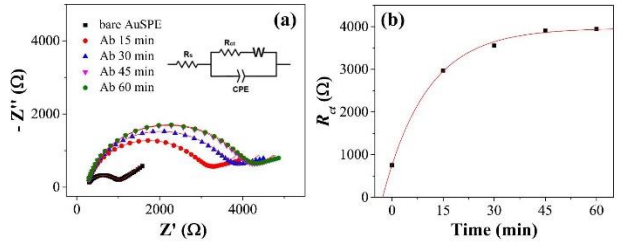

Figure 3. (**a**) EIS spectrum measured at different times while the UV irradiated antibodies are conveyed to the interaction cell; (**b**) R_{ct} as a function of time showing that the surface saturation takes place within one-hour time. The errors of R_{ct} are within the thickness of the experimental points.

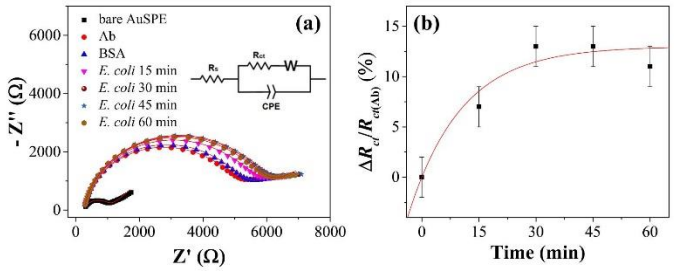

Figure 4. (**a**) EIS spectrum measured at different times with *E. coli* at 10^5 CFU mL^{-1}; (**b**) R_{ct} as a function of time showing an exponential kinetic with a constant time of 14 ± 7 min.

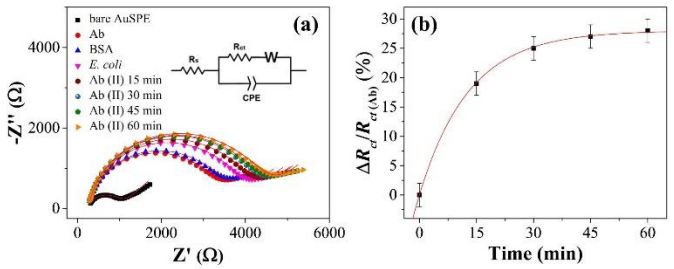

Figure 5. Kinetics of the secondary antibody. (**a**) EIS spectrum measured at different times while a 25 µg mL^{-1} Ab solution is conveyed to the cell after the detection *E. coli* (10^5 CFU mL^{-1}); (**b**) R_{ct} as a function of time showing an exponential dynamic with a constant time of 13.5 ± 0.3 min.

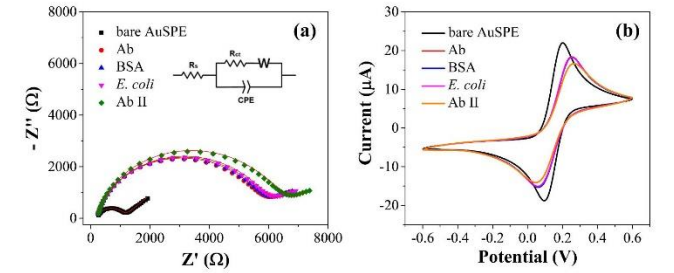

Figure 6. (**a**) EIS and (**b**) CV of the step-by-step immunosensor development and *E. coli* detection in 10 mM $Fe(CN)_6^{3-}/Fe(CN)_6^{4-}$ solution at pH 7.4.

3.2. Kinetics of the Functionalization and Detection

In the photochemical immobilization technique, the Abs are conveyed to the electrode after they have been irradiated by the UV lamp. Since the activation of the Abs only lasts approximately 5 min [57], it is necessary to optimize the time the solution is fluxed in the cell containing the working electrode (10 µL volume). The results obtained with a flow rate of 6 µL s^{-1} are reported in Figure 3a

(see Table S1 for the data), that shows EIS spectra measured at intervals of 15 min, which are required to cover the whole surface. The resulting R_{ct} is shown in Figure 3b and its behavior with the time is well fitted by an exponential function with time constant of 13 ± 1 min. Thus, the whole functionalization procedure can be considered accomplished in one-hour time. Since no significant change of R_{ct} is observed after the blocking step, we can assess that the saturation of R_{ct} shown in Figure 3b corresponds to an electrode fully covered by antibodies.

The kinetic of *E. coli* detection was studied to optimize the performance of the immunosensor. Drinking water samples incubated with a concentration on *E. coli* 10^5 CFU mL^{-1} was flowed over the antibody-modified electrode and the R_{ct} change was monitored at time intervals of 15 min. The results are reported in Figure 4a (Nyquist plot) and 4b (normalized R_{ct}) with an exponential fit of the experimental data that provides a time constant of 14 ± 7 min (see Table S2 for the data). Although with larger error, such a value is similar to that measured for surface functionalization by Abs suggesting that 30 min was a suitable incubation time to allow the completion of the analyte detection.

We also measured the kinetics of the Ab binding to the *E. coli* from the top (sandwich configuration) by carrying out EIS as a function of time during the flow of a 25 μg mL^{-1} Ab solution into the cell. The Nyquist plots are reported in Figure 5a and the corresponding values for R_{ct} are shown in Figure 5b (see Table S3 for the data) with an exponential fit of the data that provides a constant time of 13.5 ± 0.3 min. Once again, 30 min can be considered a recommended value that allows the accomplishment of the amplification step.

3.3. Electrochemical Characterization of the Immunosensor Preparation

Cyclic voltammetry (CV) and electrochemical impedance spectroscopy (EIS) measurements were carried out to investigate the layer by layer construction of the immunosensor and to verify the *E. coli* binding (Figure 6). Both characterization techniques investigate the electron transfer process and, specifically, the changes of charge transfer resistance caused by the adsorption of isolating molecules to the gold electrode. EIS plots of the step-by-step immunosensor fabrication are shown in Figure 6a, utilizing 10 mM $Fe(CN)_6^{3-}/Fe(CN)_6^{4-}$ as redox probe in 0.01 M PBS buffer.

The potential applied for the EIS studies was set to 0.16 V (vs. Ag/AgCl) according to the CV result. The impedance data are represented as Nyquist plots and R_{ct} values were extracted by fitting the data with the Randles circuit (inset Figure 6a, see Table S4 for the data),) after each preparation step since the comparison of these values indicate the change of the redox probe kinetics at the electrode interface. The R_{ct} of the bare electrode was as small as 878 Ω. The surface is functionalized using previously activated antibodies which tether the surface providing a significantly resistance increase of approximately 5.4 kΩ, since the covalent immobilization of antibodies onto the electrode surface acts as an inert electron transfer blocking layer and the penetration of the redox probe. The blocking of the surface was carried out with BSA at 50 μg mL^{-1} as well as at 100 μg mL^{-1} and in both cases a negligible increment of R_{ct} value could be detected thereby proving that the gold surface is fully covered by the antibodies (Figure S1, see Tables S5 and S6 for the data). In the next step, the solution containing the *E. coli* cells (10^2 CFU mL^{-1}) flows in the circuit and the analyte is recognized by the Abs. However, with the further attachment of the *E. coli* cells (10^2 CFU mL^{-1}) to the modified electrode surface no significant increase of impedance is observed and a solution of anti-*E. coli* Abs is conveyed to the cell giving rise to a sandwich complex which produces an increase of the charge transfer resistance caused by the realization of a further barrier towards the access of the redox probe to the electrode. In such a case, the R_{ct} value increases by a 15% after the formation of antibody *E. coli* complex.

In addition, CV measurements were carried out to corroborate the EIS results. CV curves of the step-by-step modification are shown in Figure 6b, using 10 mM $Fe(CN)_6^{3-}/Fe(CN)_6^{4-}$ as redox probe in 0.01 M PBS buffer. The bare gold electrode gave a well-defined anodic and cathodic peaks, due to the reversible interconversion of the redox probe $Fe(CN)_6^{3-}/Fe(CN)_6^{4-}$, with peak potential difference (ΔEp) of 107 mV and peak current (Ip) of 23.9 μA. After antibodies immobilization, the ΔEp increased to 192 mV and the Ip decreased to 19.1 μA confirming the attachment of charge transfer inhibiting

molecules to the gold electrode. The surface blocking with BSA caused a negligible decrease of *Ip* (18.9) confirming the complete saturation of the gold surface with antibodies. Finally, after the incubation with *E. coli* no significant decrease of current is observed and the resulting formation of antibody-*E. coli* complex lead to a further decrease of the peak current (*Ip* = 17.2 and ΔEp = 218) which coincides with EIS results.

3.4. Immunosensor Analytical Performance

The performance of the immunosensor for the detection of *E. coli* was investigated in drinking water by EIS. Drinking water samples (1 mL) were incubated with *E. coli* at different concentration in the range of 10^1–10^8 CFU mL^{-1}. Figure 7a shows the dose response curves obtained with steps I-III (red curve, direct detection protocol without amplification or DDP) and I-IV (black curve, ballasting detection protocol with amplification or BDP). The sensing parameter is $\Delta R_{ct}/R_{ct(\mathrm{Ab})}$ where ΔR_{ct} is the change in the impedance brought about by *E. coli* [in case of DDP $\Delta R_{ct} = R_{ct(E.\ coli)} - R_{ct(\mathrm{BSA})}$], whereas $R_{ct(\mathrm{Ab})}$ is the impedance value measured after the functionalization. As Figure 7a (red curve) shows, a detection range of two decades (10^3 to 10^5 CFU mL^{-1}) is achieved before reaching a saturation at concentration higher than 10^5 CFU mL^{-1}.

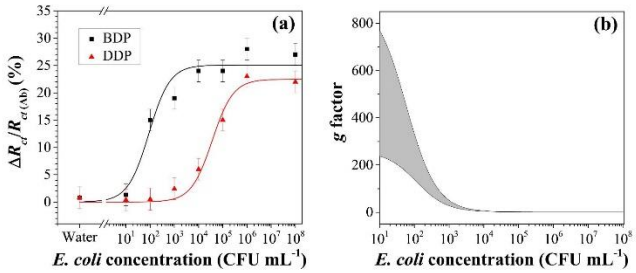

Figure 7. (**a**) Dose-response curve obtained using both protocols: DDP–direct detection protocol and BDP–ballasting detection protocol. The experimental data are fitted by Equation (6); (**b**) Gain factor *g* as a function of the *E. coli* concentration.

Each concentration has been tested three times in several days in different environmental conditions and using different electrode. The standard deviation (σ) of the measurements is approximately 2% proving that the protocol shows good accuracy and reproducibility. According to the 3σ formula, it is necessary to achieve an impedance increase ≥6% in order to consider the variation as significant. As it shown in the dose-response curve, the limit *E. coli* concentration (LOD) producing such variation in impedance increase is 10^4 CFU mL^{-1} (Figure 7a, red curve). The $\Delta R_{ct}/R_{ct(\mathrm{Ab})}$ measured for the negative sample (1 mL aliquot of drinking water) was less than 1% confirming the absence of interferences of the drinking water components (especially salts) with the biosensor surface.

In the DDP condition a LOD of approximately 10^4 CFU mL^{-1} is obtained, which can be significantly improved by including the step IV that consists of addition of anti-*E. coli* Abs so that a sandwich configuration is realized as shown in Scheme 1 (step IV with Ab II). In fact, the relative electron-transfer resistance difference in such a case is $\Delta R_{ct}/R_{ct(\mathrm{Ab})}$ where $\Delta R_{ct} = R_{ct(\mathrm{AbII})} - R_{ct(\mathrm{BSA})}$ (Figure 7a, black curve). The black curve shows a remarkable increase in the slope as well as in the saturation level, which is achieved at lower concentration. With the same criteria used before (3σ formula with σ about 2%), the detection limit of this extended protocol (BDP) is estimated to be 3×10^1 CFU mL^{-1} whereas the quantification range is 10^2–10^3 CFU mL^{-1}. It is worth noticing that a narrow quantification range is not a drawback when "on-off" biosensors are considered, as it is the case of the device proposed here.

The comparison of the two curves in Figure 7a suggests an enhancement of the signal whose factor depends on the *E. coli* concentration. In fact, by defining g as a gain factor, we have:

$$g([E-coli]) = \frac{\Delta R_{ct}^{(BDP)}([E-coli])}{\Delta R_{ct}^{(DDP)}([E-coli])}, \quad (1)$$

where the superscripts DDP and BDP refer to the three step and four step protocol, respectively. The plot of g is reported in Figure 7b as a function of *E. coli* concentration together with the 95% confidence interval (grey area) obtained by propagating the error from the curves in Figure 7a into Equation (1). The enhancement factor is more than one order of magnitude ($10 < g < 33$) at lower concentration and decreases to an expected saturation value of approximately 1 at higher concentrations. Such a behavior may well be explained by considering that at higher concentration of *E. coli*, the surface has a higher degree of occupancy by the bacteria so that the binding of additional Ab II tethered to *E. coli*, gives rise to a smaller effect on R_{ct} when compared to the effect produced at lower concentration.

The analytical performances of the developed immunosensor have been compared with other recent impedimetric immunosensors for the detection of *E. coli* (Table 1). It is remarkable that all of them share a quite long functionalization time ranging from few hours to even twenty hours to immobilize antibodies on gold electrode surface.

Table 1. Overview of the latest impedimetric biosensors for *Escherichia coli* detection.

Functionalization Scheme	Functionalization Time (h)	LOD (CFU mL^{-1})	Reference
Au-MHDA-Ab	18 *	2	[44]
Au-Cys-Ferrocene-Ab	20 *	3	[45]
Au-MUA/UDT-Ab	20 *	100	[46]
Au-PrG thiol-Ab	10	140	[47]
Au-AuNPs-PrG thiol-Ab	24 *	48	[47]
Au-PANI-Glu-Ab	>2	100	[48]
Au-Ab (PIT activated)	1	30	This work

Ab: antibody; MHDA: 16-mercaptohexadecanoic acid; Cys: Cysteamine; AuNPs: gold nanoparticles; PrG: Protein G; PANI: polyaniline; Glu: Glutaraldehyde; MUA: 11-mercaptoundecanoic acid; UDT: 1-undecanethiol. * These times have been evaluated by considering overnight as 16 h.

The immunosensors reported in Table 1 are based on immobilization procedures that include the formation of self-assembled monolayers, which usually require particularly smooth gold electrode surfaces [53] and expert personnel for the setup of complex chemical procedures. In contrast, PIT is user-friendly nor is any previous modification of the surface required. Any single electrode (AuSPE) was used "as is" that is without any pretreatment (only a rapid cleaning in H_2SO_4) or surface modification, but, even more important, the inherent differences among them in terms of bare impedance did not prevent us from building the more than satisfactory dose-response curve shown in Figure 7a.

3.5. Data Fitting

To account for the dose-response curve, we propose a simple model that describes the change of the resistance R_{ct} due to the analyte recognition as a change of the "effective" electrode area. To start with, let's consider that while R_{ct} in the bare electrode is in the range 500–900 Ω, its value increases up to tens of kΩ when the antibodies tether to the surface. Moreover, thanks to our functionalization procedure, no significant change of R_{ct} is observed after the blocking step (the surface is fully covered by antibodies), and, hence, the initial charge transfer resistance of the biosensor is due to the antibody layer and can be written:

$$R_{ct,0} = \frac{\rho d}{A_0} \quad (2)$$

In Equation (2) ρ is the resistivity of the antibody layer, d its thickness and A_0 the electrode area. Since the contact layer does not change during the detection procedure, both ρ and d are constant. On the contrary, the occurrence of the analyte detection reduces to some extent the effective area of the electrode, which in turn leads to an increase of the impedance, i.e.:

$$R_{ct}([\mathrm{C}]) = \frac{\rho d}{A_0 - \alpha A([\mathrm{C}])} \tag{3}$$

where $A([\mathrm{C}])$ represents the area occupied by the analytes and α is a coefficient that accounts for their conducting properties ($\alpha = 0$, for a "conductive" analyte that does not affect the electrolyte current, whereas $\alpha = 1$ for a fully "insulator" analyte). The occupancy area can be described by the Langmuir isotherm:

$$A([\mathrm{C}]) = A_0 \frac{[\mathrm{C}]}{K + [\mathrm{C}]} \tag{4}$$

where for convenience we used K as the inverse of the equilibrium constant. By combining Equations (3) and (4), we have:

$$R_{ct}([\mathrm{C}]) = R_{ct,0} \frac{K + [\mathrm{C}]}{K + (1 - \alpha)[\mathrm{C}]} \tag{5}$$

and the sensing parameter becomes:

$$\frac{\Delta R_{ct}}{R_{ct(\mathrm{Ab})}} = \frac{R_{ct}([\mathrm{C}]) - R_{ct,0}}{R_{ct,0}} = \frac{[\mathrm{C}]}{\frac{K}{\alpha} + \frac{(1-\alpha)}{\alpha}[\mathrm{C}]} \tag{6}$$

The best fit of the experimental data by the Langmuir-type Equation (6) is shown in Figure 7a, whereas the fitting parameters are reported in Table 2.

Table 2. Fitting parameters α and K obtained for both protocols DDP and BDP.

	α	K
DDP	0.185 ± 0.007	(3.0 ± 0.7) × 10^4
BDP	0.20 ± 0.01	70 ± 26

As expected, the conductivity coefficient α, which measures the microscopic tendency of the analyte to inhibit the electrolyte current, is larger when antibodies are tied to the bacterium. The choice of $\Delta R_{ct}/R_{ct(\mathrm{Ab})}$ as sensing parameter not only allows one to measure the values for α reported in Table 2, but even more important from the practical point of view, introduces a high degree of robustness in the biosensors as demonstrated by the fact that each experimental point reported in Figure 7a was obtained with different electrode.

The increase of α observed when antibodies are bound to bacteria from the top is due to the high "opacity" of the antibodies, the latter property being deducible from the large increment of R_{ct} brought about by the surface functionalization (see Figures 3–6). By imaging that a bacterium fully covered by antibodies would have $\alpha = 1$, we can (under)estimate the fraction f of the bacterium area covered by the antibodies as:

$$f = \frac{\alpha_2 - \alpha_1}{1 - \alpha_1} \approx 0.024 \tag{7}$$

In Equation (7) α_2 and α_1 correspond to the value of α with and without amplification step, respectively. By considering that the area of *E. coli* is $A_{E-c} \approx 1\ \mu m^2$ and that of an Ab is $A_{Ab} \approx 100\ nm^2$, for the number N_{Ab} of Abs per bacterium, we have:

$$N_{Ab} = f \frac{A_{E-c}}{A_{Ab}} \approx 240 \tag{8}$$

Since this calculation is based on the assumption that an antibody is fully "opaque" to the electrolyte current, such a value has to be meant as an underestimation for the number of antibodies binding the bacterium from the top, which is likely to be larger than one thousand.

3.6. Immunosensor Specificity

In order to evaluate the specificity of the developed immunosensor for *E. coli*, we tested the response of the functionalized immunosensor by measuring $\Delta R_{ct}/R_{ct(Ab)}$ induced by some non-specific bacteria such as *Acinetobacter baumannii* and *Salmonella enteriditis* 706 RIVM. To this end a 1mL aliquot of drinking water incubated with *Salmonella enteriditis* 706 RIVM and *Acinetobacter baumannii* (10^5 CFU mL^{-1}) flowed into the circuit for 30 min at room temperature, followed by a fresh solution of anti-*E. coli* Abs. Figure 8 shows the electron transfer resistance changes for both protocols. According to the direct detection protocol (DDP), $\Delta R_{ct}/R_{ct(Ab)}$ increased by 2% and 7% when *Salmonella enteriditis* 706 RIVM and *Acinetobacter baumannii* were assayed, respectively, compared with an 15% increase achieved with *E. coli*. Actually, a greater increase with *Salmonella enteriditis* 706 RIVM would be expected in view of the stronger morphological similarities with *E. coli* but, this unexpected behaviour can be likely ascribed to the different shape of *Acinetobacter baumannii*, which is a short, rod-shaped almost round bacterium which mostly hinder at the same concentration. With reference to the extended protocol (BDP), after the ballasting with a fresh solution of anti-*E. coli* Abs, $\Delta R_{ct}/R_{ct(Ab)}$ increased less than a 9% for both *Salmonella enteriditis* 706 RIVM and *Acinetobacter baumannii*, compared to the marked increase (24%) obtained with *E. coli* cells. This means that the amplification factor is about 1% for *Acinetobacter baumannii* and 4.5% for *Salmonella enteriditis* 706 RIVM, a difference likely due to the superior affinity between anti-*E. coli* pAbs and *Salmonella*, which share the same morphology. These results are more than satisfactory since only a slight cross-reaction arises with other bacterial species.

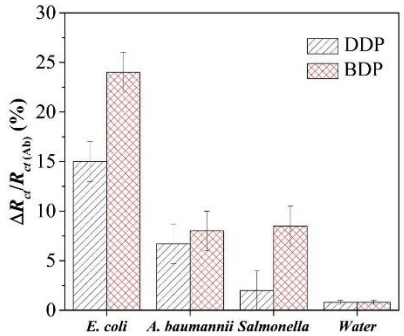

Figure 8. Specificity of the immunosensor in 10 mM $Fe(CN)_6^{3-/4-}$ solution at pH 7.4. $\Delta R_{ct}/R_{ct(Ab)}$ induced by 10^5 CFU mL^{-1} *E. coli* in comparison with the negative control (drinking water) and non-target bacteria (*Acinetobacter baumannii* and *Salmonella enteriditis* 706 RIVM).

4. Conclusions

An electrochemical impedance immunosensor based on a screen printed gold electrode for the rapid detection of *E. coli* in drinking water is proposed. Firstly, the antibodies were immobilized on the gold electrode surface in a covalent way using the Photochemical Immobilization Technique and the change in charge transfer resistance was monitored in the redox probe $Fe(CN)_6^{3-}/Fe(CN)_6^{4-}$ using the EIS. The proposed immunosensor exhibits a limit of detection of 3×10^1 CFU mL^{-1} which was obtained

by including in the measurement procedure a simple and rapid ballasting step, the latter consisting in the flowing of a fresh antibody solution onto the electrode surface so to realize a sandwich-complex.

PIT is an alternative method to bind antibodies onto gold surfaces and this is the first time it was used in biosensing by EIS. Our results demonstrate that PIT is effective proved even on commercial cheap electrodes This is major achievement since in most situations careful surface treatments are required in order to get an effective sensor response. In addition, PIT is a really a quick functionalization method since only 30 s are required for the antibodies activation and 1 h for the whole functionalization procedure (solution flowing on the electrode surface). Thus, the whole measurement can be carried out in less than 6 h (which means within a working day) since the total analysis time is 3 h and 30 min including washing and sensing processes making our approach suitable for out-of-lab use when low contamination levels need to be detected for alert emergency and, hence, an "on-off" approach is more desirable than a time-consuming quantitative procedure.

Supplementary Materials: The following are available online at http://www.mdpi.com/1424-8220/20/1/274/s1, Figure S1: (a) EIS spectrum measured with 100 μg mL^{-1} BSA solution. (b) EIS spectrum measured at different times while a 50 μg mL^{-1} BSA solution is conveyed to the cell, Table S1: Results from the fitting of impedance data (Figure 3) to the Randles circuit, Table S2: Results from the fitting of impedance data (Figure 4) to the Randles circuit, Table S3: Results from the fitting of impedance data (Figure 5) to the Randles circuit, Table S4: Results from the fitting of impedance data (Figure 6) to the Randles circuit, Table S5: Results from the fitting of impedance data (Figure S1a) to the Randles circuit, Table S6: Results from the fitting of impedance data (Figure S1b) to the Randles circuit.

Author Contributions: Conceptualization, M.C., B.D.V. and A.F.; methodology, M.C., R.G., A.F., R.C. and A.A.; validation, G.B., M.C., A.F., M.P. and R.G.; formal analysis, B.D.V., R.C., A.A. and R.V.; investigation, M.C., A.F., M.P. and R.G.; resources, A.A., A.F., R.C., R.V., R.G. and S.B.C.; data curation, M.C., A.F., A.A. and M.P.; writing—original draft preparation, M.C., A.F. and M.P.; writing—review and editing, M.C., B.D.V. and R.V.; visualization, G.B., M.C., A.F. and R.G.; supervision, B.D.V.; funding acquisition, S.B.C. and R.V. All authors have read and agreed to the published version of the manuscript.

Funding: This research was funded by Programma Operativo Nazionale (PON) Ricerca e Innovazione 2014–2020 "Dottorati innovativi con caratterizzazione industriale" and by Progetto "MultiPath-Multiplex nanostructured platform for label-free detection of foodborne pathogens and carcinogenic pesticides" - POR FESR CAMPANIA 2014/2020-O.S. 1.1–Avviso pubblico progetti di trasferimento tecnologico e di prima industrializzazione per le imprese innovative ad alto potenziale per la lotta alle patologie oncologiche.

Conflicts of Interest: The authors declare no conflict of interest.

References

1. Odonkor, S.T.; Ampofo, J.K. *Escherichia coli* as an indicator of bacteriological quality of water: An overview. *Microbiol. Res.* **2013**, *4*, e2. [CrossRef]
2. Cabral, J.P.S. Water microbiology. Bacterial pathogens and water. *Int. J. Environ. Res. Public Health* **2010**, 7, 3657–3703. [CrossRef] [PubMed]
3. World Health Organization. Drinking-Water. Available online: https://www.who.int/news-room/fact-sheets/detail/drinking-water (accessed on 17 September 2019).
4. Price, R.G.; Wildeboer, D. *E. coli* as an Indicator of Contamination and Health Risk in Environmental Waters. In *Escherichia coli—Recent Advances on Physiology, Pathogenesis and Biotechnological Applications*; InTech: London, UK, 2017.
5. Velusamy, V.; Arshak, K.; Korostynska, O.; Oliwa, K.; Adley, C. An overview of foodborne pathogen detection: In the perspective of biosensors. *Biotechnol. Adv.* **2010**, *28*, 232–254. [CrossRef]
6. Bai, Y.; Huang, W.C.; Yang, S.T. Enzyme-linked immunosorbent assay of *Escherichia coli* O157:H7 in surface enhanced poly(methyl methacrylate) microchannels. *Biotechnol. Bioeng.* **2007**, *98*, 328–339. [CrossRef]
7. Holland, J.L.; Louie, L.; Simor, A.E.; Louie, M. PCR detection of *Escherichia coli* O157:H7 directly from stools: Evaluation of commercial extraction methods for purifying fecal DNA. *J. Clin. Microbiol.* **2000**, *38*, 4108–4113. [CrossRef]
8. Guan, J.; Levin, R.E. Quantitative detection of *Escherichia coli* O157:H7 in ground beef by the polymerase chain reaction. *Food Microbiol.* **2002**, *19*, 159–165. [CrossRef]

9. Deisingh, A.K.; Thompson, M. Detection of infectious and toxigenic bacteria. *Analyst* **2002**, *127*, 567–581. [CrossRef]
10. Váradi, L.; Luo, J.L.; Hibbs, D.E.; Perry, J.D.; Anderson, R.J.; Orenga, S.; Groundwater, P.W. Methods for the detection and identification of pathogenic bacteria: Past, present, and future. *Chem. Soc. Rev.* **2017**, *46*, 4818–4832. [CrossRef]
11. Furst, A.L.; Francis, M.B. Impedance-Based Detection of Bacteria. *Chem. Rev.* **2019**, *119*, 700–726. [CrossRef]
12. Nayak, M.; Kotian, A.; Marathe, S.; Chakravortty, D. Detection of microorganisms using biosensors—A smarter way towards detection techniques. *Biosens. Bioelectron.* **2009**, *25*, 661–667. [CrossRef]
13. Xu, M.; Wang, R.; Li, Y. Electrochemical biosensors for rapid detection of *Escherichia coli* O157:H7. *Talanta* **2017**, *162*, 511–522. [CrossRef] [PubMed]
14. Dudak, F.C.; Boyaci, I.H. Development of an immunosensor based on surface plasmon resonance for enumeration of *Escherichia coli* in water samples. *Food Res. Int.* **2007**, *40*, 803–807. [CrossRef]
15. Guo, X.; Lin, C.S.; Chen, S.H.; Ye, R.; Wu, V.C.H. A piezoelectric immunosensor for specific capture and enrichment of viable pathogens by quartz crystal microbalance sensor, followed by detection with antibody-functionalized gold nanoparticles. *Biosens. Bioelectron.* **2012**, *38*, 177–183. [CrossRef] [PubMed]
16. Leahy, S.; Lai, Y. A cantilever biosensor based on a gap method for detecting *E. coli* in real time. *Sens. Actuators B Chem.* **2017**, *246*, 1011–1016. [CrossRef]
17. Felix, F.S.; Angnes, L. Electrochemical immunosensors—A powerful tool for analytical applications. *Biosens. Bioelectron.* **2018**, *102*, 470–478. [CrossRef]
18. Mollarasouli, F.; Kurbanoglu, S.; Ozkan, S.A. The Role of Electrochemical Immunosensors in Clinical Analysis. *Biosensors* **2019**, *9*, 86. [CrossRef]
19. Zhang, Z.; Zhou, J.; Du, X. Electrochemical Biosensors for Detection of Foodborne Pathogens. *Micromachines* **2019**, *10*, 222. [CrossRef]
20. Maalouf, R.; Fournier-Wirth, C.; Coste, J.; Chebib, H.; Saïkali, Y.; Vittori, O.; Errachid, A.; Cloarec, J.P.; Martelet, C.; Jaffrezic-Renault, N. Label-free detection of bacteria by electrochemical impedance spectroscopy: Comparison to surface plasmon resonance. *Anal. Chem.* **2007**, *79*, 4879–4886. [CrossRef]
21. Escamilla-Gómez, V.; Campuzano, S.; Pedrero, M.; Pingarrón, J.M. Gold screen-printed-based impedimetric immunobiosensors for direct and sensitive *Escherichia coli* quantisation. *Biosens. Bioelectron.* **2009**, *24*, 3365–3371. [CrossRef]
22. Geng, P.; Zhang, X.; Meng, W.; Wang, Q.; Zhang, W.; Jin, L.; Feng, Z.; Wu, Z. Self-assembled monolayers-based immunosensor for detection of *Escherichia coli* using electrochemical impedance spectroscopy. *Electrochim. Acta* **2008**, *53*, 4663–4668. [CrossRef]
23. Yang, H.; Zhou, H.; Hao, H.; Gong, Q.; Nie, K. Detection of *Escherichia coli* with a label-free impedimetric biosensor based on lectin functionalized mixed self-assembled monolayer. *Sens. Actuators B Chem.* **2016**, *229*, 297–304. [CrossRef]
24. Malvano, F.; Pilloton, R.; Albanese, D. Label-free impedimetric biosensors for the control of food safety—A review. *Int. J. Environ. Anal. Chem.* **2019**, *44*. [CrossRef]
25. Welch, N.G.; Scoble, J.A.; Muir, B.W.; Pigram, P.J. Orientation and characterization of immobilized antibodies for improved immunoassays (Review). *Biointerphases* **2017**, *12*, 02D301. [CrossRef] [PubMed]
26. Zhou, Y.; Fang, Y.; Ramasamy, R.P. Non-covalent functionalization of carbon nanotubes for electrochemical biosensor development. *Sensors* **2019**, *19*, 392. [CrossRef]
27. Sharma, S.; Byrne, H.; O'Kennedy, R.J. Antibodies and antibody-derived analytical biosensors. *Essays Biochem.* **2016**, *60*, 9–18.
28. Um, H.; Kim, M.; Lee, S.; Min, J.; Kim, H.; Choi, Y.; Kim, Y. Electrochemically oriented immobilization of antibody on poly-(2-cyano-ethylpyrrole)-coated gold electrode using a cyclic voltammetry. *Talanta* **2011**, *84*, 330–334. [CrossRef]
29. Alves, N.J.; Kiziltepe, T.; Bilgicer, B. Oriented surface immobilization of antibodies at the conserved nucleotide binding site for enhanced antigen detection. *Langmuir* **2012**, *28*, 9640–9648. [CrossRef]
30. Ho, J.A.; Hsu, W.; Liao, W.; Chiu, J.; Chen, M.; Chang, H.; Li, C. Ultrasensitive electrochemical detection of biotin using electrically addressable site-oriented antibody immobilization approach via aminophenyl boronic acid. *Biosens. Bioelectron.* **2010**, *26*, 1021–1027. [CrossRef]

31. Vashist, S.K.; Dixit, C.K.; MacCraith, B.D.; O'Kennedy, R. Effect of antibody immobilization strategies on the analytical performance of a surface plasmon resonance-based immunoassay. *Analyst* **2011**, *136*, 4431–4436. [CrossRef]
32. Rahman, M.A.; Shiddiky, M.J.A.; Park, J.S.; Shim, Y.B. An impedimetric immunosensor for the label-free detection of bisphenol A. *Biosens. Bioelectron.* **2007**, *22*, 2464–2470. [CrossRef]
33. Barton, A.C.; Collyer, S.D.; Davis, F.; Garifallou, G.; Tsekenis, G.; Tully, E.; Kennedy, R.O.; Gibson, T.; Millner, P.A.; Higson, S.P.J. Labeless AC impedimetric antibody-based sensors with pg mL^{-1} sensitivities for point-of-care biomedical applications. *Biosens. Bioelectron.* **2009**, *24*, 1090–1095. [CrossRef] [PubMed]
34. Ouerghi, O.; Touhami, A.; Jaffrezic-Renault, N.; Martelet, C.; Ouada, H.B.; Cosnier, S. Impedimetric immunosensor using avidin—Biotin for antibody immobilization. *Bioelectrochemistry* **2002**, *56*, 131–133. [CrossRef]
35. Lee, J.E.; Seo, J.H.; Kim, C.S.; Kwon, Y.; Ha, J.H.; Choi, S.S.; Cha, H.J. A comparative study on antibody immobilization strategies onto solid surface. *Korean J. Chem. Eng.* **2013**, *30*, 1934–1938. [CrossRef]
36. Inkpen, M.S.; Liu, Z.-F.; Li, H.; Campos, L.M.; Neaton, J.B.; Venkataraman, L. Non-chemisorbed gold–sulfur binding prevails in self-assembled monolayers. *Nat. Chem.* **2019**, *11*, 351–358. [CrossRef] [PubMed]
37. Sharafeldin, M.; Rusling, J.F. Influence of antibody immobilization strategy on carbon electrode immunoarrays. *Analyst* **2019**, *144*, 5108–5116. [CrossRef] [PubMed]
38. Fowler, J.M.; Stuart, M.C.; Wong, D.K.Y. Self-assembled layer of thiolated protein G as an immunosensor scaffold. *Anal. Chem.* **2007**, *79*, 350–354. [CrossRef] [PubMed]
39. Sun, X.; Du, S.; Wang, X.; Zhao, W.; Li, Q. A label-free electrochemical immunosensor for carbofuran detection based on a sol-gel entrapped antibody. *Sensors* **2011**, *11*, 9520–9531. [CrossRef]
40. Bereli, N.; Ertürk, G.; Tümer, M.A.; Denizli, A. Oriented immobilized anti-hIgG via Fc fragment-imprinted PHEMA cryogel for IgG purification. *Biomed. Chromatogr.* **2013**, *27*, 599–607. [CrossRef]
41. Moschallski, M.; Evers, A.; Brandstetter, T.; Rühe, J. Sensitivity of microarray based immunoassays using surface-attached hydrogels. *Anal. Chim. Acta* **2013**, *781*, 72–79. [CrossRef]
42. Yamazoe, H. Antibody immobilization technique using protein film for high stability and orientation control of the immobilized antibody. *Mater. Sci. Eng. C* **2019**, *100*, 209–214. [CrossRef]
43. Icoz, K.; Soylu, M.C.; Canikara, Z.; Unal, E. Quartz-crystal Microbalance Measurements of CD19 Antibody Immobilization on Gold Surface and Capturing B Lymphoblast Cells: Effect of Surface Functionalization. *Electroanalysis* **2018**, *30*, 834–841. [CrossRef]
44. Barreiros dos Santos, M.; Agusil, J.P.; Prieto-Simón, B.; Sporer, C.; Teixeira, V.; Samitier, J. Highly sensitive detection of pathogen *Escherichia coli* O157:H7 by electrochemical impedance spectroscopy. *Biosens. Bioelectron.* **2013**, *45*, 174–180. [CrossRef] [PubMed]
45. Malvano, F.; Pilloton, R.; Albanese, D. Sensitive Detection of *Escherichia coli* O157:H7 in Food Products by Impedimetric Immunosensors. *Sensors* **2018**, *18*, 2168. [CrossRef] [PubMed]
46. Wan, J.; Ai, J.; Zhang, Y.; Geng, X.; Gao, Q.; Cheng, Z. Signal-off impedimetric immunosensor for the detection of *Escherichia coli* O157:H7. *Sci. Rep.* **2016**, *6*, 19806. [CrossRef] [PubMed]
47. Lin, D.; Pillai, R.G.; Lee, W.E.; Jemere, A.B. An impedimetric biosensor for *E. coli* O157:H7 based on the use of self-assembled gold nanoparticles and protein G. *Microchim. Acta* **2019**, *186*, 169. [CrossRef] [PubMed]
48. Chowdhury, A.D.; De, A.; Chaudhuri, C.R.; Bandyopadhyay, K.; Sen, P. Label free polyaniline based impedimetric biosensor for detection of *E. coli* O157:H7 Bacteria. *Sens. Actuators B Chem.* **2012**, *171–172*, 916–923. [CrossRef]
49. Vericat, C.; Vela, M.E.; Benitez, G.; Carro, P.; Salvarezza, R.C. Self-assembled monolayers of thiols and dithiols on gold: New challenges for a well-known system. *Chem. Soc. Rev.* **2010**, *39*, 1805–1834. [CrossRef]
50. Mandler, D.; Kraus-Ophir, S. Self-assembled monolayers (SAMs) for electrochemical sensing. *J. Solid State Electrochem.* **2011**, *15*, 1535. [CrossRef]
51. Chaki, N.K.; Vijayamohanan, K. Self-assembled monolayers as a tunable platform for biosensor applications. *Biosens. Bioelectron.* **2002**, *17*, 1–12. [CrossRef]
52. Lee, C.Y.; Canavan, H.E.; Gamble, L.J.; Castner, D.G. Evidence of impurities in thiolated single-stranded DNA oligomers and their effect on DNA self-assembly on gold. *Langmuir* **2005**, *21*, 5134–5141. [CrossRef]
53. Butterworth, A.; Blues, E.; Williamson, P.; Cardona, M.; Gray, L.; Corrigan, D.K. SAM composition and electrode roughness affect performance of a DNA biosensor for antibiotic resistance. *Biosensors* **2019**, *9*, 22. [CrossRef] [PubMed]

54. Reimers, J.R.; Ford, M.J.; Marcuccio, S.M.; Ulstrup, J.; Hush, N.S. Competition of van der Waals and chemical forces on gold-sulfur surfaces and nanoparticles. *Nat. Rev. Chem.* **2017**, *1*, 0017. [CrossRef]
55. Häkkinen, H. The gold-sulfur interface at the nanoscale. *Nat. Chem.* **2012**, *4*, 443–455. [CrossRef] [PubMed]
56. Pensa, E.; Cortés, E.; Corthey, G.; Carro, P.; Vericat, C.; Fonticelli, M.H.; Benítez, G.; Rubert, A.A.; Salvarezza, R.C. The chemistry of the sulfur-gold interface: In search of a unified model. *Acc. Chem. Res.* **2012**, *45*, 1183–1192. [CrossRef] [PubMed]
57. Della Ventura, B.; Banchelli, M.; Funari, R.; Illiano, A.; De Angelis, M.; Taroni, P.; Amoresano, A.; Matteini, P.; Velotta, R. Biosensor surface functionalization by a simple photochemical immobilization of antibodies: Experimental characterization by mass spectrometry and surface enhanced Raman spectroscopy. *Analyst* **2019**, *144*, 6871–6880. [CrossRef] [PubMed]
58. Della Ventura, B.; Schiavo, L.; Altucci, C.; Esposito, R.; Velotta, R. Light assisted antibody immobilization for bio-sensing. *Biomed. Opt. Express* **2011**, *2*, 3223–3231. [CrossRef]
59. Gaglione, R.; Dell'Olmo, E.; Bosso, A.; Chino, M.; Pane, K.; Ascione, F.; Itri, F.; Caserta, S.; Amoresano, A.; Lombardi, A.; et al. Novel human bioactive peptides identified in Apolipoprotein B: Evaluation of their therapeutic potential. *Biochem. Pharmacol.* **2017**, *130*, 34–50. [CrossRef]
60. Funari, R.; Della Ventura, B.; Altucci, C.; Offenhäusser, A.; Mayer, D.; Velotta, R. Single Molecule Characterization of UV-Activated Antibodies on Gold by Atomic Force Microscopy. *Langmuir* **2016**, *32*, 8084–8091. [CrossRef]
61. Neves-Petersen, M.T.; Gryczynski, Z.; Lakowicz, J.; Fojan, P.; Pedersen, S.; Petersen, E.; Bjørn Petersen, S. High probability of disrupting a disulphide bridge mediated by an endogenous excited tryptophan residue. *Protein Sci.* **2002**, *11*, 588–600. [CrossRef]
62. Ellman, G.L. Tissue Sulfyd Groups. *Arch. Biochem. Biophys.* **1959**, *82*, 70–77. [CrossRef]
63. Funari, R.; Della Ventura, B.; Carrieri, R.; Morra, L.; Lahoz, E.; Gesuele, F.; Altucci, C.; Velotta, R. Detection of parathion and patulin by quartz-crystal microbalance functionalized by the photonics immobilization technique. *Biosens. Bioelectron.* **2015**, *67*, 224–229. [CrossRef] [PubMed]
64. Funari, R.; Della Ventura, B.; Schiavo, L.; Esposito, R.; Altucci, C.; Velotta, R. Detection of parathion pesticide by quartz crystal microbalance functionalized with UV-activated antibodies. *Anal. Chem.* **2013**, *85*, 6392–6397. [CrossRef] [PubMed]
65. Della Ventura, B.; Sakač, N.; Funari, R.; Velotta, R. Flexible immunosensor for the detection of salivary α-amylase in body fluids. *Talanta* **2017**, *174*, 52–58. [CrossRef] [PubMed]
66. Funari, R.; Terracciano, I.; Della Ventura, B.; Ricci, S.; Cardi, T.; D'Agostino, N.; Velotta, R. Label-Free Detection of Gliadin in Food by Quartz Crystal Microbalance-Based Immunosensor. *J. Agric. Food Chem.* **2017**, *65*, 1281–1289. [CrossRef]
67. Fulgione, A.; Cimafonte, M.; Della Ventura, B.; Iannaccone, M.; Ambrosino, C.; Capuano, F.; Proroga, Y.T.R.; Velotta, R.; Capparelli, R. QCM-based immunosensor for rapid detection of *Salmonella* Typhimurium in food. *Sci. Rep.* **2018**, *8*, 16137. [CrossRef]
68. Iarossi, M.; Schiattarella, C.; Rea, I.; De Stefano, L.; Fittipaldi, R.; Vecchione, A.; Velotta, R.; Della Ventura, B. Colorimetric Immunosensor by Aggregation of Photochemically Functionalized Gold Nanoparticles. *ACS Omega* **2018**, *3*, 3805–3812. [CrossRef]
69. Daniels, J.S.; Pourmand, N. Label-Free Impedance Biosensors: Opportunities and Challenges. *Electroanalysis* **2007**, *19*, 1239–1257. [CrossRef]

International Journal of Nanomedicine

Dovepress
open access to scientific and medical research

Open Access Full Text Article

ORIGINAL RESEARCH

Biomimetic hydroxyapatite nanocrystals are an active carrier for *Salmonella* bacteriophages

This article was published in the following Dove Medical Press journal:
International Journal of Nanomedicine

Andrea Fulgione,[1,*] Flora Ianniello,[1,*] Marina Papaianni,[1] Felice Contaldi,[1] Tiziana Sgamma,[2] Cinzia Giannini,[3] Stella Pastore,[3] Raffaele Velotta,[4] Bartolomeo Della Ventura,[5] Norberto Roveri,[6] Marco Lelli,[6] Federico Capuano,[7] Rosanna Capparelli[1]

[1]Department of Agriculture, University of Naples "Federico II", Portici, Naples, Italy; [2]Biomolecular Technology Group, School of Allied Health Sciences, De Montfort University, Leicester, UK; [3]Istituto di Cristallografia, Consiglio Nazionale delle Ricerche, Bari, Italy; [4]Department of Physics "Ettore Pancini", University of Naples "Federico II", Portici, Naples, Italy; [5]Department of Physics, Politecnico di Milano, Milano, Italy; [6]Chemical Center Srl, Granarolo dell'Emilia, Bologna, Italy; [7]Department of Food Microbiology, Istituto Zooprofilattico Sperimentale del Mezzogiorno, Portici, Naples, Italy

*These authors contributed equally to this work

Correspondence: Rosanna Capparelli
Department of Agriculture, University of Naples "Federico II", via Università 100, 80055, Portici, Naples, Italy
Tel +39 81 253 9274
Fax +39 81 253 1730
Email capparel@unina.it

Federico Capuano
Department of Food Microbiology, Istituto Zooprofilattico Sperimentale del Mezzogiorno, via Salute 2, 80055, Portici, Naples, Italy
Tel +39 81 786 5117
Email federico.capuano@cert.izsmportici.it

Purpose: The use of bacteriophages represents a valid alternative to conventional antimicrobial treatments, overcoming the widespread bacterial antibiotic resistance phenomenon. In this work, we evaluated whether biomimetic hydroxyapatite (HA) nanocrystals are able to enhance some properties of bacteriophages. The final goal of this study was to demonstrate that biomimetic HA nanocrystals can be used for bacteriophage delivery in the context of bacterial infections, and contribute – at the same time – to enhance some of the biological properties of the same bacteriophages such as stability, preservation, antimicrobial activity, and so on.

Materials and methods: Phage isolation and characterization were carried out by using Mitomycin C and following double-layer agar technique. The biomimetic HA water suspension was synthesized in order to obtain nanocrystals with plate-like morphology and nanometric dimensions. The interaction of phages with the HA was investigated by dynamic light scattering and Zeta potential analyses. The cytotoxicity and intracellular killing activities of the phage–HA complex were evaluated in human hepatocellular carcinoma HepG2 cells. The bacterial inhibition capacity of the complex was assessed on chicken minced meat samples infected with *Salmonella* Rissen.

Results: Our data highlighted that the biomimetic HA nanocrystal–bacteriophage complex was more stable and more effective than phages alone in all tested experimental conditions.

Conclusion: Our results evidenced the important contribution of biomimetic HA nanocrystals: they act as an excellent carrier for bacteriophage delivery and enhance its biological characteristics. This study confirmed the significant role of the mineral HA when it is complexed with biological entities like bacteriophages, as it has been shown for molecules such as lactoferrin.

Keywords: biomimetic hydroxyapatite nanocrystals, *Salmonella* Rissen, bacteriophages, antibiotic resistance

Introduction

Inappropriate abuse of antibiotics has led to the development of drug-resistant microorganisms.[1] Antibiotic resistance is a constantly evolving phenomenon and represents a serious problem with high death toll and a substantial economic impact worldwide; it complicates patient management and treatment strategy and prolongs hospital stays. In Europe antibiotic-resistant bacteria infect 4 million people every year.[2,3] Therefore, therapies that can serve as an alternative to antibiotics need to be developed.

A valid and alternative approach to solve the widespread phenomenon of "antibiotic resistance" of different pathogens such as *Salmonella*,[4] *Staphylococcus aureus*,[5] *Escherichia coli*,[6] and *Streptococcus*[7] – in addition to well-known antimicrobial peptides[8] – is the use of bacteriophages or phages. Bacteriophages are the most abundant viruses

http://dx.doi.org/10.2147/IJN.S195188

found in the biosphere;[9,10] they grow quickly and exponentially, and they are efficacy since the fist interaction with bacteria.[11] At the same time, phages have some disadvantages such as low stability over time and low resistance (or short half-life) in acidic environments such as that of the stomach.[12,13]

These limitations could be overcome by stabilizing the phages by combining them with nanoparticles of different materials such as carbon, silica, metal oxide, graphene, and hydroxyapatite (HA). HA, in particular, has been frequently used in several studies to stabilize, protect, and deliver molecules or radionuclides.[14–22]

HA represents the major components of bone, tooth, and cartilaginous tissues. It possesses several properties such as biocompatibility, biomimetic dimensions, osteoconductivity, and degradability, which make it suitable for several applications[16,23] when combined with different biological molecules.[19] Indeed, HA nanocrystals have been successfully employed to build bone scaffolds and implant coating materials and vehicles for drug targeting.[24–29] Furthermore, HA nanocrystals have low toxicity and remarkable stability, as reported in our previous studies.[30]

In industrialized countries, infections acquired by food and water represent a big concern for public health, and about 50% of foodborne infections in humans are caused by *Salmonella* spp.[31] Despite control measures and monitoring carried out by the healthcare authorities, cases of *Salmonella* contaminations are still very frequent.[32]

Salmonella serovars such as Enteritidis and Typhimurium are accountable for most of the salmonellosis cases.[33] In recent years, infections by other serovars such as Kentucky and Rissen became more frequent; the latter *Salmonella* strain, especially, has been isolated from pork and chicken products and in human and swineherds gastrointestinal tract.[34,35]

Based on these considerations, we decided to investigate whether the biomimetic HA nanocrystals – which mimick the natural bone mineral – could interact with *Salmonella* bacteriophages and whether the newly developed complex could control *Salmonella* bacterial infection.

Materials and methods

Bacteria

All the *Salmonella* spp. strains used in this study were provided by the Istituto Zooprofilattico Sperimentale Del Mezzogiorno (Portici, Naples, Italy). Among these, *S.* Rissen was selected as reference strain for bacteriophage (phage) isolation.

Phage isolation

Phage (SR ϕ1) from *S.* Rissen was isolated as described by Capparelli et al.[36] Briefly, *S.* Rissen was grown in 5 mL of Luria Bertani broth (LB; Sigma-Aldrich Co., St Louis, MO, USA) and, when the culture reached the exponential growth phase, Mitomycin C (1 μg/mL) was added. Then, the suspension was incubated at 37°C for 30 minutes. After incubation, it was centrifuged twice at 5,000 rpm for 10 minutes; each time the supernatant was discarded and the pellet resuspended in 5 mL of LB in order to remove any residue of Mitomycin C. Later, the suspension was incubated at 37°C for 4 hours. Then another centrifugation step was carried out but this time, the supernatant – containing bacteriophages – was collected, filtered through a 0.22 μm membrane, and screened for the presence of phages using the double-layer agar (DLA) method. The last step included a lower nutrient agar layer and an upper soft agar layer (4 mL of 0.7% bacteriological agar [Sigma-Aldrich Co.] mixed with 10^7 colony forming unit [CFU]/mL of bacterial strain used for phage isolation and previously filtered bacteriophage solution). After overnight incubation at 37°C, the plates were observed for the presence of clear zone (plaque formation) over the surface of the double agar plate. The phages isolated were stored at −20°C in buffer SM.[37] However, the pellet was streaked onto *Salmonella* Chromogenic Agar Base (CM1007, Oxoid; Thermo Fisher Scientific, Waltham, MA, USA) to confirm the presence of *Salmonella* spp. bacteria.

The titer of phage, expressed as plaque forming units (PFUs), was evaluated by using the DLA technique as reported by Sambrook et al.[38]

Phage host range

Host range of phages was evaluated against 14 different *Salmonella* strains by the overlay method.[39] Briefly, the test consisted of spotting 100 μL of SR ϕ1 on the surface of a double agar layer as reported above.

Multiplicity of infection (MOI) of phage

MOI is the ratio of virus particles to host cells.[40] To establish the best MOI, *S.* Rissen strain was grown in LB at 37°C till 10^4 CFU/mL. Later, 100 μL of bacterial suspension was treated with 100 μL of SR ϕ1 at different ratios, ranging from 10^{-3} to 10^3 PFU/CFU, in a 96-well microplate. Positive and negative controls were represented by a mixture containing 100 μL of *S.* Rissen (10^4 CFU/mL) plus 100 μL of SM buffer or 100 μL of LB broth plus 100 μL of SM buffer, respectively. After 16–18 hours of incubation at 37°C, the

optical density was measured at OD 600 nm to determine the optimal MOI. This last parameter shows that the lower phage titer is able to kill the majority of the bacteria, and it was used for all the subsequent experiments.

One-step growth curve

The "burst size" and phage life cycle were evaluated by the one-step growth assay. The culture of *S.* Rissen (10^8 CFU/mL), in exponential growth phase, was infected with phage according to the optimal MOI (previously selected). The mixture was incubated at 37°C for 5 minutes to favor phage adsorption, and later, it was serially diluted up to 10^{-4} in 20 mL of LB. The above mixture was incubated at 37°C for 90 minutes, and 100 µL of sample was taken every 5 minutes and plated, during the whole incubation period. Latent period was the interval between the beginning of the adsorption (not including 5 minutes pre-incubation) and the onset of the first burst (corresponding to the initial rise in phage titer). Burst size was the ratio between the final count of released phage particles and the initial amount of infected bacterial cells.

Electron microscopic analysis

SR ϕ1 (10^8 PFU/mL) was purified by CsCl density gradient ultracentrifugation and dialyzed against SM buffer overnight at 4°C.[41] Phage particles were negatively stained with 2% of phosphotungstic acid (pH 7.2) for 20 minutes. Later, phages were observed by using a Philips EM 300 electron microscope.

Phage phylogenetic analysis

Phylogenetic analysis was performed using the maximum likelihood method.[42] Data alignment was carried out with Blosum 65 (gap open penalty =11; gap extension penalty =3) and tree was built by using Jukes-Cantor and UPGMA models.

Phage genome sequencing, assembly, and annotation

Genomic DNA was quantified using the Qubit dsDNA BR Assay Kit (Thermo Fisher Scientific); DNA purity was assessed with a Nanodrop (Thermo Fisher Scientific), and DNA size was determined with a 2200 Tape Station Instrument (Agilent Technologies, Santa Clara, CA, USA). Illumina libraries were produced starting from 1 µg of genomic DNA, which was sheared using the Covaris S220 instrument (Covaris Inc. Woburn, MA, USA) and the TruSeq DNA Sample Prep Kit (Illumina, San Diego, CA, USA) following the manufacturer's guidelines. Sequencing was performed on a NextSeq500 instrument with the 150-nt paired-end protocol (Illumina) according to the manufacturer's guidelines. Illumina reads underwent quality filtering and trimming using Sickle and were quality corrected with Bayes Hammer before being assembled de novo. Genomes were assembled de novo from Illumina reads using SPAdes 2.9.0 with multiple k-mer combinations. The resultant contigs were scaffolded using SSPACE 3.0. Five micrograms of high-molecular-weight genomic DNA (peak >60 kb) was used to prepare ~20 kb-insert single-molecule real-time (SMRT)-bell libraries according to the manufacturer's guidelines (Pacific Biosciences, Menlo Park, CA, USA). The library templates were sequenced using the SMRT sequencing technology on a PacBio RSII sequencer (Pacific Biosciences) at Macrogen, Inc (Korea). PacBio subreads were extracted using Bash5tools (version 0.8.0), filtrated, and assembled de novo using Falcon-Integrate with the suggested settings for bacterial genome. The assembled genome sequence was polished by Quiver v 0.9.2, and gene annotation was performed using RAST web service (http://rast.nmpdr.org/).[43]

Biomimetic HA nanocrystal synthesis and characterization

Biomimetic HA nanocrystals were produced as described by Nocerino et al.[44] Briefly, HA nanocrystals were precipitated from an aqueous solution of $(CH_3COO)_2Ca$ (75 mM) by slow addition (one drop per second) of an aqueous solution of H_3PO_4 (50 mM), keeping the pH constant at 10 (by the addition of $(NH_4)OH$ solution). The synthesis was performed at room temperature. After this last process, the suspension of HA was washed with distilled water in order to remove ammonium ions and favor the interaction between nanocrystals.

Transmission electron microscopy (TEM) investigation was carried out using a 1200 EX microscope, linked to X-ray analysis detectors and a 3010 UHR operating at 300 kV (JEOL Ltd, Tokyo, Japan). Few droplets of the samples (in ultrapure water) were deposited on perforated carbon foils supported on conventional copper microgrids. The surface area was determined using a Sorpty 1750 instrument (Carlo Erba Reagents S.r.l., Milan, Italy) using N_2 absorption at 77 K.[45]

Synthesis of complex HA–SR ϕ1

The HA–SR ϕ1 complex was prepared by mixing 10 mL of HA (100 mg/mL) with 10 mL of SR ϕ1 (10^7 PFU/mL) under stirring wad. The suspension was stable, and no precipitation

phenomena were observed during the synthesis process. Later, aliquots of 1 mL of the mixture were incubated – under shaking – at room temperature for the following time intervals: 30, 90, 180, and 300 minutes and 24 hours. After proper incubation, the sample was centrifuged, and the pellet was suspended in SM buffer. The concentration of the active phage particles was evaluated by the DLA method. After overnight incubation, the optimal incubation time was selected according to the results. Next, other tests were carried out by maintaining constant concentration of the HA but increasing the bacteriophage titer. The results showed that, by increasing the phage titer, the concentration of the active phage particles estimated by the DLA method, after the optimal time of incubation, remained constant at 10^7 PFU/mL (the titer used for the above complex synthesis) (data not shown). Based on these data, we evidenced that the maximum loading capacity of the HA used for this study was 10^7 PFU/mL of bacteriophages.

Complex HA–SR ϕ1 characterization

Zeta potential, dynamic light scattering (DLS) analysis, and pH stability

SR ϕ1, HA–SR ϕ1, and HA were analyzed for the measurement of zeta potential and DLS in appropriate disposable folded capillary cells (DTS1070; Malvern Instruments, Malvern, UK) using a Zetasizer Nano ZS (Malvern Instruments). For the DLS analysis, the instrument was, in addition, equipped with a 633 nm He–Ne laser and an avalanche photodiode detector placed at a detection angle of 173°. Each analysis was carried out in triplicate for three independent experiments. The analysis temperature was 25°C and about 1 mL of sample (at pH value of 7) was used for the test. The results were examined, and, for each sample, the zeta potential average and DLS measurement value were determined.

To estimate the stability of SR ϕ1 and HA–SR ϕ1 over time, the titer of phage – or mixed with HA – was evaluated for 2 successive months, at weekly intervals. During this time, the samples were stored at +4°C.[46]

In addition, the effects of an acid or alkaline pH, on SR ϕ1 or HA–SR ϕ1 complex, were evaluated by mimicking different pH conditions (ranging from 2 to 10). Briefly, the phage suspensions were incubated at 37°C for 1 hour in buffer SM at the following pH values: 2, 4, 7, and 10. After incubation, the phage titer was estimated by the DLA method as reported by Jun et al.[47] Each assay was performed in triplicate.

X-ray analysis

X-ray powder diffraction (XPD) patterns were obtained at room temperature by using a Rigaku RINT2500 rotating anode laboratory diffractometer (50 kV, 200 mA) equipped with the silicon strip Rigaku D/teX Ultra detector. An asymmetric Johansson Ge (111) crystal was used to select the monochromatic Cu Kα1 radiation (λ=1.54056 Å). The measurements were carried out in transmission geometry by introducing the samples in a Lindemann glass capillary of 0.3 mm diameter. The XPD patterns were first indexed by the program QUALX[48] by matching the XPD patterns with the ICSD database. They were further analyzed by using a whole-profile Rietveld-based fitting program[49] to determine the crystalline domain size as follows:

1. The instrumental resolution function (IRF) was evaluated by fitting the XPD pattern of a LaB6 NIST standard recorded under the same experimental conditions as those used for measuring the samples. The IRF data file was provided separately to the program in order to allow subsequent refinement of the diffraction patterns of the samples.
2. The crystal structure of the samples, once determined, was input into the program and refined. The inhomogeneous peak broadening of the diffraction peaks was described by a phenomenological model based on a modified Scherrer formula:

$$\beta_{h,k,l} = \frac{\lambda}{h\cos\theta} = \frac{\lambda}{\cos\theta}\sum_{imp} a_{imp} y_{imp}(\theta_h, \Phi_h)$$

where $\beta_{h,k,l}$ represent the size contribution to the integral width of the (h,k,l) reflection and are real spherical harmonics. After refinement of the α_{imp} coefficients, the program calculates the apparent size of the crystal domains along each reciprocal lattice vector (h,k,l) direction.

Cytotoxicity trials

MTT assay

Human hepatocellular carcinoma HepG2 (HB-8065; American Type Culture Collection [ATCC], Manassas, VA, USA) cells were grown in minimal essential media (MEM) plus 10% FBS, 2 mM glutamine, 1% nonessential amino acids (NEAA), 100 U/mL penicillin, and 100 µg/mL streptomycin (all from Thermo Fisher Scientific). Cells (200 µL at 30,000 cells/well) were placed in a 96-well plate and were treated with SR ϕ1 (10^7 PFU/mL), HA–SR ϕ1 (100 mg/mL plus 10^7 PFU/mL), or HA (100 mg/mL) for 24, 48, and 72 hours, respectively.

The positive and negative controls contained 10% DMSO or PBS, respectively. All the conditions tested were performed in triplicate. An aliquot of 20 µL of MTT dissolved in PBS at a concentration of 5 mg/mL was added to each well. After 2 hours, the supernatant was discarded and

150 µL of isopropanol was added. The plate was incubated at 37°C for 30 minutes and then, the optical density was measured at 560 nm.

Lactate dehydrogenase (LDH) assay

An LDH assay was performed using a CytoTox 96 Non-Radio cytotoxicity assay kit (Promega Corporation, Fitchburg, WI, USA) at 24, 48, and 72 hours according to the manufacturer's protocol. The LDH levels were evaluated for all the conditions tested for the MTT assay.

Internalization of fluorescent HA–SR ϕ1

In order to evaluate the internalization of the complex, HA nanoparticles were labeled by fluorescein isothiocyanate (FITC). Briefly, HA (100 mg/mL) was mixed with 20 mL of 3-aminopropyltriethoxysilane (Sigma-Aldrich Co.) in 100 mL of anhydrous ethanol and stirred at 74°C for 3 hours. Later, fluorescein (6 µg/mL; Sigma-Aldrich Co.) was added and continued to react at 74°C for about 20 hours in the dark. The mixture was centrifuged at 5,000 rpm for 1 minute and the pellet was rinsed three times with anhydrous ethanol and deionized water, and later suspended in SM buffer.[50] Subsequently, SR ϕ1 (10^7 PFU/mL) was added to the HA previously labeled. An aliquot of 10 µL of the complex HA–SR ϕ1 at different dilutions (1:1,000, 1:100, and 1:10) was added to HepG2 cells (1.0×10^5 per well) for 24 hours. The control cells were treated with 10 µL of SM buffer. After treatment, the medium was discarded, and cells were rinsed twice with PBS and fixed in 4% paraformaldehyde for 10 minutes at room temperature. DAPI was used to counterstain nuclei. Slices were observed using a Zeiss LSM 710 Confocal Laser Scanning Microscope (Carl Zeiss MicroImaging GmbH). Samples were vertically scanned with a 63× or 40× (1.40 NA) Plan-Apochromat oil-immersion objective. Images were obtained with Zeiss ZEN Confocal Software (Carl Zeiss MicroImaging GmbH).

Intracellular killing activity

HepG2 cells were placed in a 24-well plate (0.2×10^6 cells/well), incubated overnight (37°C, 5% CO_2) in MEM supplemented with 10% FBS (Thermo Fisher Scientific). The experiment was carried out in two different ways in order to evaluate different types of antimicrobial activity of the complex according to different infection processes. First, the cells were infected with *S.* Rissen (10^8 CFU/mL) for 1 hour. The medium was discarded, and the cells were washed with PBS (three times) and incubated in MEM plus 10% FBS and gentamicin (12.5 µg/mL)[36] at 37°C in 5% CO_2 for 3 hours. Later, the cells were treated with SR ϕ1 (10^7 PFU/mL), HA–SR ϕ1 (100 mg/mL plus 10^7 PFU/mL), or HA (100 mg/mL) for 24 hours as reported by McLaughlin et al[51] and Withanage et al.[52]

In the second infection process, the cells were infected with *S.* Rissen (10^8 CFU/mL) and simultaneously treated with SR ϕ1 (10^7 PFU/mL), HA–SR ϕ1 (100 mg/mL plus 10^7 PFU/mL), or HA (100 mg/mL) for 1 hour. The cells were then treated with gentamicin as described above. After 3 hours of incubation at 37°C in 5% CO_2, the medium was discarded, and the cells were incubated in MEM containing 10% FBS for 24 hours.

The cells of both experiments were lysed with Tween 20 (0.05%) and incubated at 37°C in 5% CO_2 for 4 hours, and each lysate was then serially diluted in PBS and plated on XLT4 (Sigma-Aldrich Co.). The plates were incubated at 37°C overnight and evaluated for the presence of bacteria.

Both the above experiments were carried out using mouse macrophage cell line J774A.1 (TIB-67; ATCC) instead of HepG2 cells. J774A.1 cells were grown in DMEM supplemented with 10% FBS, 2 mM glutamine, 1% NEAA, 100 U/mL penicillin, and 100 µg/mL streptomycin (all from Thermo Fisher Scientific). Cells were maintained in a humidified, 37°C, 5% CO_2 incubator.

Bacterial reduction assay on chicken minced meat

S. Rissen was processed as reported by Sukumaran et al.[53] For the test, 250 g of chicken minced meat was divided into five equal parts. Four sections were infected with *S.* Rissen (10^3 CFU/mL) and incubated at room temperature according to ISO 16140-2: 2016;[54] while the last one was treated only with PBS (negative control). After 30 minutes, three of the four infected parts were treated respectively with SR ϕ1 (10^8 PFU/mL), HA–SR ϕ1 (100 mg/mL plus 10^8 PFU/mL), or HA (100 mg/mL). All samples were stored at 4°C for 7 days and tested for the presence of the bacteria every 24 hours. In particular, at each time point, 5 g of meat was taken from each sample and homogenized in 45 mL of 0.1% buffered peptone water (AES Laboratoire Groupe, France) at 200 rpm for 1 minute, using the Stomacher 400 Circulator (Seward Ltd, Bohemia, NY, USA). Subsequently, 100 µL of sample was plated on XLT4 agar and incubated at 37°C for 24 hours. The efficacy of each treatment was evaluated by counting the CFU formed on the plate after the incubation time.

Results

Phage isolation and characterization

Phage excision from *S.* Rissen was induced by Mitomycin C procedure.[36,55] The SR ϕ1 host range was tested against 14 *Salmonella* strains, each belonging to a different serovar, and

Table 1 Phage host range against different *Salmonella* strains

Bacteria	Lytic activity
S. Livingstone	+
S. Infantis	+
S. Potsdam	+
S. Thompson	–
S. Mbandaka	+
S. Winston	+
S. Montevideo	–
S. Virchow	+
S. Ohio	+
S. Jerusalem	–
S. Inganda	+
S. Wil	+
S. Typhimurium	+
S. Enteritidis	+

Notes: + indicates lysis after infection with SR ϕ1; – indicates lack of lysis after infection with SR ϕ1.

it was active against 11 out of 14 selected strains (Table 1). The MOI test allowed us to select the value of 0.1 as optimal MOI (Figure S1). This value has been used for all the later experiments. The one-step growth analysis highlighted that the latent period of SR ϕ1 was 60 minutes (Figure S2) and that its burst size was 54 PFU/cell.

TEM analysis of SR ϕ1 allowed us to classify the phage as a member of the *Podoviridae* family, according to a previous publication.[10] In particular, TEM analysis revealed that the tail length and head diameter were 16±2.0 nm (mean ± SD) and 57±1.0 nm (mean ± SD), respectively; and the total length was 73±2.0 nm (mean ± SD) (Figure 1).

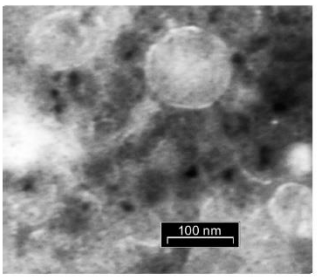

Figure 1 Electron microscopic analysis of phage. SR ϕ1 observed with a TEM analysis. Scale bar, 100 nm.
Abbreviation: TEM, transmission electron microscopy.

Comparative genomic analysis of phage

DNA sequencing yielded a total of 2,199,543 reads (660 Mb) and an average coverage of 13,200×. Phage SR ϕ1 genome consists of 51,738 bp with a G+C content of 48.4%. The genomic sequence of SR ϕ1 described in this study has been deposited in the GenBank database (accession number: KY709687). Open reading frames (ORFs) with a length of at least 38 amino acids were selected. A total of 622 ORFs were predicted to be present within the genome. However, only 87 ORFs (13.98%) were predicted to be functional based on gene predictions and annotation of the genome (Figure 2). Concrete gene information such as positions, directions, sizes, and putative functions of SR ϕ1 coding DNA sequences (CDSs) are shown in Table S1. The genome contains 87 predicted CDSs, of which 70 matched with already identified phage genes. Identified genes included 30 genes affecting bacteriophage physiology, 12 phage structures, 10 DNA replication, and three bacterial lysis. The remaining 32 CDSs encoded hypothetical proteins. Phage SR ϕ1-predicted genome did not show genes coding for toxins, antibiotic resistance, or *Salmonella* virulence.

To gain an insight into the characteristics of the phage SR ϕ1 genome, we performed a phylogenetic analysis, comparing its genome to the predicted genomes of other 37 fully sequenced phages. The phylogenetic analysis confirmed that phage ϕ1 is a *Podoviridae*, specifically showing 19 homologous genes with *PHAGE_Salmon_SPN9CC* (NC017985) (Figure 3).

Biomimetic HA nanocrystal characterization

The biomimetic HA nanocrystals used in this study had a composition very close to that of the human body.[56]

The TEM analysis revealed the length of HA nanocrystals (~30–40 nm) and its plate-like morphology (Figure S3). The high reactivity of HA is ascribed to its amorphous surface[16] and to its high surface area of about 110 m^2/g, which is only slightly lower than that of biological nanocrystals (120 m^2/g).[30]

Moreover, the degree of crystallinity and the presence of carbonate ions in the structure of biomimetic HA (data not shown) clearly confirm that the HA selected for this study is – structurally – very similar to that of the bone, not only in the size of the nanocrystals but also in ionic substitution.

Preparation and characterization of the complex (HA–SR ϕ1)

The interaction of SR ϕ1 with HA, carried out as reported in Patent IT102017000050733,[57] was evaluated at different

Figure 2 Functional genome map of phage SR ϕ1.
Notes: Hypothetical functions of encoded proteins were determined by comparison of amino acid sequences to the non-redundant databank using BLASTP. Annotation was verified using PHAST, a web server designed to rapidly and accurately identify, annotate, and graphically display prophage sequences within bacterial genomes or plasmids. The + and – stranded ORFs were colored in yellow.
Abbreviations: BLASTP, Basic Local Alignment Search Tool Protein; ORFs, open reading frames; PHAST, PHAge Search Tool.

incubation time intervals. The results showed that SR ϕ1 has interacted with HA already after 30 minutes. Furthermore, the graph showed that the amount of complexes SR ϕ1–HA increased over time (Figure 4A). Based on this result, we considered overnight incubation to be the optimal time interval for the complex synthesis.

The interaction between HA and SR ϕ1 was studied also through the zeta potential analysis, in which SR ϕ1 was negatively charged (−11.28±1.16) while HA was positively charged (2.9±0.9 mV). Therefore, the SR ϕ1 and HA complex showed a positive zeta potential of 0.9±1.60 mV (Figure 4B).

In addition, the stability of the SR ϕ1 and the HA–SR ϕ1 complex was assessed after the complex synthesis for about 2 months at 7 days intervals. Stability for long periods is essential for using phages in several biocontrol applications.[58] The titer of the phage SR ϕ1 alone started to decrease already after 1 week; instead, when the phage was complexed with HA, its titer was stable for up to 6 weeks without any variation at the different time points analyzed (Figure 4C).

The analysis of the HA–SR ϕ1 complex stability at different pH values (ranging from 2 to 10) assessed the strong stability of the complex, compared to that of SR ϕ1 alone (Figure 4D). Further characterization of the complex was carried out by DLS analysis. During this test, no rapid aggregation phenomenon was observed. As shown in Figure 4E, the diameter of HA was 300 nm while only diameter of SR ϕ1 was smaller (about 200 nm) than the HA. When HA and SR ϕ1 were complexed, the estimated hydrodynamic diameter was about 400 nm, thereby confirming the interaction between these two elements as reported by Wang at al.[59]

XPD analysis showed that HA nanocrystals[60] have a hexagonal crystalline structure (structure parameters are reported in Table S2). XPD patterns were further studied by using a whole-profile Rietveld-based fitting program[49] as shown in Figure S4. The Rietveld analysis allowed us to determine cell parameters and crystalline domain size along the [002] and [110] crystallographic directions (summarized in Table S3). This analysis also showed the structural variation of the HA crystalline domain size with or without SR ϕ1 (Figure 5, black and red dots, respectively). When the HA percentage was increased, the samples without SR ϕ1 did not show any change in the crystalline domain size along [002] and [110] directions. Instead, when the HA amount was increased, in the case of the complex (HA–SR ϕ1), the crystalline domain size decreased (Figure 5).

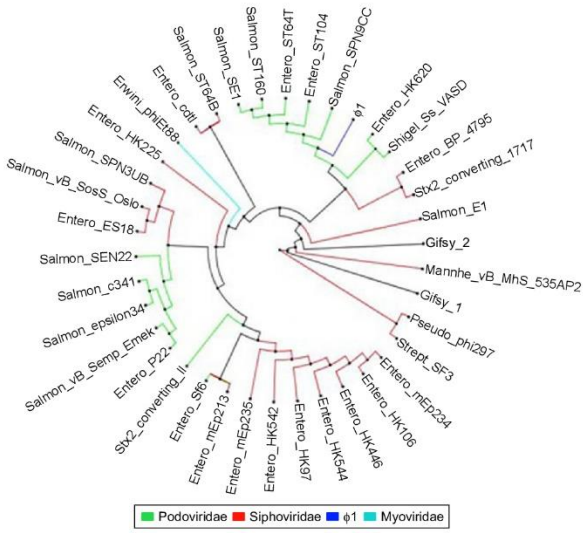

Figure 3 Assignment of SR ϕ1 to the *Podoviridae* family.
Notes: The phylogenetic tree shows a strong DNA identity between SR ϕ1 and five members of the *Podoviridae* (three Salmonella and two Entero phages). The tree is based on the alignment of 39 phage genomes. The bar indicates branch length scale.

Cytotoxicity trials

To evaluate the cytotoxic effect of SR ϕ1, HA, and the complex HA–SR ϕ1, a cell viability test was carried out by evaluating the reduction of MTT to formazan in human hepatocellular carcinoma HepG2 cells. The results showed that none of the treatments affected the cell vitality up to 72 hours (Figure S5A).

Moreover, the amount of the extracellular enzyme LDH, a cell death indicator,[61] was assessed under the same experimental conditions described above. Again, based on the amount of LHD produced, we concluded that none of the treatments produced cytotoxic effects (Figure S5B).

Internalization of fluorescent complex

As *Salmonella* spp. is an intracellular pathogen, the capacity of the complex to penetrate HepG2 eukaryotic cells was evaluated by laser scanning confocal microscopy analysis. Figure 6 evidences the cell uptake of the complex. In particular, the complex HA–SR ϕ1 (HA colored in green) was internalized into the cytoplasm of the HepG2 cells after 24 hours of treatment. Nuclei were counterstained with DAPI dye (blue). No fluorescent signal was detected in the control cells.

Intracellular killing activity

Once the ability of the complex to penetrate host cells was determined, the intracellular killing activity was gauged in two different experimental conditions: the HA–SR ϕ1 complex was administered at 1 hour postinfection or together with *Salmonella* bacteria. The results showed that 1 hour postinfection, only HA–SR ϕ1 showed lytic activity against bacteria, reducing the bacterial load significantly (Figure 7A) while the effect of phages alone was minimal. In the second experiment, in which all the treatments were carried out simultaneously with the bacteria infection, both SR ϕ1 and HA–SR ϕ1 showed comparable lytic activity (Figure 7B). The data reported in Figure 7A evidenced that 1 hour after the infection with *S.* Rissen, the presence of biomimetic HA favored the uptake of phages into the HepG2 cells, allowing phages to kill also the intracellular bacteria.

Furthermore, Figure 7B showed that the biomimetic HA nanocrystals did not compromise the lytic activity of the

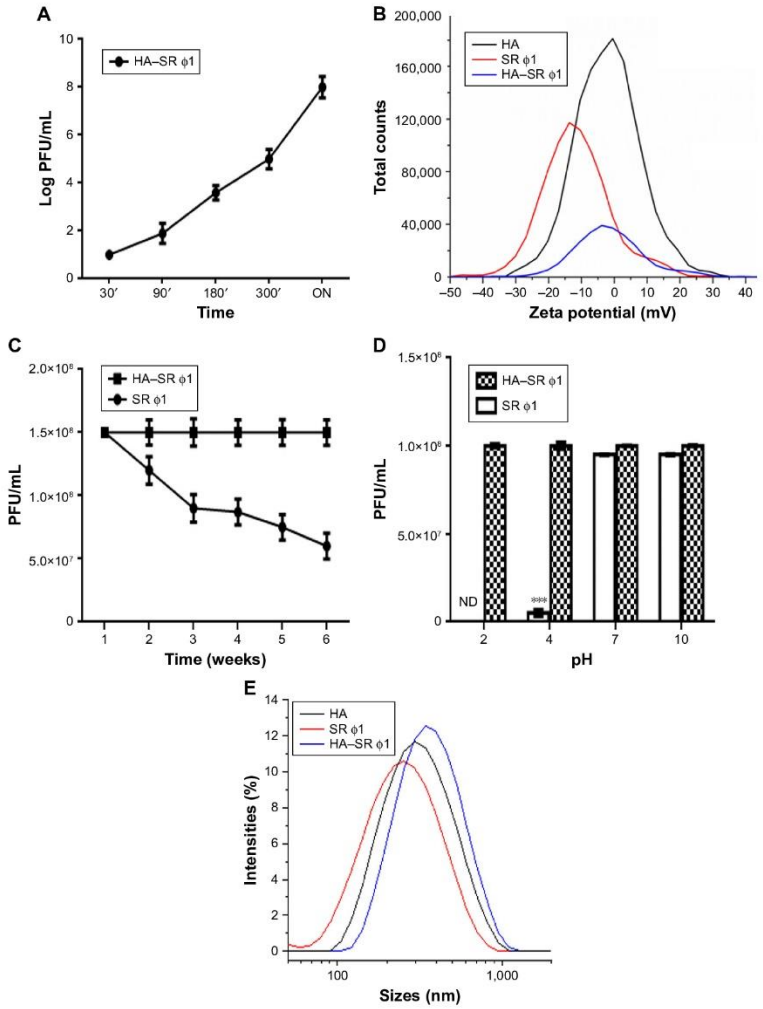

Figure 4 (**A**) The absorption of SR ϕ1 on HA after different times (30, 90, 180, 300 minutes and overnight) of incubation. Each value is the mean ± SD of three independent experiments with three replicates each. (**B**) Zeta potential analysis of SR ϕ1, HA–SR ϕ1, and HA. (**C**) The half-life of the SR ϕ1 and the complex HA–SR ϕ1. Each value is the mean ± SD of three independent experiments with three replicates each. (**D**) Effects of pH on the stability of SR ϕ1 and HA–SR ϕ1. ***$P<0.001$. Each value is the mean ± SD of three independent experiments with three replicates each. Statistical analysis was performed with Student's *t*-test. (**E**) DLS analysis of the SR ϕ1, HA–SR ϕ1, and HA.
Abbreviations: DLS, dynamic light scattering; HA, hydroxyapatite; ND, not detectable; PFU, plaque forming unit.

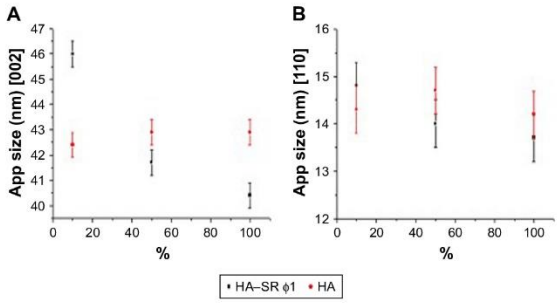

Figure 5 XPD analysis.
Note: Apparent size along the: (**A**) [002] and (**B**) [110] crystallographic directions vs the HA percentage for the complex (HA–SR ϕ1) (black dots) and for HA alone (red dots).
Abbreviations: App, apparent; HA, hydroxyapatite; XPD, X-ray powder diffraction.

phages, when the complex was applied concurrently with the bacteria. The trend observed in HepG2 cells was also observed for murine macrophage cell line J774A.1 (data not shown).

Bacterial reduction assay on chicken minced meat

The efficacy of the complex HA–SR ϕ1 to reduce *Salmonella* contamination was investigated in chicken minced meat which is considered one of the meat categories intended to be cooked before consumption (together with mechanically separated meat and meat preparations) with the highest level of noncompliance, as reported by European Food Safety Authority (EFSA).[62] *S.* Rissen colonies, in the sample treated with SR ϕ1, were reduced by 0.3 log CFU/g, while the sample treated with only HA was contaminated very similar to that of the positive control (5.5 log CFU/g). Instead, in the case of treatments with HA–SR ϕ1, the bacterial load of *S.* Rissen was reduced by 3 log CFU/g (Figure 8).

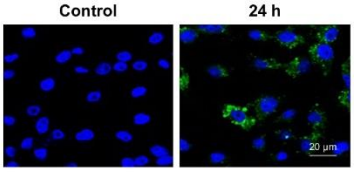

Figure 6 Confocal microscopy analysis.
Notes: Control cells or cells treated with the complex at 24 hours. Scale bars, 20 µm.

Discussion

Different material nanoparticles such as carbon, silica, metal oxide, graphene, and HA have been used in several studies to stabilize, protect, deliver, or enhance some biological properties of molecules.[14–16,30,44]

The characteristics of HA used in this study (such as composition, structure, size, and morphology) and the results obtained allow us to confirm that this mineral, due to its features, was able to chemically interact not only with molecules but also with biological structures like bacteriophages. Its low degree of crystallinity and the presence of carbonate ions in the crystal structure are other important characteristics that make HA extremely reactive in biological systems, and particularly suitable to interact and transport the bacteriophages, as reported in this study.

The bacteriophage SR ϕ1 – isolated in this study – showed an efficient bacteriolytic activity against *S. Livingstone*, *S. Infantis*, *S. Potsdam*, *S. Thompson*, *S. Mbandaka*, *S. Winston*, *S. Montevideo*, *S. Virchow*, *S. Ohio*, *S. Jerusalem*, *S. Inganda*, *S. Wil*, *S. Typhimurium*, and *S. Enteritidis* as shown in Table 1. These results evidenced that it could be used as an antimicrobial agent against the strains of *Salmonella* spp. selected for this study. Further investigations are needed to evaluate whether the phage SR ϕ1 could show antimicrobial activity against other *Salmonella* strains and serovars.

Based on these results, we evaluated whether the use of HA could improve some properties of the bacteriophage. First, we used the mineral HA, which did not affect the cell viability and was not toxic for human cells (Figure S5).

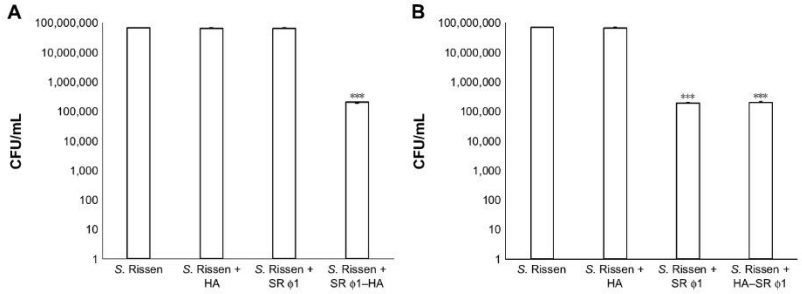

Figure 7 Intracellular killing activity.
Notes: (**A**) First experiment. (**B**) Second experiment. Positive control is represented by *Salmonella* Rissen infected cells. ***$P<0.001$. Each value is the mean ± SD of three independent experiments with three replicates each. Statistical analysis was performed with Student's *t*-test.
Abbreviation: CFU, colony forming unit.

The complex HA–SR ϕ1 showed enhanced lytic activity against *S.* Rissen than SR ϕ1 alone, thus indicating that the interaction with HA increased the antibacterial activity of the bacteriophage. Furthermore, the mineral contributed to stabilize the phage activity over time and at different pH values, making the complex suitable for long-term treatment and effective for controlling infection in harsh niches, showing acid pH (such as stomach, urinary tract, etc), or in different physiological environments of healthy tissues (including blood).

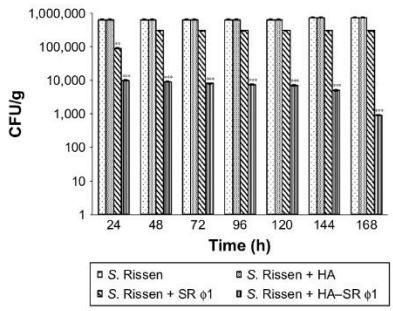

Figure 8 Bacterial reduction assay on chicken meat.
Notes: The samples of the meat were infected with *Samonella* Rissen (10^5 CFU/mL) and were treated with SR ϕ1 (10^7 PFU/mL), HA–SR ϕ1 (100 mg/mL plus 10^9 PFU/mL), and HA (100 mg/mL). Positive control was represented by *S.* Rissen infected meat. **$P<0.01$, ***$P<0.001$. Each value is the mean ± SD of three independent experiments with three replicates each. Statistical analysis was performed with Student's *t*-test.
Abbreviations: CFU, colony forming unit; HA, hydroxyapatite; PFU, plaque forming unit.

The interaction of HA with phage is a good strategy to overcome the problem related to the reduction of bacteriophage viability in acidic conditions.[12]

The zeta potential analysis and DLS measurements demonstrated the interaction of the phage with HA. In fact, Figure 4B showed the behavior of the zeta potential of SR ϕ1 and HA alone and when they were complexed. In the latter case, neutralization of the negative surface charges of SR ϕ1 was observable. Because the charges of two elements are reversed, neutralization of the surface charges could be principally due to electrostatic interactions. Furthermore, the results of the DLS analysis allow us to hypothesize that when the two elements are complexed, the HA acts as a scaffold for the phages.

These results are also supported by Wang et al.[59] Indeed, they demonstrated the ability of the bacteriophages to bind calcium ions, or non-stoichiometric HAs with positive zeta potential.[59] The HA used in this study, just like the ones mentioned above, has a positive zeta potential, a non-stoichiometric Ca/P ratio; all these characteristics induce the interaction of the HA with proteins and carboxyl groups of the phage capsid by the development of an electrostatic bond.

Some studies have shown the capacity of HA to permeate the cell membrane through the energy-dependent process of clathrin-mediated endocytosis[63] or phagocytosis[64] but have, also, highlighted that the permeabilization process is influenced by the equilibrium of multiple features such as dimension, charge, shape, and surface area.[24,64–66]

It has been reported that the bacteriophages are also able to bypass the cell membrane.[67]

Based on these evidences, we tested the capacity of the complex, and in particular the contribution of the mineral HA to penetrate into the eukaryotic cells. The results demonstrated that, in the same infection condition, the presence of the mineral increases the number of phages that are able to penetrate into cells more efficiently and consequently kill intracellular bacteria.[36] This mineral could be a good candidate in the use of phage therapy against obligate or facultative intracellular bacteria like *Mycobacterium* spp., *Chlamydia* spp., *Rickettsia* spp. or *Salmonella* spp., *Listeria* spp., and *Brucella* spp.[68]

In addition, another experiment was carried out on HepG2 cells or J774A.1 cells not infected with bacteria. The results confirmed the ability of the HA to enter into eukaryotic cells and the capacity of bacteriophage to bypass the cell membrane (both reported in literature) and, at the same time, highlighted the role of HA in increasing the number of phages that pass through the cell membrane (data not shown) although there was no infection.

The last test, carried out to evaluate the efficacy of the complex to control bacterial infection in a food matrix such as chicken minced meat and for long time, showed the ability of the complex to reduce bacterial load also in the case of food contamination.

Conclusion

The main drawback in using phages are their lack of stability over time and their low activity against intracellular infections due to their low efficiency in penetrating eukaryotic cells. In addition, phages do not tolerate the low pH present in the stomach and when used in food processing their activity can be compromised. In this study, these problems were successfully addressed by complexing phages with HA (nontoxic mineral for humans). This complex is stable, allows phages to enter eukaryotic cells more efficiently than phages alone, and, at the same time, the complexed phages were stable at very low pH. These results evidence the important contribution of HA making it a promising approach to overcome problems which could emerge when biological entities are used.

One of the most important problems in phage therapy is the application of phages as biocontrol agents against contamination in food.[69] This drawback has been addressed, and it has been resolved by carrying out a test on infected meat. The results showed how HA enhances the lytic activity of phage to control bacterial meat infection. Strikingly, the complex is able to control *Salmonella* infection in food.

Furthermore, the approach proposed here (use of biomimetic HA nanocrystals as a carrier for bacteriophages) can be extended to different fields of interest such as biomedical, agricultural, and other commercial applications.

Acknowledgments

The authors wish to thank Francesco Baldassarre and Chiara Colletti for their assistance in this research.

Author contributions

RC, FCa, and NR have made major contributions to the conception of the study; AF, FI, MP, FCo, TS, CG, SP, RV, BDV, and ML contributed to the acquisition, analysis, or interpretation of the data; AF, FI, MP, CG, and BDV performed the experiments; RC wrote the manuscript. All authors contributed to data analysis, drafting and revising the article, gave final approval of the version to be published, and agree to be accountable for all aspects of the work.

Disclosure

AF, FI, NR, ML, FCo, and RC are the inventors of the Patent IT102017000050733 presented to the Italian Ministry of Economic Development on May 10, 2017. All the other authors report no conflicts of interest in this work.

References

1. Ferri M, Ranucci E, Romagnoli P, Giaccone V. Antimicrobial resistance: a global emerging threat to public health systems. *Crit Rev Food Sci Nutr*. 2017;57(13):2857–2876.
2. Holmes AH, Moore LSP, Sundsfjord A, et al. Understanding the mechanisms and drivers of antimicrobial resistance. *The Lancet*. 2016;387(10014):176–187.
3. Berkowitz FE. Antibiotic resistance in bacteria. *South Med J*. 1995;88(8):797–804.
4. Capuano F, Mancusi A, Capparelli R, Esposito S, Proroga YT. Characterization of drug resistance and virulotypes of *Salmonella* strains isolated from food and humans. *Foodborne Pathog Dis*. 2013;10(11):963–968.
5. Capparelli R, Nocerino N, Lanzetta R, et al. Bacteriophage-resistant *Staphylococcus aureus* mutant confers broad immunity against staphylococcal infection in mice. *PLoS One*. 2010;5(7):e11720.
6. Poirel L, Madec JY, Lupo A, et al. Antimicrobial Resistance in *Escherichia coli*. *Microbiol Spectr*. 2018;6(4).
7. Marco S, Rullo R, Albino A, Masullo M, de Vendittis E, Amato M. The thioredoxin system in the dental caries pathogen *Streptococcus mutans* and the food-industry bacterium *Streptococcus thermophilus*. *Biochimie*. 2013;95(11):2145–2156.
8. Capparelli R, De Chiara F, Nocerino N, et al. New perspectives for natural antimicrobial peptides: application as antinflammatory drugs in a murine model. *BMC Immunol*. 2012;13(1):61.
9. Doss J, Culbertson K, Hahn D, Camacho J, Barekzi N. A review of phage therapy against bacterial pathogens of aquatic and terrestrial organisms. *Viruses*. 2017;9(3):50.
10. Jurczak-Kurek A, Gąsior T, Nejman-Faleńczyk B, et al. Biodiversity of bacteriophages: morphological and biological properties of a large group of phages isolated from urban sewage. *Sci Rep*. 2016;6(1):34338.
11. Inal JM. Phage therapy: a reappraisal of bacteriophages as antibiotics. *Arch Immunol Ther Exp*. 2003;51(4):237–244.
12. Ma Y, Pacan JC, Wang Q, et al. Microencapsulation of bacteriophage felix O1 into chitosan-alginate microspheres for oral delivery. *Appl Environ Microbiol*. 2008;74(15):4799–4805.

13. Colom J, Cano-Sarabia M, Otero J, et al. Microencapsulation with alginate/$CaCO_3$: A strategy for improved phage therapy. *Sci Rep*. 2017; 7(1):41441.
14. Chowdhury S, Yusof F, Salim WW, Sulaiman N, Faruck MO. An overview of drug delivery vehicles for cancer treatment: nanocarriers and nanoparticles including photovoltaic nanoparticles. *J Photochem Photobiol B*. 2016;164:151–159.
15. Krishnamoorthy K, Jeyasubramanian K, Premanathan M, Subbiah G, Shin HS, Kim SJ. Graphene oxide nanopaint. *Carbon*. 2014;72:328–337.
16. Roveri N, Palazzo B, Iafisco M. The role of biomimetism in developing nanostructured inorganic matrices for drug delivery. *Expert Opin Drug Deliv*. 2008;5(8):861–877.
17. Benedetti M, De Castro F, Romano A, et al. Adsorption of the cis-[Pt(NH3)2(P2O7)](2-) (phosphaplatin) on hydroxyapatite nanocrystals as a smart way to selectively release activated cis-[Pt(NH3)2Cl2] (cisplatin) in tumor tissues. *J Inorg Biochem*. 2016;157:73–79.
18. Benedetti M, Antonucci D, De Castro F, et al. Metalated nucleotide chemisorption on hydroxyapatite. *J Inorg Biochem*. 2015;153:279–283.
19. Lelli M, Roveri N, Marzano C, et al. Hydroxyapatite nanocrystals as a smart, pH sensitive, delivery system for kiteplatin. *Dalton Trans*. 2016;45(33):13187–13195.
20. Rimola A, Sakhno Y, Bertinetti L, Lelli M, Martra G, Ugliengo P. Toward a surface science model for biology: glycine adsorption on nanohydroxyapatite with well-defined surfaces. *J Phys Chem Lett*. 2011;2(12):1390–1394.
21. Cai Y, Gao T, Fu S, Sun P. Development of zoledronic acid functionalized hydroxyapatite loaded polymeric nanoparticles for the treatment of osteoporosis. *Exp Ther Med*. 2018;16(2):704–710.
22. Chakraborty S, Das T, Banerjee S, Sarma HD, Venkatesh M. Preparation and preliminary biological evaluation of 177Lu-labelled hydroxyapatite as a promising agent for radiation synovectomy of small joints. *Nucl Med Commun*. 2006;27(8):661–668.
23. Macchetta A, Turner IG, Bowen CR. Fabrication of HA/TCP scaffolds with a graded and porous structure using a camphene-based freeze-casting method. *Acta Biomater*. 2009;5(4):1319–1327.
24. Uskoković V, Uskoković DP. Nanosized hydroxyapatite and other calcium phosphates: chemistry of formation and application as drug and gene delivery agents. *J Biomed Mater Res B Appl Biomater*. 2011;96B(1): 152–191.
25. V Dorozhkin S. Nanodimensional and nanocrystalline calcium orthophosphates. *AJBE*. 2012;2(3):48–97.
26. Fox K, Tran PA, Tran N. Recent advances in research applications of nanophase hydroxyapatite. *Chemphyschem*. 2012;13(10):2495–2506.
27. Rodríguez-Ruiz I, Delgado-López JM, Durán-Olivencia MA, et al. pH-responsive delivery of doxorubicin from citrate-apatite nanocrystals with tailored carbonate content. *Langmuir*. 2013;29(26): 8213–8221.
28. Kozempel J, Vlk M, Málková E, et al. Prospective carriers of 223Ra for targeted alpha particle therapy. *J Radioanal Nucl Chem*. 2015;304(1): 443–447.
29. Palazzo B, Iafisco M, Laforgia M, et al. Biomimetic hydroxyapatite–drug nanocrystals as potential bone substitutes with antitumor drug delivery properties. *Adv Funct Mater*. 2007;17(13):2180–2188.
30. Fulgione A, Nocerino N, Iannaccone M, et al. Lactoferrin adsorbed onto biomimetic hydroxyapatite nanocrystals controlling – in vivo – the helicobacter pylori infection. *PLoS One*. 2016;11(7):e0158646.
31. Beuchat LR. Ecological factors influencing survival and growth of human pathogens on raw fruits and vegetables. *Microbes Infect*. 2002;4(4):413–423.
32. Finstad S, O'Bryan CA, Marcy JA, Crandall PG, Ricke SC. Salmonella and broiler processing in the United States: relationship to foodborne salmonellosis. *Food Res Int*. 2012;45(2):789–794.
33. Herikstad H, Motarjemi Y, Tauxe RV. Salmonella surveillance: a global survey of public health serotyping. *Epidemiol Infect*. 2002;129(1):1–8.
34. Oliveira CJB, Carvalho LFOS, Fernandes SA, Tavechio AT, Menezes CCP, Domingues FJ. Antimicrobial resistance of *Salmonella* serotypes isolated from slaughter-age pigs and environmental samples. *Microb Drug Resist*. 2002;8(4):407–411.
35. Angkititrakul S, Chomvarin C, Chaita T, Kanistanon K, Waethewutajarn S. Epidemiology of antimicrobial resistance in Salmonella isolated from pork, chicken meat and humans in Thailand. *Southeast Asian J Trop Med Public Health*. 2005;36(6):1510–1515.
36. Capparelli R, Parlato M, Borriello G, Salvatore P, Iannelli D. Experimental phage therapy against *Staphylococcus aureus* in mice. *Antimicrob Agents Chemother*. 2007;51(8):2765–2773.
37. SM buffer. Cold Spring Harb Protoc. 2006;2006(1):pdb.rec8111. doi:10.1101/pdb.rec8111.
38. Sambrook J, Fritsch EF, Maniatis T. *Molecular Cloning: A Laboratory Manual*. Cold Spring Harbor, NY: Cold Spring Harbor Laboratory Press; 1989.
39. Zinno P, Devirgiliis C, Ercolini D, Ongeng D, Mauriello G. Bacteriophage P22 to challenge Salmonella in foods. *Int J Food Microbiol*. 2014;191:69–74.
40. Birge EA. *Bacterial and Bacteriophage Genetics*. New York, NY: Springer New York; 2000.
41. Nasukawa T, Uchiyama J, Taharaguchi S, et al. Virus purification by CsCl density gradient using General centrifugation. *Arch Virol*. 2017;162(11):3523–3528.
42. Guindon S, Dufayard J-F, Lefort V, Anisimova M, Hordijk W, Gascuel O. New algorithms and methods to estimate maximum-likelihood phylogenies: assessing the performance of PhyML 3.0. *Syst Biol*. 2010;59(3): 307–321.
43. Aziz RK, Bartels D, Best AA, et al. The RAST server: rapid annotations using subsystems technology. *BMC Genomics*. 2008;9(1):75.
44. Nocerino N, Fulgione A, Iannaccone M, et al. Biological activity of lactoferrin-functionalized biomimetic hydroxyapatite nanocrystals. *Int J Nanomedicine*. 2014;9:1175–1184.
45. Brunauer S, Emmett PH, Teller E. Adsorption of gases in multimolecular layers. *J Am Chem Soc*. 1938;60(2):309–319.
46. Mattila S, Ruotsalainen P, Jalasvuori M. On-demand isolation of bacteriophages against drug-resistant bacteria for personalized phage therapy. *Front Microbiol*. 2015;6(96):1271.
47. Jun JW, Kim JH, Shin SP, Han JE, Chai JY, Park SC. Characterization and complete genome sequence of the Shigella bacteriophage pSf-1. *Res Microbiol*. 2013;164(10):979–986.
48. Altomare L, Fare' S. Cells response to topographic and chemical micropatterns. *J Appl Biomater Biomech*. 2008;6(3):132–143.
49. Fernández-Díaz MT, Martínez JL, Rodríguez-Carvajal J, et al. Metamagnetism in single-crystal Pr_2NiO_4. *Phys Rev B Condens Matter*. 1993;47(10):5834–5840.
50. Cui X, Liang T, Liu C, Yuan Y, Qian J. Correlation of particle properties with cytotoxicity and cellular uptake of hydroxyapatite nanoparticles in human gastric cancer cells. *Mater Sci Eng C Mater Biol Appl*. 2016;67: 453–460.
51. Mclaughlin LM, Govoni GR, Gerke C, et al. The Salmonella SPI2 effector SseI mediates long-term systemic infection by modulating host cell migration. *PLoS Pathog*. 2009;5(11):e1000671.
52. Withanage GSK, Mastroeni P, Brooks HJ, Maskell DJ, Mcconnell I. Oxidative and nitrosative responses of the chicken macrophage cell line MQ-NCSU to experimental *Salmonella* infection. *Br Poult Sci*. 2005;46(3):261–267.
53. Sukumaran AT, Nannapaneni R, Kiess A, Sharma CS. Reduction of Salmonella on chicken meat and chicken skin by combined or sequential application of lytic bacteriophage with chemical antimicrobials. *Int J Food Microbiol*. 2015;207:8–15.
54. ISO 16140-2:2016 – Microbiology of the food chain – Method validation – Part 2: Protocol for the validation of alternative (proprietary) methods against a reference method. Available from: https://www.iso.org/standard/54870.html. Accessed November 29, 2018.
55. Kaneko J, Kimura T, Kawakami Y, Tomita T, Kamio Y. Panton-Valentine leukocidin genes in a phage-like particle isolated from mitomycin C-treated *Staphylococcus aureus* V8 (ATCC 49775). *Biosci Biotechnol Biochem*. 1997;61(11):1960–1962.
56. Palazzo B, Walsh D, Iafisco M, et al. Amino acid synergetic effect on structure, morphology and surface properties of biomimetic apatite nanocrystals. *Acta Biomater*. 2009;5(4):1241–1252.

Papaianni et al. BMC Microbiology (2018) 18:208
https://doi.org/10.1186/s12866-018-1360-z

BMC Microbiology

RESEARCH ARTICLE Open Access

Role of phage ϕ1 in two strains of *Salmonella* Rissen, sensitive and resistant to phage ϕ1

Marina Papaianni[1], Felice Contaldi[1], Andrea Fulgione[1], Sheridan L. Woo[2,3,4], Angela Casillo[5], Maria Michela Corsaro[5], Ermenegilda Parrilli[5], Luca Marcolungo[6], Marzia Rossato[6], Massimo Delledonne[7], Marianna Garonzi[7], Domenico Iannelli[1*] and Rosanna Capparelli[1,4]

Abstract

Background: The study describes the *Salmonella* Rissen phage φ1 isolated from the φ1-sensitive *Salmonella* Rissen strain R^W. The same phage was then used to select the resistant strain R^Rφ1+, which can harbour or not φ1.

Results: Following this approach, we found that φ1, upon excision from R^W cells with mitomycin, behaves as a temperate phage: lyses host cells and generates phage particles; instead, upon spontaneous excision from R^Rφ1+ cells, it does not generate phage particles; causes loss of phage resistance; switches the O-antigen from the smooth to the rough phenotype, and favors the transition of *Salmonella* Rissen from the planktonic to the biofilm growth. The R^W and R^Rφ1+ strains differ by 10 genes; of these, only two (phosphomannomutase_1 and phosphomannomutase_2; both involved in the mannose synthesis pathway) display significant differences at the expression levels. This result suggests that phage resistance is associated with these two genes.

Conclusions: Phage φ1 displays the unusual property of behaving as template as well as lytic phage. This feature was used by the phage to modulate several phases of *Salmonella* Rissen lifestyle.

Keywords: Phage selection, *Salmonella* Rissen, Cost of resistance, Phase variation, Repeatable evolution

Background

Bacteria are under constant attack by bacteriophages (phages), the most abundant life forms in the biosphere [1]. They have evolved a variety of defense mechanisms against phages, which in turn have evolved mechanisms to offset the defense plans set up by bacteria [2]. Generally, phages recognize only very few strains of the same bacterial species [3], a tactic maximizing the benefits from recombination with phages having the same lifestyle and genomic organization [4]. Bacteria frequently gain resistance by losing the phage receptor [2] or reducing its binding specificity [5]. Bacteria can also promote a temporary change of the phage receptor specificity. They do it through a mechanism known as phase variation. In a context of antagonistic co-evolution [6], rapidity in the response to a phage attack is fundamental for bacterial survival. Phase variation confers resistance at a much faster rate than random mutation [7]. Bacteria and phages both exploit phase variation: *S. enterica* ser. Typhimurium to express alternative forms of the O-antigen and escape phage attack [8, 9]; *Escherichia* (*E.*) *coli* phage Mu [10] and other phages [11] to alternatively express different ligands and expand their host range. Phage receptors often function also as bacterial virulence factors. The reversibility of phase variation curbs this toll by limiting it strictly to the duration of phage infection. In addition to reversibility, phase variation displays the property of regulating the expression of several traits in a co-ordinate fashion [8], a feature that adds efficiency to this mechanism. Recent studies show that - to maximize survival of a fraction of the population in case of sudden environmental changes - reversible phase variation can occur randomly [12]. In conclusion, the above examples well explain how the role of phase variation in the

* Correspondence: iannelli@unina.it
[1]Department of Agriculture, University of Naples "Federico II", via Università 100, 80055 Portici, Naples, Italy
Full list of author information is available at the end of the article

bacterial world is to rapidly generate diversity and enable bacteria to colonize different hosts and survive in changing environments [8].

The term superinfection exclusion (SE) describes the property of a preexisting prophage to inhibit a secondary infection by the same – or a very close – phage [13, 14]. SE is mediated by proteins that block the penetration of phage DNA inside the host cell soon after infection [2]. As an example, the SE protein A of *S. enterica* ser. Typhimurium carrying the lysogenic phage P22 confers protection against infection by the phages L, MG178, or MG40 [15]. The proteins blocking the phage DNA penetration can be of bacterial or phage origin. SE in fact can benefit the phage as well as the host. SE, reducing the cost of phage infection, sets conditions for a mutualistic relationship [16], where the phage benefits of increased transmission opportunities and protection against predators, while providing the host with virulence factors [17], toxins [18], or promoting gene transfer and thus bacterial genome variability [19].

Here we describe the *S.* Rissen phage ϕ1. This phage was excised from the ϕ1-sensitive *S.* Rissen strain R^W and then used to select the ϕ1-resistant strain R^Rϕ1+, which can spontaneously lose ϕ1. The ϕ1 excised from R^W cells with mitomycin behaves as an inducible temperate phage since lyses host cells and generates phage particles. Instead, the spontaneous excision of ϕ1 from R^Rϕ1+ cells does not generate phage particles, promotes biofilm production, loss of phage resistance, and the switch of the O-antigen from smooth to rough. To carry out the above tasks, phage ϕ1 uses all the resources described earlier: phase variation, SE, and SE inhibition.

Finally, because of their rapid evolution and easy replication of experiments, bacteria are frequently used to investigate whether evolution is contingent or repeatable, an issue still debated [20]. Here we show that four independent ϕ1-resistant clones isolated from the same ϕ1-sensitive strain R^W, all display identical mutations at two *phosphomannomutase* genes.

Results

Phage isolation and bacterial strains characterization

Following incubation with mitomycin C, the wild type *S.* Rissen bacteria (R^W) yielded phage ϕ1 (titer: 10^7 PFU/mL; burst size: 50 PFU/cell) and release of ϕ1 particles was followed by host cell lysis. Instead, the spontaneous release of ϕ1 from R^Rϕ1+ cells (R^Sϕ1-) occurs without recovery of phage particles and is also associated with increased biofilm production (Fig. 1a-d) and the phage-sensitive phenotype (Table 1). Ordinarily, lysogenic strains are immune to the phage that they produce (phenomenon known as SE). Remarkably, R^W bacteria were positive by the double layer agar (DLA) method with ϕ1, indicating that the ϕ1 prophage is resistant to the SE mechanism.

Moreover, R^Rϕ1+ and R^W colonies differ in curli production: R^Rϕ1+ colonies express the "*ras*" (red and smooth) phenotype, while R^W colonies display the "*pdar*" (pink red and dry) phenotype (characterized by a reduced amount of curli) [21] (Table 1). Furthermore, the strains R^Sϕ1- and R^W are both ϕ1-sensitive, while that R^Rϕ1+ is ϕ1-resistant (Table 1). Also, DOC- polyacrylamide gel electrophoresis of lipopolysaccharide (LPS) showed that the ϕ1-sensitive strains R^W and R^Sϕ1- display the semi-rough and rough phenotypes, respectively, while the ϕ1-resistant strain R^Rϕ1+ shows the smooth phenotype (Fig. 2a). Accurate phage ϕ1 adsorption experiments confirmed that ϕ1 binds to the semi-rough or rough strains but not to the smooth one (Fig. 2b). Phages specific for rough strains have already been described in *S. enterica* ser. Typhimurium [22, 23] and *Pseudomonas (P.) aeruginosa* [24]. Further, carbohydrate analysis of LPS indicated that ϕ1-sensitive cells - compared to the ϕ1-resistant ones - are associated with higher mannose synthesis (Additional file 1: Figure S1).

Genome sequencing and assembling

Phage ϕ1 yielded a total of 2,199,543 reads (660 Mb) and an average coverage of 13,200 x. The de-novo assembled phage ϕ1 genome is 51,738 bp long with a GC content of 48,4%. The genome contains 87 predicted coding sequences (CDSs): 30 affecting bacteriophage physiology, 12 encoding phage structures, 10 regulating DNA replication, and 3 encoding bacterial lysis. Genome sequence and general phage organization can be found in the annotation (available on GenBank accession: KY709687). The phylogenetic tree of phage ϕ1 genome was reconstructed by comparing its proteome with those of 37 fully sequenced phage genomes. Phage ϕ1 disclosed a robust orthology with 5 members of *Podoviridae* (3 *Salmon* and 2 *Entero phages*: 53–72% DNA identity) and therefore assigned to this family (Fig. 3a). The short, stubby, and non-contractible tail confirmed ϕ1 as a member of the *Podoviridae* family (Fig. 3b). Data generated from the R^Rϕ1+ bacteria by PacBio sequencing evidenced that the phage is circular and double-stranded. Upon mitomycin-induced excision, ϕ1 transduces a 5 kb-long portion of the host genome from R^Rϕ1+, and R^W (Fig. 3c). Apparently, transduction of the 5 kb fragment occurs randomly (Additional file 2: Figure S2).

Illumina sequencing of R^W and R^Rϕ1+ was generated 8,036,355 (2.4 Gb; coverage 602x) and 12,639,370 reads (3.8 Gb; coverage 948x), respectively. To identify the insertion site of ϕ1, we assembled de novo the reads generated from R^W and R^Rϕ1+ and compared them. This approach yielded 104,974 reads with an average length of 5305 bp for a total of 556 Mb and an average coverage

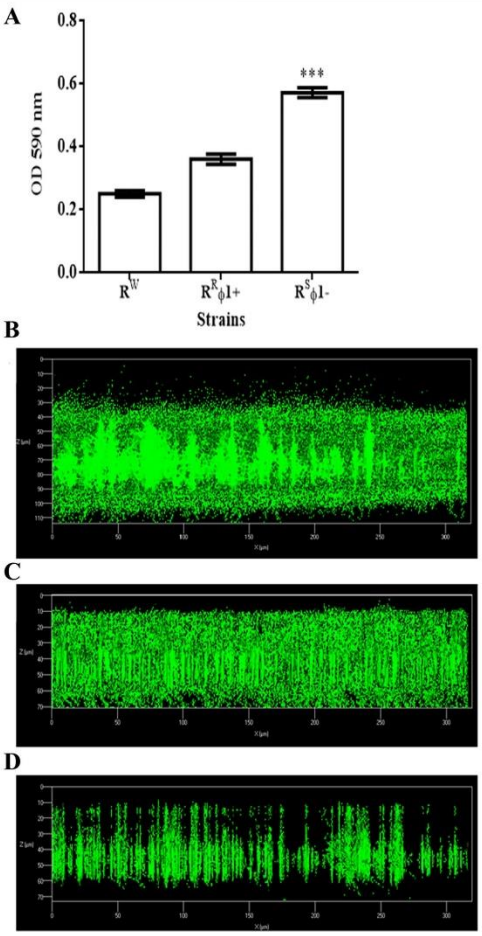

Fig. 1 Phage φ1 influences biofilm production. **a** Quantitative and **b-d** Confocal Laser Scanning Microscopy (CLSM) analyses of biofilm produced by: **b** R^Sφ1-; **c** R^Rφ1+; and **d** R^W bacteria. Bacteria were grown in 8-well chamber slide for 20 h and then stained with LIVE/DEAD reagents. Green fluorescence (SYTO9) indicates viable cells and red fluorescence (PI) dead cells

Table 1 Distinctive traits of the different *Salmonella* Rissen strains

Strain	Biofilm production	Φ1 presence	Morphology phenotype	Φ1 resistance
R^W	+/−	+	*pdar*	−
R^Rφ1+	++	+	*ras*	+
R^Sφ1-	++++	−	*pdar*	−

1–4: Amount of Biofilm production; +: positive; −: negative; *pdar* Pink dry and red phenotype, *ras* Red and smooth phenotype

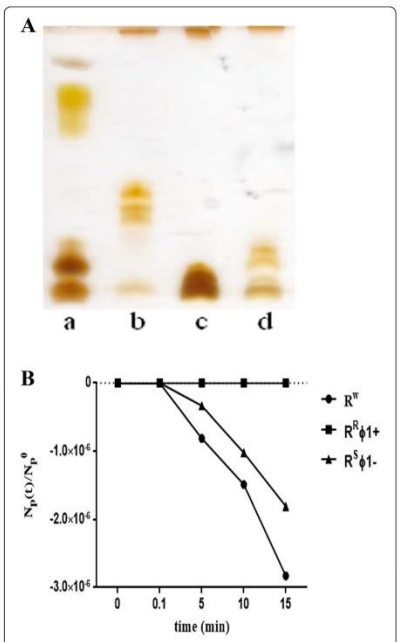

Fig. 2 Strains chemical phenotypes and phage φ1 binding activities. **a** R^Rφ1+ (lane b), R^Sφ1- (lane c), and R^W (lane d) display the smooth, rough, and semi-rough phenotypes, respectively. The reference marker (lane a) is the LPS from *E. coli* O55:B5. **b** R^Rφ1+ strain (φ1-resistant and smooth) does not bind the phage; R^W strain (φ1-sensitive and semi-rough) binds the phage, while R^Sφ1- strain (φ1-sensitive and rough) displays an intermediate level of phage binding activity

of 116X. We could thus establish that in the R^Rϕ1+ strain phage ϕ1 is inserted at the end of the genome (from 4,828,664 to 4,834,023 bps) (Fig. 3d).

Phage resistance results from frameshift mutations in two genes of the mannose pathway

Comparative genomics showed that the two strains R^W and R^Rϕ1+ differ by 10 genes, each displaying from 1 to 15 SNP sites (Additional file 3: Table S1). The expression levels of the genes *phosphomannomutase1* and *phosphomannomutase2* participating to the mannose synthesis are higher in the susceptible strain R^Sϕ1- compared to the resistant strain R^Rϕ1+ (Fig. 4). This result concurs with evidence from carbohydrate analysis of LPS (Additional file 1: Figure S1). We conclude that phage ϕ1 resistance is associated with reduced expression levels of the *phosphomannomutase1* and *phosphomannomutase2* genes. As often observed in bacteria [25–27], phage ϕ1 resistance was gained by phase variation via frameshift mutation in homopolymeric tracts (HTs) (Fig. 5a and b). Four independent phage-resistant mutants from R^W (R^{R1-4}) all displayed the same differential gene expression already observed in the original strains R^W and R^R ϕ1 + .

Discussion

This study describes the properties of ϕ1, a prophage which modulates several phases of *S.* Rissen life style. In general, prophages aid bacteria with the production of virulence molecules [18], toxins [28], antibiotics [18], or (as in this study) support the bacterial host conferring phage resistance (Fig. 2b), increasing biofilm production (Fig. 1a-d), and providing new genetic material (Fig. 5a and b and Additional file 3: Table S1).

Given the importance of ϕ1 in the life style of the *S.* Rissen, it seems plausible to suggest that the absence of superinfection immunity serves to permit ϕ1 to rapidly abandon or re-infect the host, as environmental circumstances require.

We found that induction of ϕ1 excision with mitomycin in R^W cells leads to replication and release of phage particles. Instead, ϕ1 excision from R^Rϕ1+ cells - spontaneous or induced by thermal shock – does not lead to replication and release of phage particles. This result suggests that phage replication is inhibited in R^Rϕ1+ cells. As already proposed for the *Listeria (L.) monocytogenes* ϕ10403S, we

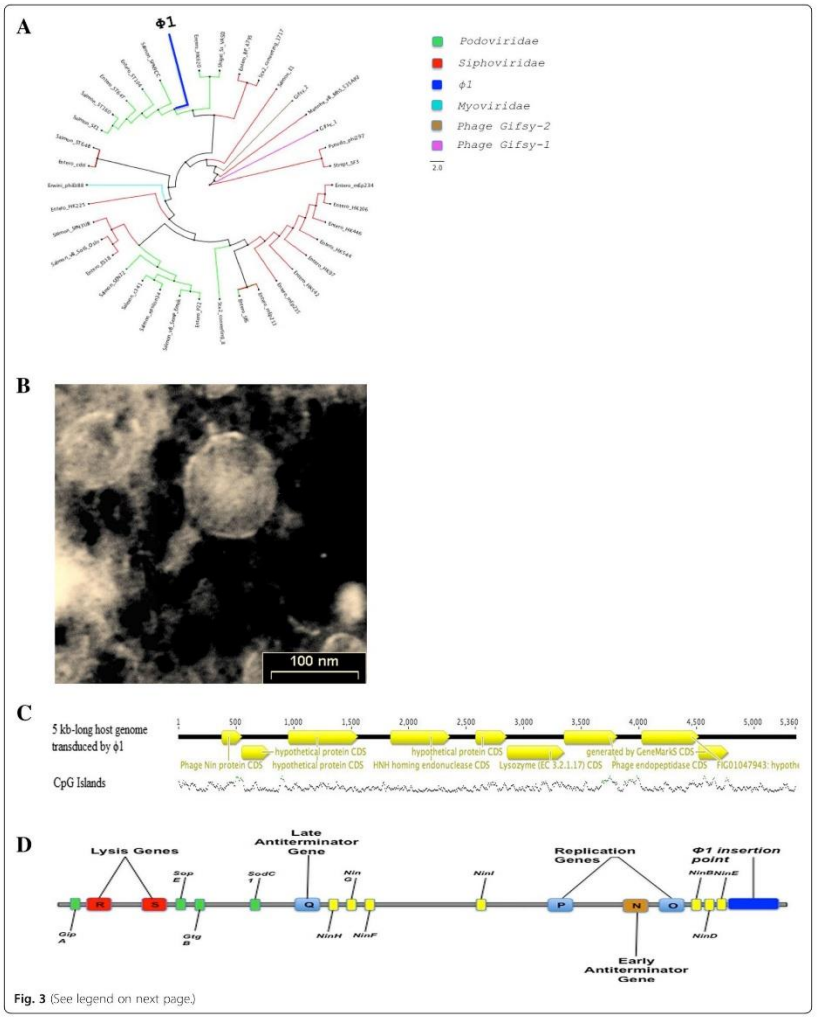

Fig. 3 (See legend on next page.)

(See figure on previous page.)
Fig. 3 Phage φ1 properties. **a** The phylogenetic tree shows a strong DNA identity between φ1 and 5 members of the Podovoridae (3 Salmon and 2 Entero phages). The tree is based on the alignment of 39 phage genomes. The bar indicates branch length scale. **b** Transmission Electron Microscopy (TEM) of bacteriophage φ1. The short and non-contractile tail, characteristic of Podoviridae, confirms φ1 as a member of this family. The scale bar corresponds to 100 nm. **c** Upon excision, phage φ1 transduces a 5 kb long region of the host genome. The region includes the following genes: 5 hypothetical proteins, 1 phage endopeptidase, 1 HNH homing endonuclease, 1 lysozyme and 1 phage Nin protein. **d** The phage φ1 insertion point is at the end of the R^{R}φ1+ strain genome (from 4,828,664 to 4, 834, 023 bps)

speculate that ϕ1 or the R^{R}ϕ1+ host cells can disconnect phage excision from phage replication and release [29].

The cases of bacterial genes controlled by prophage excision generally involve cryptic prophages [30, 31]. Phage ϕ1 is not cryptic since, following induction with mitomycin, produces infective particles. Thus, ϕ1 is a rare - but not unique [31] – example of non-cryptic prophage influencing the expression of the host cell genes.

Many bacterial species, including *Salmonella*, gain phage resistance by altering the genes of the LPS biosynthesis pathway [24]. In *E. coli*, nine different genes are involved in the LPS biosynthesis pathway, which potentially could lead to T7 phage resistance, but bacteria reach resistance by altering *waaG*, the gene associated with reduced biological cost [32].

Our study describes similar results. Four independent ϕ1-resistant strains isolated from the same strain (R^{W}) and grown under the same conditions displayed the same regulatory alteration at two genes (*phosphomannomutase1* and p*hosphomannomutase2*) (Fig. 4). Parallel evolution has also been reported in *L. monocytogenes* [33], *E. coli* [34] and *Propionibacterium* (*P.) acnes* [35]. These results suggest that whenever it is possible, phage resistance is acquired using the path requiring a lower cost. The same explanation could be extended to the acquisition of phage resistance by phase variation, as observed in several bacterial species: *Campylobacter (C.) jejuni* [25], *Vibrio* (*V.) cholerae* [26], *L. monocytogenes* [27, 33], *Herpes* (*H.) influenzae* [36], *Staphylococcus* (*S.) aureus* [37], and *S.* Rissen (this study). Also, in most of these bacterial species (including *S.* Rissen), phase variation originates from HTs frameshift mutations (Fig. 5a and b) and is reversible. Phage resistance by frameshift mutations instead is rapid and reversible: once phage infection ends, the phage-resistant bacteria can revert to the more adaptive phage-sensitive genotype.

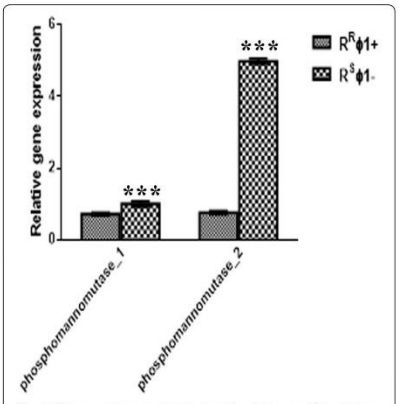

Fig. 4 Differences in expression levels of the 10 genes differentiating the R^{R}φ1+ and R^{S}φ1- strains. The resistant strain (R^{R}φ1+) displays significantly reduced expression levels of the *phosphomannomutase1* and *phosphomannomutase2* genes, compared to the sensitive strain (R^{S}φ1-). The relative gene expression levels are expressed using the R^{W} strain as internal comparison

Conclusions

This study describes a phage which modulates several properties of its host. The results of this study may stimulate researchers to better understand benefits and negative outcomes associated with the therapeutic use of phages; how the stability of mutations is influenced by environmental stresses; how phages affect evolution and pathogenicity of bacteria. Finally, the study demonstrates that, at least in bacteria, natural selection uses repeatedly the same evolutionary path, when it requires a lower biological cost.

Methods

Bacterial strains

The *S.* Rissen strain R^{W} (serotype 6; antisera were from Staten Serum, Copenhagen, Denmark) was isolated from a food matrix and characterized by Istituto Zooprofilattico Sperimentale Del Mezzogiorno (Portici, Naples, Italy). The *S.* Rissen strain R^{R} was derived - in the course of this research - from the R^{W} strain following selection for resistance to phage ϕ1 as described in this study. R^{R} cells can spontaneously lose the prophage and thus occur with (R^{R}ϕ1+) or without ϕ1 (R^{S}ϕ1-) (the superscript S indicates that loss of ϕ1 causes loss of phage resistance). All the bacterial strains were analyzed for cellulose production and LPS phenotype and stored at – 20 °C in LB (Sigma-Aldrich, Milan, Italy) supplemented with glycerol (10%; Sigma-Aldrich, Milan, Italy).

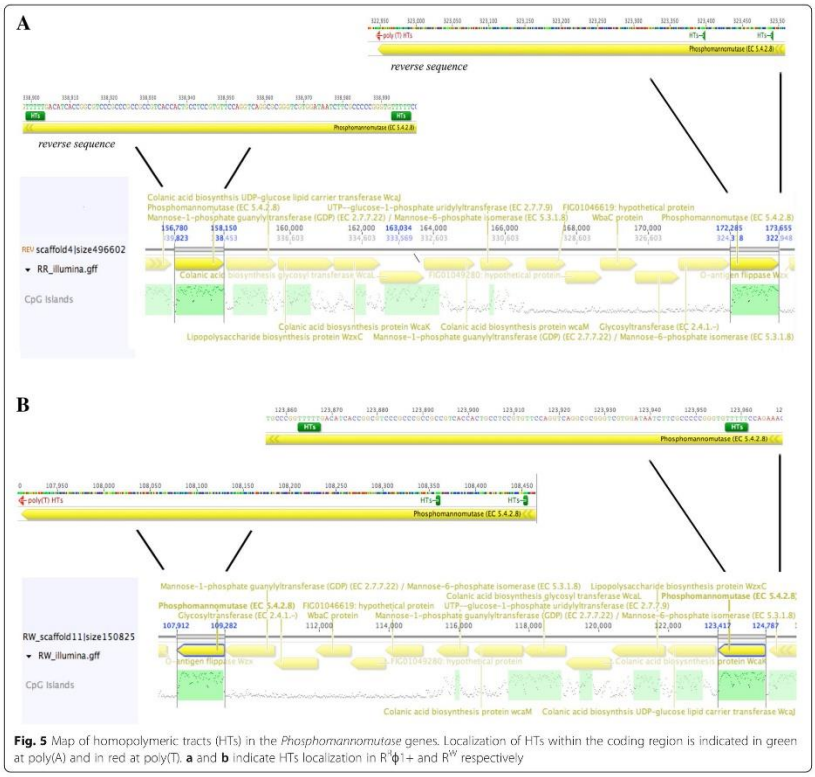

Fig. 5 Map of homopolymeric tracts (HTs) in the *Phosphomannomutase* genes. Localization of HTs within the coding region is indicated in green at poly(A) and in red at poly(T). **a** and **b** indicate HTs localization in $R^{W}\phi1+$ and R^{W} respectively

Isolation of the phage φ1

Phage ϕ1 excision was induced by incubating R^{W} cells (2×10^{8} CFU/5 mL) in LB broth containing 1 μg/mL mitomycin C (Sigma-Aldrich, Milan, Italy) for 1 h at 37 °C. Following centrifugation (5.7×10^{3} g), the supernatant was stored at + 4 °C, and the pellet resuspended in 5 mL of LB broth and incubated again at 37 °C for 4 h and then centrifuged. The pellet was discarded, while the supernatants from the two centrifugations were pooled and filtered (filter pore size: 0.22 μm; MF-Millipore, Darmstadt, Germany) [38].

The titer of phage, expressed as plaque forming units (PFU), was evaluated by using the DLA technique as reported by Sambrook et al. [39] Phage ϕ1 was stored in SM buffer at − 20 °C. The aliquot in use was kept at + 4 °C.

Isolation of the phage φ1-resistant strain R^{R}

R^{W} bacteria in early exponential growth phase were mixed with warm soft agar. The mixture was poured on LB agar (Sigma-Aldrich, Milan, Italy) plates and allowed to solidify. Phage ϕ1 was then spotted (10 μL/spot) and the plates were incubated overnight at 37 °C. The following morning, the colonies grown inside the lysis plaques were picked with a sterile loop and streaked on LB agar plate. This procedure was repeated 3 times. Phage-resistant bacteria were further tested for phage ϕ1 resistance by the spot test. Plaque absence after overnight

incubation confirmed that bacteria were phage ϕ1-resistant (R^Rϕ1+). Phage ϕ1-resistant colonies were detected after about 24 h of selection.

Lysogenization

R^Sϕ1- bacteria (10^8 CFU in 500 μL LB) were incubated with ϕ1 isolated from R^W bacteria (10^8 PFU/mL) for 72 h. The suspension was mixed with soft agar (4 mL) and then poured on a solid agar. Phage ϕ1was spotted on soft agar (10 μL/spot) and plates were incubated at + 37 °C and inspected daily for plaque formation.

Analysis of cellulose production

Cellulose production was detected by growing bacteria on LB agar supplemented with 200 μg/mL calcofluor (Sigma-Aldrich, Milan, Italy). Plates were incubated at 37 °C for 2–4 days. Colonies were visualized under a 366-nm light source [40]. Congo red binding was detected by growing bacteria on LB agar supplemented with Congo red (40 μg/mL; Sigma-Aldrich, Milan, Italy).

Biofilm thickness determined by confocal laser scanning microscopy

Biofilms were formed on polystyrene Chamber Slides (n ° 177,445; Thermo Scientific, Ottawa, Canada). For this purpose, overnight cultures of R^Rϕ1+, R^Sϕ1-, and R^W strains grown in LB medium were diluted to a final concentration of 0.001 and seeded into a chamber slide at 37 °C for 36 h to assess biofilm thickness and cell viability. The biofilm cell viability was determined with the FilmTracer™ LIVE/DEAD® Biofilm Viability Kit (Molecular Probes, Invitrogen, Carlsbad, California, USA) following the manufacturer's instructions. Microscopic observations and image acquisitions were performed as described [41].

Salmonella genome sequencing, assembly and annotation

The R^W or R^R strains were expanded in LB broth starting from a single colony. Genomic DNA was then extracted by the phenol-chloroform method, purified with Agencourt AMPure XP beads (Beckman Coulter; beads to DNA ratio 1.8:1), and quantified by the Qubit dsDNA BR Assay Kit (Thermo Fisher, MA, USA). DNA size and purity were measured by the 2200 Tape Station Instrument (Agilent Genomics) and Nanodrop (Thermo Fisher), respectively. Illumina libraries were obtained from 1 μg of genomic DNA, and sequenced with the NextSeq500 instrument using the 150 nt paired-end protocol (Illumina, San Diego, CA). Illumina reads were quality filtered, trimmed using Sickle and finally quality corrected with BayesHammer. Genomes were assembled de novo from Illumina reads using SPAdes 2.9.0 with multiple k-mer combinations: from 101 to 125 with 2 nt steps for the 202 R^R genome, with 95, 97, 111, 113 for the R^W genome and 101, 105, 109, 113, 117, 121,125 for the ϕ1 genome. The resultant contigs were scaffolded using SSPACE 3.0. Five μg high-molecular-weight genomic DNA (peak >60Kb) were used to prepare ~ 20 Kb-insert SMRT-bell libraries (Pacific Biosciences, CA, USA). The library templates were sequenced using the single molecule real time (SMRT) Sequencing technology on a PacBio RSII sequencer (Pacific Biosciences, Macrogen Inc., Korea). PacBio subreads were extracted using Bash5tools (version 0.8.0), filtered and assembled de-novo with Falcon-Integrate and the settings suggested for bacterial genome. The assembled genome sequence was polished by Quiver v 0.9.2. and gene annotation performed using RAST web service (http://rast.nmpdr.org/) [42]. The ϕ1 insertion site was identified by mapping PacBio reads from R^Rϕ1+ bacteria against the phage genome assembly and soft-clipped bases were retrieved.

Variant SNP calling

SNP calling was carried out using MUMmer 3.23 tool [43]. Single-nucleotide polymorphisms (SNPs) were identified by Show-SNPs, a script associated with MUMmer 3.23.

The output was filtered by BUFF > 50 with the Show-SNPs flags CIIrx 25 and the SNP position was assembly by quality > 80. The R^W *Salmonella* genome was used as reference. Each assembly was queried with each SNP context from the MUMmer output using BLAST + [44], retaining only SNPs for which exactly one occurrence of either of the two genomes was found in all assemblies.

Chemical analysis

PAGE was performed using the system of Laemmli [45] with sodium deoxycholate (DOC; Thermo Scientific, Waltham, MA USA) as detergent as described [46]. Glycosyl analysis was performed as reported [47].

Real time PCR

Total RNA was extracted from individual bacterial strains according to the Allprep Bacterial DNA/RNA/Protein Kit protocol (Quiagen) and then reverse-transcribed using the high-capacity cDNA reverse transcription kit (Applied Biosystem). Real-time PCR was carried out using the Step One Real-Time PCR Systems machine (Thermo-Fisher scientific). Reactions were carried out in a 20 μl of Master SYBR Green I mix (Roche Diagnostics Ltd., Lewes, UK). The amplification protocol included 10 min at 95 °C and 40 cycles, each consisting of 10 s at 95 °C for denaturation, 120 min at 57 °C for annealing, and 60 s at 60 °C for extension; the final step was at 4 °C. PCR reactions were carried out in triplicate. Expression values were normalized versus the R^W strain. The reference gene was the housekeeping

InvA. The relative gene expression was carried out using the Delta Delta ct Method [48].

Other methods

Following the genome sequencing experiment, we designed the primers for the 5 kb region using primer 3 as primer design tool. We used the following overlapping eight primer pairs. Primers are designed to amplify regions within a size range of 400–600 bp.

The thermal shock of R^W or $R^R\phi1+$ cells was carried out by exposing the cells at − 20 °C for 1 h and + 40 °C for 2 h. The cells were then tested for loss of phage resistance. The phylogenetic tree was constructed using the maximum likelihood method [49]; for data alignment were used the Blosum 65 (gap open penalty = 11; gap extension penalty = 3), Jukes-Cantor, and UPGMA models. Biofilm production was measured by the crystal violet assay [50].

Additional files

Additional file 1: Figure S1. Gas chromatography-mass spectrometry (GC-MS) analysis of the (A) R^W, (B) $R^R\varphi1+$, and (C) $R^R\varphi1$-strains. All of the strains display the presence of glucose, glucosamine, heotose, and KDO. Acquisition of phage resistance by $R^R\varphi1+$ strain is associated with loss of mannose. Peaks marked with X represent methyl esters of fatty acids. (PDF 673 kb)

Additional file 2: Figure S2. Electrophoresis gel of PCR for detecting the presence of 5 kb region. Lines 1–5: RWφ1+; lines 6–9: RWφ1-; lines 10–14: RRφ1+; lines 15–18: RSφ1-; M = marker (100 kb). (PDF 35 kb)

Additional file 3: Table S1. SNPs detection analysis of R^W and $R^3\phi1+$ strains. (PDF 107 kb)

Abbreviations

CDSs: Coding sequences; DLA: Double layer agar; HTs: Homopolymeric tracts; LPS: Lipopolysaccharide; Pdar: Pink red and dry; Ras: Red and smooth; SE: Superinfection exclusion

Acknowledgements

The authors thank two anonymous reviewers for their insightful suggestions, which improved the manuscript substantially.

Funding

The work was made possible by internal funding awards to RC, SLW and MD. The funding source had no role in the design of the study and collection, analysis, and interpretation of data.

Availability of data and materials

All data generated or analysed during this study are included in this published article [and its supplementary information files].

Authors' contributions

DI, RC, MD have made major contributions to the conception and design of the study; FC, LM, MG, MR, AC, MMC, EP, SLW to the acquisition, analysis, or interpretation of the data; FC, VL, AF, MP, SLW performed the experiments and participated to the interpretation of data; DI, RC wrote the manuscript. All authors read and approved the final manuscript.

Ethics approval and consent to participate

Not applicable.

Consent for publication

Not applicable.

Competing interests

The authors declare that they have no competing interests.

Publisher's Note

Author details

[1]Department of Agriculture, University of Naples "Federico II", via Università 100, 80055 Portici, Naples, Italy. [2]Department of Pharmacy, University of Naples "Federico II", via Domenico Montesano 49, 80131 Naples, Italy. [3]National Research Council, Institute for Sustainable Plant Protection, via Università 133, 80055 Portici, Naples, Italy. [4]Task Force on Microbiome Studies, University of Naples "Federico II", via Università 100, 80055 Portici, Naples, Italy. [5]Department of Chemical Sciences, University of Naples "Federico II", via Cintia 4, 80126 Naples, Italy. [6]Department of Biotechnology, University of Verona, Strada Le Grazie 15, 37134 Verona, Italy. [7]Personal Genomics, Strada le Grazie 15, 37134 Verona, Italy.

Received: 18 September 2018 Accepted: 28 November 2018
Published online: 07 December 2018

References

1. Suttle CA. Marine viruses — major players in the global ecosystem. Nat Rev Microbiol. 2007;5:801–12.
2. Labrie SJ, Samson JE, Moineau S. Bacteriophage resistance mechanisms. Nat Rev Microbiol. 2010;8:317–27.
3. Hyman P, Abedon ST. Bacteriophage host range and bacterial resistance. In: Advances in applied microbiology; 2010. p. 217–48.
4. Hendrix RW. Bacteriophage evolution and the role of phages in host evolution. In: Phages. Washington: American Society of Microbiology; 2005. p. 55–65.
5. Drexler K, Riede I, Montag D, Eschbach ML, Henning U. Receptor specificity of the Escherichia coli T-even type phage Ox2. Mutational alterations in host range mutants. J Mol Biol. 1989;207:797–803.
6. Buckling A, Rainey PB. Antagonistic coevolution between a bacterium and a bacteriophage. Proc Biol Sci. 2002;269:931–6.
7. Bayliss CD. Determinants of phase variation rate and the fitness implications of differing rates for bacterial pathogens and commensals. FEMS Microbiol Rev. 2009;33:504–20.
8. Kwan LY, Isaacson RE. Identification and characterization of a phase-variable nonfimbrial Salmonella typhimurium gene that alters O-antigen production. Infect Immun. 1998;66:5725–30.
9. Broadbent SE, Davies MR, van der Woude MW. Phase variation controls expression of Salmonella lipopolysaccharide modification genes by a DNA methylation-dependent mechanism. Mol Microbiol. 2010;77:337–53.
10. Kamp D, Kahmann R, Zipser D, Broker TR, Chow LT. Inversion of the G DNA segment of phage mu controls phage infectivity. Nature. 1978;271:577–80.
11. Sandmeier H, Iida S, Arber W. DNA inversion regions min of plasmid p15B and Cin of bacteriophage P1: evolution of bacteriophage tail fiber genes. J Bacteriol. 1992;174:3936–44.
12. Dybvig K. DNA rearrangements and phenotypic switching in prokaryotes. Mol Microbiol. 1993;10:465–71.
13. Bertani G. Studies on lysogenesis. III. Superinfection of lysogenic Shigella dysenteriae with temperate mutants of the carried phage. J Bacteriol. 1954; 67:696–707.
14. McCloy EW. Lysogenicity and immunity to Bacillus phage W. J Gen Microbiol. 1958;18:198–220.
15. Hofer B, Ruge M, Dreiseikelmann B. The superinfection exclusion gene (sieA) of bacteriophage P22: identification and overexpression of the gene and localization of the gene product. J Bacteriol. 1995;177:3080–6.
16. Ferdy J, Godelle B. Diversification of transmission modes and the evolution of mutualism. Am Nat. 2005;166:613–27.
17. Wagner PL, Neely MN, Zhang X, Acheson DW, Waldor MK, Friedman DI. Role for a phage promoter in Shiga toxin 2 expression from a pathogenic Escherichia coli strain. J Bacteriol. 2001;183:2081–5.
18. Wagner PL, Waldor MK. Bacteriophage control of bacterial virulence. Infect Immun. 2002;70:3985–93.
19. Stern A, Sorek R. The phage-host arms race: shaping the evolution of microbes. BioEssays. 2011;33:43–51.

20. Meyer JR, Dobias DT, Weitz JS, Barrick JE, Quick RT, Lenski RE. Repeatability and contingency in the evolution of a key innovation in phage lambda. Science. 2012;335:428–32.
21. Römling U, Bian Z, Hammar M, Sierralta WD, Normark S. Curli fibers are highly conserved between Salmonella typhimurium and Escherichia coli with respect to operon structure and regulation. J Bacteriol. 1998; 180:722–31.
22. Kim M, Kim S, Park B, Ryu S. Core lipopolysaccharide-specific phage SSU5 as an auxiliary component of a phage cocktail for Salmonella biocontrol. Appl Environ Microbiol. 2014;80:1026–34.
23. Wilkinson RG, Gemski P, Stocker BA. Non-smooth mutants of Salmonella typhimurium: differentiation by phage sensitivity and genetic mapping. J Gen Microbiol. 1972;70:527–54.
24. Jarrell KF, Kropinski AM. Isolation and characterization of a bacteriophage specific for the lipopolysaccharide of rough derivatives of Pseudomonas aeruginosa strain PAO. J Virol. 1981;38:529–38.
25. Scott AE, Timms AR, Connerton PL, Loc Carrillo C, Adzfa Radzum K, Connerton IF. Genome dynamics of campylobacter jejuni in response to bacteriophage predation. PLoS Pathog. 2007;3:e119.
26. Seed KD, Faruque SM, Mekalanos JJ, Calderwood SB, Qadri F, Camilli A. Phase variable O antigen biosynthetic genes control expression of the major protective antigen and bacteriophage receptor in Vibrio cholerae O1. PLoS Pathog. 2012;8:e1002917.
27. Orsi RH, Bowen BM, Wiedmann M. Homopolymeric tracts represent a general regulatory mechanism in prokaryotes. BMC Genomics. 2010;11:102.
28. Johnson LP, Schlievert PM. Group a streptococcal phage T12 carries the structural gene for pyrogenic exotoxin type a. Mol Gen Genet. 1984;194:52–6.
29. Rabinovich L, Sigal N, Borovok I, Nir-Paz R, Herskovits AA. Prophage excision activates Listeria competence genes that promote phagosomal escape and virulence. Cell. 2012;150:792–802.
30. Kirby JE, Trempy JE, Gottesman S. Excision of a P4-like cryptic prophage leads to alp protease expression in Escherichia coli. J Bacteriol. 1994;176: 2068–81.
31. Scott J, Thompson-Mayberry P, Lahmamsi S, King CJ, McShan WM. Phage-associated Mutator phenotype in group a streptococcus. J Bacteriol. 2008; 190:6290–301.
32. Perry EB, Barrick JE, Bohannan BJM. The molecular and genetic basis of repeatable coevolution between Escherichia coli and bacteriophage T3 in a laboratory microcosm. PLoS One. 2015;10:e0130639.
33. Denes T, den Bakker HC, Tokman JI, Guldimann C, Wiedmann M. Selection and characterization of phage-resistant mutant strains of Listeria monocytogenes reveal host genes linked to phage adsorption. Appl Environ Microbiol. 2015;81:4295–305.
34. Blount ZD, Borland CZ, Lenski RE. Historical contingency and the evolution of a key innovation in an experimental population of Escherichia coli. Proc Natl Acad Sci U S A. 2008;105:7899–906.
35. Scholz CFP, Brüggemann H, Lomholt HB, Tettelin H, Kilian M. Genome stability of Propionibacterium acnes: a comprehensive study of indels and homopolymeric tracts. Sci Rep. 2016;6:20662.
36. Zaleski P, Wojciechowski M, Piekarowicz A. The role of dam methylation in phase variation of Haemophilus influenzae genes involved in defence against phage infection. Microbiology. 2005;151(Pt 10):3361–9.
37. Brooks JL, Jefferson KK. Phase variation of poly-N-Acetylglucosamine expression in Staphylococcus aureus. PLoS Pathog. 2014;10:e1004292.
38. Capparelli R, Parlato M, Borriello G, Salvatore P, Iannelli D. Experimental phage therapy against Staphylococcus aureus in mice. Antimicrob Agents Chemother. 2007;51:2765–73.
39. Sambrook J, Fritsch EF, Maniatis T. Molecular cloning: a laboratory manual. New York: Cold Spring Harbor Laboratory Press; 1989.
40. Barak JD, Gorski L, Naraghi-Arani P, Charkowski AO. Salmonella enterica virulence genes are required for bacterial attachment to plant tissue. Appl Environ Microbiol. 2005;71:5685–91. https://doi.org/10.1128/AEM.71.10.5685-5691.2005.
41. Casillo A, Papa R, Ricciardelli A, Sannino F, Ziaco M, Tilotta M, et al. Anti-biofilm activity of a long-chain fatty aldehyde from Antarctic Pseudoalteromonas haloplanktis TAC125 against Staphylococcus epidermidis biofilm. Front Cell Infect Microbiol. 2017;7:46. https://doi.org/10.3389/fcimb.2017.00046.
42. Aziz RK, Bartels D, Best AA, DeJongh M, Disz T, Edwards RA, et al. The RAST server: rapid annotations using subsystems technology. BMC Genomics. 2008;9:75.
43. Kurtz S, Phillippy A, Delcher AL, Smoot M, Shumway M, Antonescu C, et al. Versatile and open software for comparing large genomes. Genome Biol. 2004;5:R12. https://doi.org/10.1186/gb-2004-5-2-r12.
44. Camacho C, Coulouris G, Avagyan V, Ma N, Papadopoulos J, Bealer K, et al. BLAST+: architecture and applications. BMC Bioinformatics. 2009;10:421.
45. Laemmli UK. Cleavage of structural proteins during the assembly of the head of bacteriophage T4. Nature. 1970;227:680–5. https://doi.org/10.1038/227680a0.
46. Carillo S, Casillo A, Pieretti G, Parrilli E, Sannino F, Bayer-Giraldi M, et al. A unique capsular polysaccharide structure from the psychrophilic marine bacterium *Colwellia psychrerythraea* 34H that mimics antifreeze (Glyco)proteins. J Am Chem Soc. 2015;137:179–89. https://doi.org/10.1021/ja5075954.
47. Casillo A, Parrilli E, Filomena S, Lindner B, Lanzetta R, Parrilli M, et al. Structural investigation of the oligosaccharide portion isolated from the Lipooligosaccharide of the permafrost Psychrophile Psychrobacter arcticus 273-4. Mar Drugs. 2015;13:4539–55. https://doi.org/10.3390/md13074539.
48. Rao X, Huang X, Zhou Z, Lin X. An improvement of the 2^(−delta delta CT) method for quantitative real-time polymerase chain reaction data analysis. Biostat Bioinforma Biomath. 2013;3:71–85 http://www.ncbi.nlm.nih.gov/pubmed/25558171. Accessed 22 Nov 2018.
49. Guindon S, Dufayard J-F, Lefort V, Anisimova M, Hordijk W, Gascuel O. New algorithms and methods to estimate maximum-likelihood phylogenies: assessing the performance of PhyML 3.0. Syst Biol. 2010;59:307–21.
50. Djordjevic D, Wiedmann M, McLandsborough LA. Microtiter plate assay for assessment of Listeria monocytogenes biofilm formation. Appl Environ Microbiol. 2002;68:2950–8.

57. Capparelli R, Ianniello F, Capuano F, et al. Complesso comprendente almeno un calcio fosfato ED almeno un virus. 2017.
58. Goode D, Allen VM, Barrow PA. Reduction of experimental Salmonella and Campylobacter contamination of chicken skin by application of lytic bacteriophages. *Appl Environ Microbiol*. 2003;69(8):5032–5036.
59. Wang F, Cao B, Mao C. Bacteriophage bundles with Pre-Aligned Ca initiate the oriented nucleation and growth of hydroxylapatite. *Chem Mater*. 2010;22(12):3630–3636.
60. Kay MI, Young RA, Posner AS. Crystal structure of hydroxyapatite. *Nature*. 1964;204(4963):1050–1052.
61. Awad WA, Aschenbach JR, Zentek J. Cytotoxicity and metabolic stress induced by deoxynivalenol in the porcine intestinal IPEC-J2 cell line. *J Anim Physiol Anim Nutr*. 2012;96(4):709–716.
62. The European Union summary report on trends and sources of zoonoses, zoonotic agents and food–borne outbreaks in 2016. *EFSA J*. 2017;15(12):5077.
63. Bauer IW, Li SP, Han YC, Yuan L, Yin MZ. Internalization of hydroxyapatite nanoparticles in liver cancer cells. *J Mater Sci Mater Med*. 2008;19(3):1091–1095.
64. Motskin M, Wright DM, Muller K, et al. Hydroxyapatite nano and microparticles: correlation of particle properties with cytotoxicity and biostability. *Biomaterials*. 2009;30(19):3307–3317.
65. Yang X, Li Y, Liu X, Zhang R, Feng Q. In vitro uptake of hydroxyapatite nanoparticles and their effect on osteogenic differentiation of human mesenchymal stem cells. *Stem Cells Int*. 2018;2018(34):1–10.
66. Yin M, Xu W, Cui B, et al. Effects of the interaction between hydroxyapatite nanoparticles and hepatoma cells. *J Wuhan Univ Technol Mat Sci Edit*. 2014;29(3):635–642.
67. Nguyen S, Baker K, Padman BS, et al. Bacteriophage transcytosis provides a mechanism to cross epithelial cell layers. *MBio*. 2017;8(6):6.
68. Silva MT. Classical labeling of bacterial pathogens according to their lifestyle in the host: inconsistencies and alternatives. *Front Microbiol*. 2012;3:71.
69. Cooper IR. A review of current methods using bacteriophages in live animals, food and animal products intended for human consumption. *J Microbiol Methods*. 2016;130:38–47.

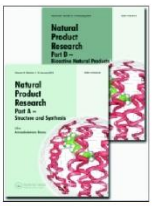

Natural Product Research
Formerly Natural Product Letters

ISSN: 1478-6419 (Print) 1478-6427 (Online) Journal homepage: https://www.tandfonline.com/loi/gnpl20

Structural data and immunomodulatory properties of a water-soluble heteroglycan extracted from the mycelium of an Italian isolate of *Ganoderma lucidum*

Raffaele Carrieri, Rosanna Manco, Daniela Sapio, Marco Iannaccone, Andrea Fulgione, Marina Papaianni, Bruna de Falco, Laura Grauso, Paola Tarantino, Flora Ianniello, Virginia Lanzotti, Ernesto Lahoz & Rosanna Capparelli

To cite this article: Raffaele Carrieri, Rosanna Manco, Daniela Sapio, Marco Iannaccone, Andrea Fulgione, Marina Papaianni, Bruna de Falco, Laura Grauso, Paola Tarantino, Flora Ianniello, Virginia Lanzotti, Ernesto Lahoz & Rosanna Capparelli (2017) Structural data and immunomodulatory properties of a water-soluble heteroglycan extracted from the mycelium of an Italian isolate of *Ganoderma lucidum*, Natural Product Research, 31:18, 2119-2125, DOI: 10.1080/14786419.2017.1278593

To link to this article: https://doi.org/10.1080/14786419.2017.1278593

1. Introduction

Fungi play an important role in several aspects of human life, in particular as source of therapeutics and food. Many fungi naturally produce antibiotics, which are able to inhibit the growth of the competing micro-organisms. The edible fungi (mushrooms) are often favoured in the human diet because they are poor in fat and rich in proteins, minerals and fibres (Manzi et al. 1999). Fungal cell walls are rich in bioactive polysaccharides (glycans), which are different from each other in chemical structure and biological activity (Herrera 2012). Glucans are the most abundant (and most studied as well) fungal glycans and they have only D-glucose as structural component: it is possible to distinguish linear or branched α-, β- as well as mixed α,β-glucans (Synytsya & Novak 2014). β-glucans of several fungi show numerous biological properties, including antitumour, antimicrobial, antidiabetic, antihypercholesterolemic and immunomodulating activities (Wasser 2011; Chang & Wasser 2012). Krestin – a heteroglycan isolated from *Polysticus versicolor* and consisted of glucose and other simple sugars – has antitumour, antihepatitis and antihyperlipidemic properties. Pachymaran – a heteroglycan purified from *Poria cocos* and consisted of glucose, galactose and mannose units – has antitumour activity and is used to treat insomnia and schizophrenia. *Grifola frondosa* heteroglycans – consisted of glucose, xylose, fucose, galactose and mannose units – show anticancer and immunomodulatory properties (Zhou et al. 2014).

Biological properties of fungal glycans vary depending on their water solubility, chemical composition and conformational structure (Polishchuk & Kovalenko 2009), but the basic requirements for biological activity are not still completely clear (Brown & Gordon 2003). Eight fungal glycans-based drugs are marketed in China, each of them displays unique polysaccharide composition and biological effects (Zhou et al. 2014). In general, water-soluble glycans are considered pharmacologically more active (Hu et al. 2013). Moreover, isolation methods may influence the features of the glycans and differences can be observed among compounds differentially isolated from the same source (Volman et al. 2008).

Ganoderma lucidum (Curtis) P. Karst is a lignocellulose-degrading mushroom of the Polyporaceae family. Over the past centuries, its fruiting bodies have been widely used in the Chinese and Japanese traditional medicine for the treatment of several disorders (such as gastritis, diabetes, hypercholesterolemia, hepatitis and cardiovascular problems). Modern research – by confirming the antitumour, antihypertensive, antidiabetic and immunomodulatory properties of *G. lucidum* extracts (Boh et al. 2007; Rex 2014) – has sensibly contributed to the success of this mushroom as nutraceutical so that the annual sale of *G. lucidum*-derived products is estimated about 2.5 billion U.S. dollars (Li et al. 2013). The major bioactive compounds of *Ganoderma* species are polysaccharides (such as β-glucans, glycoproteins and heteroglycans) and triterpenoids (Nie et al. 2013; Ruan et al. 2014), both usually isolated from the fruiting bodies of Asian isolates. In particular, polysaccharides are known for their anticancer and antimicrobial effects and their capacity to enhance the host immune system (Lin 2005), but there are few available studies about polysaccharides obtained from mycelium of European isolates of *G. lucidum* (Boh et al. 2007).

This study investigated immunomodulatory properties and capacity to improve glucose metabolism of a water-soluble heteroglycan (HGlyc), extracted from the mycelium of an Italian isolate of *G. lucidum*. For this purpose, gene expression analyses and two different bioenergetic assays were carried out in a cell line model. The report also describes an alkaline method, that combines purity with high yield, for the extraction of HGlyc and the chemical characterisation by NMR spectroscopy.

2. Results and discussion

2.1. Extraction of HGlyc

Eight grams of dry material were obtained from 80 g of fresh mycelium. About 20 mg of a water-soluble heteroglycan (composed by units of several monosaccharides) were extracted from 2 g of lyophilised mycelium. Simplicity and high yield suggest the possibility to use the method for a large-scale production of HGlyc from the mycelium of *G. lucidum*.

2.2. Monosaccharide composition and ^{1}H NMR spectrum

Preliminary studies were performed to determine the structure of HGlyc. The monosaccharide composition was determined by complete hydrolysis of the glycan at 100°C in water/TFA, followed by $NaBH_4$ reduction and acetylation with acetic anhydride. GC–MS analysis of the resulting alditol acetates showed the glycan to be composed of glucose, mannose, fucose, xylose and galactose, in the molar ratios 58:16:14:7:5 (see Experimental Part for details).

The ^{1}H NMR spectrum of the glycan in D_2O was recorded to obtain information about the anomeric configurations of the sugars. Firstly, the anomeric protons were identified from their correlation with the relevant anomeric carbons using an HSQC 2D NMR (Figure S1). To make ^{1}H signals as sharp as possible, the spectrum was acquired at 70°C. Even so, all signals appeared as unresolved broad singlets, and proton-proton coupling constants (the most reliable parameter for determination of anomeric configurations) could not be measured. Therefore, the determination of anomeric configuration was based on chemical shifts of anomeric protons (typically δ 5.2–4.9 for α-sugars and δ 4.6–4.3 for β-sugars) (Synytsya & Novak 2014). The anomeric region of the spectrum of HGlyc was quite complex (Figure S1), with multiple signals of different intensity both in the region of α-sugars and β-sugars. Integration showed an approximate 3:1 ratio between the overall areas of the signals of α-anomeric protons and β-anomeric protons, showing that most sugars were in the α configuration.

A more detailed analysis of the structure of HGlyc is in progress and the results will be reported in the due course.

2.3. Cell viability and NO_2 measurements

At the concentrations of 200, 500 and 1000 μg mL^{-1}, HGlyc did not affect cell viability, while the positive control (THP-1 cells treated with 50% ethanol) showed a 70% reduction of cell viability. Compared to the cells treated only with 10 μg mL^{-1} LPS, HGlyc (at the concentration of 200 μg mL^{-1}) reduced NO_2 production by 67% (Figure S2).

2.4. Bioenergetic analyses

Basal and maximal glycolysis values and glycolytic capacity were calculated (Figure 1(a–b)). Upon glucose addition, the medium of LPS-treated cells showed a significant increase of acidification (422%), compared to untreated cells, indicating a higher rate of basal glycolysis. Instead, when cells were treated with HGlyc and then LPS, a reduction of basal glycolysis was observed (53%). Next, incubating cells with oligomycine, the property of HGlyc to curb the maximal glycolysis was measured. Again, the HGlyc significantly reduced the maximal

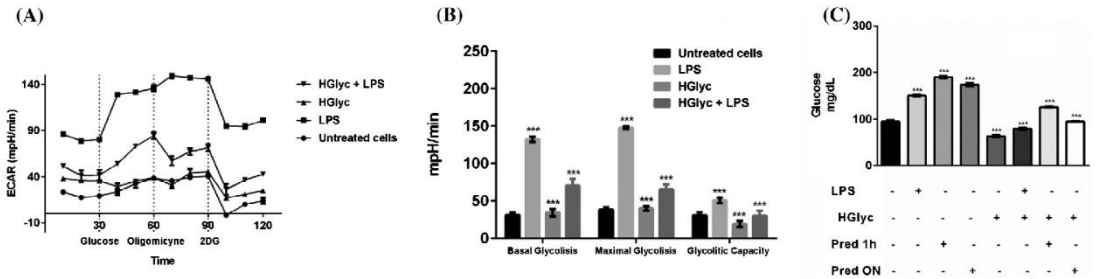

Figure 1. Bioenergetic assays. (a) ECAR parameters by extracellular flux technology. The values were measured, at baseline and after sequential addition of glucose, oligomycine and 2-DG, in: untreated THP-1 cells; cells treated 12 h with HGlyc 200 µg mL^{-1}; cells treated 1 h with LPS (10 µg mL^{-1}); cells treated with HGlyc and then LPS. Data are expressed as the rate of extracellular acidification in mpH/min. Data are shown as mean ± SE of triplicates for each measure. (b) Basal glycolysis, maximal glycolysis and glycolytic capacity. The parameters were measured in the following experimental conditions: untreated THP-1 cells; cells treated 12 h with HGlyc 200 µg mL^{-1}; cells treated 1 h with LPS (10 µg mL^{-1}); cells treated with HGlyc and then LPS. Data are expressed as mean ± SE of three measurements, each of them in triplicate. (c) Glucose-oxidase activity assay. Glucose amount secreted into the medium was measured in: THP-1 untreated cells; cells treated 1 h with LPS 10 µg mL^{-1}; cells incubated 1 h and 12 h (ON) with Prednisone 200 µg mL^{-1}; cells treated 12 h with HGlyc 200 µg mL^{-1}; cells treated with HGlyc and LPS; cells treated with HGlyc and Prednisone for 1 h or 12 h. Values represent the average determination ± SE for three experiments. Each experiment was carried out in triplicate.

glycolysis (44%). Finally, to measure the glycolytic capacity of the cells, 2-DG reagent was added. As expected, the glycolytic capacity was also significantly reduced (36%).

Glucose-oxidase activity, an index of glucose uptake in cells, was evaluated in eight experimental conditions (Figure 1(c)). Glucose level was markedly higher in cells treated with LPS or prednisone (1 h and 12 h), compared to untreated cells (58.5, 100 and 83%, respectively). LPS and prednisone are reported to determine an increase of glucose uptake, up-regulating the expression of glucose-transporter genes (Chung 2008; Hwang & Weiss 2014). Further, the property of HGlyc to curb the glucose uptake was measured: in cells treated with HGlyc and then with LPS or prednisone (1 h and 12 h), a reduction of glucose level (52, 66 and 95%, respectively) was registered. Cells treated only with HGlyc showed a glucose level lower (66%) than untreated cells.

Taken together, NO_2 measurements and ECAR values showed the capacity of HGlyc to reduce stress in inflammatory conditions induced by LPS in the model cell line. In our knowledge, ECAR analysis was used for the first time to investigate the effect of a fungal polysaccharide on cellular glucose metabolism. In addition, GOA assay indicated a hypoglycemic activity of HGlyc. Ability to reduce glucose levels in blood was already reported for polysaccharides from *G. lucidum* (He et al. 2006; Jia et al. 2009).

2.5. Gene expression

The expression levels of four important pro-inflammatory cytokines (TNF-α, IL-6, IL1-α and IL-1β) were measured. HGlyc was used at the optimal concentration of 200 μg mL^{-1}. The cells incubated with HGlyc and LPS displayed down-regulation of three cytokine genes: TNF-α by 28.5%; IL-6 and IL-1α by 94%, compared to the positive control (cells incubated only with LPS). On the contrary, IL-1β gene was up-regulated by 40%. The cytokines mRNA level was identical in cells treated with HGlyc and in untreated cells. The analysis was extended to the mediator of inflammation COX-2, that resulted significantly down-regulated (33% compared to positive control) (Figure 2). Down-regulation of pro-inflammatory molecules mediated

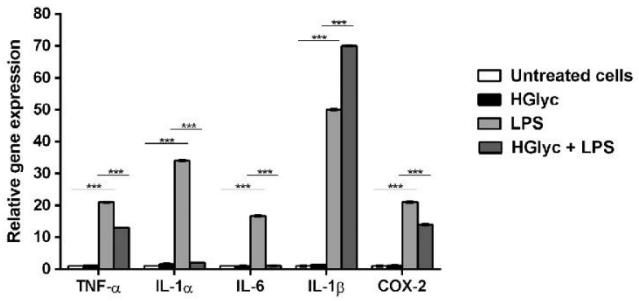

Figure 2. Expression levels of TNF-α, IL-6, IL1-α, IL-1β and COX-2 genes involved in immune response. The gene expression was evaluated in: untreated THP-1 cells; cells treated 12 h with HGlyc 200 μg mL^{-1}; cells treated 1 h with LPS (10 μg mL^{-1}); cells treated with HGlyc and then LPS. Values represent the average determination ± SE for three experiments, carried out in triplicate. A pool of THP-1 untreated cells was used as a calibrator for real time PCR experiments. *** = $p < 0.0001$. *P*-values express statistical significance for LPS-treated cells versus untreated cells, and for cells treated with HGlyc + LPS versus LPS-treated cells.

by *G. lucidum* polysaccharides was described in a previous report (Wang et al. 2014), in which water insoluble β-glucans extracted from fruit bodies reduced LPS-induced inflammation in mouse macrophages.

3. Conclusions

Different types of bioactive glycans – which vary in monosaccharide composition, glycosidic bonds, tertiary structure and molecular weight – have been purified from fruiting bodies of *G. lucidum* (Zhou et al. 2014). This study reports a method – easily reproducible – for the extraction of a water-soluble heteroglycan (HGlyc) from the mycelium of *G. lucidum*. HGlyc has glucose as major monosaccharide and it contains mannose, fucose, xylose and galactose. HGlyc exhibited the capacity to significantly reduce the inflammation induced by LPS in THP-1 cells in a dose-dependent manner. In cells incubated with HGlyc and then LPS, the expression levels of the mediators of inflammation TNF-α, IL-6, IL1-α and COX-2 were significantly down-regulated, compared to LPS-treated cells. On the contrary, HGlyc up-regulated the expression of IL-1β. This result is consistent with the property of fungal glucans to activate the transcription of this cytokine via the dectin-1-dependent pathway (Kankkunen et al. 2010). Bioenergetics assays and NO_2 measurements also confirmed the property of HGlyc to reduce cellular stress in inflammatory conditions, indicating at same time a hypoglycemic activity. HGlyc from *G. lucidum* are able to control excessive inflammation and to establish a homeostasis between pro- and anti-inflammatory responses, so they could be used as a probiotic or as ingredient in functional foods, with protective effects in pro-inflammatory conditions and benefits for people characterised by suppressed immune response.

In the last years, the idea to develop functional foods or drugs containing fungal polysaccharides is attracting great attention (Aida et al. 2009). Numerous health products based on *G. lucidum* are internationally marketed (Chang & Buswell 2008). Fruiting bodies are very rare in nature, so the amount of wild *G. lucidum* is not sufficient to meet the demands in international markets and its cultivation *in vitro* is essential. In the present work, a water-soluble heteroglycan was efficiently and economically isolated from the mycelium of *G. lucidum*, suggesting the possibility of a large scale production by submerged cultivations in bio-reactors. The benefits of liquid cultivations include: i) the ability to manipulate the medium to optimise mycelium growth; ii) reduced costs; iii) shorter cultivation time and lower risk of contamination, compared to the cultivation of fruiting bodies.

Furthermore, water solubility makes HGlyc easier to disperse in a food matrix and so more favourable for therapeutic applications, because they are easy to be absorbed by the organism and consequently more effective.

However, further studies are needed and these concepts should be confirmed in future trials *in vivo* using realistic food matrices.

Disclosure statement

No potential conflict of interest was reported by the authors.

References

Aida FMNA, Shuhaimi M, Yazid M, Maaruf AG. 2009. Mushroom as a potential source of prebiotics: a review. Trends Food Sci Tech. 20:567–575.

Boh B, Berovic M, Zhang J, Zhi-Bin L. 2007. *G. lucidum* and its pharmaceutically active compounds. Biotechnol Ann Rev. 13:265–301.

Brown GB, Gordon S. 2003. Fungal β-glucans and mammalian immunity. Immunity. 19:311–315.

Chang ST, Buswell JA. 2008. Development of the world mushroom industry: applied mushroom biology and international mushroom organizations. Int J Med Mushrooms. 10:195–208.

Chang ST, Wasser SP. 2012. The role of culinary-medicinal mushrooms on human welfare with a pyramid model for human health. Int J Med Mushrooms. 14:95–134.

Chung JS. 2008. A trehalose 6-phosphate synthase gene of the hemocytes of the blue crab, *Callinectes sapidus*: cloning, the expression, its enzyme activity and relationship to hemolymph trehalose levels. Saline Syst. 4:18–25.

He CY, Li WD, Guo SX, Lin SQ, Lin ZB. 2006. Effect of polysaccharides from *Ganoderma lucidum* on streptozotocin-induced diabetic nephropathy in mice. J Asian Nat Prod Res. 8:705–711.

Herrera JR. 2012. Fungal cell wall structure, synthesis and assembly. 2nd ed. Boca Raton: CRC Press. Chapter 2.

Hu DJ, Cheong KL, Zhao J, Li SP. 2013. Chromatography in characterization of polysaccharides from medicinal plants and fungi. J Sep Sci. 36:1–19.

Hwang JL, Weiss RE. 2014. Steroid-induced diabetes: a clinical and molecular approach to understanding and mechanism. Diabetes-Metab Res. 30:96–102.

Jia J, Zhang X, Hu YS, Wu Y, Wang QZ, Li NN, Guo QC, Dong XC. 2009. Evaluation of *in vivo* antioxidant activities of *Ganoderma lucidum* polysaccharides in STZ-diabetic rats. Food Chem. 115:32–36.

Kankkunen P, Teirila L, Rintahaka J, Alenius H, Wolff H, Matikainen S. 2010. (1,3)-β-glucans activate both dectin-1 and NPRP3 inflammasome in human macrophages. J Immunol. 184:6335–6342.

Li J, Zhang J, Chen H, Chen XQ, Lan L, Liu C. 2013. Complete mitochondrial genome of the medicinal mushroom *Ganoderma lucidum*. PLoS One. 8:1–11.

Lin ZB. 2005. Cellular and molecular mechanisms of immune-modulation by *Ganoderma lucidum*. J Pharmacol Sci. 99:144–153.

Manzi P, Gambelli L, Marconi S, Vivanti V, Pizzoferrato L. 1999. Nutrients in edible mushrooms: an inter-species comparative study. Food Chem. 65:477–482.

Nie S, Zhang H, Li W, Xie M. 2013. Current development of polysaccharides from Ganoderma: isolation, structure and bioactivities. Bioact Carbohydr Dietary Fibre. 1:10–20.

Polishchuk EN, Kovalenko AG. 2009. Biological activity of glycopolymers from Basidiomycetes mushrooms. Biopolym Cell. 25:181–193.

Rex DAB. 2014. Selenium enriched mushrooms as a food supplement for prevention of neurodegenerative diseases. Int J Pharm Pharm Sci. 6:1–2.

Ruan W, Lim AH, Huang LG, Popovich DG. 2014. Extraction optimization and isolation of triterpenoids from *Ganoderma lucidum* and their effect on human carcinoma cell growth. Nat Prod Res. 28:2264–2272.

Synytsya A, Novak M. 2014. Structural analysis of glucans. Ann Transl Med. 2:17–30.

Volman J, Ramakers JD, Plat J. 2008. Dietary modulation of immune function by β-glucans. Physiol Behav. 94:276–284.

Wang J, Yuan Y, Yue T. 2014. Immunostimulatory activities of β-D-glucan from *Ganoderma lucidum*. Carbohyd Polym. 102:47–54.

Wasser SP. 2011. Current findings, future trends and unsolved problems in studies of medicinal mushrooms. Appl Microbiol Biot. 89:1323–1332.

Zhou Z, Han Z, Zeng Y, Zhang M, Cui Y, Xu L, Zhang L. 2014. Chinese FDA approved fungal glycan-based drugs: an overview of structures, mechanisms and clinical related studies. Transl Med. 4:141–151.